Scientific
Research

Natural
Science
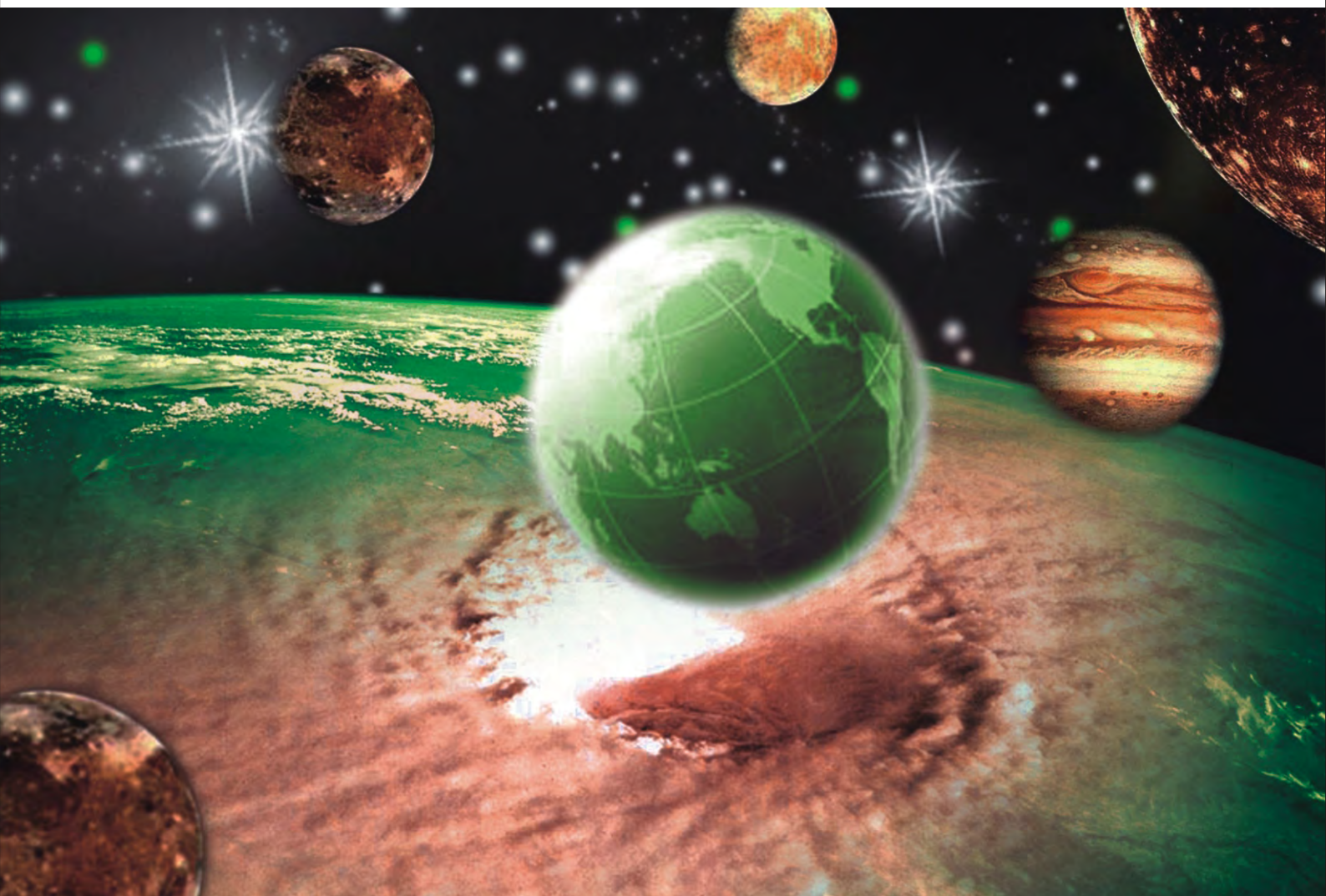
Editor-in-Chief
Kuo-Chen Chou

www.scirp.org/journal/ns/

TABLE OF CONTENTS

Volume 2, Number 8, August 2010

COPYRIGHT

PRODUCTION INFORMATION

Natural Science

Potentiometric, spectrophotometric, conductimetric and thermodynamic studies on some transition metal complexes derived from 3-methyl-1-phenyl- and 1, 3-diphenyl-4-arylazo-5-pyrazolones

Samir A. Abdel-Latif[1]*, Saber E. Mansour[2], Abdulrahman A. Fatouh[2]

1Chemistry Department, Faculty of Science, Helwan University, Helwan, Egypt; *Corresponding Author: salatif_1@yahoo.com
2Chemistry Department, Faculty of Science, Omar Al-Mukhtar University, Al-Beidaa, Libya

ABSTRACT

A new 3-methyl-1-phenyl-4-arylazo-5-pyrazolone and 1, 3-diphenyl-4-arylazo-5-pyrazolone have been synthesized and characterized by elemental analysis, IR, mass and ^{1}H NMR spectra. The acid dissociation constants (pK_a values) of the investigated ligands were determined potentiometrically and spectrophotometrically. The stability constants of the transition metal ions (VO^{2+}, Cr^{3+}, Mn^{2+}, Co^{2+}, Ni^{2+}, Cu^{2+} and Zn^{2+}) with the investigated ligands were determined potentiometrically at different ionic strengths (0.167, 0.1, 0.05 and 0.025 M) NaCl at 25⁰C and different temperature (25, 30, 35, and 45⁰C). The values of stability constants were found to decrease with increasing ionic strengths and temperature. The stoichiometries were studied using spectrophotometric and conductimetric methods, the results indicate the existence of 1:1 and 1:2 (M:L) metal:ligand species. The relationships between the stability constants of the complexes, ionization constants of the ligands have been discussed and correlated. The thermodynamic parameters (ΔG, ΔH and ΔS) and the thermodynamic stability constants for all of the investigated complexes were determined potentiometrically.

Keywords: Azopyrazolones; Lonization Constants; Stability Constants; Thermodynamic Parameters; Transition Metal Complexes; Potentiometry; Spectrophotometry

1. INTRODUCTION

Pyrazolone and azopyrazolone compounds are widely used as analytical reagents, they are capable of forming chelates with a number of metal cations [1,2], the formation of which is accompanied by change in color, pH, conductivity, and absorption spectra [3]. Azo derivatives have attracted much attention by virtue of their applicability as potential ligands for a large number of metal ions [1]. The 4-position of pyrazoline-5-one system is highly reactive and undergoes coupling reaction with diazonium salts to give 4-arylazo derivatives [4]. The azo-derivatives of 5-pyrazolones as well as their metal complexes have wide applications in dye industry as well as analytical reagents for determination of trace metals and it is predicted to have some medical and biological applications [5,6]. Different methods were reported for the syntheses of azopyrazolone derivatives [7-12].

The present paper deals with the determination of the stability constants of the binary complexes of VO^{2+}, Cr^{3+}, Mn^{2+}, Co^{2+}, Ni^{2+}, Cu^{2+} and Zn^{2+} metal ions with the investigated ligands (L1-L6) in the presence of 0.167, 0.1, 0.05 and 0.025 M at 25ºC. The thermodynamic parameters (ΔG, ΔH and ΔS) and the thermodynamic stability constants of the investigated complexes were evaluated in the presence of 0.1 M NaCl in the temperature range 25-45ºC. The Irving and Rossotti pH-metric titration using Sarin and Munchi technique [13] was used to determine the acid dissociation constants as well as the formation constants for the various complexes at 25ºC. The acid dissociation constants were also done in 40% ethanolic buffer solutions of varying pH values spectrophotometrically [14]. The molar ratio of the metal ions to ligands [M]/[L] were studied spectrophotometrically using molar-ratio and continuous variation methods and were also determined using conductimetric titrations in aqueous ethanolic solutions (40% v/v).

2. EXPERIMENTAL

2.1. Materials and Methods

All chemicals used in this investigation were chemically pure grade derived from BDH. They include chlorides of Cr^{3+}, Mn^{2+}, Co^{2+}, Ni^{2+}, Cu^{2+}, Zn^{2+} and $VOSO_4 \cdot 3H_2O$, sodium hydroxide (NaOH), sodium nitrite ($NaNO_2$), hydrochloric acid (HCl), acetic acid (CH_3COOH), sodium chloride (NaCl), ethylacetoacetate, ethylbenzoylacetate, phenyl hydrazine, ethanol, 2-hydroxyaniline (o-aminophenol), o-aminobenzoic acid, p-aminobenzoic acid and diethyl ether; purchased from BDH. Water used was bidistilled water; distillation process was carried out using both of condensation process and ion exchange technique. 10^{-3} M of azopyrazolone solutions were prepared by dissolving a known mass of the azo compound in a proper volume of ethanol. 10^{-3} M solution of the metal ion in 0.1 M HCl was prepared by dissolving the appropriate weight of the corresponding metal chlorides of Cr^{3+}, Mn^{2+}, Co^{2+}, Ni^{2+}, Cu^{2+}, Zn^{2+} and $VOSO_4 \cdot 3H_2O$ in a proper volume of 0.1 M HCl to prevent the hydrolysis of the metal salt solutions. Pure aqueous solutions of metal ions were also prepared for conductimetric studies. 0.1 M HCl was prepared and standardized against standard sodium carbonate solution, the exact concentration of the HCl solution was determined and used in calculations (0.1185 M). 0.2 M (CO_2-free) NaOH solution was prepared and standardized against standard HCl solution. NaCl solutions with different concentrations (1, 0.6, 0.3 and 0.15 M) were also prepared. A series of buffer solutions covering the range (1.5-12) of pH values were prepared according to Britton method [14] with the modification involving titration of 100 ml of the mixture (0.1 M solution of equal amounts of boric, acetic and phosphoric acids) with 0.5 M NaOH to the desired pH and then making with water up to 250 ml so as to keep the ionic strength constant at all pH values [15].

2.2. Preparation of 3-Methyl-1-Phenyl-5-Pyrazolone and 1, 3-Diphenyl-5-Pyrazolone

A mixture of ethylacetoacetate (6.5 g; 0.05 M) and phenyl hydrazine (5.4 g; 0.05 M) or ethylbenzoylacetate (9.6 g; 0.05 M) and phenyl hydrazine (5.4 g; 0.05 M) was heated in water bath at 100℃ for one hour [7]. The resulting oil was cooled and stirred with diethyl ether (50 ml) until solidification occurred, the crude product was then filtered off, washed with ether until all colored material removed. The final product was recrystallized with 20% ethanol-water solution and collected as white powder of 3-methyl-1-phenyl-5-pyrazolone, yield 90%, m.p. 131℃ or 1,3-diphenyl-5-pyrazolone, yield 90%,

m.p.143℃.

2.3. Preparation of Azopyrazolone Derivatives

A well-stirred solution of 2-aminophenol, 2-aminobenzoic acid or 4-aminobenzoic acid 0.01 M in 40 ml ethanol and 20 ml of 2 M HCl was cooled in an ice-salt bath and diazotized with aqueous sodium nitrite solution (20 ml, 0.01 M). The cooled (0-5°C) diazonium solution was added slowly to a well-stirred solution of 0.01 M 3-methyl-1-phenyl-5-pyrazolone or 1, 3-diphenyl-5-pyrazolone in 100 ml ethanol containing sodium hydroxide (10 g). The reaction mixture was stirred for one hour at room temperature, and then acidified with dilute HCl (100 ml, 2.5 M) to neutralize the reaction mixture and precipitate the azopyrazolone derivatives [16]. The products were recrystallized from ethanol to give the derivatives of both 3-methyl-1-phenyl-4-arylazo-5-pyrazolone and 1, 3-diphenyl-4-arylazo-5-pyrazolone. The resulting derivatives have the following formulae:
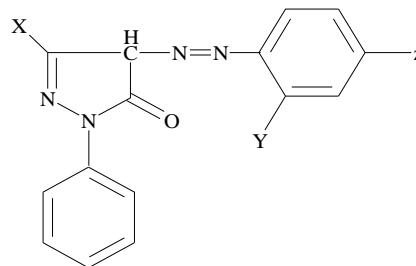
$X = C_6H_5$, $Y = COOH$, $Z = H$;
1, 3-diphenyl-4-(o-carboxyphenylazo)-5-pyrazolone (L1),
$X = CH_3$, $Y = COOH$, $Z = H$;
3-methyl-1-phenyl-4-(o-carboxyphenylazo)-5-pyrazolone (L2), $X = C_6H_5$, $Y = OH$, $Z = H$;
1, 3-diphenyl-4-(o-hydroxyphenylazo)-5-pyrazolone (L3), $X = CH_3$, $Y = OH$, $Z = H$;
3-methyl-1-phenyl-4-(o-hydroxyphenylazo)-5-pyrazolone (L4), $X = C_6H_5$, $Y = H$, $Z = COOH$;
1, 3-diphenyl-4-(p-carboxyphenylazo)-5-pyrazolone (L5), $X = CH_3$, $Y = H$, $Z = COOH$;
3-methyl-1-phenyl-4-(p-carboxyphenylazo)-5-pyrazolone (L6).

Elemental analysis, IR, mass and ^1H NMR spectra were carried out to confirm their structures.

2.4. pH-Metric Titration

The experimental procedure involved the titration of the following solutions (total volume = 50 ml) against a standard CO_2-free (0.21 M) NaOH solution:

1) 5 ml of HCl (0.12 M) + 5 ml of NaCl (1 M) + 20 M ethanol,

2) Solution a + 20 ml of 10^{-3} M of the ligand under investigation, and,

3) Solution b + 5 ml of metal salt solution (10^{-3} M).

These titrations were repeated for 1) ionic strengths I = 0.167, 0.1, 0.05, and 0.25 M NaCl, at 25ºC, 2) various temperatures (25, 30, 35, and 45ºC) at I = 0.167 M NaCl.

The pH measurements were carried out using a Jenway, pH-meter 3310 with a glass combined electrode. The water thermostat was a Thermo Haake WKL 26, Karlsruhe, Germany accurate to ±0.1ºC. The solutions were equilibrated in the thermostat for about 15 min before titration. The equations used for the various calculations [17] were programmed into IBM computer.

2.5. Determination of the Thermodynamic Parameters

The following thermodynamic parameters: ΔG°, ΔH° and ΔS° were determined for each chelate depending on their stability constants [18]. The free energy of formation (ΔG°) of a complex is related to its stability constant by the relation [18]: $-\Delta G^{\circ}$ = 2.303 RT logβ where, R = universal gas constant, T = absolute temperature and logβ = stability constant of the complex. Enthalpy of formation (ΔH°) and entropy (ΔS°) were calculated by plotting logβ versus $1/T$. We can specify the quantitative dependence of the stability constant on temperature from the relation [18]:

$$\Delta G^{\circ} = \Delta H^{\circ} - T\Delta S^{\circ}$$
$$\Delta G^{\circ} = -2.303\ RT \log\beta = \Delta H^{\circ} - T\Delta S^{\circ}$$

By rearranging, we get

$$\log\beta = -\Delta H^{\circ}/(2.303\ RT) + \Delta S^{\circ}/(2.303\ R)$$

This is a linear equation of the form y = mx + b, where y = logβ, m = $-\Delta H^{\circ}$/(2.303 R) = slope, x = $1/T$, and b = ΔS°/(2.303 R) = intercept. This means that if the values of K for a given reaction are determined at various temperature, a plot of logβ versus $1/T$ will be linear, with slope ΔH°/(2.303 R) and intercept ΔS°/(2.303 R). This result assumes that both ΔH° and ΔS° are independent of temperature over the temperature range considered. This assumption is a good approximation over a relatively small temperature range [18].

2.6. Conductimetric Measurements

The conductivities of VO^{2+}, Cr^{3+}, Mn^{2+}, Co^{2+}, Ni^{2+}, Cu^{2+} and Ni^{2+} metal ions with the investigated ligands (L1-L6) were measured using conductivity meter (Philips pw 9526, digital conductivity meter). The experimental procedure involves a conductimetric titration of 40 ml alcohol-water mixture (50% v/v) solution containing 4×10^{-5} M of a given azopyrazolone derivative against a standard solution of 10^{-3} M aqueous metal ion solution using microburette with continuous magnetic stirring. The instrument reading was recorded after each addition. All of the conductivity values were corrected for the

effect of dilution during titration. Corrections were made by multiplying conductivity value (instrument reading) by the ratio (V + v)/V, where V is the original volume of the titrand (40 ml and v is the added volume of titrant [19]). The corrected conductivity values were plotted versus the molar ratio (L:M). The resulting curves are composed of straight lines with inflection points indicating the number of ligands around each central metal ion.

2.7. Spectrophotometric Method Applied for Determination of PK$_a$ Values

The absorption spectra of azopyrazolone compounds under investigation (L1-L6) were scanned over a range of wavelengths in universal buffer solutions of different pH values. For this purpose a known volume of (10^{-3} M) solution of the azopyrazolone derivative was added to the buffer solution in a 10 ml volumetric flask dropwise with continuous shaking. The mixture was then made up to the mark with the buffer solution of appropriate pH. The spectra were obtained at room temperature using spectrophotometer (Jenway, 6305 UV-VIS spectrophotometer).

The method applied for the determination of pK$_a$ values of the different azopyrazolone derivatives is the half height method [20]. This method depends on the fact that the limiting absorbance (A_1) represents complete conversion of the compound from one form to other. Since pKa is equal to the pH value at which the two forms exist in equivalent amounts (pK$_a$ = pH (at $A_{½}$), the pH corresponding to half the height of the absorbance-pH curve ($A_{½}$) is equal to pK$_a$. The ($A_{½}$) value is given by the relation:

$$A_{1/2} = \frac{A_1 - A_{min}}{2} + A_{min}$$

where A_1 = maximum absorbance, A_{min} = minimum absorption.

The absorption spectra of 3×10^{-5} M solutions of the azopyrazolones under investigation (ligands L1-L6) were dissolved in 40% v/v ethanolic buffer solutions of varying pH values.

2.8. Determination of the Molar Ratio of the Metal Lons to the Ligands Spectrophotometrically

The mole ratio of the metal ions to the ligands was studied spectrophotometrically using molar ratio and continuous variation methods. The spectrophotometric method was used to confirm the data obtained by conductimetric and pH-metric methods. UV absorption can be used to determine stoichiometry of the complexes and this method appears to be valuable for studying complexes with low stabilities.

2.8.1. Molar Ratio Method

In this investigation, the concentration of the metal ions were maintained constant and the ligands concentrations were varied [21], so a series of metal-ligand aqueous ethanolic solutions were prepared with different [L]/[M] ratios. The absorptions of these solutions were measured using UV spectrophotometer at λ_{max} of the expected complex ML_2. Absorbance versus [L]/[M] curves were drawn for all complexes.

2.8.2. Continuous Variation Method

This method was used to confirm the data obtained using molar ratio and conductivity methods. In this method, the mole fraction was varied by changing the concentrations of the two components, maintaining the total number of moles constant [21]. A series of metal-ligand aqueous ethanolic solutions were prepared with different metal mole fractions. The mole fraction of the metal was plotted against the absorbance of the expected complex at λ_{max} of the complex. The measured absorbance increase as the molar ratio [M]/([L] + [M]) increase until the actual molar ratio of the complex is reached, after this point the absorbance becomes lower because the metal has no absorption at λ_{max} of the complex.

3. RESULTS AND DISCUSSION

3.1. Determination of Stability Constants

Titration curves were obtained for the titrations of VO^{2+}, Cr^{3+}, Mn^{2+}, Co^{2+}, Ni^{2+}, Cu^{2+} and Zn^{2+} metal ions in the presence of different molarities of NaCl and different temperatures. The stability constants of the formed complexes were investigated in the pH range of 4-6.

The mean values of n_H (the average number of protons associated with the ligand) for the investigated ligands (L1-L6) at different pH values were calculated from the titration curves of solutions 1 and 2 by employing the relationship derived by Irving and Rossotti [17]. On plotting $\log n_H/(1 - n_H)$ vs. pH, a straight lines having an intercept equal to pK_a on the pH axis are obtained. From the titration curves of solutions 1-3, the metal + ligand formation number values $\bar{n}$ (the average number of ligand molecules coordinated to the metal ion) of the metal complexes were obtained at various pH values. The $\bar{n}$ values were found to be less or equal to 2, indicating the formation of 1:1 and 1:2 complexes. The $\bar{n}$ values were calculated using the Irving and Rossotti formulation [17]. The free ligand exponent pL was calculated from the so obtained values of $\bar{n}$ by the equation:

$$pL = \log \left[\frac{\sum_{y=0}^{y=1} \beta_y^H \left(\dfrac{1}{10^B} \right)}{C_L - \bar{n} C_M} \frac{V_o + V_c}{V_o} \right]$$

where, C_M is the concentration of ions M^{n+} used, C_L is the concentration of the ligand, y is the number of dissociable protons ($y = 1$ for the investigated ligands), and V_o is the original volume (50 ml), V_c is the volume of alkali (NaOH) consumed to reach the same pH values in curve c corresponding to the titration of solution 3, β_y^H is the formation constant values of the investigated ligands, and B is the pH value. The mean pK_a values obtained from the corresponding different experimental formation curves using the average value and straight line methods. The results obtained for proton-ligand systems (pK_a values) were 3.98, 4.04, 7.68, 7.93, 3.45 and 3.66 for the investigated ligands L1-L6, respectively. Referring to these data, the pK_a values of ligands L5 and L6 have the lowest values from all of the six ligands used in this work because the ionizble group (–COOH) locates in the para position where there is no attraction with the carbonyl group of the pyrazolone ring, so it is easy to lose H^+ ion, whereas the ligands L1 and L2 have pK_a values higher than L5 and L6 because the ionizable group (–COOH) locates in ortho position, so there is a hydrogen bond between the carbonyl group of the pyrazolone ring and –COOH, as a result; it is more difficult to lose H^+, so these two ligands have pK_a values higher than L5 and L6 [22]. The pK_a values of ligands L3 and L4 have the highest values from all because the ionizable group of these two ligands (–OH) locates in ortho position with lower ability to librate H^+ ion because hydroxyl group has lower acidity than carboxyl group and because of the presence of hydrogen with the carbonyl group of the pyrazolone ring [23]. Ligand L1 has pK_a value < L2, and L3 < L4, and L5 < L6, that is because of the presence of additional phenyl group (electron withdrawing group) in ligands L1, L3 and L5. The formation curves for the complexes were obtained by plotting the relation between average number of ligands attached per metal ion ($\bar{n}$) and free ligand exponent (pL), $\bar{n}$ and pL were calculated as previously mentioned. To compute successive stability constants ($\log \beta_1$ and $\log \beta_2$) the method of interpolation is used [17], where $\log \beta_1$ and $\log \beta_2$ are equal to the values of (pL) when ($\bar{n}$) = 0.5 and 1.5, respectively. $\log \beta_1$ and $\log \beta_2$ for all complexes are given in **Table 1**.

3.2. Relations between the Properties of Central Metal Lons and the Stability Constants of the Complexes

The transition metal ions form predominantly ionic and coordinate bonds. If the bonds are ionic, the born rela-

Table 1. Collective data of stability constants ($\log\beta_1$ and $\log\beta_2$) for all of the investigated complexes.

Ligand	VO^{2+}		Cr^{3+}		Mn^{2+}		Co^{2+}		Ni^{2+}		Cu^{2+}		Zn^{2+}	
	$\log\beta_1$	$\log\beta_2$	$\log\beta_1$	$\log\beta_2$	$\log\beta_1$	$\log\beta_2$	$\log\beta_1$	$\log\beta_2$	$\log\beta_1$	$\log\beta_2$	$\log\beta_1$	$\log\beta_2$	$\log\beta_1$	$\log\beta_2$
L1	3.78	5.83	3.92	6.04	3.53	5.29	3.99	6.18	4.08	6.38	4.21	6.60	4.02	6.23
L2	4.72	7.70	4.78	7.31	4.71	7.52	4.90	8.04	4.83	7.53	4.87	7.41	4.82	7.25
L3	5.63	9.54	5.65	9.93	5.43	8.81	5.67	10.06	5.75	10.07	5.76	9.94	5.73	9.87
L4	5.77	9.76	5.79	10.15	5.63	9.50	5.80	9.91	5.90	10.14	5.94	10.47	5.84	10.19
L5	3.26	4.29	3.60	5.68	3.25	5.34	3.75	5.85	3.83	6.71	3.83	5.68	3.78	6.66
L6	4.26	6.34	4.33	6.78	4.25	6.78	4.37	8.05	4.52	8.55	4.58	8.01	4.46	8.37

tion ($E = Z^2/2r [1 - 1/D]$) [24] can be hold for the energy change on complexation of an ion of charge (Z) and radius (r) [25-27] in a medium of dielectric constant (D). Since the stability constant is related directly to this energy, $\log\beta$ values should increase linearly with Z^2/r. The stability constants of some transition metal complexes show different behaviors which suggest the probable existence of linearity and nonlinearity of $\log\beta$ with Z^2/r [28]. The plots of $\log\beta_1$ and $\log\beta_2$ versus Z^2/r of the transition metal ions (VO^{2+}, Cr^{3+}, Mn^{2+}, Co^{2+}, Ni^{2+}, Cu^{2+} and Zn^{2+}) complexes with the investigated ligands (L1-L6), does not exhibit linear increase of $\log\beta$ with increase of Z^2/r. Interpretation in term of the assumption about ionic character of metal-ligand on which the linearity based is not valid. The other probable case is steric effects. It is also interest to study the $\log\beta_1$ and $\log\beta_2$ values of the transition metal complexes with the investigated ligands (L1-L6) as a function of atomic number 1/r (the inverse of ionic radius) as well as EN (electronegativity) [28] of metal ions. In this investigation, it was found that the stability constants of the first raw transition metal complexes with the investigated ligands (L1-L6) ($\log\beta$ values) are generally increase with decreasing ionic radius r (or increasing 1/r) and increase with increasing atomic number [29], also $\log\beta$ increases with increasing electonegativity, this is because upon increasing electronegativity of the metal ions, the electronegativity difference between the metal atom and the donor atom of the ligand would expectedly associate with increase of covalent character of the metal-ligand bond. These relations are not linear and there are some exceptions from the mentioned observations because of the presence of steric effects and ionic bonds. The relations between the ionization constants (pK_a) of the ligands and the stability constants ($\log\beta_1$, $\log\beta_2$) of their complexes with the transition metal ions (VO^{2+}, Cr^{3+}, Mn^{2+}, Co^{2+}, Ni^{2+}, Cu^{2+} and Zn^{2+}) can be studied. It is

observed that as pK_a of the ligand increases, the stability constant $\log\beta$ of the complex increase. The semi linear correlation observed in this study demonstrates that factors which increase or decrease pK_a of the ligand also affect the $\log K_{ML}$ values for the metal ions in a parallel fashion. This means that substituent groups that tend to increase electron density on donor atom and hence tend to increase the coordination ability of the ligand increase $\log K_{ML}$, and also increase the value of pK_a of the ionizable hydrogen [29]. The assumption here is that ligand basicity is directly related to ligand stability *i.e.*, more stable complexes being formed from basic ligands [29]. Such correlation cannot be generalized because of the presence of some exceptions from linearity and because this result was observed form the ligands and the metal ions used in this study only.

3.3. Effect of Lonic Strength on Stability Constants

The stability constants of the metal ions (VO^{2+}, Cr^{3+}, Mn^{2+}, Co^{2+}, Ni^{2+}, Cu^{2+} and Zn^{2+}) complexes with the investigated ligands (L1-L6) were found to decrease with increasing ionic strength of the medium as shown in **Table 2**. For each complex the relationship between the stability constant and the square root of the ionic strength is plotted in **Figures 1**, **2** and was in agreement with the Debye-Hückel equation [30]. The thermodynamic stability constants ($\log\beta°$) were obtained by extrapolating the straight line plots of $\log\beta$ versus $\sqrt{I}$ to zero ionic strength. From the plots of $\log\beta$ versus $\sqrt{I}$ which illustrated in **Figures 1** and **2**, the $\log\beta°$ (thermodynamic stability constants) values were obtained and listed in **Table 3**. Also values of pK_a were found to decrease with increasing ionic strength of the medium which are in agreement with Debye-Hückel equation [30,31]. The equation $\Delta G = -2.303\ RT\ \log\beta$ gives the relationship between the thermodynamic stability con-

Table 2. Stability constants of VO^{2+}, Cr^{3+}, Mn^{2+}, Co^{2+}, Ni^{2+}, Cu^{2+} and Zn^{2+} complexes with the investigated ligands L1-L6 at different ionic strengths at room temperature.

Complex	I (mol/l NaCl)			
	0.167	0.1	0.05	0.025
L1-				
VO^{2+}	5.83	6.16	6.64	6.99
Cr^{3+}	6.04	6.38	6.90	7.18
Mn^{2+}	5.29	5.78	6.12	6.54
Co^{2+}	6.18	6.5	7.00	7.29
Ni^{2+}	6.23	6.72	7.30	7.67
Cu^{2+}	6.60	7.27	7.59	8.03
Zn^{2+}	6.23	6.60	7.15	7.41
L2-				
VO^{2+}	7.70	8.10	8.63	8.87
Cr^{3+}	7.31	7.65	7.98	8.29
Mn^{2+}	7.52	7.95	8.35	8.69
Co^{2+}	8.04	8.40	8.90	9.23
Ni^{2+}	7.53	7.85	8.20	8.63
Cu^{2+}	7.41	7.70	8.10	8.50
Zn^{2+}	7.25	7.50	7.90	8.07
L3-				
VO^{2+}	9.54	9.96	10.45	10.85
Cr^{3+}	9.87	10.23	10.60	10.92
Mn^{2+}	8.81	9.26	9.85	10.29
Co^{2+}	10.06	10.50	10.86	11.21
Ni^{2+}	10.07	10.60	11.10	11.52
Cu^{2+}	9.94	10.25	10.70	11.03
Zn^{2+}	9.93	10.35	10.90	11.45
L4-				
VO^{2+}	9.76	10.15	10.60	1.00
Cr^{3+}	10.15	10.50	11.00	11.33
Mn^{2+}	9.50	10.00	10.48	10.82
Co^{2+}	9.91	10.36	10.75	11.12
Ni^{2+}	10.14	10.45	10.89	11.20
Cu^{2+}	10.47	10.85	11.31	11.66
Zn^{2+}	10.19	10.68	11.14	11.51
L5-				
VO^{2+}	4.29	4.70	5.20	5.71
Cr^{3+}	5.68	6.05	6.60	6.81
Mn^{2+}	5.34	5.6	5.90	6.32
Co^{2+}	5.85	6.20	6.70	7.12
Ni^{2+}	6.71	7.00	7.40	7.89
Cu^{2+}	6.70	7.25	7.60	8.12
Zn^{2+}	6.66	6.80	7.20	7.60
L6-				
VO^{2+}	6.34	6.67	7.02	7.45
Cr^{3+}	6.87	7.20	7.51	7.99
Mn^{2+}	6.27	6.50	6.90	7.26
Co^{2+}	8.05	8.51	9.03	9.50
Ni^{2+}	8.55	9.14	9.63	9.84
Cu^{2+}	8.01	8.23	8.80	9.05
Zn^{2+}	8.37	8.80	9.35	9.72

Table 3. The Thermodynamic stability constants ($\log\beta°$) of VO^{2+}, Cr^{3+}, Mn^{2+}, Co^{2+}, Ni^{2+}, Cu^{2+} and Zn^{2+} complexes with the investigated ligands (L1–L6).

Metal ion	VO^{2+}	Cr^{3+}	Mn^{2+}	Co^{2+}	Ni^{2+}	Cu^{2+}	Zn^{2+}
L1	7.73	7.92	7.30	8.00	8.58	8.89	8.18
L2	9.63	8.90	7.42	9.99	9.30	9.18	8.61
L3	11.67	11.56	11.23	11.90	12.41	11.73	12.38
L4	11.77	12.1	11.65	11.87	11.87	12.41	12.33
L5	6.59	7.55	6.92	7.92	8.62	8.97	8.19
L6	8.13	8.72	7.88	10.4	10.66	9.74	10.58
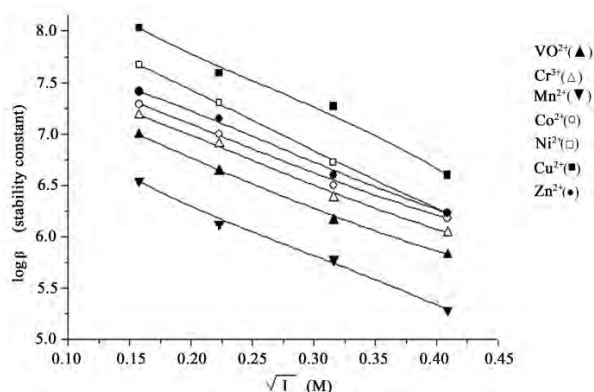
Figure 1. Plots of $\log\beta$ versus $\sqrt{I}$ for L1 with the investigated metal ion complexes.
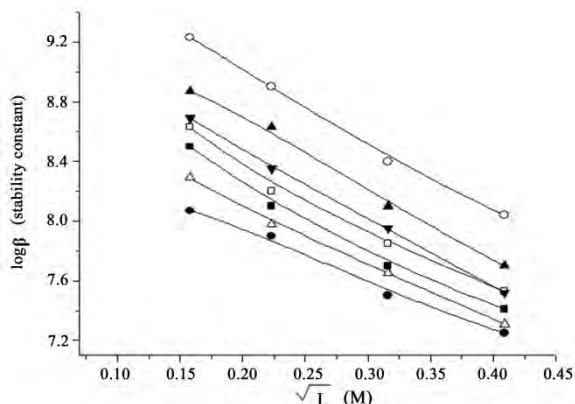
Figure 2. Plots of $\log\beta$ versus $\sqrt{I}$ for L2 with the investigated metal ion complexes.

stant and the free energy change according to the complex formation.

3.4. Effect of Temperature on Stability Constants

From the pK_a and $\log\beta$ values and their temperature dependence, the values of the thermodynamic functions ΔG, ΔH and ΔS were calculated [32]. The values of stability constants in **Table 4** reveal that the stability con-

stants decrease with increasing temperature, along with the pK_a value (**Figures 3**, **4**).

3.5. Conductimetric Measurements

The calculated molar ratio [L]/[M] were plotted against the corrected molar conductance values. The results indicated that the conductance increases with the addition of the metal ion solutions due to the release of the highly conducting hydrogen ions as a result of chelation. In-
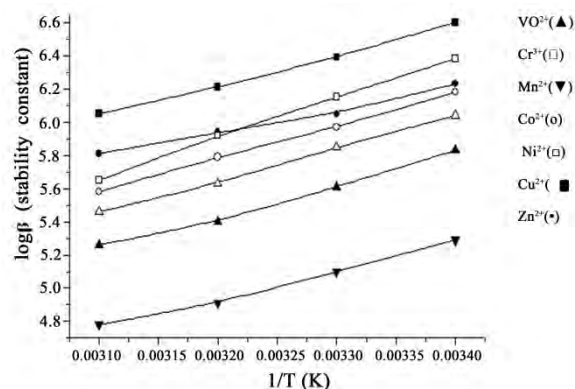
Figure 3. Plots of $\log\beta$ versus 1/T for L1 with the investigated metal ion complexes.
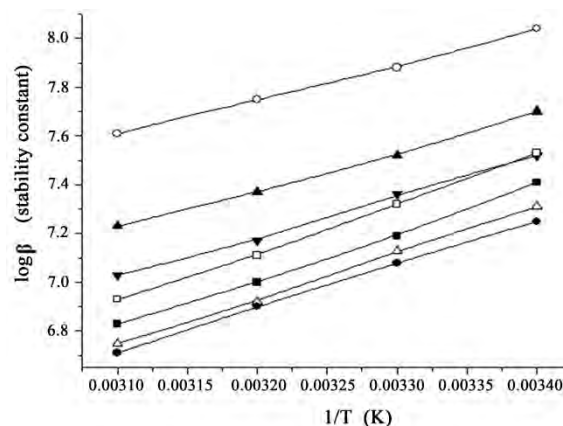
Figure 4. Plots of $\log\beta$ versus 1/T for L2 with investigated metal ion complexes.

Table 4. The thermodynamic parameters ($\triangle H°$, $\triangle G°$ and $\triangle S°$) for VO^{2+}, Cr^{3+}, Mn^{2+}, Co^{2+}, Ni^{2+}, Cu^{2+} and Zn^{2+} complexes with the investigated ligands (L1-L6).

		VO^{2+}	Cr^{3+}	Mn^{2+}	Co^{2+}	Ni^{2+}	Cu^{2+}	Zn^{2+}
	$-\triangle G°$(kJ/mol)	32.984	34.318	29.899	34.974	36.047	37.29	35.224
L1	$-\triangle H°$(kJ/mol)	36.77	37.53	32.94	37.92	46.34	35.04	26.23
	$+\triangle S°$(kJ/mol. K)	–0.013	–0.013	–0.011	–0.011	–0.035	0.007	0.03
	$-\triangle G°$(kJ/mol)	43.122	40.966	42.157	44.995	42.184	41.47	40.63
L2	$-\triangle H°$(kJ/mol)	29.87	36.19	31.79	27.19	38.49	36.96	34.47
	$+\triangle S°$(kJ/mol. K)	0.046	0.017	0.036	0.062	0.013	0.016	0.022
	$-\triangle G°$(kJ/mol)	54.194	56.314	49.963	57.071	57.147	56.371	55.955
L3	$-\triangle H°$(kJ/mol)	35.85	34.47	39.64	36.96	33.32	40.98	42.89
	$+\triangle S°$(kJ/mol. K)	0.064	0.073	0.034	0.067	0.08	0.051	0.043
	$-\triangle G°$(kJ/mol)	55.724	58.001	54.258	56.561	57.932	59.878	58.179
L4	$-\triangle H°$(kJ/mol)	31.41	27.77	35.24	36.77	38.49	40.98	33.70
	$+\triangle S°$(kJ/mol. K)	0.08	0.1	0.062	0.065	0.063	0.061	0.081
	$-\triangle G°$(kJ /mol)	24.518	32.473	30.499	33.4	38.284	38.292	38.012
L5	$-\triangle H°$(kJ /mol)	20.68	36.19	28.34	41.94	55.53	29.68	32.94
	$+\triangle S°$(kJ /mol. K)	0.012	-0.014	0.006	–0.031	-0.06	0.027	0.016
	$-\triangle G°$(kJ/mol)	35.87	38.307	35.438	45.514	48.357	45.288	47.307
L6	$-\triangle H°$(kJ/mol)	34.85	34.09	39.26	24.13	36.19	32.17	35.42
	$+\triangle S°$(kJ/mol. K)	0.003	0.014	-0.013	0.072	0.041	0.044	0.04

spection of the titration curves shows the presence of two distinctive breaks at metal to ligand molar rations of 1:1 and 1:2, respectively.

3.6. Spectrophotometric Determination of the pK$_a$ Values of the Investigated Ligands

The absorption spectra were recorded to investigate the spectral properties of the species liable to exist in such media and to determine the ionization constant (pK$_a$) values of the acidic groups present. Britton-Robinson universal buffers [14] were used to control the pH over the range 1.5-12.0. The maximum absorption of the ligand increases as pH of the buffer increase. The spectra in acidic solutions of pH 1.5-6.0 are characterized by a strong band absorbing maximally within the wavelength range 370-400 nm. These bands are due to absorption of the nonionized form liable to exist in such solutions and may be assigned to π-π* electronic transition within the ligand molecule influenced by intramolecular charge transfer. The spectra in alkaline solutions are characterized by the presence of a strong band absorbing maximally at the same range, which may be assigned to the absorption of the ionized form liable to exist at high pH values as a result of acid base equilibrium. It is noted in this investigation that the absorption bands assigned to the ionized form increases gradually by increasing of pH, attaining the maximum value at pH 10-12.0. The absorbance-pH curves show that the absorbance attains a limiting value at the extreme pH values in highly acidic or alkaline solutions indicating the existence of only one ionization step which is the ionization of -OH or -COOH groups. The variation of absorbance with pH is used for the calculation of ionization constants (pK$_a$ values) of

the investigated ligands using the half height method [20]. The results obtained are of the same order compared to those obtained potentiometrically and are 3.98, 4.08, 7.67, 7.98, 3.40 and 3.64 for the investigated ligands (L1-L6), respectively. The ionization of strong acidic carboxylic group is ionized at lower pH value, due to the high stability of the corresponding anion by resonance. They do not impart any spectral changes as the ionizable proton is not conjugated with the π-system of the molecule.

3.7. Determination of the Stoichiometry of the Complexes Spectrophotometrically

The mole ratio of the metal ions to the ligands was studied spectrophotometrically using molar ratio and continuous variation methods. The spectrophotometric method was used to confirm the data obtained by conductimetric method. UV absorption spectra can be used to determine stoichiometry of the complexes, and this method appears to be valuable for studying complexes with low stabilities.

3.7.1. Molar Ratio Method

It was observed that the absorption increases linearly as the ligand concentration increase, because of the formation of the complex until the solution reaches the actual molar ratio of the investigated complex. At this point all of the added materials were completely reacted and the absorption observed is the absorption of the investigated complex alone. After this point, the excess amount of the added ligand causes an inflection in the straight line that is because the ligand has an absorption value differ from that of the complex at λ_{max} of the complex [21]. [L]/[M] ratio corresponding to the inflection point in (Abs-[L]/[M] curve) indicates to the actual [L]/[M] ratio of the investigated complex. It was found that all of the complexes in this investigation are able to be stable in the form ML_2.

3.7.2. Continuous Variation Method

This method was used to confirm the data obtained using molar ratio and conductivity methods. In this method, The measured absorbance increases as the molar ratio [M]/([L] + [M]) increase until the actual molar ratio of the complex is reached, after this point the absorbance becomes lower because the metal has no absorption at λ_{max} of the complex. It was found that all of the curves have inflection points at mole fraction around (0.33); this means that all of the complexes in this investigation have the form ML_2 and this form is the most stable form.

4. CONCLUSIONS

The results obtained from the potentiometric measure-

ments for proton-ligand systems (pK_a values) were 3.98, 4.04, 7.68, 7.93, 3.45 and 3.66 for the investigated ligands L1-L6, respectively. It is observed that as pK_a of the ligand increases, the stability constant $\log\beta$ of the complex increase. The stability constants of the metal ions (VO^{2+}, Cr^{3+}, Mn^{2+}, Co^{2+}, Ni^{2+}, Cu^{2+} and Zn^{2+}) complexes with the investigated ligands (L1-L6) were found to decrease with increasing ionic strength of the medium which was in agreement with the Debye-Hückel equation. The thermodynamic stability constants ($\log\beta^{\circ}$) were obtained by extrapolating the straight line plots of $\log\beta$ versus $\sqrt{I}$ to zero ionic strength. Also the values of pK_a were found to decrease with increasing ionic strength of the medium. The values of the thermodynamic functions ΔG, ΔH and ΔS were calculated. The values of stability constants reveal that the stability constants decrease with increasing temperature, along with the pK_a value. Conductimetric measurements show the presence of two distinctive breaks at metal to ligand molar rations of 1:1 and 1:2, respectively. The results obtained from the spectrophotometric measurements are of the same order compared to those obtained potentiometrically and are 3.98, 4.08, 7.67, 7.98, 3.40 and 3.64 for the investigated ligands (L1-L6), respectively. The ionization of strong acidic carboxylic group is ionized at lower pH value due to the high stability of the corresponding anion by resonance. They do not impart any spectral changes as the ionizable proton is not conjugated with the π-system. The mole ratio of the metal ions to the ligands was studied spectrophotometrically using molar ratio and continuous variation methods. All the investigated complexes are found to be stable in the form ML2, which is also the most stable one.

REFERENCES

[1] Wisniewski, M.Z. (1997) Pd(II) complexes with some derivatives of pyrazol-5-one. *Polish Journal of Chemistry*, **71(2)**, 259-260.

[2] Lu, J., Zhang, L., Liu, L., Liu, G., Jia, D., Wu, D. and Xu, G. (2008) Study of fluorescence properties of several 4-acyl pyrazolone derivatives and their Zn(II) complexes. *Spectrochimica Acta Part A*, **71(3)**, 1036-1041.

[3] Kuncheria, B. and Indrasenan, P. (1988) Thorium (IV) nitrate complexes with some substituted pyrazole-5-ones. *Indian Journal of Chemistry*, **27A**, 1005-1007.

[4] Vogel, I. (1978) A text book of practical organic chemistry. 4th Edition, Longman, London.

[5] Tantawy, F., Goda, F. and Abdelal, A.M. (1995) Synthesis and characterization of certain new 3-methyl-4-(substituted phenylazo) isoxasol-5-ones and 3-methyl-4-(substituted phenylazo)-pyrazole-5-ones as potential antibacterial agents. *The Chinese Pharmaceutical Journal*, **47(1)**, 37-45.

[6] Rao, S. and Mittra, A.S. (1978) Synthesis and fungitoxicity of 1-phenyl-3-methyl-4-mono arylidene-2-pyrazolin-5-thione. *Journal of the Indian Chemical Society*, **55(7)**, 745-746.

[7] Fitton, A.O. and Smalley, R.K. (1968) Practical heterocyclic chemistry. Academic Press, London and New York.

[8] Karci, F. and Ertan, N. (2002) Hetarylazo disperse dyes derived from 3-methyl-1-(3′, 5′-dipiperidino-s-triazinyl)-5-pyrazolone as coupling component. *Dyes and Pigments*, **55(2-3),** 99-108.

[9] Ibrahim, S.A., El-Gahami, M.A., Khafagi, Z.A. and El-Gyar, S.A. (1991) Structure and antimicrobial activity of some new azopyrazolone chelates of Ni(II) and Cu(II) acetates, sulfates and nitrates. *Journal of Inorganic Biochemistry*, **43(1)**, 1-7.

[10] Abdel-Latif, S.A. (2001) Synthesis and characterization of some 3-phenyl-4-arylazo-5-pyrazolones with La(III), Ce(III), Th(IV) and UO_2(VI) complexes. *Synthesis and Reactivity in Inorganic*, *Metal-Organic and Chemistry*, **31(8)**, 1355-1374.

[11] Abdel-Latif, S.A. and Hassib, H.B. (2002) Studies of Mn(II), Co(II), Ni(II) and Cu(II) Chelates with 3-Phenyl-4-(p-methoxyphenylazo)-5-pyrazolone. *Journal of Thermal Analysis and Calorimetry*, **68(3)**, 983-995.

[12] Hassib, H.B. and Abdel-Latif, S.A. (2003) Potentiometric, spectrometric thermal and conductimetric studies on some 3-phenyl-4-(arylazo)-5-pyrazolones and their complexes with divalent cobalt metal ion. *Spectrochimica Acta Part A*, **59(11)**, 2425-2434.

[13] Sarin, R. and Munshi, K.N. (1972) Thermodynamics of complex formation of indium metal ion with mercapto hydroxyl and amino substituted succinic acid. *Journal of Inorganic and Nuclear Chemistry*, **34(2)**, 581-590.

[14] Britton, H.T.S. (1952) Hydrogen ions. 2nd Edition, Chapman and Hall, London.

[15] West, T.S. (1969) Complexemetry with EDTA and related reagents. 3rd Edition, B. D. H. Chemical Ltd Poole, London.

[16] Vogel, I. (1956) Practical organic chemistry including quantitative organic analysis. 3rd Edition, Longmans, London.

[17] Irving, H. and Rossotti, H.S. (1953) Methods for computing successive stability constants from experimental formation curves. *Journal of Chemical Society*, 3397-3405.

[18] Zumdal, S.S. (1997) Chemistry. 4th Edition, Houghton Mifflin Company.

[19] Vogel, A.I. (1956) Practical organic chemistry including quantitative organic analysis. 3rd Edition, Longmans, London.

[20] Issa, Y.M., Abdel-Ghani, N.T. and Abdel-Latif, S.A. (1996) Spectrophotometric studies on some hydroxy nitrocoumarins. *Egyptian Journal of Chemistry*, **39(3)**, 235-248.

[21] Bauer, H.H., Christian, G.D. and O'Reilly, J.E. (1978) Instrumental analysis. Allyn and Bacon Inc.

[22] McMurry, J. (2000) Organic chemistry. 5th Edition, Brooks/Cole, USA.

[23] Schwarzenbach, G. and Flaschk, H. (1969) Complexometric titrations. Methuen and Co. Ltd., London.

[24] Moeller, T., Martin, D.F., Thompson, L.C., Ferrus, R., Feistel, G.R. and Randal, W.J. (1965) The coordination chemistry of yttrium and the rare earth metal ions. *Chemical Reviews*, **65(1)**, 1-50.

[25] Gutmann, K. (1966) Conductimetric titration of charge transfer complexes in solution. *Electrochimica Acta*, **11(6)**, 555-568.

[26] Singh, P. and Ojha, A.C. (1980) Synthesis of N-isonictinyl-3-methyl-4-(substituted-hydrazono)-2-pyrazolin-5-one. *Journal of the Indian Chemical Society*, **57(12)**, 1172-1173.

[27] Snavely, F.A. and Krecker, B.D. (1959) Metal derivatives of arylazopyrazolone dyes III, molarity quotients of para- and meta-substituted pyrazolone dyes. *Journal of the American Chemical Society*, **81(16)**, 4199-4200.

[28] William, W.P. (1993) Inorganic chemistry. 2nd Edition, Academic Press Inc.

[29] Manku, G.S., Gupta, R.D., Bhat, A.N. and Jain, B.D. (1968) Determination of the stability constants of some lanthanon complexes with 1-nitroso-2-naphthol, 2-nitroso-1-naphthol, and 3-nitroso-4-hydroxycoumarin. *Journal of the Less Common Metals*, **16(4)**, 343-350.

[30] Debye, P. and Hückel, E. (1923) *Physik. Z.*, **24**, 185-206.

[31] Saxena, R.S. and Gupta, A. (1984) Potentiometric determination of dissociation constants of dithiodipropionic acid in different media. *Journal of the Electrochemical Society India*, **33(1)**, 89-90.

[32] Yadav, S.S. and Saxena, R.S. (2009) Formation constants and thermodynamic parameters of some tri-ligand complexes of lanthanides. *Journal of the Indian Chemical Society*, **86(2)**, 168-170.

Oxidative coupling polymerization of *p*-alkoxyphenols with Mn(acac)₂-ethylenediamine catalysts

Soichiro Murakami[1], Yuuta Akutsu[2], Shigeki Habaue[3*], Osamu Haba[2], Hideyuki Higashimura[4]

[1]Department of Chemistry and Chemical Engineering, Graduate School of Science and Engineering, Yamagata University, Yonezawa, Japan
[2]Graduate Program of Human Sensing and Functional Sensor Engineering, Graduate School of Science and Engineering, Yamagata University, Yonezawa, Japan
[3]Faculty of Health and Nutrition, Shubun University, Ichinomiya, Japan; *Corresponding Author: habaue@shubun-ac.jp
[4]Tsukuba Laboratory, Sumitomo Chemical Co. Ltd., Tsukuba, Japan

ABSTRACT

The oxidative coupling polymerization of *p*-alkoxyphenols with Mn(acac)₂-ethylenediamine catalysts was carried out. The polymerization of *p*-methoxyphenol with the manganese(II) acetylacetonate [Mn-(acac)₂]-*N,N'*-diethylethylenediamine catalyst in CH₂Cl₂ at room temperature under an O₂ atmosphere afforded a polymer, which mainly consists of the *m*-phenylene unit, whereas the polymer obtained with Mn(acac)₂ was rich in the oxyphenylene structure. The polymer yield and regioselectivity were significantly affected by the monomer and catalyst structures. The former catalyst system was also used for the coupling reaction of 2-methoxy-4-methylphenol. The corresponding carbon-carbon coupling product was isolated with a regioselectivity of 95%.

Keywords: Oxidative Coupling Polymerization; Phenol; Polyphenylene; Manganese Catalyst; Regioselectivity

1. INTRODUCTION

Phenolic polymers bearing a polyphenylene main chain structure have been mainly synthesized by the transition-metal-catalyzed coupling reactions of aryl halides, such as the Wurtz coupling, Ullmann reaction, Kumada-Tamao-Corriu coupling, etc [1-4]. These reactions are suitable for the regio and/or coupling selective formation of carbon-carbon bonds between aromatics. However, from the viewpoint of a convenient and green chemical method, they have some problems, such as the synthesis of aryl halides, protection of the hydroxyl group, and disposing of a large amount of the metal halide from the reaction system.

On the other hand, the catalytic oxidative coupling polymerization (OCP) of 2,6-dimethylphenol is industrially utilized for the synthesis of poly(2,6-dimethyl-1,4-phenylene ether) (PPE), which is one of the most common engineering plastics [5-7]. The OCP is known as the environmentally conscious method, due to the fact that the reaction proceeds under mild conditions producing only water as the by-product. Meanwhile, the OCP mediates a free radical coupling process; therefore, it is generally very difficult to control the coupling regioselectivity of the phenoxy radicals without producing a branched chain. For example, the OCP of *p*-substituted phenols **1** generally affords a polymer composed of a mixture of the phenylene (*CC*) and oxyphenylene (*CO*) units (**Scheme 1**).

The highly regiocontrolled polymers having a poly(*m*-phenylene) skeleton should have a conjugated higher-order structure which is applicable as novel electronic and electrochemical materials [8-11]. For instance, a unique conformation change caused by the cisoid and transoid main chain structures was reported [1], and a helix-induction in a chiral environment was also achieved [2]. The precise coupling regiocontrol of the phenoxy radicals during the OCP will significantly contribute to the facile synthesis of novel phenolic polymer materials.
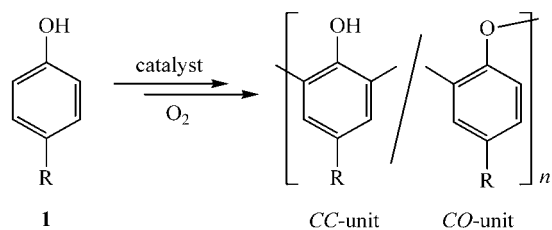
Scheme 1. OCP of **1**.

Studies of the catalyst systems for the regioselective OCP leading to a poly(phenylene ether) or poly(phenylene) derivative, such as the enzymatic and enzyme-model metal ones, and the copper-amine immobilized on mesopores, have been reported [12-16]. We also reported that the OCP of the bifunctional *p*-alkoxyphenol monomer **2** (**Scheme 2**) using the commercially available and typical copper catalyst, di-μ-hydroxo-bis[(*N,N,N',N'*-tetramethylethylenediamine)copper(II)] chloride [CuCl(OH)-TMEDA] proceeds in a regioselective manner to afford a polymer with a *CC*-unit selectivity of up to 88% [17]. However, the reigoselectivity has still not been sufficiently controlled.

p-Alkoxyphenol is one of the attractive phenolic monomers, because its polymer possesses the poly(hydroquinone) structure, which is a typical redox-active polymer. In this study, the OCP of the *p*-alkoxyphenols **1** with various metal catalysts was investigated, and novel manganese (II) acetylacetonate [Mn(acac)$_2$]-ethylenediamine catalysts for the *CC*-selective coupling formation were found.

2. EXPERIMENTAL

2.1. Materials

The monomers, *p*-methoxyphenol (**1-OMe**, Kanto), 4-*tert*-butoxyphenol (**1-O^{t}Bu**, TCI), *p*-hydroxybenzoic acid methyl ester (**1-CO$_2$Me**, TCI) (**Scheme 2**), and **2**, were purchased or synthesized as previously reported [17]. Mn(acac)$_2$, Mn(acac)$_3$ (Wako), manganese(II) acetate [Mn(OAc)$_2$] (Kanto), VO(acac)$_2$, and Co(acac)$_2$ (TCI) were used as received. The dry solvents, CH$_2$Cl$_2$, tetrahydrofuran (THF), MeOH, and *N,N*-dimethylformamide (DMF) (Kanto), were employed for the oxidative coupling. The diamines (**Scheme 2**) were used without further purification.

2.2. Polymerization

A monomer was added to a mixture of Mn(acac)$_2$ and ethylenediamine ([monomer]/[Mn(acac)$_2$]/[ethylenediamine] = 1/0.08/0.08) in a solvent (0.6 M), and the mixture was stirred at room temperature under an O$_2$ atmosphere. The product was isolated as the MeOH-1N HCl (10/1 (v/v))-insoluble part by centrifugation and drying under reduced pressure at 50℃. The regioselectivity (*CC/CO*) of the obtained polymers was estimated from H$_2$ volume generated by adding a polymer solution in THF to a mixture of an excess amount of lithium aluminum hydride (LiAlH$_4$) in THF [10,12-14,17].

2.3. Measurements

The ^{1}H NMR spectra were measured using a Varian Unity-Inova (500 Mz) or Mercury 200 (200 MHz) spec-
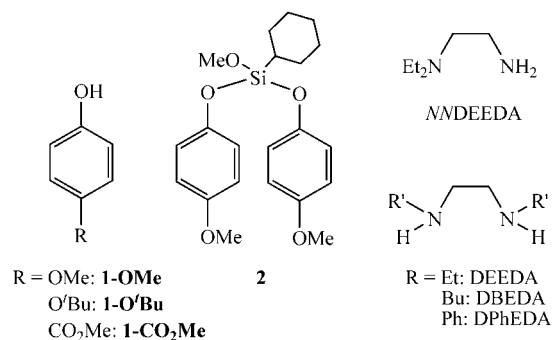
Scheme 2. Monomers and ligands.

trometer in CDCl$_3$. The infrared (IR) spectra were recorded using a HORIBA FT-720 spectrometer. The ultraviolet (UV) absorption spectra were taken by a JASCO V-630 spectrophotometer. The size exclusion chromatographic (SEC) analyses were performed using a JASCO PU-2080-Plus equipped with a JASCO UV-2075-Plus detector and Shodex AC-8025 and TSK-GEL columns connected in series [eluent: CHCl$_3$, flow rate = 1.0 mL/min]. Calibration was carried out using standard polystylenes.

3. RESULTS AND DISCUSSION

3.1. OCP with Manganese Catalyst

The OCP of **1-OMe** with various catalysts was carried out. The results are summarized in **Table 1**. The regioselectivity of *CC/CO* could not be estimated from the ^{1}H NMR spectra, because the peaks of the aromatic rings and hydroxyl group were broad and overlapped, as reported in previous studies [10,12-14,17]. Therefore, it was evaluated by titration of the hydroxyl group of the poly(**1-OMe**).

The polymerization with VO(acac)$_2$ or Co(acac)$_2$, the former of which was effective as a catalyst for the OCP of 2,3-dihydroxynaphthalene [18-20], in CH$_2$Cl$_2$-MeOH [7/1 (v/v)] at room temperature under an O$_2$ atmosphere did not proceed (entries 1 and 2), whereas Mn(acac)$_2$ showed a catalytic activity to afford a polymer as a methanol-1N HCl [10/1 (v/v)]-insoluble fraction in 69% yield with a regioselectivity (*CC/CO*) of 24/76 (entry 3). The polymerization in CH$_2$Cl$_2$ also resulted in good to high yields, and the selectivity was slightly affected by the solvent (entries 4 and 5). The polar solvents, such as THF and DMF, however, prevented the production of a polymer (entries 6 and 7). Therefore, the polymerization solvent significantly influenced the catalytic activity during the polymerization with Mn(acac)$_2$. The polymerization with Mn(acac)$_3$ also gave a polymer, although the catalytic activity was lower than that of Mn(acac)$_2$ (entry 8). This result suggests that the polymerization

proceeds through the Mn(III) species generated by the one-electron oxidation of the Mn(II) ones as mentioned later. The counter anion also affected the catalyst performance (entry 9).

3.2. OCP with Mn(acac)$_2$-Diamine Catalyst

The OCP of **1-OMe** with Mn(acac)$_2$ in the presence of various ethylenediamines ([Mn(acac)$_2$]/[ethylenediamine] = 1) in CH$_2$Cl$_2$ was then examined (**Table 2**). The OCP with TMEDA resulted in a poor yield (entry 1). However, the polymerizations with pyridine (2 equiv.) and the ethylenediamines having primary and secondary amino groups, such as *N,N*-diethylethylenediamine [*NN*DEEDA],

N,N'-diethylethylenediamine [DEEDA], *N,N'*-di-*n*-bu-tylethylenediamine [DBEDA], and *N,N'*-diphenylethy-lenediamine [DPhEDA] (**Scheme 2**), gave a polymer in moderate to good yields, whose regioselectivity was quite different from that of the polymer obtained without the amine ligand, especially, the polymers obtained with the ethylenediamine were rich in the *CC*-unit (entries 3-6). For example, the polymerization with DEEDA for 96 h gave a polymer in 47% yield with the regioselectiv-ity (*CC/CO*) of 87/13.

The effects of the Mn(acac)$_2$-DEEDA catalyst system during the polymerization under various conditions were further investigated (**Table 3**). Although the 24 h-po-

Table 1. OCP of **1-OMe** with Various Catalysts[a].

Entry	Catalyst[a]	Solvent	Time (h)	Yield (%)[b]	$M_w \times 10^{-3}$ (M_w/M_n)[c]	Selectivity[d] (*CC/CO*)
1	VO(acac)$_2$	CH$_2$Cl$_2$-MeOH[e]	72	0	—	—
2	Co(acac)$_2$	CH$_2$Cl$_2$-MeOH[e]	72	0	—	—
3	Mn(acac)$_2$	CH$_2$Cl$_2$-MeOH[e]	48	69	5.8 (1.1)	24/76
4	Mn(acac)$_2$	CH$_2$Cl$_2$	48	72	5.1 (1.2)	33/67
5	Mn(acac)$_2$	CH$_2$Cl$_2$	96	91	5.6 (1.2)	28/72
6	Mn(acac)$_2$	THF	48	0	—	—
7	Mn(acac)$_2$	DMF	48	0	—	—
8	Mn(acac)$_3$	CH$_2$Cl$_2$	48	40	4.6 (1.2)	31/69
9	Mn(OAc)$_2$	CH$_2$Cl$_2$	48	0	—	—

[a]Conditions: [catalyst]/[1-OMe] = 0.08, [**1-OMe**] = 0.6 M, temp. = room temperature, O$_2$ atmosphere. [b]MeOH-1N HCl (10/1 (v/v))-insoluble part. [c]Determined by SEC in CHCl$_3$ (polystyrene standard). [d]Estimated from the generated H$_2$ volume by the reaction of the obtained polymer with LiAlH$_4$. [e]CH$_2$Cl$_2$/MeOH = 7/1 (v/v).

Table 2. OCP of **1-OMe** with Mn(acac)$_2$-Ethylenediamine Catalysts[a].

Entry	Catalyst[a]	Yield (%)[b]	$M_w \times 10^{-3}$ (M_w/M_n)[c]	Selectivity[d] (*CC/CO*)
1	Mn(acac)$_2$-TMEDA	7	—	—
2	Mn(acac)$_2$-2Pyridine	60	7.4 (1.3)	50/50
3	Mn(acac)$_2$-*NN*DEEDA	77	4.4 (1.3)	56/44
4	Mn(acac)$_2$-DEEDA	47	5.2 (1.2)	87/13
5	Mn(acac)$_2$-DEEDA	37	5.7 (1.2)	68/32
6	Mn(acac)$_2$-DPhEDA	62	5.6 (1.2)	79/21

[a]Conditions: [catalyst]/[**1-OMe**] = 0.08, [**1-OMe**] = 0.6 M, solvent = CH$_2$Cl$_2$, temp. = room temperature, time = 96 h, O$_2$ atmosphere. [b]MeOH-1N HCl (10/1 (v/v))-insoluble part. [c]Determined by SEC in CHCl$_3$ (polystyrene standard). [d]Estimated from the generated H$_2$ volume by the reaction of the obtained polymer with LiAlH$_4$.

Table 3. OCP of **1-OMe** with Mn(acac)$_2$-DEEDA under Various Conditions[a].

Entry	Catalyst[a]	Time (h)	Yield (%)[b]	$M_w \times 10^{-3}$ (M_w/M_n)[c]	Selectivity[d] (*CC/CO*)
1	Mn(acac)$_2$-DEEDA	24	14	4.4 (1.2)	92/8
2	Mn(acac)$_2$-DEEDA[e]	96	0	—	—
3	Mn(acac)$_2$-DEEDA[f]	96	61	5.6 (1.6)	67/33
4	Mn(acac)$_2$-DEEDA[g]	96	86	7.3 (1.4)	64/36
5	Mn(acac)$_2$-2DEEDA	96	30	6.1 (1.4)	61/39

[a]Conditions: [catalyst]/[**1-OMe**] = 0.08, [**1-OMe**] = 0.6 M, solvent = CH$_2$Cl$_2$, temp. = room temperature, O$_2$ atmosphere. [b]MeOH-1N HCl (10/1 (v/v))-in-soluble part. [c]Determined by SEC in CHCl$_3$ (polystyrene standard). [d]Estimated from the generated H$_2$ volume by the reaction of the obtained polymer with LiAlH$_4$. [e]Temperature = 50℃. [f][Catalyst]/[**1-OMe**] = 0.16. [g]Solvent = CH$_2$Cl$_2$/MeOH [7/1 (v/v)].

lymerization produced a polymer in a low yield, the regioselectivity of the obtained polymer was *CC/CO* = 92/8 (entry 1). Accordingly, during the first stage of the polymerization, a highly regioselective coupling reaction should occur. The polymerization at 50℃ did not give a polymer. The other polymerization conditions, such as catalyst ratio and solvent, also affected the regioselectivity and catalytic activity (entries 2-4). When two equivalents of DEEDA to Mn(acac)$_2$ was used, both the polymer yield and *CC*-unit ratio significantly decreased (entry 5), indicating that the 1:1 complex of Mn(acac)$_2$ and DEEDA should be an active species. Although this catalyst system showed a lower catalytic activity than that of the polymerization without the diamine, the *CC*-unit selectivity was much higher.

The OCP of various monomers, such as **1-O^{t}Bu**, **1-CO$_2$Me**, **2**, with the Mn(acac)$_2$-DEEDA catalyst in CH$_2$Cl$_2$ at room temperature for 96 h under an O$_2$ atmosphere was also performed. The polymerizations of **1-O^{t}Bu** and **1-COOMe** did not afford a MeOH-1N HCl (10/1 (v/v))-insoluble fraction, and the polymerization of **2** resulted in a trace yield. These results suggest that the steric and/or electronic effects of the *p*-substituent significantly influence the polymerizability.

Figure 1 shows the FT-IR spectra of poly(**1-OMe**) with a unit ratio of (A) *CC/CO* = 28/72 and (B) 92/8. In each spectrum, the absorptions due to the vibrations of the O-H and C-O-C linkages were observed, indicating that the polymers are composed of a mixture of *CC*- and *CO*-units. The latter spectrum showed a much larger phenolic O-H peak due to the fact that this polymer is rich in the *CC*-unit [12].

Both polymers with *CC/CO* = 28/72 and 92/8 were completely soluble in chloroform, acetone, THF, DMF, and dimethyl sulfoxide, whereas insoluble in hexane and methanol. However, the latter polymer was almost solu-

ble in an equivolume mixture of methanol and a 2N NaOH aqueous solution, while the former was insoluble.

In order to clarify the applicability of this Mn(acac)$_2$-DEEDA catalyst, the oxidative coupling reaction of 2-methoxy-4-methylphenol **3**, which can afford two coupling dimer products, the *CC*-dimer and *CO*-dimer [21-23], as well as the polymeric compounds, was investigated (**Scheme 3**). The reaction was conducted under the same reaction conditions as the polymerization in CH$_2$Cl$_2$ for 96 h at room temperature under an O$_2$ atmosphere, and the dimers were isolated by silica gel column chromatography (hexane/AcOEt = 10/1). The coupling reaction with only Mn(acac)$_2$ afforded a 31% yield of the *CC*-dimer and 10% yield of the *CO*-dimer, that is, the regioselectivity (*CC/CO*) was 76/24. In the case of the reaction using Mn(acac)$_2$-DEEDA, the isolated yields were 57% and 3%, respectively, giving a selectivity of *CC/CO* = 95/5. The Mn(acac)$_2$-DEEDA catalyst was quite effective for the regioselective oxidative coupling.

The UV-Vis spectra of poly(**1-OMe**) and the obtained dimeric products of **3** are shown in **Figure 2**. The maxi-
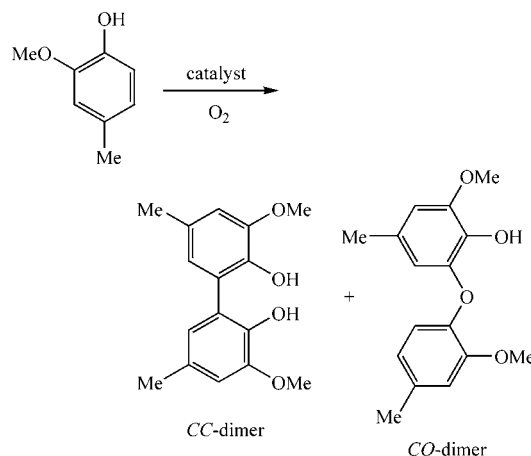
Scheme 3. Oxidative coupling reaction of **3**.

Figure 1. IR spectra of poly(**1-OMe**) with (A) *CC/CO* = 28/72, and (B) *CC/CO* = 92/8.
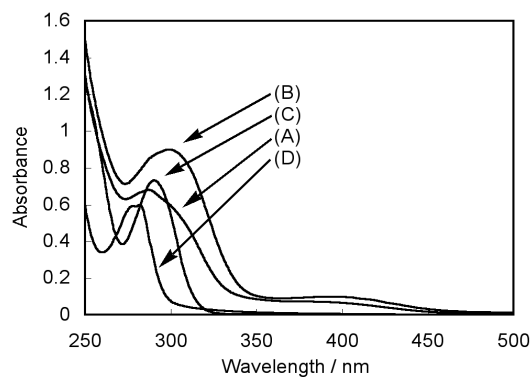
Figure 2. UV-Vis spectra of poly(**1-OMe**) with (A) *CC/CO* = 28/72, (B) *CC/CO* = 92/8, (C) *CC*-dimer, (D) *CO*-dimer (in CHCl$_3$).

mum absorption wavelength was observed at 287 nm for the polymer with *CC/CO* = 28/72, whereas the red-shifted absorption with the maximum of 299 nm was observed for the polymer with *CC/CO* = 92/8. This should be explained by the extension of the π-conjugation length due to the phenylene main chain structure for the latter polymer. Actually, the *CC*-dimer of **3** also showed a maximum absorption at 290 nm, which is greater than that of the *CO*-dimer of 282 nm.

The plausible OCP mechanism with Mn(acac)$_2$-DEEDA was proposed as follows (**Figure 3**): The complex of an *in situ* generated Mn(III) species and **1-OMe** causes the one-electron oxidation of the phenol to form a species of Mn(II) and the phenoxy radical, which concertedly induces the regioselective intermolecular radical-radical coupling to produce the corresponding carbon-carbon coupling product [15]. The dissociated manganese species are oxidized by dioxygen to regenerate the active Mn(III) species.

4. CONCLUSIONS

The OCP with Mn(acac)$_2$-ethylenediamine catalyst systems, that regioselectively produces a polymer with the poly(*m*-phenylene) backbone, was developed. The catalytic activity and regioselectivity during the polymerization were significantly affected by the monomer and catalyst structures, and polymerization conditions. Especially, the Mn(acac)$_2$-DEEDA catalyst showed a high regiocontrol ability. The catalyst can be readily and simply prepared by mixing of the commercially available Mn(acac)$_2$ and DEEDA.
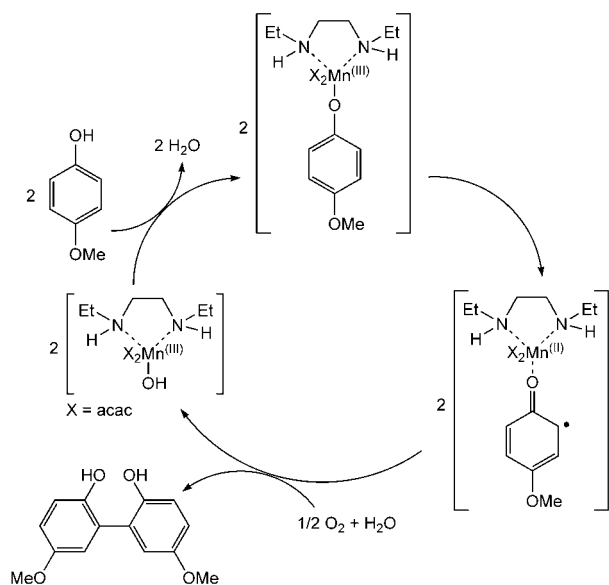
Figure 3. Plausible mechanism for OCP of **1-OMe** with Mn(acac)$_2$-DEEDA.

REFERENCES

[1] Xu, M.H., Lin, A.M. and Pu, L. (2001) Construction of an *ortho*-phenol polymer. *Tetrahedron Letters*, **42(36)**, 6235-6238.

[2] Katagiri, H., Miyagawa, T., Furusho, Y. and Yashima, E. (2006) Synthesis and optical resolution of a double helicate consisting of *ortho*-linked hexaphenol strands bridged by spiroborates. *Angewandte Chemie International Edition in English*, **45(11)**, 1741-1744.

[3] Ueda, M. and Ichikawa, F. (1990) Synthesis of aromatic poly (ether ketone)s by nickel-catalyzed coupling polymerization of aromatic dichlorides. *Macromolecules*, **23(4)**, 926-930.

[4] Colon, I. and Kwiatkoeski, G.T. (1990) High molecular weight aromatic polymers by nickel coupling of aryl polychlorides. *Journal of Polymer Science*: *Part A*: *Polymer Chemistry*, **28(2)**, 367-383.

[5] Hay, A.S., Blanchard, H.S., Endres, G.F. and Eustance, J.W. (1959) Polymerization by oxidative coupling. *Journal of American Chemical Society*, **81(23)**, 6335-6336.

[6] Hay, A.S. (1998) Polymerization by oxidative coupling: Discovery and commercialization of PPO® and Noryl® resins. *Journal of Polymer Science*: *Part A*: *Polymer Chemistry*, **36(4)**, 505-517.

[7] Kobayashi, S. and Higashimura, H. (2003) Oxidative polymerization of phenols revisited. *Progress in Polymer Science*, **28(6)**, 1015-1048.

[8] Wang, P., Martin, B.D., Parida, S., Rethwisch, D.G. and Dordick, J.S. (1995) Multienzymic synthesis of poly (hydroquinone) for use as a redox polymer. *Journal of American Chemical Society*, **117(51)**, 12885-12886.

[9] Reihmann, M.H. and Ritter, H. (2000) Enzymatically catalyzed synthesis of photocrosslinkable oligophenols. *Macromolecular Chemistry and Physics*, **201(14)**, 1593-1597.

[10] Fukuoka, T., Uyama, H. and Kobayashi, S. (2004) Effect of phenolic monomer structure of precursor polymers in oxidative coupling of enzymatically synthesized polyphenols. *Macromolecules*, **37(16)**, 5911-5915.

[11] Etori, H., Kanbara, T. and Yamamoto, T. (1994) New type of─conjugated polymers constituted of quinone units in the main chain. *Chemistry Letters*, **23(3)**, 461-464.

[12] Tonami, H., Uyama, H., Kobayashi, S. and Kubota, M. (1999) Peroxidase-catalyzed oxidative polymerization of *m*-substituted phenol derivatives. *Macromolecular Chemistry and Physics*, **200(10)**, 2365-2371.

[13] Oguchi, T., Tawaki, S., Uyama, H. and Kobayashi, S. (1999) Soluble polyphenol. *Macromolecular Rapid Communications*, **20(7)**, 401-413.

[14] Kim, Y.J., Uyama, H. and Kobayashi, S. (2003) Regioselective synthesis of poly(phenylene) as a complex with poly(ethylene glycol) by template polymerization of phenol in water. *Macromolecules*, **36(14)**, 5058-5060.

[15] Higashimura, H., Fujisawa, K., Kubota, M. and Kobayashi. S. (2005) "Radical-controlled" oxidative polymerization of phenol: Comparison with that of 4-phenoxyphenol.

Journal of Polymer Science: *Part A*: *Polymer Chemistry*, **43(9)**, 1955-1962.

[16] Shibasaki, Y., Suzuki, Y. and Ueda, M. (2007) Copper-catalyzed regio-controlled oxidative coupling polymerization of 2,5-dimethylphenol. *Macromolecules*, **40(15)**, 5322-5325.

[17] Habaue, S., Ohnuma, M., Mizoe, M. and Temma, T. (2005) Oxidative coupling polymerization of silicon-tethered p-alkoxyphenol derivatives with CuCl(OH)-*N*,*N*, *N'*,*N'*-Tetramethylethylenediamine Catalyst. *Polymer Journal*, **37(8)**, 625-628.

[18] Habaue, S., Murakami, S. and Higashimura, H. (2005) New asymmetric vanadium catalyst for highly selective oxidative coupling polymerization. *Journal of Polymer Science*: *Part A*: *Polymer Chemistry*, **43(23)**, 5872-5878.

[19] Murakami, S., Habaue, S. and Higashimura, H. (2007) Novel vanadium catalyst system with tartaric acid salts for highly selective asymmetric oxidative coupling polymerization. *Polymer*, **48(22)**, 6565-6570.

[20] Habaue, S., Aoyagi, H., Murakami, S. and Higashimura,

H. (2007) Asymmetric oxidative coupling polymerization of dihydroxynaphthalene derivatives with cobalt-Salen complexes. *Polymer Bulletin*, **59(3)**, 303-310.

[21] Sun, Y., Fenster, M., Yu, A., Brerry, R.M. and Argyropoulos, D.S. (1999) The effect of metal ions on the reaction of hydrogen peroxide with kraft lignin model compounds. *Canadian Journal of Chemistry*, **77(5-6)**, 667-675.

[22] Fabbri, D., Dettori, M.A., Delogu, G., Forn, I.A., Casalone, G., Palmieri, G., Pisano, M. and Rozzo, C. (2007) 2,2'-Dihydroxy-3,3'-dimethoxy-5,5'-dimethyl-6, 6'-dibromo-1,1'-biphenyl: Preparation, resolution, structure and biological aActivity. *Tetrahedron Asymmetry*, **18(3)**, 414-423.

[23] Alexakis, A., Polet, D., Rosset, S. and March, S. (2004) Biphenol-based phosphoramidite ligands for the enantioselective copper-catalyzed conjugate addition of diethylzinc. *Journal of Organic Chemistry*, **69(17)**, 5660-5667.

Tracking chloride and metal diffusion in proofed and unproofed concrete matrices using ablative laser technology (ICP-MS)

Avin Pillay[1]*, Mirella Elkadi[1]*, Fadi Feghali[2], Sai Cheong Fok[3], Ghada Bassioni[4], Sasi Stephen[1]

[1]Department of Chemistry, The Petroleum Institute, Abu Dhabi, UAE; *Corresponding Author: apillay@pi.ac.ae
[2]PO Box, 2431, Abu Dhabi, UAE; *Corresponding Author: melkadi@pi.ac.ae
[3]Department of Mechanical Engineering, The Petroleum Institute, Abu Dhabi, UAE
[4]Department of Chemical Engineering, The Petroleum Institute, Abu Dhabi, UAE. On leave from the Chemistry Department, Faculty of Engineering, Ain Shams University, Cairo, Egypt

ABSTRACT

Depth profiling studies (laser ICP-MS) of ions (Cl^-, Na^+, Mg^{2+}) in concrete-based material can be used to provide useful information on the migration paths of these ionic species. In particular, deterioration of concrete through infiltration of chloride could lead to costly corrosion problems with serious impact on the environment. Many modeling studies on concrete matrices depend on the tortuosity of these transport paths. Our work showed that dispersion paths of ionic species in concrete are intermittent and sporadic, suggesting that applications of simplifying assumptions in treatment of such data could lead to appreciable perturbations in related mathematical models. This paper examines the capability of using a high resolution ICP-MS laser ablation technique to track Cl^- migration in concrete samples in the presence of other ions such as Na^+ and Mg^{2+}. Cationic migration in such materials is underexplored and data in this particular area could contribute to modeling studies. Concrete bricks (with and without surface coatings) were specially prepared in cubic configurations and allowed to saturate in a ponding medium (sea water). The study subsequently examined the distribution of Cl^-, Na^+ and Mg^{2+} with depth in protected (epoxy coated) and unprotected cored concrete slivers (5 mm diameter; 2 mm thick) using an 80 μm-diameter laser beam coupled to an ICP-MS instrument. The laser (213 nm) was programmed to ablate a total depth of 50 μm at each point at 5-μm intervals. The results in unprotected samples indicated that chloride intensity showed a general decline with depth, suggesting that mo-

bility of the chloride is a function of its interaction with the concrete matrix. In some cases 'hotspots' were observed at certain points indicating that transport of the intruding ion was limited. No significant mobility was observed in coated samples. The depth-profiling results for Na^+ and Mg^{2+} were somewhat unexpected. Strong similarities in their spectra purported that the matrix was indifferent to charge and size of the ion. Our experimental data further showed that the matrix itself offers natural protection to the reinforced steel rebars by limiting chloride and metal diffusion at certain locations. Clearly, if the composition of these protective environments within the concrete could be simulated on a larger scale and introduced into the matrix it would offer scope for extended research in this area. Our work would be of definite interest to materials and environmental research; and mechanistic studies on aggregates.

Keywords: Concrete; Cl^-, Na^+; Mg^{2+}; Laser Ablation; Depth-Profiling; ICP-MS

1. INTRODUCTION

In vitro tracking of chloride diffusion (by ICP-MS depth profiling) in the presence of multi-ionic species (Na^+, Mg^{2+}) can provide information on two fronts: 1) the tortuosity of the migration pattern through the bulk material; and 2) the extent of diffusion in proofed concrete. It has been widely reported that concrete matrices incur serious environmental damage through invasive attacks of Cl^- in the bulk material [1-5]. Concrete structures in contact with seawater or salt water are, therefore, expected to incur some form of environmental degradation. Oil and

gas companies that have colossal concrete structures offshore tend to incur financial losses through salt-degradation of this nature. Salt sprays and splashes can also affect roadside concrete structures and buildings in the vicinity of the sea. The mechanism of corrosion due to Cl^- invasion in concrete is still a subject of active study. It has been documented that when a concrete structure is exposed to seawater, chloride ions from this medium will gradually infiltrate the matrix, largely through the pores and fissures in the hydrated cement mixture [6]. Some migration studies have alleged that chloride ions linked to $MgCl_2$ have different migratory properties than those associated with NaCl [7], and further work in this area would be useful. In the case of reinforced concrete, penetration of the chloride ions to the steel rebars, and subsequent accumulation to beyond a certain level, initiates corrosion in the steel, especially in the presence of moisture and oxygen at the steel-concrete interface.

Knowledge of the dispersion of Cl^- and other species in a concrete matrix could contribute to mechanistic studies of ionic diffusion in such materials. Chloride mobility is particularly important and several factors could influence its dispersion pattern [8-11], such as: 1) the extent of transportation through the bulk material (by aqueous media); 2) salinity of the aqueous medium in contact with the concrete; 3) the level of interaction of the Cl^- with chemicals and ingrained impurities in the concrete itself; 4) the porosity of the material; 5) temperature; 6) humidity; and 7) material homogeneity. A point to note about the last factor is that uneven mixing of the concrete could lead to considerable material inhomogeneity, which in turn could lead to aberrations in Cl^- migration patterns.

We have developed an ultrasensitive technique for assessing the diffusion of Cl^- (and cations such as Na^+ and Mg^{2+}) in bulk concrete samples, and pinpointing areas in the matrix to study their spatial and depth dispersion. The technique uses laser ablation linked to a high performance ICP-MS instrument. Our work demonstrates that systematic depth profiling in concrete samples can provide clues to the tortuosity of the transport path, which could be useful in modeling studies. The aim of this paper, therefore, is to explore the potential of our method for rapidly tracking migration of Cl^- and other ionic species in suitable bulk samples.

2. MATERIALS AND METHODS

2.1. Sample Preparation/Sample Handling

The cement samples used in this study were regular Portland cement material (**Type 1**), manufactured by the

---

Ras Al Khaimah cement plant in the United Arab Emirates (UAE)[1]. The concrete mix was designed using fine and coarse aggregates from the UAE. The maximum aggregate size was 10 mm. The concrete mix preparation was based on the British Method Design (BRE 106). Two lots of concrete mixes were prepared to meet minimum target strengths of 20 N/mm^2 and 40 N/mm^2 (labeled Grade 20 & Grade 40 respectively). The details of mix proportions are given in **Table 1**. Slump tests were conducted to ensure the practical workability of the concrete mixtures.

Bricks were cast from the two lots of concrete mixture. After casting, the bricks were cured under wet hessian blankets and polyethylene film. Compressive strength tests were performed on three concrete cubes ($150 \times 150 \times 150$ mm) from each lot of concrete mix after seven days to establish if the samples had attained the appropriate strengths. **Table 2** shows the compressive strength results, which confirmed the quality of the cast concretes.

The cured bricks in each lot were further separated into two batches. Solvent free 100% epoxy resin (waterproof, chloride and carbonation resistant coating for protection of concrete) was applied to the bricks in one batch. The coating generally has excellent resistance to chemicals and UV exposure (*i.e.*, suitable for the petrochemical industry) with an expected life span of about ten years. No coating treatment was applied to the bricks in the other batch. The two batches of coated and uncoated bricks in each lot were immersed in a pond of sea water. After several months, all the bricks were removed from the pond and samples were cored (discs of 5 mm diameter by 2 mm thick) from the bulk material using a standard coring tool [Makita TB131, Taiwan] (**Figure 1**). Laser experiments were conducted on coated and uncoated samples (bottom left and right of **Figure 1**, respectively).

2.2. ICP-MS Laser Ablation Technology

Samples were investigated with a Perkin Elmer SCIEX DRC-e ICP-MS (Connecticut, USA) fitted with a New Wave UP-213 laser ablation system. Laser ablation technology uses a micro-beam (from an Nd: YAG solid state laser) to ablate samples in a special sample chamber. The fine ablated material is transported by a carrier gas (Ar) to a hot plasma where it is atomized and converted to ions (characteristic of the elements of the sample), which are subsequently carried to a mass spectrometer for detection (**Figure 2**).

The extremely high temperature of the plasma (about 10,000 K) separates the sample into individual atoms. The plasma subsequently ionizes these atoms ($M \rightarrow M^+ + e^-$) so that they can be detected by the mass spec-

---

Table 1. Concrete mix proportions.

Concrete Targeted Strength (N/mm^2)	Mix Proportion				
	Cement kg/m^3	Water Cement Ratio	Density kg/m^3	Aggregate Cement Ratio	% Fine aggregate
20 (Grade 20)	320	0.54	2409	5.98:1	53.0
40 (Grade 40)	400	0.41	2440	4.68:1	52.0

Table 2. Compressive strength of concrete mixes.

Concrete Targeted Strength N/mm^2	Compressive strength after 7 days (N/mm^2)			Average Measured Compressive Strength N/mm^2
	Cube 1	Cube 2	Cube 3	
20 (Grade 20)	37	38	37.5	37.5
40 (Grade 40)	48	50	53	50

Figure 1. The coring instrument (top); and typical samples of proofed and unproofed cored discs (bottom left and right, respectively).

Figure 2. The ICP-MS instrument (top); 16-point grid showing the arrangement of points on a sample irradiated by the laser (bottom).

trometer. The technique is highly sensitive and can attain a limit of detection of 10^{-6} mg/kg (parts per trillion) for most elements. The concrete cored discs were placed into a special sample holder with dimensions 5 cm × 5 cm. No serious pre-treatment was necessary prior to irradiation. Samples were subjected to 213-nm laser irradiation at different points on the sample (16-point grid—**Figure 2**). The level of the beam energy was 30%, with a fluence of approximately 3 J/cm^2 and beam diameter of 50 μm. The laser was programmed to ablate a depth of 5 μm at each point and repeatedly scanned the surface; recording measurements after each ablation to a total depth of 50 μm.

2.3. Instrumental Performance

Characteristic intensities originating from the elements of interest were measured; and valid considerations were given to potential interferences and matrix effects. Prior to each run, the performance of the instrument was validated [12,13]. The study was largely semi-quantitative in the absence of standardization, and for purposes of comparison, all measurements were conducted under identical experimental conditions. Appropriate spectra were produced to observe variations in characteristic elemental profiles spatially and with penetration depth. A point to note is that the ponding medium produced Cl$^-$,

Na$^+$ and Mg^{2+} ions which are in elemental form in the solid matrix. Validating the analytical performance of the laser technique was conducted on an available certified NIST standard (National Institute of Standards and Technology, Maryland, USA; Certificate 613, glass bead). To ascertain that the instrument was optimally functional we examined its performance for different isotopes by taking replicate measurements (n = 3) for equivalent counting times at random points on the standard. Relative standard deviations of less than 5% were attained in general (**Table 3**) indicating that the operational performance of the instrument was acceptable. It is necessary to underscore that in the absence of matching-matrix standards our method was based on evaluating relative intensities (counts/sec) for purposes of comparison.

3. RESULTS AND DISCUSSION

3.1. Chloride Diffusion in Unprotected Concrete Matrices-Depth Profiling

Laser ablation technology is capable of depth and surface analysis, displays the elemental (ionic) intensities and produces an elemental profile [14]. Ablative technology is particularly useful for the measurement of ultra-trace intensities of metals in solids. Chloride detection is more energetically demanding due to the higher ionization potential of chlorine; therefore, the technique is limited to determination of minor concentrations of this element. Interferences from the matrix are generally common in ICP-MS, but with the availability of sophisticated software and collision reaction cells they are becoming easy to detect and handle.

Depth profiling is a special process to investigate elemental distribution beneath the surface. Very few contemporary instrumental methods have the capability to study metal intensity with depth [12]. X-ray methods are useful, but lack the ability to control depth penetration. Nuclear particle irradiation is equally useful, but such techniques require nuclear accelerators, and tend to be limited to only a few microns below the surface. The competence, therefore, of the laser approach to delve to discreet depths below the surface of a sample is attractive for homogeneity studies in bulk materials. A typical spectrum depicting the profile of chloride with depth appears in **Figure 3(a)**. The general trend portrays oscillating intensities suggesting that migration of chloride through the bulk material leads to interaction with the matrix. Similar trends appeared in both sample grades. Such interaction ultimately results in undesirable metamorphosis of the sample [15] causing material damage [16]. Clearly, the path of migration through the concrete would depend on its compositional make-up. The spectrum in **Figure 3(a)** shows that at certain depths the chloride intensity changes sharply. This could be due to minor 'blockages' that limit permeability and create a diversion in the migration path itself. These blockages could be made up of conglomerates of gravel/sand/cement in certain proportions and knowledge of such constitutions would be useful to limit the infiltration of chloride through the bulk material.

A good example of an obstructed path is shown in **Figure 3(b)**, which represents a spectrum delineating an abrupt end to the diffusion of chloride after a depth of about 25 μm. Evidently, some obstruction in the migration path at a depth of 25 μm prevented the chloride from travelling any further. The data in **Figure 3(b)** suggests that either permeability is limited or chloride migration stops. The mechanistic details are difficult to devise and it is not clear at this stage exactly how permeability and chloride migration are linked. The spectrum in **Figure 3(c)** is interesting for the simple reason that it shows dispersion of chloride up to 22 μm and then a blocked path between 22-32 μm followed by continued migration beyond a depth of 32 μm. This continued migration could be attributed to either another stream of chloride ions that overlapped with the track of the laser beam; or the same stream that went via another route and again aligned itself with the main stream. This spectrum in particular delineates the tortuosity of the transport path, which if understated could lead to deviations in related modeling studies.

3.2. Spatial Variation of Chloride

Iterative surface scans provided useful information on the distribution of chloride on the surfaces of the concrete samples. **Figure 4** presents a bar-graph showing the typical variation of chloride intensity at different ablation points on the surface of a selected sample. For convenience, points on the plot represent maximum to minimum intensities to exemplify the dramatic fluctuation of chloride intensity.

The reason for such sharp variations on the surface is not clear and could possibly be attributed to the inhomogeneous nature of the matrix itself. The pronounced difference in intensity by as much as a factor of about 20 would indicate that there are sites on the surface that are

Table 3. Measurements (counts/sec) of reproducibility in a NIST 613 standard.

Measurement	^{59}Co	^{85}Rb	^{51}V	^{138}Ba	^{140}Ce	^{238}U
1	567	1700	2900	7069	1333	1167
2	567	1767	2900	7103	1367	1200
3	633	1733	3101	7069	1367	1267
Mean±	589±	1733±	2967±	7080±	1356±	1211±
RSD	5.2%	1.6%	3.2%	0.23%	1.2%	3.4%
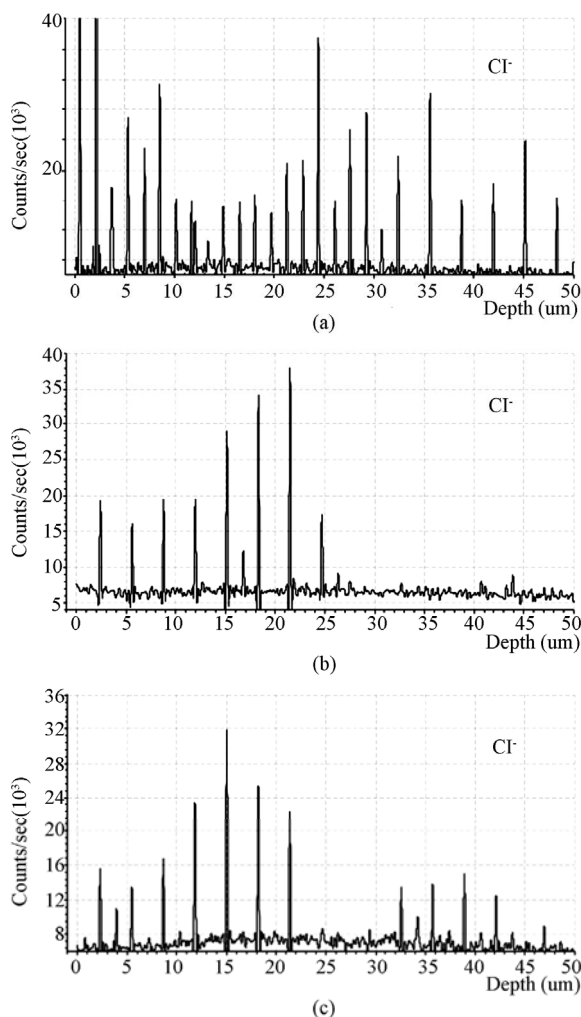
Figure 3. Depth-profiling spectra of chloride: (a) an example of an unbroken path (Grade 20); (b) an example of a blocked path (Grade 20); and (c) an example of a path that is blocked between 22-32 μm and continued chloride migration thereafter (Grade 40).
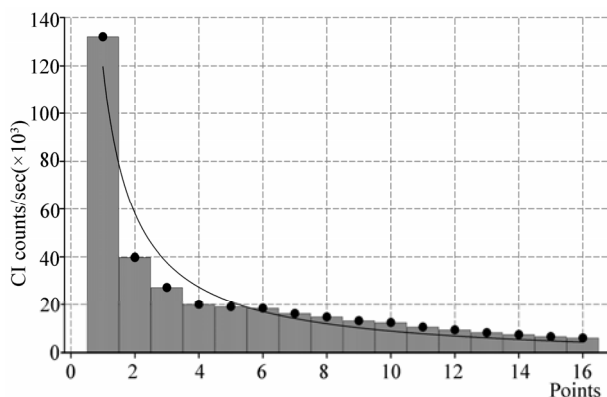
Figure 4. Typical spatial distribution of chloride on sample surface.

prone to accumulation of chloride—whereas at other points chloride can easily infiltrate the sample (through the medium of the ponding solvent). It would be of considerable interest to identify the locations on the surface matrix that tend to inhibit chloride diffusion. From the accumulated data it would seem that the matrix itself offers natural protection to the reinforced concrete by limiting chloride diffusion at certain spots. A knowledge of the composition of those inhibiting sites would be useful and if simulated could be converted into a chemical additive or inhibitor to serve as a protective layer.

3.3. Hotspots/Degradation Problems

The appearance of sporadic abnormally tall peaks in a spectrum demonstrates the presence of 'hotspots', (**Figure 5**). 'Hotspots' are sites in the interior of the sample where chloride 'agglomerates'. Once again, such accumulation of chloride ions could be due to several factors. Sudden blockages in the diffusion path; 'bottlenecks;' pores and pockets where the ponding solvent decelerates in its progressive dispersion could collectively be responsible for the 'hotspot' phenomenon. The mechanism linked to corrosion of reinforced steel is difficult to define. However, reports in the literature suggest that chloride plays a key role in the degradation process [6]. Chloride tends to weaken and destroy the thin coatings of iron oxides on the rebars. The steel is subsequently exposed to oxygen and moisture and begins to corrode. It is known that a minimum level of chloride is necessary to initiate corrosion [6,17]. Our data indicate that 'hotspots' are convenient internal sites in the matrix where chloride ions have the opportunity to accumulate and contribute to internal degradation. Such interactions combined with increased stress in the material lead to delamination in the matrix, which subsequently results in staining of the concrete. Typical staining resulting from these factors appears in one of our samples shown in **Figure 6**.

3.4. Proofed Concrete

Most protective layers in concrete tend to shield it from internal degradation. Effective proofing on concrete should be impervious to infiltration of chloride ions. **Figure 7(a)** represents a depth-profile spectrum of the proofing itself. Clearly, no chloride or other metals are present. The proofing itself works efficiently provided no cracks or fissures exist in the coating. A point to bear in mind is that minor fissures and cracks permit permeation of the ponding solvent and access of chloride into the sample. A meticulous scan of the coating was made with the laser and **Figure 7(b)** represents an imperfection in the epoxy where the ponding medium infiltrated the coating and traces of chloride were seen. In general the
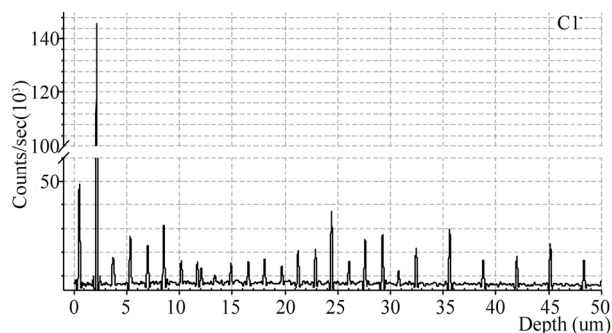
Figure 5. Example of 'hotspot' in depth-profiling spectrum of chloride (Grade 20).

Figure 6. Staining and corrosion damage due to invasive attack of chloride.
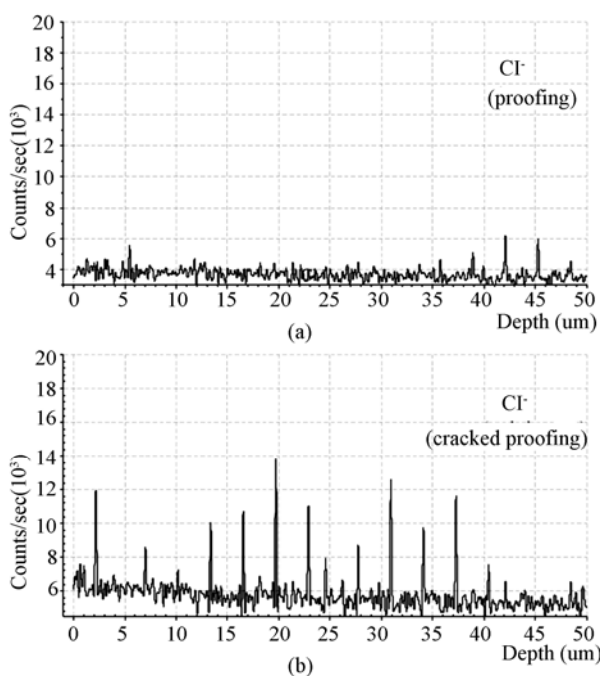
Figure 7. (a) Depth-profiling spectrum of epoxy proofing (Grade 20); (b) depth-profiling spectrum of cracked epoxy proofing showing chloride infiltration (Grade 40).

absence of chloride would proclaim the efficiency of the proofing. However, as with all epoxies exposure to a combination of solar radiation and sea water tends to cause the surface to 'chalk' and degrade a few microns each year. Hairline cracks are formed in this way through which the immersion solvent can gain free passage.

3.5. Na$^+$ and Mg^{2+} Diffusion

A report by Mussato *et al.* [7] suggests that the migratory properties of chloride ions originating from $MgCl_2$ differ from those linked to NaCl. Whether or not this theory has been verified is not clear, but our work tends to lend credence to the view that differences in such transport properties could exist. **Figures 8(a)** and **8(b)** represent typical depth profiling spectra of Na$^+$ and Mg^{2+} respectively in the unproofed sample. Similar trends appeared in both sample grades. Control samples showed no serious levels of ionic species.

Both spectra seem to mimic each other. This was an unexpected development and purported that the matrix 'adsorbs' both cations concurrently irrespective of size and charge of the ion. It could also suggest that there are points or 'bottlenecks' within the matrix where physical conditions promote supersaturation of the salts of these metals thus leading to their agglomeration and the spectral similarities observed in **Figure 8**. However, of significance is that the level of sodium chloride is about five times higher than magnesium chloride in sea water and a comparison of the heights of the peaks in **Figures**
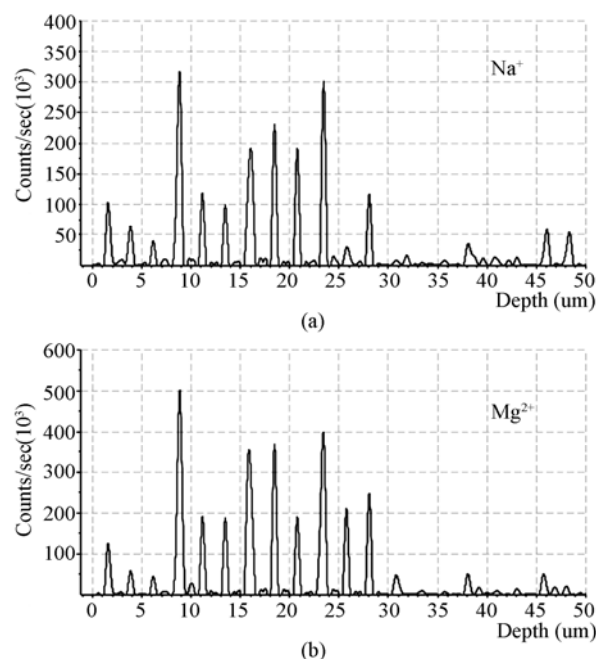
Figure 8. Typical depth-profiling spectra of a Grade 20 sample: (a) sodium; and (b) magnesium.

8(a) and 8(b) indicate that the intensities of Mg^{2+} and Na^+ do not vary appreciably, indirectly suggesting that transport differences linked to chloride could exist and should be more closely investigated. Both spectra also delineate areas of high and diminished intensity. The areas of low intensity indicate that the region in the interior of the sample is not conducive to 'adsorption' of the metal cations, and could be attributed to meager interaction with the matrix. As in the case of chloride, the areas of high intensity suggest that the metals linger due to some interaction with the matrix. **Figures 9(a)** and **9(b)** portray typical depth-profiling spectra of a proofed sample. Again the spectrum of Na^+ mirrors that of Mg^{2+}. Both spectra (**Figure 9**) reveal peaks up to a depth of 10 μm suggesting that the ponding medium penetrated the proofing and left traces of these metals on the surface. This leads us to believe that such penetration could have taken place through a hairline crack or fissure as we observed in **Figure 7(b)**, and that the unbroken proofing itself was impervious to the seawater.

4. CONCLUSIONS

Our experimental data showed that the matrix itself offers natural protection to the reinforced steel rebars by limiting chloride and metal diffusion at certain locations. Clearly, if the composition of these protective environments within the concrete could be simulated on a larger scale and introduced into the matrix (in the form of additives or inhibitors) it would offer scope for extended research in this area. Unquestionably, adding 'chemical inhibitors' to the concrete mixtures could be a useful way to control the rate of corrosion (provided that they complement the natural function of the matrix in shielding the steel rebars). Exploring the possibility of differences in migratory properties of chloride ions associated with $MgCl_2$ and $NaCl$ could also be the subject of future study.

5. AKNOWLEDGEMENTS

Figure 9. Spectra of Na^+ and Mg^{2+} in the proofed sample (Grade 40) showing infiltration up to about 10 μm.

REFERENCES

[1] McPolin, D., Basheer, P.A.M., Long, A.E., Grattan, K.T.V. and Sun, T. (2005) Obtaining progressive chloride profiles in cementitious materials. *Construction and Building Materials*, **19(9)**, 666-673.

[2] Meck, E. and Sirivivatnanon, V. (2003) Field indicator of chloride penetration depth. *Concrete and Concrete Research*, **33(8)**, 1113-1117.

[3] Tang, L. and Nilsson, L.O. (1992) Rapid determination of the chloride diffusivity in concrete by applying an electrical field. *ACI Materials Journal*, **89(1)**, 49-53.

[4] Tang, L. (1996) Electrically accelerated methods for determining chloride diffusivity in concrete-current development. *Magazine of Concrete Research*, **48(176)**, 173-179.

[5] Yang, C.C. (2004) The relationship between migration coefficient of chloride ions for concrete and charge passed in steady state using the accelerated chloride migration test. *ACI Materials Journal*, **101(2)**, 124-130.

[6] Rosenberg, A.M. and Gaidis, J.M. (2001) Avoiding corrosion damage in reinforced concrete. *Concrete International*, **23(11)**, 80-83.

[7] Mussato, T., Gepraegs, O.K. and Farnden, G. (2004) Relative effects of sodium chloride and magnesium chloride on reinforced concrete: State of the art. *Journal of the Transportation Research Board*, **1866**, 59-66.

[8] Climent, M.A., de Vera, G., Lőpez, J.F., Viqueira, E. and Andrade, C. (2002) A test method for measuring chloride diffusion coefficients through non-saturated concrete, Part I: The instantaneous plane source diffusion case. *Cement and Concrete Research*, **32(7)**, 1113-1123.

[9] Yamada, Y., Oshiro, T. and Masuda, Y. (1999) Study on chloride penetration into concrete. *Summaries of Technical Papers of Annual Meeting*, *AIJ*, Japan, September, 1999, 961-962.

[10] Ulrich, S. (1988) Concrete at high temperatures. *Fire Safety Journal*, **13(1)**, 155-168.

[11] Friedmann, H., Amiri, O., Aït-Mokhtar, A. and Dumargue, P. (2009) A direct method for determining chloride diffusion coefficient by using migration test. *Cement and Concrete Research*, **34(11)**, 1967-1973.

[12] Robinson, J.W., Skelly-Frame, E.M. and Frame, G.M. (2005) Undergraduate instrumental analysis. 6th Edition, Marcel Dekker, New York.

[13] Jarvis, K.E., Gray, A.L. and Houk, R.S. (1992) Handbook
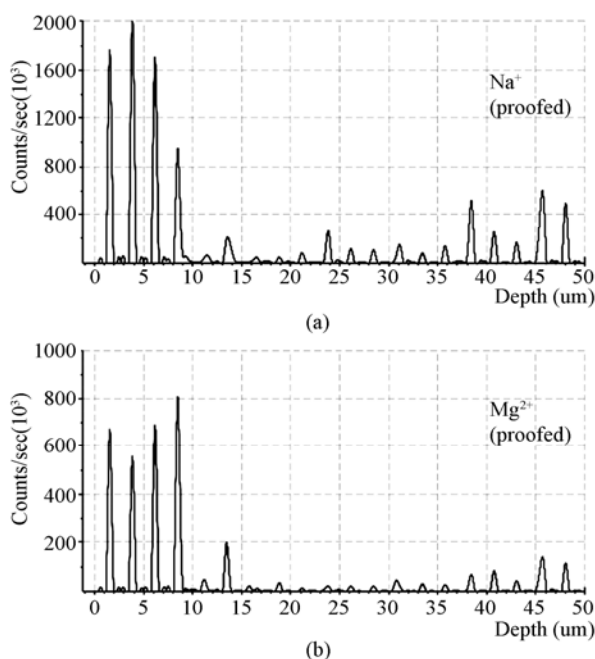
of ICP-MS. Blackie Publishers, Glasgow.

[14] Gastel, M., Becker, J.S., Kuppers, G. and Dietze, H.J. (1997) Determination of long-lived radionuclides in concrete matrix by laser ablation inductively coupled plasma mass spectrometry. *Spectrochimica Acta Part B*: *Atomic Spectroscopy*, **52(14)**, 2051-2059.

[15] Bassioni, G. and Plank, J. (2006) Untersuchungen zur kompetitiven adsorption anorganischer anionen am modellsystem kalksteinmehl. *GDCh Monographie*, **36**, 225-232.

[16] Plank, J., Bassioni, G., Dai, Z., Keller, H., Sachsenhauser, B. and Zouaoui, N. (2006) Neues zur Wechselwirkung zwischen Zementen und Polycarboxylat-Fließmitteln. *Ibausil-Tagungsband*, **16**, 579-598.

[17] Bassioni, G. (2009) Studies on halide-induced corrosion on different types of steel. *International Reviews in Chemical Engineering*, **1(6)**, 547-551.

Synthesis and thermal studies of mixed ligand complexes of Cu(II), Co(II), Ni(II) and Cd(II) with mercaptotriazoles and dehydroacetic acid

Dina M. Fouad*, Ahmed Bayoumi, Mohamed A. El-Gahami, Said A. Ibrahim, Abbas M. Hammam

Chemistry department, Faculty of Science, Assiut University, Assiut, Egypt; *Corresponding Author: dinafouad93@hotmail.com

ABSTRACT

A series of new mixed ligand complexes of cobalt(II), nickel(II), copper(II) and cadmium(II) have been synthesized with 3-benzyl-1H-4-[(2-methoxybenzylidine) amino]-1, 2, 4-triazole-5-thione (MBT), 3-bezyl-1H-4-[(4-chlorobenzylidine) amino]-1, 2, 4-triazole-5-thione (CBT), 3-benzyl-1H-4-[(4-nitrobenzylidine)amino]-1, 2, 4-triazole-5-thione (NBT) and dehydroacetic acid sodium salt (Nadha). The mixed ligand complexes have been characterized by elemental analysis, spectroscopic spectral measurements (IR, UV-Vis.), molar conductance, magnetic measurements and thermal studies. The stoichiometry of these complexes is M:L_1:L_2 = 1:1:1, 1:2:1 or 1:1:2 where L_1 = NBT, CBT and MBT and L_2 = Nadha. Tetrahedral structure was proposed for all Cd(II) mixed ligand complexes while the square planar geometry was proposed for Cu(II) mixed ligand complex with NBT. Octahedral structure was proposed for Ni(II), Co(II) mixed ligand complexes and Cu(II) mixed ligand complexes with CBT and MBT ligands. The thermal decomposition study of the prepared complexes was monitored by TG, DTG and DTA analysis in dynamic nitrogen atmosphere. TG, DTG and DTA studies confirmed the chemical formulations of theses complexes. The kinetic parameters were determined from the the thermal decomposition data using the graphical methods of Coats-Redfern and Horwitz-Metzger. Thermodynamic parameters were calculated using standard relations.

Keywords: Mix Ligand Complexes; Mercaptotriazoles; Dehydroacetic Acid

1. INTRODUCTION

3-acetyl-6-methyl-2H-pyran-2, 4(3H)-dione, a commer- cially available compound usually obtained through the auto condensation of ethyl acetoacetate [1], it has been shown to posses modest antifungal properties [2]. The importance of similar pyrones as potential fungicides is reinforced by the existence of several natural fungicides possessing structures analogous to 5, 6-dihydro dehy-droacetic acid, like alternaric acid, the podoblastins and lachnelluloic acid [3-5], studies have shown that such compounds and their complexes have very interesting biological properties[6-13]. Like dehydroacetic acid, mercaptotriazoles and their complexes have been shown to posses enhanced biological activities [14-27]. The work of the present paper is devoted to the synthesis and characterization of some new mixed ligand complexes containing mercaptotriazoles and dehydroacetic acid. The mercaptotriazole ligands containing the thioamide groups which are capable of undergoing thione-thiol (HN – C = S $\leftrightarrow$ N = C – SH) tautomerism and can coordinate to the metal atom through both nitrogen and sulphur atoms. While the sodium salt of dehydroacetic acid behaves as a monobasic bidentate ligand through two oxygen atoms. Hence the present paper reports the thermal analysis studies of some mixed ligand complexes. The associated thermal decomposition mecha- nisms are reported.

2. EXPERIMENTAL

2.1. Materials and Measurements

All chemicals used in the preparative work were of ana- lytical grade, they include the following: dehydroacetic acid sodium salt (Nadha), carbon disulphide, potassium hydroxide, absolute ethanol, methanol, Dimethylforma- mide (DMF), phenylacetic acid, o-methoxy benzaldehyde, p-nitrobenzaldehyde, p-chlorobenzaldehyde, $CuCl_2 \cdot 2H_2O$, $NiCl_2 \cdot 6H_2O$, $CoCl_2 \cdot 6H_2O$, $CdCl_2 \cdot 2.5H_2O$. They were used without further purification.

2.2. Synthesis of the Mercaptotriazole Ligands

The ligands 3-benzyl-1H-4-[(2-methoxybenzylidine)amino]-1, 2, 4-triazole-5-thione (MBT), 3-benzyl-1H-4-[(4-chlorobenzylidine)amino]-1, 2, 4-triazole-5-thione (CBT) and 3-benzyl-1H-4-[(4-nitrobenzylidine)amino]-1, 2, 4-triazole-5-thione (NBT) were synthesized according to literature survey [28-30]. The purity of the ligands was checked by elemental analysis (**Table 1**). The structures of ligands are shown in **Figure 1**.

2.3. Synthesis Cu(II) Mixed Ligand Complexes

To a solution of copper chloride 1 mmol in 10 mL methanol, a solution of the (MBT, CBT or NBT) ligands (1 mmol in 25 mL hot methanol was added dropwise with constant stirring in one direction. When the precipitate was formed, 2 mmols in 10mL methanol of (Nadha) ligand was added. Refluxing of the resulting solution carried for 8 hours. The product obtained was left overnight, filtered through sintered glass, washed with methanol and dried in vacuum over anhydrous $CaCl_2$.

2.4. Synthesis of Co(II), Ni(II) and Cd(II) Mixed Ligand Complexes

To 1 mmol of $CoCl_2.6H_2O/NiCl_2.6H_2O$ or $CdCl_2.2.5H_2O$ and 2 mmols of sodium acetate in 25 mL methanol, a solution of MBT, CBT or NBT (1 mmol in 25 mL hot methanol) was added dropwise with constant stirring in one direction. When the precipitate was formed, 2 mmols: 0.3802 grams in 10mL methanol of Nadha was added. Refluxing of the resulting solution carried for 8 hours. The mixed ligand complex appears on cooling the solution after 4-6 hours. The product obtained was left overnight, filtered through sintered glass, washed with methanol and dried in vacuum over anhydrous $CaCl_2$.

Table 1. The Analytical data for the mercaptotriazole ligands.

Free ligand (Empirical formula) Formula weight	Analytical Data % Found (Calculated)			
	C	H	N	S
MBT ($C_{17}H_{16}N_4OS$) M.Wt.= 324.401	63.09 (62.94)	5.11 (4.97)	17.47 (17.27)	9.71 (9.88)
NBT ($C_{16}H_{13}N_5O_2S$) M.Wt.= 339.379	56.55 (56.62)	3.282 (3.86)	19.82 (20.63)	9.39 (9.44)
CBT ($C_{16}H_{13}N_4SCl$) M.Wt.= 328.820	58.79 (58.44)	4.10 (3.98)	17.04 (17.03)	9.64 (9.75)
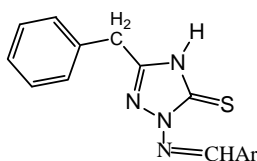
triazole ligands

where Ar is:

, 3-benzyl-4-[(2-methoxybenzylidene)amino]-1H-1,2,4-triazole-5-thione (MBT)

,3- benzyl-4-[(4-nitrobenzylidene)amino]-1H-1,2,4-triazole-5-thione(NBT)

, 3-benzyl-4-[(4-chlorobenzylidene)amino]-1H-1,2,4-triazole-5-thione(CBT)

Dehydroacetic acid(Sodium salt)
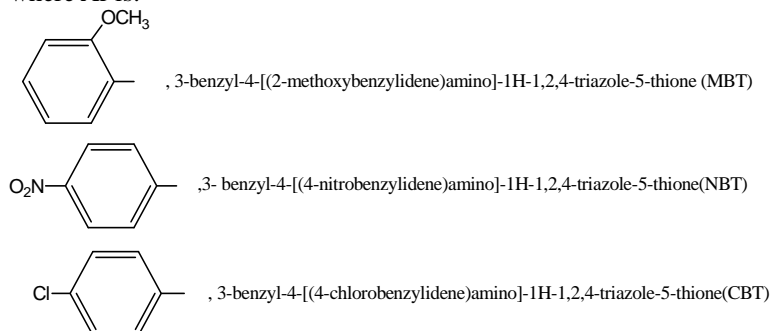
Figure 1. structures for the ligands.
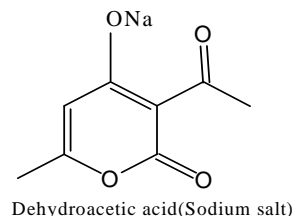
2.5. Physical Measurements

The carbon, hydrogen, nitrogen and sulfur of the solid complexes were determined by Elementar analyzer system Gmbh Vario El. Conductivity measurements for the various complexes were carried out using Jenway 4320 meterlab conductivity meter in DMF solutions at 10^{-3} M concentrations at room temperature. Electronic spectra of the solid complexes were run on perkin Elmer UV/VIS spectrophotometer Lambda 40 using 1-cm matched silica cells. Magnetic susceptibility measurements were carried out at room temperature using a magnetic susceptibility balance of the type MSB-Auto. Molar susceptibilities were corrected for diamagnetism of the component atoms by the use of Pascal's constants. The calibrant used was $Hg[Co(SCN)_4]$. The infrared spectra of the free ligands and the metal complexes were recorded on a shimadzu 470 infrared spectrophotometer (4000-400 cm^{-1}) using KBr discs. Thermogravimetric studies of the various complexes was carried out using a shimadzu DTG-60Hz thermal analyzer, at heating rate 10^oC min^{-1} in dynamic nitrogen atmosphere.

3. RESULTS AND DISCUSSION

3.1. Elemental Analyses and Conductivity Measurements

The analytical data of the metal complexes are given in **Table 2**. The data reveal the formation of complexes having 1:1:1, 1:1:2 or 1:2:1 (metal ion: mercaptotriazole ligand: Nadha) ratio with Co(II), Ni(II), Cu(II) and Cd(II). The methods used for the preparation and isolation of the mixed ligand complexes give materials of good purity as supported by their analyses. All the mixed ligand complexes are colored except Cd(II) complexes are white. They are stable in air and nonhygroscopic. The synthesized complexes are sparingly soluble in the common organic solvents but they are completely soluble in DMF or DMSO.

The molar conductance values for complexes (2, 4-9) recorded as DMF solutions are within the range 8.14-30.9 Ohm^{-1}cm^{2}mol^{-1} (**Table 2**) which indicates the nonelectrolyte nature of these complexes. While the mixed ligand complexes (1, 3, 10-12) show molar conductance values within the range 71.0-84.9 Ohm^{-1} cm^{2}mol^{-1} indicating that these complexes are 1:1 electrolytes [31].

3.2. UV-Visible Spectra and Magnetic Susceptibility Measurements

The electronic spectra of the Cu(II), Ni(II),Co(II) and Cd(II) mixed ligand complexes have been recorded as DMF solutions in the wavelength range 250-1100 nm. The ν_{max} in kK. and ε_{max} in cm^{2}mol^{-1} are depicted in **Table 3**. The corrected magnetic moment (μ_{eff}) in Bohr magneton units of the mixed ligand complexes are given in **Table 2**.

Table 2. Analytical and physical data for the complexes.

| No. | Complex [Empirical formula] (Formula weight) | Color | Analytical Data % Found (Calculated) | | | | Λ_o ohm^{-1} cm^2 mol^{-1} | μ_{eff} (BM) |
			C	H	N	S		
1	$[Cu(NBT)(dha)]Cl$ $CuC_{24}H_{20}N_5O_6SCl$(605.51)	Red	47.59 (47.60)	3.10 (3.32)	11.92 (11.56)	4.43 (5.29)	79.83	-
2	$[Cu(CBT)(dha)Cl(H_2O)]$ $CuC_{24}H_{22}N_4O_5SCl_2$(612.97)	Green	47.45 (47.02)	4.02 (3.61)	9.43 (9.14)	5.81 (5.23)	16.47	-
3	$[Cu(MBT)_2(dha)]Cl.H_2O$ $CuC_{42}H_{41}N_8O_7S_2Cl$(932.95)	Green	54.85 (54.07)	3.58 (4.42)	11.43 (12.01)	6.38 (6.87)	71.0	-
4	$[Co(NBT)(dha)_2].H_2O$ $CoC_{32}H_{29}N_5O_{11}S$(750.59)	Green	51.08 (51.20)	3.92 (3.89)	9.20 (9.33)	4.18 (4.27)	24.2	5.12
5	$[Co(CBT)(dha)Cl(H_2O)].H_2O$ $CoC_{24}H_{24}N_4O_6SCl_2$(626.37)	Grey	46.56 (46.01)	3.72 (3.86)	9.12 (8.94)	5.38 (5.11)	30.9	4.86
6	$[Co(MBT)(dha)Cl(H_2O)]$ $CoC_{25}H_{25}N_4O_6SCl$(603.94)	Grey	49.63 (49.71)	4.60 (4.17)	9.16 (9.27)	5.49 (5.30)	8.14	4.55
7	$[Ni(NBT)(dha)_2].2H_2O$ $NiC_{32}H_{31}N_5O_{12}S$(768.37)	Green	49.96 (50.02)	3.90 (4.06)	8.96 (9.11)	4.09 (4.17)	22.6	3.16
8	$[Ni(CBT)(dha)Cl(H_2O)].H_2O$ $NiC_{24}H_{24}N_4O_6SCl_2$(626.13)	Green	46.21 (46.03)	4.24 (3.86)	8.19 (8.94)	5.34 (5.12)	14.3	2.98
9	$[Ni(MBT)(dha)Cl(H_2O)]$ $NiC_{25}H_{25}N_4O_6SCl$(603.70)	Green	49.25 (49.73)	4.02 (4.17)	8.83 (9.28)	5.26 (5.31)	17.2	3.05
10	$[Cd(NBT)(dha)]Cl.H_2O$ $CdC_{24}H_{22}N_5O_7SCl$(672.39)	White	42.70 (42.87)	3.10 (3.29)	9.65 (10.41)	4.84 (4.76)	71.8	-
11	$[Cd(CBT)(dha)]Cl.H_2O$ $CdC_{24}H_{22}N_4O_5SCl_2$(661.83)	White	43.88 (43.55)	3.23 (3.35)	12.72 (8.46)	4.66 (4.84)	84.9	-
12	$[Cd(MBT)(dha)]Cl$ $CdC_{25}H_{23}N_4O_5SCl$(639.40)	White	47.35 (46.96)	3.67 (3.62)	8.93 (8.76)	4.93 (5.01)	75.2	-

-: diamagnetic

Table 3. Electronic spectral data of the synthesized mixed ligand complexes.

No.	Complex	υ(k.K) (ε_{max}cm^{2}mol^{-1})	assignment
1	[Cu(NBT)(dha)]Cl	33.17(35140.84) 25.80(5948.31) 12.40(29.60)	Intraligand LMCT $^2B_{1g}\rightarrow^2A_{1g}$
2	[Cu(CBT)(dha)Cl(H$_2$O)]	36.27(23049.82) 34.29(21219.11) 15.44(26.69)	Intraligand Intraligand $^2B_{1g}\rightarrow^2B_{2g}$, $^2B_{1g}\rightarrow^2A_{1g}$, $^2B_{1g}\rightarrow^2E_g$
3	[Cu(MBT)$_2$(dha)]Cl.H$_2$O	36.93(53248.13) 30.79(25121.52) 13.33(48.33)	Intraligand Intraligand $^2B_{1g}\rightarrow^2B_{2g}$, $^2B_{1g}\rightarrow^2A_{1g}$, $^2B_{1g}\rightarrow^2E_g$
4	[Co(NBT)(dha)$_2$].H$_2$O	34.85(84126.39) 26.91(20410.62) 17.24(143.6)	Intraligand LMCT $^4T_{1g}(F)\rightarrow^4A_{2g}(\upsilon_2)$, $^4T_{1g}(F)\rightarrow^4T_{1g}(P)(\upsilon_3)$
5	[Co(CBT)(dha)Cl(H$_2$O)].H$_2$O	37.09(57420.32) 15.62(131.05)	Intraligand $^4T_{1g}(F)\rightarrow^4A_{2g}(\upsilon_2)$, $^4T_{1g}(F)\rightarrow^4T_{1g}(P)(\upsilon_3)$
6	[Co(MBT)(dha)Cl(H$_2$O)]	36.76(38944.24) 31.21(55761.13) 15.71(131.62)	Intraligand Intraligand $^4T_{1g}(F)\rightarrow^4A_{2g}(\upsilon_2)$, $^4T_{1g}(F)\rightarrow^4T_{1g}(P)(\upsilon_3)$
7	[Ni(NBT)(dha)$_2$].2H$_2$O	32.30(45142.33) 22.42(56013.97) 15.89(118.74)	Intraligand LMCT $^3A_{2g}(F)\rightarrow^3T_{1g}(F)$
8	[Ni(CBT)(dha)Cl(H$_2$O)].H$_2$O	34.39(12535.04) 15.64(26.70)	Intraligand $^3A_{2g}(F)\rightarrow^3T_{1g}(F)$
9	[Ni(MBT)(dha)Cl(H$_2$O)]	35.66(12174.10) 31.42(14453.81) 15.02(12.30)	Intraligand Intraligand $^3A_{2g}(F)\rightarrow^3T_{1g}(F)$
10	[Cd(NBT)(dha)]Cl.H$_2$O	37.12(16417.18) 33.46(8509.42) 29.47(5046.47)	Intraligand Intraligand LMCT
11	[Cd(CBT)(dha)]Cl.H$_2$O	36.92(46607.37) 32.11(12100.81) 29.54(6728.32)	Intraligand Intraligand LMCT
12	[Cd(MBT)(dha)]Cl	37.10(115683.04) 30.96(78832.13)	Intraligand Intraligand

Three sets of bands could be recognized in the electronic spectra of the obtained mixed ligand complexes as listed in **Table 3**. The first set with υ_{max} in the range 30.79-37.12 kK., could be attributed to intraligand charge transfer transitions [32]. The second set of includes bands having υ_{max} in the range 22.42-29.54 kK. These bands are assigned as LMCT transitions [32].

The third set of bands of Cu(II) complexes 2 and 3 have υ_{max} at 15.44, 13.33 kK. and is assigned for a d-d transition which is typical for distorted octahderal Cu(II) complexes [33]. These bands are assigned to all the three transitions $^2B_{1g}\rightarrow^2B_{2g}$, $^2B_{1g}\rightarrow^2A_{1g}$ and $^2B_{1g}\rightarrow^2E_g$ [33]. While complex (1) shows an absorption d-d band at 12.40 kK. which has been attributed to $^2B_{1g}\rightarrow^2A_{1g}$ transition suggesting square planar geometry [33,34].

The d-d transition bands observed for Co(II) mixed ligand complexes(4-6) are found to have υ_{max} in the range 15.62-17.24 kK. could be attributed to $^4T_{1g}(F)\rightarrow$ $^4A_{2g}(\upsilon_2)$ and $^4T_{1g}(F)\rightarrow^4T_{1g}(P)(\upsilon_3)$ transitions, suggesting distorted octahedral environment around Co(II) ions [33,34].

The d-d transition bands observed for Ni(II) mixed ligand complexes (7-9) are found to have υ_{max} in the range 15.02-15.89 kK. could be attributed to $^3A_{2g}(F)\rightarrow$ $^3T_{1g}(F)$ transitions, suggesting octahedral geometry for the Ni(II) complexes [33].

All the mixed ligand Cd(II) complexes are diamagnetic as expected for d^{10} electronic configuration. On the basis of elemental analyses, infrared spectra, molar conductance values and thermal analyses, tetrahedral geometry is proposed for all the complexes.

The corrected magnetic moment values for Cu(II), Co(II) and Ni(II) mixed ligand complexes are reported in **Table 2**. All the Cu(II) mixed ligand complexes (1-3) display a dimagnetic nature which is attributed either to their polymeric nature or super exchange interaction [35]

in the complex molecules and/or high polarizability [36] of the ligands which supplies more electron density to copper ion and consequently the ions interact more strongly. The room temperature magnetic moment values of the Co(II) mixed ligand complexes (4-6) are within the range 4.55-5.12 B.M. expected for octahedral Co(II) complexes [35,37]. These lower magnetic moment values of the complexes may be attributed to the presence of low symmetry component in the ligand field as well as the covalent nature of the metal ligand bonds [38]. The room temperature magnetic moment values of Ni(II) mixed ligand complexes (7-9) are 3.16, 2.98 and 3.05 B.M., respectively suggesting octahedral geometry [37,39].

3.3. IR Spectra

Relevant IR bands that provide considerable structural evidence for the formation of mixed ligand complexes are reported in **Table 4**.

The IR spectrum of the free (Nadha) ligand exhibit a series of significant IR absorption bands appearing in the vibrational regions at 1713, 1642 and 1252 cm^{-1} have been ascribed to the stretching vibrations of $\upsilon(C=O)$ lactone, $\upsilon(C=O)$carbonyl and $\upsilon(C–O)$ phenolic, respectively [40,41]. In all the complexes $\upsilon(C=O)$ lactone remains unaltered while the other two peaks shift to lower frequency. This shift has been attributed to the coordination of the ligand to form the mixed ligand complexes.

NBT, CBT and MBT ligands show four bands at 1565-1588, 1275-1340, 1008-1040 and 780-815 cm^{-1} which are assignable to thioamide I, II, III, IV vibrations, respectively [42]. Theses bands have contributions from $\delta(C-H) + \delta(N-H)$, $\upsilon(C=S) + \upsilon(C-N) + \delta(C-H)$, $\upsilon(C-N) + \upsilon(C-S)$ and $\upsilon(C=S)$ modes of vibrations, respectively.

These bands are expected to be affected differently by the modes of coordination to the metal ions. In the complexes, these bands shift to lower frequency suggesting the coordination of the sulfur atom to the metal ions [43].

All the ligands and their complexes show a band within the range 3102-3030 cm^{-1} which is attributed to $\upsilon(NH)$ vibration, indicating that the mercaptotriazole ligands and the complexes are in the thione form. The strongest bands observed in the range 1619-1625 cm^{-1} in the IR spectra of NBT, CBT and MBT ligands can be assigned to $\upsilon(C=N)$ vibrations of the azomethine group. This band in the complexes shifts to lower frequency indicating the coordination of the azomethine nitrogen to the metal ions. The bands observed in the region 480-520 cm^{-1} may be assigned to $\upsilon(M-N)$ vibration [44].

The IR spectra of the mixed ligand complexes containing hydration and/or coordination water molecules display a broad band within the range 3340-3489 cm^{-1} due to $\upsilon(OH)$ vibrational modes of the water molecules [45] and this was confirmed by the results of thermal analysis. **Figure 2** shows the Proposed structure for some mixed ligand complexes.

3.4. Thermal Decomposition Studies

The measured curves obtained during TGA scanning were analysed to give the percentage mass loss as a function of temperature .The different kinetic parameters were computed from thermal decomposition data using Coats-Redfern. And Horwitz-Metger methods [46,47]. Thermodynamic parameters: entropy ($\Delta S^{\#}$), enthalpy ($\Delta H^{\#}$) and free energy ($\Delta G^{\#}$) of activation were calculated as shown in **Table 5** using the following standard relations [48].

Table 4. Relevant IR Spectral data for the complexes.

| Compound | υ(O-H) (H$_2$O) | Thioamide Bands | | | | dha characterstic bands | |
		I δ(C-H)+ δ(N-H)	II υ(C=S)+ υ(C-N)+ δ(C-H)	III υ(C-N)+ υ(C-S)	IV υ(C=S)	υ(C=O) carbonyl	υ(C–O)
[Cu(NBT)(dha)]Cl	-	1550	1240	1000	790	1630	1240
[Cu(CBT)(dha)Cl(H$_2$O)]	-	1550	1240	1000	790	1630	1240
[Cu(MBT)$_2$(dha)]Cl.H$_2$O	3350	1550	1260	1000	780	1630	1230
[Co(NBT)(dha)$_2$].H$_2$O	3300	1550	1270	1000	790	1640	1220
[Co(CBT)(dha)Cl(H$_2$O)].H$_2$O	3350	1540	1260	1010	800	1640	1240
[Co(MBT)(dha)Cl(H$_2$O)]	3350	1560	1250	1020	770	1620	1240
[Ni(NBT)(dha)$_2$].2H$_2$O	3400	1560	1270	1000	810	1630	1240
[Ni(CBT)(dha)Cl(H$_2$O)].H$_2$O	3350	1560	1270	1010	780	1600	1200
[Ni(MBT)(dha)Cl(H$_2$O)]	3350	1550	1180	1000	770	1620	1250
[Cd(NBT)(dha)]Cl.H$_2$O	3400	1540	1250	990	810	1630	1190
[Cd(CBT)(dha)]Cl.H$_2$O	3440	1560	1260	1010	760	1620	1220
[Cd(MBT)(dha)]Cl	-	1570	1250	1010	750	1620	1230

M = Cu(II), Co(II), Ni(II) or Cd(II); x = 0 or 1
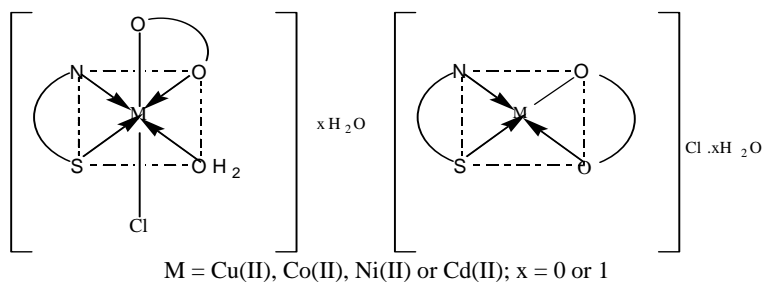
Figure 2. The Proposed structure for some mixed ligand complexes.

3.4.1. Thermal Analysis of [Cu(NBT)(dha)]Cl

The TGA of the square planar complex [Cu(NBT)-(dha)]Cl gave three steps (**Figure 3, 4**). The first step (T = 26.04-291.4°C, $E^{\#}$ = 98.78 KJ/mol) is assignable to removal of $C_{15}H_{13}N_5O_2S$ moiety (calcd. = 54.063%; found = 53.829%). Step two (T = 291.61-392.12°C, $E^{\#}$ = 211.85 KJ/mol) is assignable to removal of chlorine atom and $COCH_3$ moiety (calcd. = 12.986%; found = 12.666%). The third step (T = 394.14-751.73°C, $E^{\#}$ = 160.68 KJ/mol) is assignable to removal of carbon atom and $C_6H_4O_3$ moiety (calcd. = 22.477%; found = 23.102%). The residual product is assignable to be Cu (calcd. = 10.494%; found = 10.403%).

$$[Cu(NBT)(dha)]Cl \xrightarrow{\text{I, } -C_{15}H_{13}N_5O_2S} [Cu(C)(dha)]Cl \xrightarrow{\text{II,} -Cl, \ -COCH_3}$$

$$[Cu(C)(C_6H_4O_3)] \xrightarrow{\text{III, } -C, -C_6H_4O_3} Cu$$
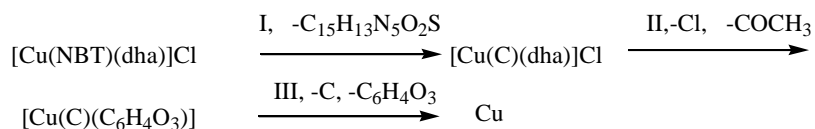
3.4.2. Thermal Analysis of Some Complexes

The TGA of the complexes 1, 2, 3, 4, 5, 6, 7, 10 gave three steps. The first step (T = 29.69-208.26°C, $E^{\#}$ = 17-178.34 KJ/mol) is assignable to removal of one water molecule. Step two (T = 169.55-388.84°C, $E^{\#}$ = 35.48-430 KJ/mol) is assignable to removal of $C_{15}H_{13}N_4Cl$ moiety. The third step (T = 321.16-751.62°C, $E^{\#}$ = 93-261 KJ/mol) is assignable to removal of $C_8H_7O_3$ moiety and chlorine atom giving CuO + CS as residual products:

$$[Cu(CBT)(dha)Cl(H_2O)] \xrightarrow{\text{I, } -H_2O} [Cu(CBT)(dha)Cl] \xrightarrow{\text{II, } -C_{15}H_{13}N_4Cl}$$

$$[Cu(CS)(dha)Cl] \xrightarrow{\text{III, } -Cl, -C_8H_7O_3} CuO + CS$$
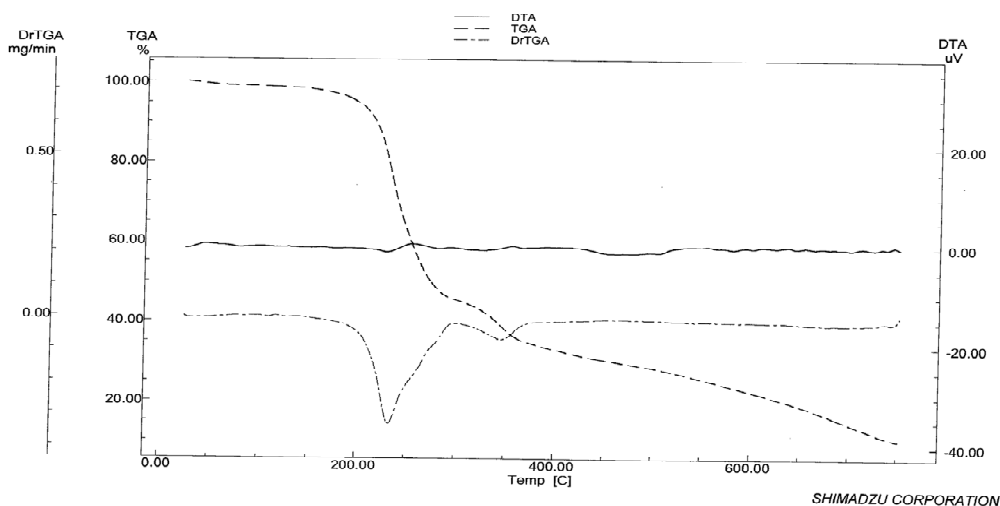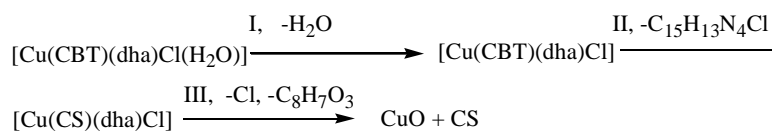
Figure 3. TG-DTG curves of complex 1.
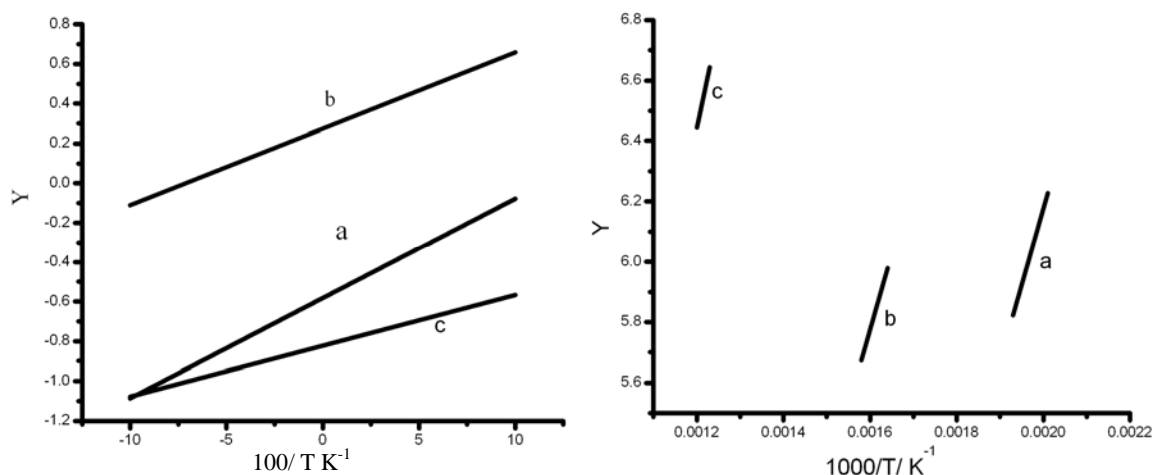
Figure 4. Coats-Redfern and Horwitz-Metzger plots of complex 1(a: 1st step, b: 2nd step, c: 3rd step).

The TGA of the complexes 8, 9, 12 gave four steps. The first step (T = 27.51-316°C, $E^{\#}$ = 42.69-58 KJ/mol) is assignable to removal of two water molecules. Step two (T = 191.98-339.03°C, $E^{\#}$ = 53.18-205.84 KJ/mol) is assignable to removal of $C_8H_7O_3$ moiety and chlorine atom. The third step (T = 318-529.38.57°C, $E^{\#}$ = 136-205.91 KJ/mol) is assignable to removal of C_6H_4Cl moiety. The fourth step (T = 444.59-751.64°C, $E^{\#}$ = 62.35-196.92 KJ/mol) is assignable to removal of $C_{10}H_9N_4$ moiety giving NiO + S as residual products.
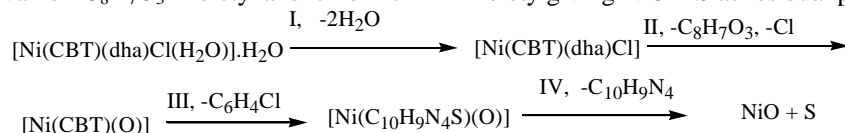
$$[Ni(CBT)(dha)Cl(H_2O)].H_2O \xrightarrow{\text{I, } -2H_2O} [Ni(CBT)(dha)Cl] \xrightarrow{\text{II, } -C_8H_7O_3, -Cl}$$

$$[Ni(CBT)(O)] \xrightarrow{\text{III, } -C_6H_4Cl} [Ni(C_{10}H_9N_4S)(O)] \xrightarrow{\text{IV, } -C_{10}H_9N_4} NiO + S$$

3.4.3. Thermal Analysis of [Cd(CBT)(dha)]Cl.H$_2$O

The TGA of the tetrahedral complex [Cd(CBT)(dha)]Cl.H$_2$O gave five steps. The first step (T = 37.43-173.98°C, $E^{\#}$ = 94.16 KJ/mol) is assignable to removal of one water molecule (calcd. = 2.722%; found = 2.322%). Step two (T = 175.18-218.69°C, $E^{\#}$ = 67.71 KJ/mol) is assignable to removal of chlorine atom (calcd. = 5.356%; found = 5.289%). The third step (T = 219.89-284.97°C, $E^{\#}$ = 194.96 KJ/mol) is assignable to removal of $C_7H_5N_2Cl$

moiety (calcd. = 23.054%; found = 23.186%). The fourth step (T = 286.97-475.42°C, $E^{\#}$ = 78.45 KJ/mol) is assignable to removal of $C_6H_7O_2$ and CHN_2 moieties (calcd. = 22.988%; found = 22.154%). Step five (T = 477.41-751.71°C, $E^{\#}$ = 193.02 KJ/mol) is assignable to removal of sulphur atom and CO and C_8H_7 moieties (calcd. = 24.661%; found = 23.154%) giving CdO + C as residual products (calcd. = 21.216%; found = 20.804%).

$$[Cd(CBT)(dha)]Cl.H_2O \xrightarrow{\text{I, } -H_2O} [Cd(CBT)(dha)]Cl \xrightarrow{\text{II, } -Cl} [Cd(CBT)(dha)]$$

$$\xrightarrow{\text{III, } -C_7H_5N_2Cl} [Cd(C_9H_8N_2S)(dha)] \xrightarrow{\text{IV, } -CHN_2 \ -C_6H_7O_2} [Cd(C_8H_7S)(C_2O_2)]$$

$$\xrightarrow{\text{V, } -CO, -S, -C_8H_7} CdO + C$$
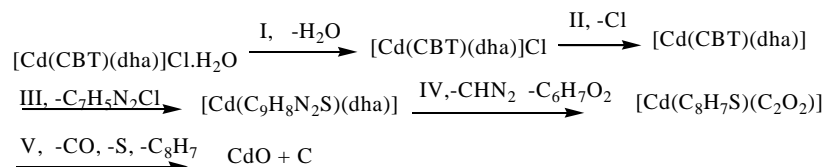
3.5. Thermal Stability

Comparing the values of the initial decomposition temperatures ($T_{i,dec.}$) of the organic part or the activation energy data for the prepared mixed ligand complexes the following data is obtained:

MBT rather than CBT and NBT forms the most stable complexes with Cu(II), Co(II) and Cd(II) while the most

stable Ni(II) complex in presence of CBT as a S, N donor ligand (**Figure 5**).

For complexes containing the same mercaptotriazole ligand; Cd(II) have been found to form the most stable complexes in presence of NBT or MBT ligands. While in case of presence of CBT ligand, Cu(II) forms the most stable complex.
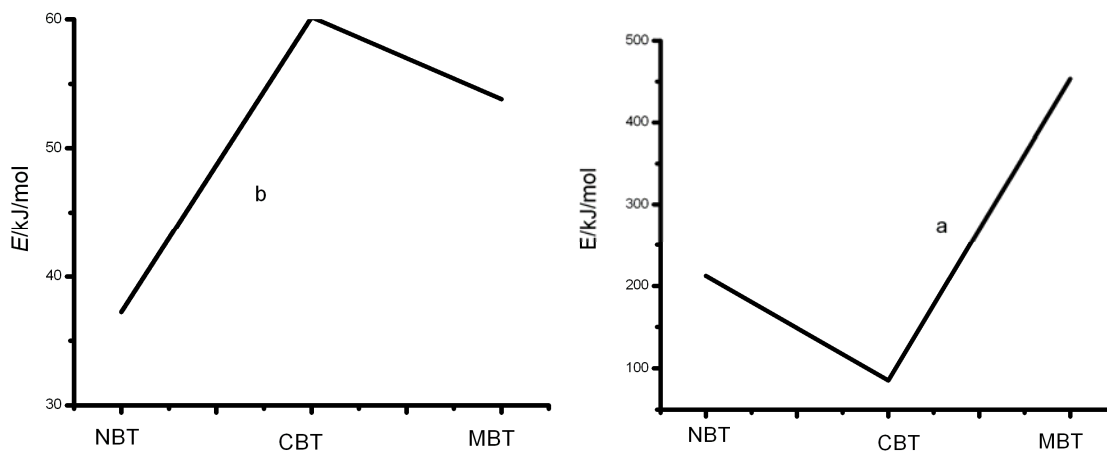
Figure 5. Relationships between the activation energy for the first decomposition step for the mixed ligand complexes and the S, N donor ligand: Cu(II)(A) and Ni(II)(B) complexes.

Table 5. Kinetic and thermodynamic parameters for the thermal decomposition of the synthesized complexes.

Complex No.	Step	n	Coats-Redfern equation (Kinetic Parameters)			(Thermodynamic parameters)			Horwitz-Metzger equation (Kinetic Parameters)			(Thermodynamic parameters)		
			r	E	Z	ΔS	ΔH	ΔG	r	E	Z	ΔS	ΔH	ΔG
1	1	1.0	1.0000	98.78	1578.17	−188.10	103.00	198.39	0.999	107.20	4.75×10^8	−83.20	111.39	153.59
	2	2.0	0.9991	211.85	3407.68	−183.36	217.00	330.53	0.9988	222.27	1.97×10^{17}	80.12	227.39	177.77
	3	2.0	0.9997	160.68	2566.76	−188.02	167.48	321.12	0.9997	174.50	3.85×10^8	−88.92	181.25	253.92
2	1	0.0	0.9998	58.56	937.11	−188.98	61.35	124.63	1.0000	64.25	2.69×10^7	−103.6	67.02	101.72
	2	0.0	1.0000	85.48	1369.69	−189.47	89.79	188.10	1.0000	94.41	8.91×10^6	−116.4	98.70	159.13
	3	2.0	1.0000	257.51	4138.54	−181.58	262.56	372.78	0.9999	267.55	3.06×10^{21}	160.51	272.5	175.14
3	1	1.0	0.9995	76.98	1232.71	−189.14	80.71	165.59	0.9992	84.60	3.81×10^7	−103.1	88.32	134.61
	2	2.0	0.9988	453.67	7256.60	−176.09	458.25	555.15	0.9602	336.07	7.15×10^{29}	321.52	340.62	163.69
	3	0.5	1.0000	57.76	935.37	−195.66	63.97	210.04	1.0000	70.52	158.19	−210.44	76.69	233.80
4	1	0.5	1.0000	58.72	941.80	−190.37	62.03	137.71	0.9999	65.35	2.52×10^6	−124.73	68.63	118.22
	2	1.0	1.0000	29.71	482.62	−198.33	34.13	139.38	0.9999	38.66	11.10	−229.69	43.05	164.94
	3	1.0	1.0000	102.44	1652.87	−192.18	109.65	276.47	1.0000	117.13	29439.29	−168.24	124.31	270.34
5	1	2.0	0.9999	28.06	454.21	−196.43	31.36	109.42	1.0000	34.74	117.06	−207.70	38.02	120.56
	2	0.0	0.9990	51.59	833.72	−194.04	56.14	162.42	0.9997	60.77	1181.68	−191.14	65.30	169.99
	3	1.0	1.0000	90.97	1463.43	−190.93	96.46	222.67	0.9999	101.53	3.70×10^5	−144.91	107.00	202.79
	4	1.0	1.0000	266.18	4280.90	−182.62	272.10	402.03	0.9998	276.69	2.06×10^{18}	98.47	282.57	212.51
6	1	2.0	0.9995	178.34	2771.21	−182.18	181.97	261.54	0.9923	185.69	3.54×10^{20}	145.31	189.31	125.84
	2	2.0	0.9986	268.70	4316.30	−180.55	273.35	374.39	0.9981	278.43	2.58×10^{23}	198.06	283.06	172.22
	3	0.0	0.9863	93.38	1505.70	−192.24	100.00	253.12	0.9904	106.49	18225.42	−171.51	113.07	249.68
7	1	0.33	1.0000	17.13	555184.60	−138.27	20.83	82.38	1.0000	24.41	1.40	−245.41	28.09	137.33
	2	0.0	0.9984	35.86	581.46	−197.03	40.41	148.25	0.9995	44.84	23.76	−223.62	49.36	171.75
	3	2.0	0.9970	186.82	2965.89	−186.33	193.23	336.75	0.9967	199.69	2.30×10^{11}	−35.28	206.06	233.24
8	1	0.0	0.9914	42.69	688.84	−193.36	46.16	126.77	0.9953	49.72	4726.17	−177.35	53.17	127.10

	2	0.5	1.0000	60.18	970.55	−192.84	64.77	171.16	0.9999	69.22	9083.61	−174.25	73.78	169.92
	3	2.0	0.9986	205.91	3316.03	−185.51	212.41	357.28	0.9984	218.87	1.19×10^{12}	−21.71	225.33	242.29
	4	2.0	0.9999	196.92	3172.60	−187.12	204.46	374.11	1.0000	212.76	1.03×10^{10}	−62.43	220.25	276.86
	1	0.0	0.9999	58.40	934.77	−188.99	61.18	124.38	1.0000	64.07	1.86×10^{7}	−106.69	66.84	102.51
9	2	0.0	0.9982	53.00	856.16	−193.50	57.38	159.346	0.9992	61.76	1959.32	−186.62	66.11	164.44
	3	2.0	0.9996	136.12	2170.36	−187.74	141.67	267.04	0.9994	146.75	2.00×10^{9}	−73.54	152.28	201.39
	4	0.0	0.9968	122.46	1965.60	−189.79	128.90	275.86	0.9977	135.86	3.05×10^{6}	−128.70	142.26	241.92
	1	0.33	0.9993	23.05	373.88	−198.97	26.74	115.11	0.9999	30.34	10.10	−228.99	34.01	135.72
10	2	2.0	0.9938	496.60	7928.71	−174.71	500.83	589.74	0.9951	506.27	1.48×10^{51}	730.26	510.48	138.86
	3	2.0	1.0000	261.18	4197.54	−181.55	266.29	377.74	0.9547	271.43	2.06×10^{21}	157.11	276.50	180.06
	1	0.0	0.9999	94.16	1516.85	−186.87	97.65	176.19	1.0000	101.22	1.31×10^{10}	−54.07	104.70	127.42
	2	1.0	1.0000	67.71	1088.20	71.70	−190.73	163.28	0.9998	75.49	7.75×10^{5}	−136.12	79.46	144.81
11	3	2.0	0.9957	194.96	3136.70	−183.48	199.77	305.84	0.9952	204.54	1.29×10^{16}	58.05	209.32	175.76
	4	0.5	1.0000	78.45	1265.17	−192.73	84.34	221.06	1.0000	89.88	12913.82	−173.41	95.74	218.75
	5	0.5	0.9997	193.02	3109.77	−186.37	199.77	351.11	0.9948	256.82	9.27×10^{13}	14.14	263.54	252.05
	1	2.0	0.9982	511.43	8173.13	−175.35	516.15	615.49	0.9988	522.15	1.12×10^{47}	650.47	526.84	158.30
12	2	1.0	0.9997	323.45	5192.46	−179.77	328.55	438.69	0.9995	333.73	6.93×10^{26}	262.93	338.79	177.70
	3	0.5	1.0000	205.84	3314.81	−185.32	212.18	353.47	1.0000	218.72	6.68×10^{12}	−7.20	225.02	230.51
	4	0.0	0.9944	62.35	1012.09	−196.88	70.13	254.30	0.9946	80.32	24.03	−227.98	88.05	301.31

3.6. Conclusions

Studying the TGA and DTA curves for the complexes indicates that there is a series of thermal changes on the DTA curves associate the weight loss in the TGA curves. This study leads to the following conclusions:

1) The presence of more than one exothermic peak in the DTA curves of all the complexes reveals that the pyrolysis occurs in several steps [49].

2) The difference in the shape of the DTA curves of the complexes containing the same metal ion with respect to each other may be attributed to the structural features of the ligand or the strength of the chelation between the metal ion and the ligand; this also led to the variety in the thermal behaviour of the complexes [50].

3) The thermal behaviour of the complexes displays an observable difference with respect to each other. This difference indicates that the thermal behaviour of these complexes depends mainly on the type of the ligands rather than the type of the metal ion.

4) Most complexes having DTA curves characterized by the presence of main sharp and strong exothermic peaks in their ends. These peaks are associated with a weight loss on the TGA curves corresponding to the decomposition of one stable intermediate compounds into the corresponding final residue [50].

5) The entropy values for all degradation steps of all degradation steps of all complexes were found to be negative, which indicates a more ordered activated state that may be possible through the chemisorption of some decomposition products [51-53].

6) The relatively low values of values of $\Delta H^{\#}$ for the prepared complexes confirm the M-S or M-N bond rupture [54,55]

7) The high values of the free energy of activation ($\Delta G^{\#}$) for most of the steps in the decomposition reactions of the complexes mean that the decomposition reactions are slower than that of the normal ones [48].

8) In general there are no obvious trends in the values of $\Delta H^{\#}$ and $\Delta S^{\#}$ for the studied complexes. This may be attributed to the fact that the thermal decomposition of the complexes is controlled not only by the structure of the ligands but also by the configuration of the coordination sphere [56,57].

9) The values of the free energy of activation ($\Delta G^{\#}$) of a given complex, generally increase significantly for the subsequent decomposition stages. This is due to the increase $T\Delta S^{\#}$ values significantly from one step to another which overrides the values of $\Delta H^{\#}$ [48].

10) Increasing the $\Delta G^{\#}$ values for the subsequent of a

given complex reflects that the rate of removal of a given species will be lower than that of the precedent one [48]. This may be attributed to the structure rigidity of the remaining complex.

11) There is much closeness in the enthalpy ($\Delta H^{\#}$) values obtained by Coats-Redfern equation and Horwitz-Metzger equation, indicating that the thermal degradation of these complexes follow the standard methods.

REFERENCES

[1] Arndt, F. (1955) *Org. Synth. Coll. II*, **231**.

[2] Rao, D.S., Ganorkar, M.C.D., Rao, L.S. and John, V.T. (1978) *Natl. Acad. Sci. Lett.*, **1**, 402.

[3] Bartels-Keith, J.R. (1960) *J. Chem. Soc.*, 1662.

[4] Miyakado, M., Inoue, S., Tanabe, Y., Watanabe, K., Ohno, N., Yoshioka, H. and Mabay, T.J. (1982) *Chem. Lett.*, 1539.

[5] Figueroa-Villar, J.D., Ayer, W.A. and Migaj, B. (1988) *Can. J. Chem.*, **66**, 506-512.

[6] Reddy, G.S.R. and Rao, N.R. (1994) *Indian J. Chem. B*, **33**, 113.

[7] Chalaca, M.Z., Figueroa-Villar, J.D., Ellena, J.A. and Castellano, E.E. (2002) *Inorg. Chim. Acta*, **328**, 45.

[8] Kureshy, R.I., Khan, N.H., Abdi, S.H.R., Iyer, P. and Patel, S.T. (1999) *Polyhedron*, **18**, 1773.

[9] Kureshy, R.I., Khan, N.H., Abdi, S.H.R. and Iyer, P. (1997) *J. Mol. Catal.*, **124**, 91.

[10] Rao, P.V. and Narasaiah, A.V. (2003) *Indian J. Chem. A*, **42**, 1896.

[11] Puerta, D.T. and Cohen, S.M. (2003) *Inorg. Chem.*, **42**, 3423.

[12] Battaini, G., Monzani, E., Casella, L., Santagostini, L. and Pagliarin, R. (2000) *J. Biol. Inorg. Chem.*, **5**, 262.

[13] Thaisrivongs, S., Romero, D.L., Tommasi, R.A., Janaki-raman, M.N., Strohbach, J.W., Turner, S.R., Biles, C., Morge, R.R., Johnson, P.D., Aristoff, P.A., Tomich, P.K., Lynn, J.C., Horng, M.M., Chong, K.T., Hinshaw, R.R., Howe, W.J., Finzel, B.C. and Watenpaugh, K.D. (1996) *J. Med. Chem.* **39**, 4630.

[14] Eweiss, N., Bahajaj, A. and Elsherbini, E. (1986) *Heterocycl. Chem.*, **23**, 1451.

[15] Holla, B., Poojary, K., Kalluraya, B. and Gowda, P. (1996) *Farmaco*, **51**, 793.

[16] Jantova, S., Greif, G., Pavlovicova, R. and Cipak, L. (1998) *Folia Microbiol.*(*Prague*), **43**, 75.

[17] Awad, I., Abdel-Rahman, A. and Bakite, E. (1991) *J. Chem. Technol. Biotechnol.*, **51**, 483.

[18] Kucukguzel, I., Kucukguzel, S.G., Rollas, S. and Kiraz, M. (2001) *Bioorg.Chem. Lett.*, **11**, 1703.

[19] Bala, S., Gupta, R.P., Sachedeva, M.L., Lal, M., Singh, A.K. and Pujari, H.K. (1978) *Ind. J. Chem.*, **16B**, 481.

[20] Jantova, S., Greif, G., Pavlovicova, R. and Cipak, L. (1998) *Folia Microbiol.*, **43**, 75.

[21] Sadadudam, Y.S., Shetty, M.M. and Dlawan, P.V. (1992) *Eur. J. Med. Chem.*, **27**, 87.

[22] Bermejo, E., Carballo, R., Castineiras, A., Dominguez, R., Maichle-Mossmer, C., Strahle, J. and West, D. (1999) *Polyhedron*, **18**, 3695.

[23] Almajan, G.L., Barbuceanu, S., Almajan, E., Draghici, C.

and Saramet, G. (2008) *European Journal of Medicinal Chemistry*, 1-7.

[24] Joshi, S.D., Vagdevi, H.M., Vaidya, V.P. and Gadaginamath, G.S. (2008) *European Journal of Medicinal Chemistry*, **43**, 1989-1996.

[25] Akbar Ali, M. and Livingstone, S.E. (1974) *Coord. Chem. Rev.*, **13**, 101.

[26] Severin, K., Bergs, R. and Beck, W. (1998) *Angew. Chem., Int. Ed.*, **37**, 1722.

[27] Shikkargol, R.K., Angadi, S.D. and Kulkami, V.H. (1996) *Orient. J. Chem.*, 1172.

[28] Cansiz, A., Koparir, M. and Demitdag, A. (2004) *Molecules*, **9**, 204.

[29] Ragenovic, K.C., Dimova, V., Kakurinov, V., Molnar, D. G. and Buzarovska, A. (2001) *Molecules*, **6**, 815.

[30] Reid, J.R. and Heindel, D. (1976) *J. Heterocyclic Chem.*, **13**, 925.

[31] Geary, W.J. (1971) *Coord. Chem. Rev.*, **7**, 81.

[32] Macias, B., Villa, V.M. and Gallego, R.R. (1995) *Tran. Met. Chem.*, **20**, 347.

[33] Lever, A.B.P. (1984) Inorganic electronic spectroscopy. Elsevier Amsterdam, 4th Edition.

[34] Dubey, S.N. and Kaushik, B. (1985) *Indian J. Chem.*, **24A(11)**, 950-953.

[35] Kishita, M., Inoue, M. and Kubo, M. (1964) *Inorg. Chem.*, **3**, 237.

[36] Dubey, S., Handa, R. and Vaid, B. (1994) *Monatsh. Chem.*, **125**, 395-401.

[37] Earnshow, A. (1968) Introduction to magnetochemistry. Academic Press, London.

[38] Beena, K. and Dubey, S.N. (1989) *Indian. J. Chem.*, **28A(5)**, 425-427.

[39] Figgis, B.N. and Lewis, J. (1960) Modern coordination chemistry. In: Lewis, J. and Wilkins, R.G., Eds., Interscience, New York, 403-406.

[40] Chalaca, M. Z., Villar, J.D.F., Ellena, J.A., Castellano, E. E. (2002) *Inorg. Chim. Acta*, **328**, 45.

[41] Chitrapriya, N., Mahalingam, V., Zeller, M., Jayabalan, R., Swaminathan, K. and Natarajan, K. (2008) *Polyhedron*, **27**, 939-946.

[42] Gupta, B.K., Gupta, D.S., Dikshit, S.K. and Agarwala, V. *Ind. J. Chem.* (1977) **15A**, 624.

[43] Subramanian, M.S. and Viswanatha, A.J. (1969) *Inorg. Nucl. Chem.*, **31**, 2575.

[44] Issleib, K. and Batz, G.Z. (1969) *Anorg. Allg. Chem.*, **369**, 83.

[45] Nakamoto, K. (1978) Infrared spectra and raman spectra of inorganic and coordination compounds. 3rd Edition, John Wiley, New York.

[46] Coats, A.W. and Redfern, J.P. (1964) *Nature*, **20**, 68.

[47] Horwitz, H.H. and Metzger, G. (1963) *Anal. Chem.*, **35**, 1464.

[48] Kandil, S.S., El-Hefnawy, B.G. and Baker, A.E. (2004) *Thermochim. Acta*, **414**, 105.

[49] Ali, F.B., Al-Akramawi, S.W., Al-Obaidi, H.K. and Al-Karboli, H.A. (2004) *Thermchim. Acta*, **419**, 39.

[50] Said, A.A. and Hassan, M.R. (1993) *Poly. Degard. Stab.*, **39**, 393.

[51] Madhusudanan, M.P., Yusuff, M.K.K. and Nair, R.G.C. (1975) *J. Therm. Anal.*, **8**, 31.

[52] Gudasi, K.B., Maravalli, P.B. and Goudar, T.R. (2005) *J. Serb. Chem. Soc.*, **70**, 643.

[53] Maravalli, P.B., Gudasi, K.B. and Goudar, T.R. (2000) *Transition Met. Chem.*, **25**, 411.

[54] Dakternieks, R.D. and Gradon, P.D. (1971) *Aust. J. Chem.*, **24**, 2509.

[55] Shetty, S.P. and Fernando, Q. (1970) *J. Am. Chem. Soc.*, **92**, 3964.

[56] Hill, O.J., Murrary, P.J. and Patil, C.K. (1994) *Rev. Inorg. Chem.*, **363**, 14.

[57] Roman, P., Beitia, I.J., Luque, A. and Miralles, G.C. (1994) *Polyhedron*, **13**, 2311.

Spectophotometric method for determination of certain cephalosporins using 4-chloro-7-nitrobenzo-2-oxa-1, 3-diazole (NBD-Cl)

Azza H. Rageh*, Salwa R. El-Shaboury, Gamal A. Saleh, Fardous A. Mohamed

Department of Pharmaceutical Analytical Chemistry, Facutly of Pharmacy, Assiut University, Assiut, Egypt; *Corresponding Author: azhesham@yahoo.com

ABSTRACT

A simple, accurate and precise spectrophotometric method has been proposed for the determination of eleven cephalosporins, namely; cefaclor monohydrate, cefadroxil monohydrate, cefalexin anhydrous, cefradine anhydrous, cefotaxime sodium, cefoperazone sodium, ceftriaxone sodium, ceftazidime penthydrate, cefazolin sodium, cefixime and cefpodoxime proxetil in bulk drug and in pharmaceutical formulations. The method depends on hydrolysis of the studied drugs using 0.5M NaOH at 100°C and subsequent reaction of the formed sulfide ions with NBD-Cl (4-chloro-7-nitrobenzo-2-oxa-1, 3-diazole) to form a yellow-colored chromogen measured at 390 nm. Different variables affecting the reaction (e.g. NaOH concentration, hydrolysis time, NBD-Cl concentration and diluting solvent) were studied and optimized. Under the optimum conditions, linear relationships with good correlation coefficients (0.9990-0.9999) were found in the range of 5-160 µg mL^{-1} for all studied drugs. The limits of assay detection and quantitiation ranged from 0.289 to 5.867 and from 0.878 to 17.778 µg mL^{-1}; respectively. The accuracy and precision of the proposed method were satisfactory. The method was successfully applied for analysis of the studied drugs in their pharmaceutical formulations and the recovery percentages ranged from 96.6 to 103.5%.

Keywords: Spectrophotometry; Cephalosporins; NBD-Cl; Pharmaceutical Analysis

1. INTRODUCTION

Cephalosporins have been used since 1948. These anti-

biotics have assumed a prominent role in modern antimicrobial therapy due to enhanced intrinsic microbiological activities and favorable safety profile. Chemical structures of cephalosporins drive from the 7-aminocephalosporanic acid (7-ACA) composed of a β-lactam ring fused with a dihydrothaizine ring (**Figure 1**), but differ in the nature of substituents at the 3- and/or 7-positions of the cephem ring. These substituents affect either the pharmacokinetic properties (3-position) or the antibacterial spectrum (7-position) of the cephalosporins [1,2]. Traditionally, cephalosporins are divided into first-, second-, third-, and fourth-generation agents. **Table 1** shows cephalosporins studied in this work. Several methods have been reported for cephalosporins determination. The official procedures in pharmaceutical preparations utilize high-performance liquid chromatography (HPLC) [3] which is expensive. Other reported procedures include spectrophotometric [4-9], spectrofluorimetric [10-13], chemiluminescence [14-16], chromatographic [17-20] and electrochemical methods [21-24] and most of them are lengthy and/or tedious.
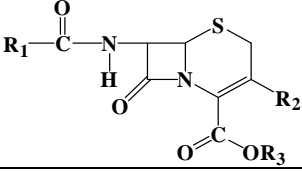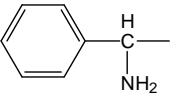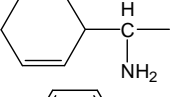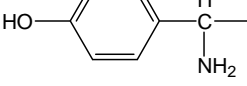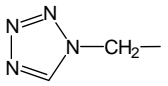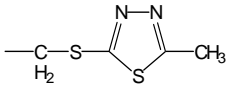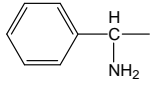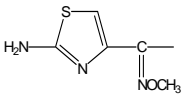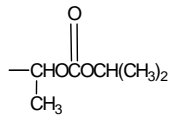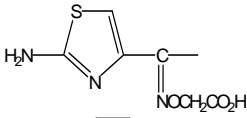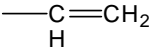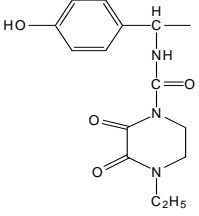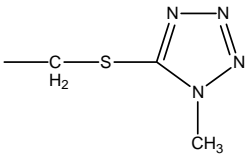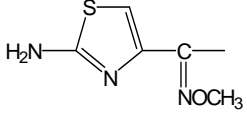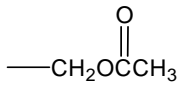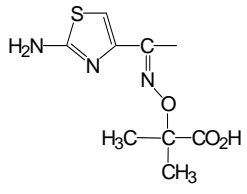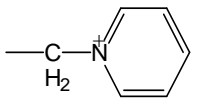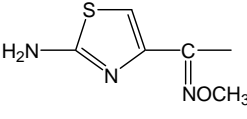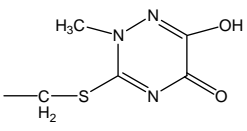
The hydrolytic degradation of cephalosporins was very often used as a preliminary step in the analytical procedure used for their determinations [25-32]. The literature reveals that many spectrophotometric methods were developed for cephalosporins determinations that based on hydrolysis of these drugs using alkaline degra-
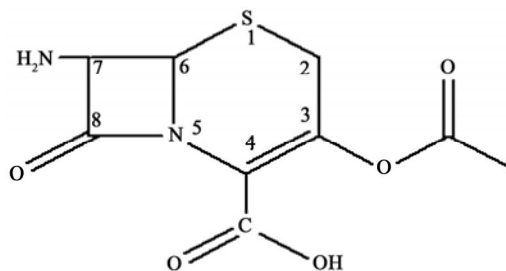
Figure 1. Chemical structure of 7-aminocephalosporanic acid.

Table 1. Chemical structures of the investigated cephalosporin antibiotics.

No.	Name	R_1	R_2	R_3	Generation
1.	Cefalexin anhydrous	phenyl-CH(NH₂)–	$-CH_3$	-H	First
2.	Cefradine anhydrous	cyclohexadienyl-CH(NH₂)–	$-CH_3$	-H	First
3.	Cefadroxil monohydrate	HO-phenyl-CH(NH₂)–	$-CH_3$	-H	First
4.	Cefazolin sodium	tetrazolyl-CH₂–	–CH₂–S–(thiadiazolyl)–CH₃	-Na	First
5.	Cefaclor monohydrate	phenyl-CH(NH₂)–	-Cl	-H	Second
6.	Cefpodoxime proxetil	(2-amino-thiazolyl)-C(=NOCH₃)–	$-CH_2OCH_3$	–CHOCOCH(CH₃)₂ with CH₃	Third
7.	Cefixime	(2-amino-thiazolyl)-C(=NOCH₂CO₂H)–	–C(H)=CH₂	-H	Third
8.	Cefoperazone sodium	HO-phenyl-CH(NH)- with C=O, piperazinedione N-C₂H₅	–CH₂–S–(tetrazolyl)–CH₃	-Na	Third
9.	Cefotaxime sodium	(2-amino-thiazolyl)-C(=NOCH₃)–	$-CH_2OCCH_3$ (O)	-Na	Third
10.	Ceftazidime pentahydrate	(2-amino-thiazolyl)-C(=N–O–C(CH₃)(CH₃)–CO₂H)–	–CH₂–N⁺(pyridinyl)	-H	Third
11.	Ceftriaxone sodium	(2-amino-thiazolyl)-C(=NOCH₃)–	–CH₂–S–(triazinone, H₃C–N, OH, =O)	-Na	Third

dation and subsequent reaction of the formed sulfide ions with chromogenic reagents [26,27].

NBD-Cl (**Figure 2**) has been reported as fluorogenic reagent for determination of amines [33] and for spectrophotometric determination of many compounds [34-41]. Thiocompounds have been reported to form intensely colored products in an alkaline medium with NBD-Cl which could be used for their colorimetric determination [42]. It is always required to develop analytical methods using low cost techniques. UV-Vis spectrophotometry is still considered a convenient and economical technique for routine analysis of drugs in pharmaceutical formulations. On the basis of the aforementioned reasons, it was decided to develop a quantitative method for the determination of the studied cephalosporins based on their alkaline hydrolysis and subsequent reaction of the resulting hydrolysates with NBD-Cl, which may be used for their analysis either in pure forms or in pharmaceutical formulations. This method is selective for cephalosporins, since other β-lactam antibiotics such as penicillins do not give sulfide ions under the degradation conditions employed [27,43-45].

2. EXPERIMENTAL

2.1. Apparatus

Shimadzu UV-1700 PC, UV-Visible Spectrophotometer (Tokyo, Japan), ultrasonic cleaner (Cole-Parmer, Chicago, USA), sartorious handy balance-H51 (Hannover, Germany) and MLV type thermostatically controlled water bath (Salvis AG Emmenbruck, Luzern, Germany).

2.2. Materials and Reagents

All solvents used were of analytical-reagent grade, sodium hydroxide (El-Nasr Chemical Co. Cairo, Egypt) 0.5 M aqueous solution, hydrochloric acid (El-Nasr Chemical Co. Cairo, Egypt), 4-cholor-7-nitrobenzofurazan [NBD-Cl] (Fluka Chemie AG, Switzerland) freshly prepared (3×10^{-3} M) equivalent to 0.060% w/v in acetone, samples of cephalosporins were generously supplied by their respective manufacturers and were used as supplied: cefaclor monohydrate and cefradine
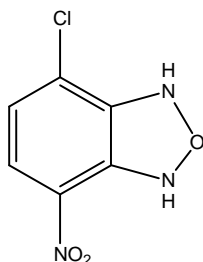
Figure 2. Chemical structure of NBD-Cl.

anhydrous (Sigma Chemical Co., St. Louis, USA), cefadroxil monohydrate (Amoun Pharmaceutical Industries Co., APIC, Cairo, Egypt), cefalexin anhydrous (GalaxoWellcome, S.A.E., El Salam City, Cairo, Egypt), cefotaxime sodium (CID, Cairo, Egypt), cefoperazone sodium (Pfizer Co., Egypt), ceftazidime pentahydrate and ceftriaxone sodium (T3A Pharma Group, Assiut, Egypt), cefpodoxime proxetil (Hoechst Marion Roussel, S. A. E., Cairo, Egypt), cefixime (El-Hekma Co., Cairo, Egypt) and cefazolin sodium (Bristol-Myers Squibb Pharmaceutical Co., Cairo, Egypt) and pharmaceutical formulations containing the studied drugs were purchased from local market.

2.3. Preparation of Standard Solutions

Stock solutions containing 100 mg mL^{-1} of each cephalosporin were prepared in double distilled water (methanol was used in case of cefadroxil monohydrate, cefalexin anhydrous, cefaclor monohydrate, cefradine anhydrous, cepodoxime proxetil and cefixime). Working standard solutions containing 0.5-2.5 mg mL^{-1} (in case of cefadroxil monohydrate and cefalexin anhydrous), 1-6 mg mL^{-1} (in case of cefradine anhydrous), 2-8 mg mL^{-1} (in case of cefaclor monohydrate, cefazolin sodium, cefotaxime sodium, ceftriaxone sodium and cefpodoxime proxetil), 2-10 mg mL^{-1} (in case of cefixime) and 2-16 mg mL^{-1} (in case of cefoperazone sodium and ceftazidime pentahydrate) were prepared by suitable dilution of the stock solution with double distilled water (in case of cefadroxil monohydrate, cefalexin anhydrous, cefaclor monohydrate, cepodoxime proxetil and cefixime, dilution was made using methanol). The stock and working standard solutions must be freshly prepared.

2.4. Preparation of Sample Solutions

Tablets and capsules. Twenty tablets or the contents of 20 capsules were weighed, finely powdered and mixed thoroughly. An accurately weighed amount of the powder obtained from tablets or capsules equivalent to 250 mg of each drug was transferred into a 25-mL volumetric flask, dissolved in about 10 mL double distilled water (10 mL methanol was used in case of cefadroxil monohydrate, cefalexin anhydrous, cefaclor monohydrate, cefradine anhydrous, cepodoxime proxetil and cefixime), sonicated for 15 min, diluted to the mark with double distilled water (in case of cefadroxil monohydrate, cefalexin anhydrous, cefaclor monohydrate, cefradine anhydrous, cefpodoxime proxetil and cefixime**,** dilution was made using methanol), mixed well and filtered; the first portion of the filtrate was rejected. Further dilutions with the same solvent were made to obtain sample solution containing the specified concentration for each drug

as mentioned under the preparation of standard solutions and then the general procedure was followed.

Vials and powder for oral suspension. An accurately weighed amount of powder equivalent to 250 mg of each drug was transferred into a 25-mL volumetric flask, then the procedure was followed as under tablets and capsules beginning from (dissolved in about 10 mL double distilled water……….).

2.5. General Procedure

Accurately measured one milliliter aliquot volume of the standard or sample solutions was transferred into 10-mL volumetric flask. 5 mL of 0.5 M NaOH were added and the flask was heated in a boiling water-bath for 30 min, cooled to room temperature and completed to volume with double distilled water. One milliliter of the resulting drug hydrolysate was pipetted into 10-mL volumetric flask, 1.0 mL of 3×10^{-3} M NBD-Cl was added followed by 1 mL of concentrated HCl. The resulting solution was mixed well and the flask was completed to volume with ethanol. The absorbance was measured at 390 nm against reagent blank treated similarly.

3. RESULTS AND DISCUSSION

3.1. Absorption Spectra

As shown in **Figure 3**, the absorption spectrum of NBD-Cl in acetone shows a maximum absorption at 340 nm. All the investigated drugs after alkaline hydrolysis give a very weak absorption taking cefalexin anhydrous hydrolysate as a representative example which gives a very broad absorption maximum at 350 nm. The interaction colored product of cefalexin anhydrous hydrolysate with NBD-Cl shows absorption maximum at 390 nm (**Figure 3**).
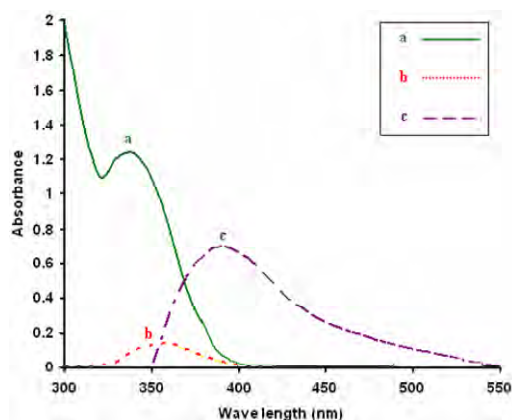
Figure 3. Absorption spectra of (a) NBD-Cl (3×10^{-3} M), (b) cefalexin anhydrous hydrolysate alone (20 μg mL^{-1}) and (c) the reaction colored product between NBD-Cl and cefalexin anhydrous hydrolysate.

3.2. Optimization of Reaction Variables

Since the developed method depends on the formation of colored product by the interaction of NBD-Cl with sulfide ions resulted from the alkaline degradation of cephalosporins so, optimization studies were carried out extensively to find the optimum conditions for the alkaline degradation and subsequently the optimum yield of sulfide ions and the maximum stability of the chromogen formed taking cefalexin anhydrous (15 μg mL^{-1}) as a representative example for these studies. These variables include:

Effect of NaOH concentration. The influence of sodium hydroxide concentration on producing the maximum absorption intensity was investigated using 0.1-1.0 M NaOH keeping other factors constant. Maximum absorption readings were obtained upon using 0.5 M NaOH; above this concentration and up to 1 M NaOH, the absorbance remains constant. So, this concentration was selected for further work (**Figure 4**).

Effect of hydrolysis time. The effect of hydrolysis time on the absorption intensity was studied using different heating times in a boiling water bath (at 100°C) starting from 10 min until 2 hours and the reaction was carried out as usual. The obtained absorbance readings were plotted against hydrolysis time. The maximum absorption intensity was attained after 20 min and remained stable for at least 100 min. Thirty minutes hydrolysis time was used in all subsequent experiments as shown in **Figure 5**.

Effect of NBD-Cl concentration. The concentration of NBD-Cl, for the maximum color development was varied in the range of 0.75×10^{-3}-4×10^{-3} M. It was found that 1 mL of 3×10^{-3} M NBD-Cl was the most suitable con-
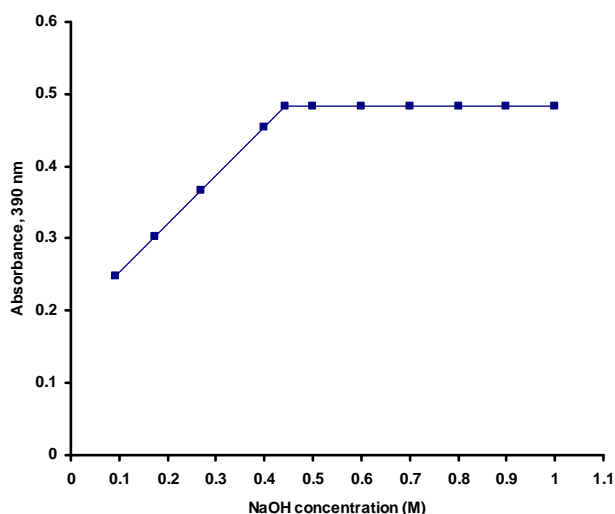
Figure 4. Effect of NaOH concentration on the absorbance of the reaction colored product at 390 nm.
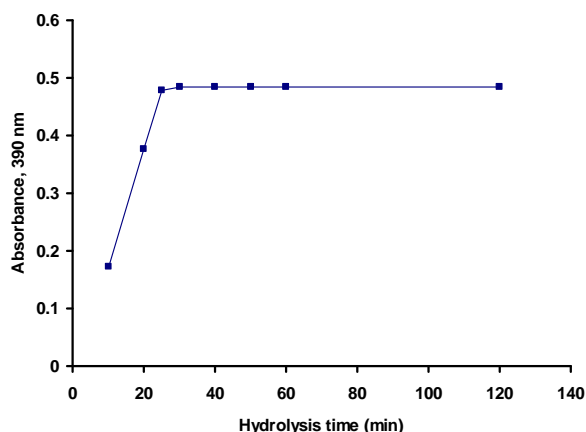
Figure 5. Effect of hydrolysis time on the absorbance of the reaction colored product at 390 nm.
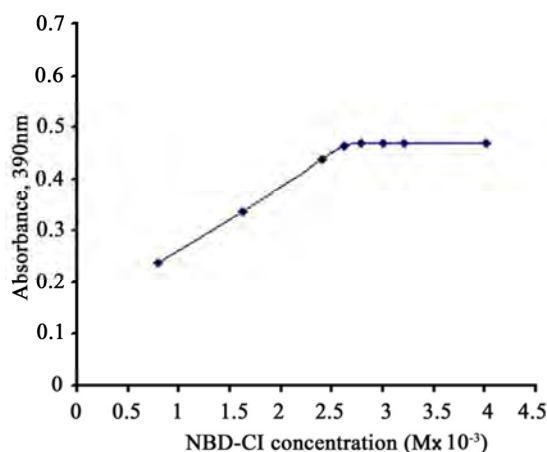
Figure 6. Effect of NBD-Cl concentration on the absorbance of the reaction colored product at 390 nm.

centration for determination of the studied drugs as shown in **Figure 6**. Owing to the presence of labile chloride, a daily fresh solution is recommended.

Effect of type and concentration of acid. Different acids such as sulfuric, hydrochloric, perchloric, nitric and acetic acids were tested to determine the most suitable acid for the reaction. One milliliter of concentrated hydrochloric acid was selected in this study as it gave the highest absorbance readings taking cefalexin anhydrous (15 µg mL^{-1}) as a representative example (**Table 2**).

Further investigations were carried out in order to find the most suitable concentration of hydrochloric acid. It was observed that higher absorbance readings and more reproducible results were obtained upon increasing hydrochloric acid concentration. As a result of these investigations, 1 mL of concentrated hydrochloric acid was used for subsequent work.

Effect of reaction time. The reaction between the investigated drugs hydrolysates and NBD-Cl was very

Table 2. Effect of different acids on the absorbance readings of the reaction colored product of cefalexin anhydrous[a] with NBD-Cl.

Acid (1mL)	Absorbance[b]
Hydrochloric acid	0.460
Sulfuric acid	0.400
Perchloric acid	0.413
Acetic acid	0.210
Nitric acid	0.315

[a]Cefalexin anhydrous concentration used is 15 µg mL^{-1}; [b]Average of three determinations.

rapid and the interaction colored product can survive before dilution unchanged for at least 1 hour. However, measurements were achieved instantaneously.

Effect of diluting solvent. Different solvents were tested in order to select the most appropriate solvent for optimum color development. The results given in **Table 3** show small shifts in the position of the maximum absorption peak. The absorption intensities were slightly influenced. Ethanol was used throughout this work because it gave the highest absorbance readings and the most reproducible results.

Stability of the reaction colored product. Stability time was obtained by following the absorbance readings of the developed reaction product for 24 hours at room temperature (25 ± 5°C). It was found that the produced color was stable for 24 hours for all studied drugs.

3.3. Calibration Curves

Linear relationship was obtained for all studied drugs by applying the developed method (**Table 4**). Good linearity of the calibration curves were clearly evident by excellent correlation coefficients which ranged from 0.9990 to 0.9999 and coefficients of determination ranged from 0.9978 to 0.9998. This wide variation in the linearity range may be attributed to the different yields

Table 3. Effect of solvent on λ_{max} and the absorbance of the formed chromogen between cefalexin anhydrous[a] and NBD-Cl.

Solvent	λ_{max}(nm)	A[b]
Water	404	0.404
Ethanol	390	0.470
Methanol	391	0.401
Acetone	392	0.427
Acetonitrile	398	0.456
Propan-1-ol	390	0.467
Propan-2-ol	389	0.463
Dimethylformamaide	393	0.425
Dimehtylsulfoxide	401	0.458

[a]Cefalexin anhydrous concentration is 15 µg mL^{-1}; [b]Average of 3 determinations.

Table 4. Summary of quantitative parameters and statistical data using the proposed procedure.

Drug	Intercept (a) ± SD[a]	Slope (b) ± SD[a]	Linearity Range ($\mu g\ mL^{-1}$)	Correlation coefficient (r)	Determination coefficient (r^2)	LOD[b] ($\mu g\ mL^{-1}$)	LOQ[c] ($\mu g\ mL^{-1}$)
Cefadroxil monhydrate	$-0.013 \pm (3.6 \times 10^{-3})$	$0.041 \pm (0.2 \times 10^{-3})$	5-25	0.9999	0.9998	0.29	0.88
Cefalexin anhydrous	$-0.126 \pm (5.0 \times 10^{-2})$	$0.398 \pm (1.2 \times 10^{-3})$	5-25	0.9999	0.9998	0.42	1.26
Cefradine anhydrous	$0.076 \pm (7.5 \times 10^{-3})$	$0.013 \pm (1.5 \times 10^{-4})$	10-60	0.9999	0.9998	1.90	5.77
Cefaclor monohydrate	$0.055 \pm (1.3 \times 10^{-2})$	$0.010 \pm (2.1 \times 10^{-4})$	20-80	0.9996	0.9992	4.29	13.00
Cefazolin sodium	$0.016 \pm (4.3 \times 10^{-3})$	$0.009 \pm (1.9 \times 10^{-4})$	20-80	0.9994	0.9988	1.58	4.78
Ceftriaxone sodium	$0.033 \pm (5.3 \times 10^{-3})$	$0.010 \pm (0.5 \times 10^{-4})$	20-80	0.9996	0.9992	1.75	5.30
Cefotaxime sodium	$0.056 \pm (1.2 \times 10^{-2})$	$0.010 \pm (1.5 \times 10^{-4})$	20-80	0.9990	0.9980	3.96	12.00
Cefpodoxime proxetil	$0.046 \pm (1.6 \times 10^{-2})$	$0.009 \pm (1.3 \times 10^{-4})$	20-80	0.9990	0.9980	5.87	17.78
Cefixime	$0.095 \pm (3.2 \times 10^{-3})$	$0.007 \pm (0.2 \times 10^{-4})$	20-100	0.9989	0.9978	1.51	4.57
Cefoperazone sodium	$0.019 \pm (8.3 \times 10^{-3})$	$0.005 \pm (0.6 \times 10^{-4})$	20-160	0.9998	0.9996	5.48	16.60
Ceftazidime pentahydrate	$0.048 \pm (7.4 \times 10^{-3})$	$0.005 \pm (0.7 \times 10^{-4})$	20-160	0.9994	0.9988	4.88	14.80

[a] Average of six determinations; [b] Limit of detection; [c] Limit of quantitation.

of sulfide ions from the studied cephalosporins [45].

3.4. Method Validation Study

The method was validated according ICH guidelines on the validation of analytical methods [46] and complied with USP 31 validation guidelines [3]. All results were expressed as percentages, where *n* represents the number of values. For the statistical analysis Excel 2003 (Microsoft Office) was used. A 5% significance level was selected.

LOD and LOQ. The limits of detection and quantitation for all studied drugs ranged from 0.29 to 5.87 and from 0.88 to 17.78 $\mu g\ mL^{-1}$; respectively which indicate high sensitivity of the proposed method (**Table 4**).

Accuracy. The accuracy of the method was determined by investigating the recovery of each of the studied drugs at three concentration levels covering the specified range (six replicates of each concentration). The results shown in **Table 5** depict good accuracy and recovery percentage ranged from 98.0 to 102.3%.

Precision. As shown in **Table 6**, the small values of SD and % RSD point to high precision of the proposed method.

Selectivity. The effect of the presence of common excipients such as; starch, talc, lactose, glucose, sucrose, magnesium-stearate and gum acacia was studied. It was found that no interference was introduced by any of them.

Robustness. Robustness was examined by evaluating the influence of small variation in the experimental parameters on the analytical performance of the proposed method [47]. The studied parameters were: NaOH con-

centration, NBD-Cl concentration, heating temperature and heating time on the method suitability and sensitivity. It was found that none of these variables significantly affects the performance of the method (**Table 7**) which indicates the robustness of the proposed method.

3.5. Applications to the Analysis of Pharmaceutical Dosage Forms

The proposed method was applied successfully for determination of the studied drugs in their pharmaceutical dosage forms. Six replicate measurements were made in each case, the results obtained were validated by comparison with a previously reported method [48]. No significant difference was found by applying *t*- and *F*-tests at 95% confidence level indicating good accuracy and precision (**Table 8**). Recovery studies were also carried out by standard addition method [49]. The results in **Table 9** indicate good recoveries (96.0 to 103.8%) and confirm that there is no interference from frequently encountered excipients or additives.

3.6. Suggested Reaction Mechanism

Cephalosporins were previously reported to produce sulfide ions upon alkaline degradation and it was found to be one of their major degradation products [43-45, 50-55]. NBD-Cl is an active halide derivative, which was considered as a likely target for good nuclophiles, under alkaline conditions, such as amines, amino acids and thiocompounds [40-42].

In the proposed method, sulfide ions were allowed to react with NBD-Cl via SN_2 mechanism. The high nucleophilicity of sulfide ions, the presence of Cl^- anion as

Table 5. Accuracy of the proposed method for analysis of the studied drugs at three concentration levels.

Drug	Recovery (%) ± SD[a]		
	25 µg mL^{-1}	50 µg mL^{-1}	75 µg mL^{-1}
Cefaclor monohydrate	100.6 ± 0.93	101.4 ± 0.75	102.1 ± 0.30
Ceftriaxone sodium	99.3 ± 0.52	100.6 ± 0.96	100.2 ± 0.51
Cefotaxime sodium	99.7 ± 1.35	101.5 ± 0.83	101.3 ± 1.16
Cefixime	98.3 ± 1.24	98.7 ± 0.58	98.6 ± 0.73
Cefazolin sodium	101.1 ± 1.08	98.9 ± 0.60	102.3 ± 0.68
Cefpodoxime proxetil	99.4 ± 0.35	99.4 ± 0.47	99.0 ± 0.29
Drug	Recovery (%) ± SD[a]		
	10 µg mL^{-1}	15 µg mL^{-1}	20 µg mL^{-1}
Cefadroxil monohydrate	99.9 ± 1.31	100.4 ± 0.83	99.1 ± 0.90
Cefalexin anhydrous	98.6 ± 0.26	102.2 ± 1.29	98.0 ± 0.41
Drug	Recovery (%) ± SD[a]		
	40 µg mL^{-1}	80 µg mL^{-1}	120 µg mL^{-1}
Ceftazidime pentahydrate	102.3 ± 0.86	98.9 ± 1.25	99.6 ± 0.82
Cefoperazone sodium	98.0 ± 0.70	100.3 ± 1.11	101.4 ± 1.03
Drug	Recovery (%) ± SD[a]		
	15 µg mL^{-1}	30 µg mL^{-1}	45 µg mL^{-1}
Cefradine anhydrous	98.3 ± 0.51	100.8 ± 0.66	100.7 ± 0.87

[a]Average of six replicates.

Table 6. Intra- and inter-day precision of the proposed spectrophotometric method.

Drug	Drug Conc. (µg mL^{-1})	Intra-day precision		Inter-day precision	
		Mean ± SD[a]	% RSD	Mean ± SD[a]	% RSD
Cefaclor monohydrate	25	99.6 ± 0.93	0.93	99.4 ± 1.29	1.30
	50	99.9 ± 1.65	1.66	98.5 ± 0.90	0.91
	75	100.1 ± 1.40	1.40	100.7 ± 1.12	1.12
Cefalexin anhydrous	10	100.3 ± 1.17	1.16	98.9 ± 1.23	1.25
	15	100.4 ± 1.53	1.52	99.0 ± 0.97	0.98
	20	100.1 ± 1.16	1.16	100.5 ± 0.88	0.88
Cefadroxil monohydrate	10	99.4 ± 0.99	1.00	101.0 ± 1.09	1.08
	15	99.9 ± 0.85	0.85	100.5 ± 0.77	0.76
	20	100.2 ± 1.37	1.37	98.7 ± 0.68	0.69
Cefradine anhydrous	15	100.1 ± 1.03	1.02	99.5 ± 1.13	1.14
	30	100.0 ± 1.15	1.15	98.4 ± 0.85	0.86
	45	100.6 ± 1.16	1.15	100.4 ± 1.54	1.54
Cefoperazone sodium	40	99.6 ± 0.93	0.93	101.3 ± 1.43	1.41
	80	99.7 ± 0.67	0.67	101.7 ± 1.63	1.61
	120	100.3 ± 1.35	1.34	99.1 ± 1.40	1.41
Ceftazidime pentahydrate	40	100.0 ± 1.39	1.39	100.9 ± 0.99	0.98
	80	99.6 ± 1.30	1.31	101.3 ± 1.27	1.25
	120	99.9 ± 1.04	1.05	98.9 ± 1.12	1.13

Table 6. (Continued).

Drug	Drug Conc. (μg mL⁻¹)	Intra-day precision		Inter-day precision	
		Mean ± SD[a]	% RSD	Mean ± SD[a]	% RSD
Ceftriaxone sodium	25	100.4 ± 1.57	1.56	99.2 ± 0.99	1.00
	50	101.0 ± 1.27	1.26	100.8 ± 1.15	1.14
	75	99.8 ± 1.38	1.39	98.6 ± 1.54	1.57
Cefotaxime sodium	25	99.3 ± 1.05	1.06	99.0 ± 0.77	0.78
	50	98.8 ± 0.78	0.79	101.4 ± 1.46	1.44
	75	99.4 ± 1.29	1.30	98.5 ± 0.91	0.93
Cefixime	25	99.5 ± 0.81	0.81	100.9 ± 0.99	0.98
	50	99.8 ± 1.02	1.03	99.7 ± 1.17	1.17
	75	99.6 ± 1.48	1.48	98.3 ± 1.65	1.67
Cefazolin sodium	25	100.5 ± 1.15	1.14	100.6 ± 0.68	0.67
	50	100.6 ± 1.36	1.35	99.6 ± 1.35	1.35
	75	101.4 ± 0.74	0.73	98.8 ± 1.12	1.14
Cefpodoxime proxetil	25	100.4 ± 0.89	0.89	101.3 ± 0.77	0.76
	50	100.5 ± 1.15	1.15	99.7 ± 1.55	1.55
	75	100.0 ± 1.70	1.70	100.6 ± 1.63	1.62

[a]Average of six determinations.

Table 7. Robustness of the proposed spectrophotometric method.

Experimental parameter variation	Recovery (%) ± SD[a]					
	Cefadroxil monohydrate (20 μg mL⁻¹)	Cefalexin anhydrous (20 μg mL⁻¹)	Cefradine anhydrous (40 μg mL⁻¹)	Cefaclor monohydrate (60 μg mL⁻¹)	Cefopera-zone sodium (80 μg mL⁻¹)	Ceftazidime pentahydrate (80 μg mL⁻¹)
No variation[b]	99.4 ± 1.21	99.8 ± 0.31	99.5 ± 1.82	99.5 ± 1.13	99.2 ± 0.56	99.5 ± 0.47
1- NaOH concentration						
0.45 M	98.3 ± 0.85	97.9 ± 1.20	101.5 ± 1.32	97.5 ± 0.54	101.8 ± 1.11	97.4 ± 1.12
0.55 M	98.6 ± 1.19	100.9 ± 1.15	98.2 ± 0.52	101.3 ± 0.77	99.4 ± 1.31	98.3 ± 1.34
2- NBD-Cl concentration						
2.8×10^{-3}M	102.0 ± 0.25	100.3 ± 1.35	98.2 ± 1.56	102.1 ± 0.35	100.9 ± 1.58	100.9 ± 1.15
3.2×10^{-3}M	98.5 ± 1.31	100.9 ± 0.92	98.0 ± 1.15	98.5 ± 0.91	98.5 ± 0.83	102.0 ± 0.88
3- Heating temperature						
95°C	98.8 ± 0.78	97.9 ± 1.20	102.4 ± 156	102.7 ± 2.21	101.0 ± 1.27	101.4 ± 2.04
100°C	99.6 ± 1.35	100.8 ± 1.60	100.4 ± 0.90	99.8 ± 1.02	101.3 ± 1.27	98.0 ± 2.15
4- Heating time						
25 min	100.5 ± 1.23	99. 2 ± 0.99	98.5 ± 1.57	97.5 ± 1.98	99.1 ± 1.40	99.4 ± 1.29
35 min	100.1 ± 1.40	100.4 ± 1.53	98.7 ± 0.68	99.6 ± 0.93	100.9 ± 0.99	98.5 ± 0.90

Table 7. (Continued).

Experimental parameter variation	Recovery (%) ± SD[a]				
	Ceftriaxone sodium (60 μg mL⁻¹)	Cefotaxime sodium (60 μg mL⁻¹)	Cefixime (60 μg mL⁻¹)	Cefazolin sodium (60 μg mL⁻¹)	Cefpodoxime proxetil (60 μg mL⁻¹)
No variation[b]	99.5 ± 0.66	97.6 ± 1.55	100.7 ± 0.98	99.5 ± 1.23	99.5 ± 1.01
1- NaOH concentration					
0.45 M	100.2 ± 1.35	99.5 ± 0.67	99.6 ± 1.27	98.6 ± 0.88	98.1 ± 0.60
0.55 M	98.7 ± 0.98	98.3 ± 0.49	98.4 ± 0.73	102.4 ± 1.145	99.5 ± 1.27
2- NBD-Cl concentration					
2.8×10^{-3}M	99.6 ± 1.15	102.0 ± 0.71	102.3 ± 1.30	99.7 ± 1.35	98.4 ± 1.40
3.2×10^{-3}M	98.0 ± 0.75	102.3 ± 0.58	99.5 ± 0.69	101.5 ± 0.70	99.9 ± 0.49
3- Heating temperature					
95°C	99.0 ± 1.30	99.4 ± 0.66	98.7 ± 0.66	100.6 ± 0.48	100.8 ± 0.72
100°C	97.5 ± 0.68	98.4 ± 1.13	101.9 ± 1.35	97.5 ± 1.44	99.1 ± 0.65
4- Heating time					
25 min	101.1 ± 1.44	97.8 ± 0.90	99.6 ± 0.56	99.7 ± 0.70	97.8 ± 0.49
35 min	98.1 ± 0.81	101.4 ± 1.41	100.8 ± 1.27	101.9 ± 0.72	98.0 ± 1.34

[a]Average of three determinations;
[b]Following the general assay procedure conditions.

Table 8. Determination of the studied drugs in their pharmaceutical dosage forms.

Drug	Pharmaceutical product	Recovery % ± SD	
		Proposed method (n = 6)	Reported method[b] (n = 6)
Cefaclor monohydrate	Ceclor® suspension[c] 250 mg of *cefaclor monohydrate*/5 mL	97.8 ± 0.5, t = 0.382[a] F = 1.562[a]	97.7 ± 0.40
	Bacticlor® suspension[d] 250 mg of *cefaclor anhydrous*/5 mL	97.2 ± 0.5, t = 1.913 F = 1.562	96.7 ± 0.40
Cefadroxil monohydrate	Duricef® tablets[e] 1 g of *cefadroxil monohydrate*/tablet	98.7 ± 0.3, t = 2.038 F = 2.250	99.0 ± 0.20
	Duricef® suspension[e] 250 mg of *cefadroxil monohydrate*/5 mL	96.6 ± 1.3, t = 1.605 F = 2.641	97.6 ± 0.80
	Duricef® capsules[e] 500 mg of *cefadroxil monohydrate*/capsule	97.9 ± 1.3, t = 1.332 F = 1.032	98.9 ± 1.30
	Biodroxil® capsules[f] 500 mg of *cefadroxil monohydrate*/capsule	102.4 ± 1.4, t = 0.930 F = 1.361	101.7 ± 1.20
	Biodroxil® suspension[f] 250 mg of *cefadroxil monohydrate*/5 mL	103.1 ± 0.6, t = 1.359 F = 2.250	102.7 ± 0.40
Cefalexin anhydrous	Ceporex® tablets[g] 500 mg of *cefalexin anhydrous*/tablet	99.3 ± 1.6, t = 0.646 F = 1.778	98.7 ± 1.20
	Ceporex® suspension[g] 250 mg of *cefalexin anhydrous*/5 mL	99.0 ± 1.5, t = 0.735 F = 3.516	98.5 ± 0.80
	Ospexin® suspension[h] 250 mg of *cefalexin anhydrous*/5 mL	103.5 ± 1.5, t = 0.576 F = 3.516	103.1 ± 0.80
Cefradine anhydrous	Velosef® capsules[e] 250 mg of *cefradine anhydrous*/capsule	97.7 ± 0.5, t = 1.530 F = 1.562	97.3 ± 0.40
	Velosef® tablets[e] 1 g of *cefradine anhydrous*/tablet	103.3 ± 1.2, t = 1.019 F = 2.250	102.7 ± 0.80
	Velosef® suspension[e] 205 mg of *cefradine anhydrous*/5mL	99.0 ± 1.5, t = 0.588 F = 3.516	98.5 ± 0.80
	Velosef® vials[e] 1 g of *cefradine anhydrous*/vial	97.9 ± 1.2, t = 0.267 F = 1.778	97.7 ± 0.90
Cefotaxime sodium	Cefotax® vials[i] 500 mg of *cefotaxime sodium*/vial	98.2 ± 1.8, t = 0.365, F = 3.932;	97.9 ± 0.90
	Claforan® vials[j] 500 mg of *cefotaxime sodium*/vial	97.9 ± 1.2, t = 0.326, F = 1.778;	97.7 ± 0.90
Ceftazidime pentahydrate	Fortum® vials[k] 500 mg of *ceftazidime pentahydrate*/vial	98.9 ± 0.6, t = 1.460, F = 4.001;	98.5 ± 0.30
Cefoperazone sodium	Cefozon® vials[l] 500 mg of *cefoperazone sodium*/vial	102.3 ± 1.4, t = 1.721, F = 4.003;	101.2 ± 0.70
Ceftriaxone sodium	Ceftriaxone® vials[m] 500 mg of *ceftriaxone sodium*/vial	97.7 ± 0.4, t = 1.643, F = 4.002;	98.0 ± 0.20
Cefixime	Ximacef® capsules[n] 400 mg of *cefixime*/capsule	102.1 ± 1.4, t = 0.797 F = 1.361	101.5 ± 1.20
Cefazolin sodium	Zinol® vials[o] 500 mg of *cefazolin sodium*/vial	98.9 ± 1.3, t = 1.493 F = 3.449	98.0 ± 0.70
Cefpodoxime proxetil	Orelox® tablets[q] 100 mg of *cefpodoxime proxetil*/tablet	98.2 ± 1.8, t = 0.298 F = 3.932	97.9 ± 0.90

[a] Theoretical value for t and F at 95% confidence limit, t = 2.228 and F = 5.053; [b] Reference 48; [c] Egyptian Pharmaceuticals and chemicals industries Co., S.A.E., Bayad El-Arab, Beni Suef, Egypt; [d] Pharco Pharmaceuticals, Alexandria under license from Ranbaxy UK; [e] Bristol-Myers Squibb Pharmaceutical Co., Cairo, Egypt; [f] Kahira Pharm. & Chem. Ind. Co. under license from Novartis Pharma S.A.E., Cairo, Egypt;

Table 9. Standard addition method for the assay of the studied drugs in their pharmaceutical dosage forms by the proposed method.

Drug	Pharmaceutical formulation	Authentic drug added ($\mu g\ mL^{-1}$)	Authentic drug found ($\mu g\ mL^{-1}$)	Recovery (%) ± SD[a]
Cefaclor monohydrate	Ceclor® suspension	10.00	9.97	99.7 ± 1.21
		20.00	19.40	97.0 ± 1.80
		30.00	28.83	96.1 ± 1.52
	Bacticlor® suspension	10.00	10.06	100.6 ± 1.10
		20.00	19.26	96.3 ± 0.81
		30.00	29.40	98.0 ± 0.90
Cefadroxil monohydrate	Duricef® tablets	5.00	5.11	102.2 ± 1.41
		10.00	9.95	99.5 ± 1.72
		15.00	14.85	99.0 ± 0.50
	Duricef® suspension	5.00	4.90	98.0 ± 1.81
		10.00	10.02	100.2 ± 1.63
		15.00	14.64	97.6 ± 1.12
	Duricef® capsules	5.00	4.83	96.6 ± 1.50
		10.00	9.60	96.0 ± 1.30
		15.00	14.78	98.5 ± 0.71
	Biodroxil® capsules	5.00	4.89	97.8 ± 1.54
		10.00	10.36	103.6 ± 0.91
		15.00	14.98	99.9 ± 0.60
	Biodroxil® suspension	5.00	4.87	97.4 ± 1.91
		10.00	9.84	98.4 ± 0.42
		15.00	15.38	102.5 ± 1.20
Cefalexin anhydrous	Ceporex® tablets	5.00	4.98	99.6 ± 1.41
		10.00	10.07	100.7 ± 1.73
		15.00	14.82	98.8 ± 0.62
	Ceporex® suspension	5.00	5.05	101.0 ± 1.00
		10.00	9.79	97.9 ± 1.81
		15.00	15.06	100.4 ± 0.91
	Ospexin® suspension	5.00	4.95	99.0 ± 1.30
		10.00	9.92	99.2 ± 1.81
		15.00	14.68	97.9 ± 1.94
Cefradine anhydrous	Velosef® capsules	10.00	9.85	98.5 ± 0.85
		20.00	20.09	100.5 ± 0.63
		30.00	28.86	96.2 ± 1.11
	Velosef® tablets	10.00	9.69	96.9 ± 0.80
		20.00	19.85	99.3 ± 0.50
		30.00	30.10	100.3 ± 0.71
	Velosef® suspension	10.00	9.72	97.2 ± 0.92
		20.00	19.94	99.7 ± 1.50
		30.00	31.14	103.8 ± 1.93
	Velosef® vials	10.00	10.16	101.6 ± 1.10
		20.00	19.62	98.1 ± 1.63
		30.00	29.85	99.5 ± 1.94
Ceftazidime pentahydrate	Fortum® vial	20.00	20.34	101.7 ± 1.33
		40.00	38.76	96.6 ± 1.63
		60.00	61.32	102.2 ± 1.32
Cefotaxime Sodium	Cefotax® vials	10.00	9.66	96.6 ± 0.7
		20.00	20.20	101.0 ± 0.9
		30.00	29.30	97.6 ± 1.5
	Claforan® vials	10.00	10.35	103.5 ± 1.8
		20.00	19.60	98.0 ± 1.6
		30.00	29.19	97.3 ± 0.7
Cefoperazone Sodium	Cefozon® vials	20.00	19.50	97.5 ± 1.8
		40.00	38.88	97.2 ± 0.9
		60.00	59.46	99.1 ± 0.7
Ceftriaxone Sodium	Ceftriaxone vials	10.00	10.08	100.8 ± 1.4
		20.00	19.36	96.8 ± 1.5
		30.00	30.98	103.3 ± 1.3

Table 9 (Continued)

Drug	Pharmaceutical formulation	Authentic drug added ($\mu g\ mL^{-1}$)	Authentic drug found ($\mu g\ mL^{-1}$)	Recovery (%) $\pm$ SD[a]
Cefixime	Ximacef® capsules	15.00	14.76	98.4 $\pm$ 0.5
		30.00	29.82	99.4 $\pm$ 1.1
		45.00	44.91	99.8 $\pm$ 1.4
Cefazolin Sodium	Zinol® vials	10.00	9.78	97.8 $\pm$ 0.8
		20.00	19.87	99.4 $\pm$ 0.7
		30.00	30.27	100.9 $\pm$ 1.7
Cefpodoxime proxetil	Orelox® tablets	10.00	9.84	98.4 $\pm$ 0.9
		20.00	19.83	99.2 $\pm$ 1.5
		30.00	29.60	98.6 $\pm$ 1.6

[a] Average of six determinations.

a good leaving group at position 4 in addition to the presence of nitro group as an electron withdrawing group at position 7 of the aromatic ring in NBD-Cl result in replacement of Cl^- anion with the attacking sulfide ions which in turn lead to the formation of a yellow-colored chromophore (λ_{max} at 390 nm). The reaction product is stable in strong acidic medium, moreover acidification could minimize possible competition between the generated sulfide nucleophile and excess OH^- which may lead to decrease in the chromogen formed. The proposed reaction mechanism is given in the following scheme:
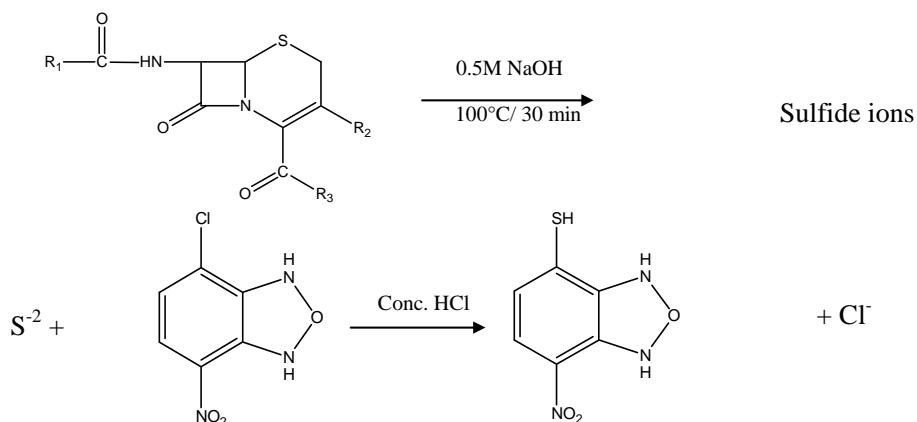
Scheme 1 Suggested reaction mechanism between sulfide ions and NBD-Cl

The production of sulfide ions was confirmed by carrying out specific qualitative tests such as dilute hydrochloric acid, cadmium acetate, sodium nitroprusside and methyelene blue tests [56] or by comparing λ_{max} of the formed chromogen with that obtained after applying the developed method to sodium sulfide and the same results were obtained.

4. Conclusions

The developed spectrophotometric method is precise, accurate and sensitive. No interference from the frequently encountered excipients and additives. Statistical analysis proves that the method could be applied for the analysis of the studied drugs in their pure forms and in pharmaceutical formulations.

REFERENCES

[1] Delgado, J.N. and Remers, W.A. (2004) Wilson and Gisvold's textbook of organic medicinal and pharmaceutical chemistry. 10th Edition, Lippincott Williams & Wilkins, New York.

[2] Dollery, C. (1999) Therapeutic drugs. Vol. I. 3rd Edition, Churchill Livingstone, Edinburgh.

[3] American Pharmaceutical Association. (2008) United States Pharmacopoeia 31 and NF 26. Washington, DC.

[4] Abdel-Hamid, M.E. (1998) FSQ spectrophotometric and HPLC analysis of some cephalosporins in the presence of their alkali-induced degradation products. *Il Farmaco*, **53(2)**, 132-138.

[5] Kelani, K., Bebawy, L.I. and Abdel-Fattah, L. (1998) Stability-indicating spectrophotometric and densitometric methods for determination of some cephalosporins. *Journal of AOAC International*, **81(2)**, 386-393.

[6] El-Walily, A.F.M., Gazy, A.A., Belal, S.F. and Khamis,

E.F. (2000) Quantitative determination of some thiazole cephalosporins through complexation with palladium (II) chloride. *Journal of Pharmaceutical and Biomedical Analysis*, **22(2)**, 385-392.

[7] Agbaba, D., Eric, S., Karljikovic-Rajic, K., Vladimirov, S. and Zivanov-Stakic, D. (1997) Spectrophotometric determination of certain cephalosporins using ferrihydroxamate method. *Spectroscopy Letters*, **30(2)**, 309-319.

[8] El-Walily, A.F.M., Gazy, A.A., Belal, S.F. and Khamis, E.F. (2000) Use of cerium (IV) in the spectrophotometric and spectrofluorimetric determinations of penicillins and cephalosporins in their pharmaceutical preparations. *Spectroscopy Letters*, **33(6)**, 931-948.

[9] Yang, J., Zhou, G.J., Cao, X.H., Ma, Q.L. and Dong, J. (1998) Study on the fluorescence characteristics of alkaline degradation of cefadroxil, cefradine, cefotaxime sodium and amoxicillin. *Analytical Letters*, **31(6)**, 1047-1060.

[10] Aly, F.A., Hefnawy, M.M. and Belal, F. (1996) A selective spectrofluorimetric method for the determination of some *α*-aminocephalosporins in formulations and biological fluids. *Analytical Letters*, **29(1)**, 117-130.

[11] Yang, J.H, Ma, Q.L., Wu, X., Sun, L.M. and Cao, X.H. (1999) A new luminescence spectrometry for the determination of some *β*-lactamic antibiotics. *Analytical Letters*, **32(3)**, 471-480.

[12] Hefnawy, M., El-Shabrawy, Y. and Belal, F. (1999) Spectrofluorometric determination of alpha-aminocephalosporins in biological fluids and pharmaceutical preparations. *Journal of Pharmaceutical and Biomedical Analysis*, **21(4)**, 703-707.

[13] El-Walily, A.F.M., Gazy, A.A., Belal, S.F. and Khamis, E.F. (1999) Selective spectrofluorimetric determination of phenolic *β*-lactam antibiotics through the formation of their coumarin derivatives. *Journal of Pharmaceutical and Biomedical Analysis*, **20(4)**, 643-653.

[14] Li, Y. and Lu, J. (2006) Chemiluminescence flow-injection analysis of *β*-lactam antibiotics using the luminol-permanganate reaction. *Luminescence*, **21(4)**, 251-255.

[15] Yao, H., Tang, Y., Li, Y. and Sun, Y. (2003) Flow injection chemiluminescence determination of cephalosporin antibiotics by their enhancing effects on luminal-potassium periodate system. *Analytical Letters*, **36(14)**, 2975-2983.

[16] Thongpoon, C., Liawruangrath, B., Liawruangrath, S., Wheatley, R.A. and Townshend, A. (2006) Flow injection chemiluminescence determination of cefadroxil using potassium permanganate and formaldehyde system. *Journal of Pharmaceutical and Biomedical Analysis*, **42(2)**, 277-282.

[17] Shinde, V.M. and Shabadi, C.V. (1997) Simultaneous determination of cefadroxil and cefalexin from capsules by reversed phase HPLC. *Indian Drugs*, **34**, 399-402.

[18] Misztal, G. (1998) Determination of cefotaxime and cefotriaxone in pharmaceuticals by HPLC. *Pharmazie*, **53**, 723-724.

[19] Shinde, V.M. and Shabadi, C.V. (1998) Simultaneous determination of ceazolin and cefotaxime from injections by reversed phase HPLC. *Indian Journal of Pharmaceutical Sciences*, **60(5)**, 313-315.

[20] LaCourse, W.R. and Dasenbrock C.O. (1999) Pulsed electrochemical detection of sulfur-containing antibiotics following high performance liquid chromatography. *Journal of Pharmaceutical and Biomedical Analysis*, **19(1-2)**, 239-252.

[21] Özkan, S.A., Erk, N., Uslu, B., Yilmaz, N. and Biryol, I. (2000) Study on electrooxidation of cefadroxil monohydrate and its determination by differential pulse voltammetry. *Journal of Pharmaceutical and Biomedical Analysis*, **23(2-3)**, 263-273.

[22] Rodrigues, L.N.C., Zanoni, M.B.V. and Fogg, A.G. (1999) Indirect polarographic and cathodic-stripping voltammetric determination of cefaclor as an alkaline degradation product. *Journal of Pharmaceutical and Biomedical Analysis*, **21(3)**, 497-505.

[23] El-Maali, N.A., Ali, A.M.M. and Ghandour, M.A. (1993) Electrochemical reduction and oxidation of two cephalosporin antibiotics: Ceftriaxone (Rocephin) and cefoperazone (Cefobid). *Electroanalysis* (*N. Y.*), **5(7)**, 599-604.

[24] Ferreira, V.S., Zanoni, M.V.B. and Fogg, A.G. (1999) Cathodic stripping voltammetric determination of ceftazidime with reactive accumulation at a poly-L-lysine modified hanging mercury drop electrode. *Analytia Chimica Acta*, **384(2)**, 159-166.

[25] El-Obeid, H.A., Gad-Kariem, E.A., Al-Rashood, K.A., Al-Khames, H.A., El-Shafie, F.S. and Bawaseer, G.A.M. (1999) A selective colorimetric method for the determination of penicillins and cephalosporins with *α*-aminoacyl functions. *Analytical Letters*, **32(14)**, 2809-2823.

[26] Mohamed, F.A. (1998) Spectrophotoemtric determination of sulphide and some sulphide producing compounds. *In Proceedings of Assiut University 1st Pharmaceutical Science Conference*, Faculty of Pharmacy, Assiut, 1998, 1-18.

[27] Metwally, F.H., Alwarthan, A.A. and Al-Tamimi, S.A. (2001) Flow-injection spectrophotometric determination of certain cephalosporins based on the formation of dyes. *Il Farmaco*, **56(8)**, 601-607.

[28] Sastry, C.S.P., Rao, S.G., Naidu, P.Y. and Srinivas, K.R. (1998) New spectrophotometric method for the determination of some drugs with iodine and wool fast blue BL. *Talanta*, **45(6)**, 1227-1234.

[29] Helaleh, M.I.H. and Abu-Nameh, E.S.M. (1998) A kinetic approach for determination of cefadroxil in pharmaceuticals by alkaline hydrolysis. *Journal of AOAC International*, **81(3)**, 528-533.

[30] Ivama, V.M., Rodrigues, L.N.C., Guaratini, C.C.I. and Zanoni, M.V.B. (1999) Spectrophotometric determination of cefaclor in pharmaceutical preparations. *Quimica Nova*, **22(2)**, 201-204.

[31] Al-Momani, I.F. (2004) Flow-Injection spectrophotometric determination of amoxycillin, cefalexin, ampicillin, and cefradine in pharmaceutical formulations. *Analytical Letters*, **37(10)**, 2099-2110.

[32] Amin, A.S. and Shama, S.A. (2000) Vanadophosphoric acid as a modified reagent for the spectrophotometric determination of certain cephalosporins and their dosage forms. *Monatshefte fur Chemie*, **131(4)**, 313-319.

[33] Omai, K., Toyo'oka, T. and Miyano, H. (1984) Fluorigenic reagents for primary and secondary amines and thiols in high-performance liquid chromatography. A review. *The Analyst* (*London*), **109(11)**, 1365-1372.

[34] Olgun, N., Erturk, S. and Atmaca, S. (2002) Spectro-

fluorimetric and spectrophotometric methods for the determination of vigabatrin in tablets. *Journal of Pharmaceutical and Biomedical Analysis*, **29(1-2)**, 1-5.

[35] Onal, A., Kepekci, S.E. and Oztunc, A. (2005) Spectrophotometric methods for the determination of antidepressant drug paroxetine hydrochloride in tablets. *Journal of AOAC International*, **88(2)**, 490-495.

[36] Olojo, R.O., Xia, R.H. and Abramson, J.J. (2005) Spectrophotometric and fluorometric assay of superoxide ion using 4-chloro-7-nitrobenzo-2-oxa-1,3-diazole. *Analytical Biochemistry*, **339(2)**, 338-344.

[37] El-Emam, A.A., Hansen, S.H., Moustafa, M.A., El-Ashry, S.M. and El-Sherbiny, D.T. (2004) Determination of lisinopril in dosage forms and spiked human plasma through derivatization with 7-chloro-4-nitrobenzo-2-oxa-1,3-diazole (NBD-Cl) followed by spectrophotometry or HPLC with fluorimetric detection. *Journal of Pharmaceutical and Biomedical Analysis*, **34(1)**, 35-44.

[38] Taha, E.A. (2003) Kinetic spectrophotometric methods for the determination of dothiepin hydrochloride in bulk and in drug formulation. *Analytical and Bioanalytical Chemistry*, **376(7)**, 1131-1136.

[39] Amin, A.S., Ragab, G.H. and Saleh, H. (2002) Colorimetric determination of *β*-blockers in pharmaceutical formulations. *Journal of Pharmaceutical and Biomedical Analysis*, **30(4)**, 1347-1353.

[40] Abdellatef, H.E. (2002) Kinetic spectrophotometric determination of tramadol hydrochloride in pharmaceutical formulation. *Journal of Pharmaceutical and Biomedical Analysis*, **29(5)**, 835-842.

[41] El-Enany, N., Belal F. and Rizk, M. (2004) Spectrophotometric determination of salbutamol in bulk and dosage forms after derivatization with 4 Chloro-7-nitrobenzo-2-oxa-1,3-diazole (NBD Cl). *Chemia Analityczna* (*Warsaw*), **49(2)**, 261-269.

[42] Askal, H.F., Abdelmaged, O.H. and Kashaba, P.Y. (1995) *Egyptian Journal of Analytical Chemistry*, **4**, 89-103.

[43] Alwarthan, A.A., Metwally, F.H. and Al-Tamimi, S.A. (1993) Spectrophotometric assay of certain cephalosporins based on formation of ethylene blue. *Analytical Letters*, **26(12)**, 2619-2635.

[44] Fogg, A.G. and Abdalla, M.A. (1985) Visible spectrophotometric determination of cephalosporins and penicillins by indophenol derivatisation with and without alkaline degradation to ammonia. *Journal of Pharmaceutical and Biomedical Analysis*, **3(4)**, 315-321.

[45] Abdalla, M.A., Fogg, A.G. and Burgess, C. (1982) Selective spectrophotometric determination of cephalosporins by alkaline degradation to hydrogen sulphide and formation of methylene blue. *Analyst* (*London*), **107(1273)**,

213-217.

[46] Topic Q2 (R1). (2005) Validation of analytical procedures: Text and methodology. *International Conference on Harmonisation* (*ICH*). http://www.emea.europa.eu/pdfs/human/ich/038195en.pdf

[47] Heyden, Y.V., Nijhuis, A., Smeyers-Verbeke, J., Vandeginste, B.G.M. and Massart D.L. (2004) Guidance for rubustness/ruggedness test in method validation. *Journal of Pharmaceutical and Biomedical Analysis*, **24(5-6)**, 723-753.

[48] Saleh, G.A., Askal, H., Darwish, I. and El-Shorbagi, A. (2003) Spectroscopic analytical study for the charge-transfer complexation of certain cephalosporins with chloranilic acid. *Analytical Sciences*, **19(2)**, 281-287.

[49] Harvey, D. (2000) Modern analytical chemistry. McGraw-Hill, Boston, MA.

[50] Fogg, A.G., Fayad, N.M., Burgess, C. and McGlynn, A. (1979) Differential pulse polarographic determination of cephalosporins and their degradation products. *Analytica Chimica Acta*, **108**, 205-211.

[51] Fogg, A.G., Fayad, N.M. and Burgess, C. (1979) Differential pulse polarographic study of the degradation of cephalexin: Determination of hydrogen sulphide and other degradation products. *Analytica Chimica Acta*, **110(1)**, 107-115.

[52] Fogg, A.G. and Martin, M.J. (1981) Differential pulse polarographic determination of degradation products of cephalosporins: Comparison of the degradation of cephaloglycin in neutral solution with that of cephalexin. *Analyst* (*London*), **106(1268)**, 1213-1217.

[53] Fogg, A.G., Abdalla, M.A. and Henriques, H.P. (1982) Titrimetric determination of the yield of sulphide formed by alkaline degradation of cephalosporins. *Analyst* (*London*), **107(1273)**, 449-452.

[54] Abdalla, M.A., Fogg, A.G., Baber, J.G. and Burgess, C. (1983) Air-segmented continuous-flow visible spectrophotometric determination of cephalosporins in drug formulations by alkaline degradation to hydrogen sulphide and formation of methylene blue and determination of sulphide-producing impurities including cephalosporins in penicillin samples. *Analyst* (*London*), **108(1282)**, 53-57.

[55] Grekas, N. and Calokerinos, A.C. (1990) Continuous flow molecular emission cavity analysis of cephalosporins by alkaline degradation to sulphide. *Analyst* (London), **115(5)**, 613-616.

[56] Svehla, G. (1979) Vogel's textbook of macro and semimicro qualitative inorganic analysis. 5th Edition, The Chaucer Press, Great Britain.

Assessment of biotechnological potential of phosphate solubilizing bacteria isolated from soils of Southern Kazakhstan

Rakhilya Aipova[1]*, Svetlana A. Aitkeldiyeva[1], Askar A. Kurmanbayev[1], Amangeldy K. Sadanov[2], Olga B.Topalova[3]

[1]Institute of Microbiology and Virology, Almaty, Republic of Kazakhstan; *Corresponding Author: Rakhilya_73@mail.ru
[2]Center of biological investigations, Almaty, Republic of Kazakhstan
[3]Kazakh Nationality pedagogical university, Almaty, Republic of Kazakhstan

ABSTRACT

Phosphorus (P) is a vital plant nutrient, available to plant roots only in soluble forms that are in short supply in the soil. Adding phosphate-based fertilizers to increase agricultural yields is a widely used practice; however, the bioavailability of P remains low due to chemical transformations of P into insoluble forms. Thus, phosphate solubilizing bacteria (PSB) play an important role in reducing P deficiency in soil. The goal of this study was to assess biotechnological potential of phosphate-solubilizing bacterial strains. In this study, phosphate solubilizing microorganisms (PSM) were isolated from different soil samples of Southern regions of Kazakhstan. The biological activity of PSM was studied based on their effect on the growth of wheat seeds. The different taxonomic genera of these PSM were identified: Arthrobacter spp., Aureobacterium spp., Azotobacter spp., Bacterium spp., Baccillus spp. Finally, phosphate-solubilizing activity of isolated strains of PSM was assessed.

Keywords: Soil; Phosphate Solubilizing Bacteria; Identification; Labile Phosphorus; Fertilizers; Phosphate; Phosphorus

1. INTRODUCTION

Phosphorus (P) is the second most important plant nutrient after nitrogen. However, most Phosphorus in soil (up to 95-99%) is part of insoluble compounds, which makes P unavailable for plant nutrition [1]. In order to increase crop yields, mineral phosphate fertilizers are regularly incorporated into the soil. However, immedi-

ately after fertilizer application is done, most of the applied phosphorus transforms into an insoluble form [2]. As a result, most P in the soil is found in poorly soluble, highly stable forms with limited availability to plants. Only 5% or less of the total amount of P in soil is available for plant nutrition [3]. The vicious cycle continues as such low bioavailability of P requires regular application of phosphate-based fertilizers [4].

According to assessments made by the experts from the U.S. Geological Survey and the International Association of Fertilizer Producers, the demand for fertilizers over the next 5 years will increase by 2.5-3% annually [5]. At such rate of phosphate consumption, all global phosphate resources would be exhausted within 100-125 years [5]. Taking into account the long-term increase in demand for P and phosphate production, peaking in 20 years, the importance of partial P recycling continues to grow. Recovering phosphates from livestock waste is one of the examples of reusing P for agriculture [5]. Other ways to control the wastage of phosphate resources include reducing P run-off into the oceans.

Considering the anticipated food production crisis as it relates to phosphate deficit in the future, efforts to study and apply microbiological phosphate solubilization processes are well justified. Phosphate solubilizing Microorganisms (PSM) play an important role in plant nutrition and growth promotion, especially when phosphate fertilizers are used extensively for long periods of time. It has been proven that agricultural application of PSM boosts crop yields [6]. On the other hand, soil activity depends on the activity of phosphate solubilizing bacteria [7].

P solubilization mechanisms include acid formation, chelating metal ions and exchange reactions. The most active among PSM are micromycetes of following genera: Aspergillus, Penicillium, Curvularia, and phos-

phate-solubilizing yeast, which is more active in solubilizing phosphates than bacteria. However, since bacteria are more suitable for high-volume production of biotechnology products, the goal of our research was to assess biotechnological potential of phosphate-solubilizing bacterial strains, isolated over the course of our research.

2. MATERIAL AND METHODS

The subject of this research was to study microorganisms identified from the soils of Southern Kazakhstan. Soil samples were taken in accordance with the aseptic regulations and recommendations and were stored in sterile parchment paper bags [8].

Calcium orthophosphate-dissolving bacteria were identified in the Muromcev medium of the following composition (g/l): glucose–10.0, asparagines–1.0, K_2SO_4–0.2, $MgSO_4$–0.2, corn extract–0.02; agar–20.0, tap water, pH = 6.8, sterilized at 0.5 atm. for 20 minutes. The salts were added in dry form, which provided gradual interaction with the medium over the course of sedimentation. The proportion of dissolving agent was 1.5 grams of $Ca_3(PO_4)_2$ per liter of liquid medium. Nistatin was introduced additionally to suppress the growth of micromycetes, in proportion 500 000 units per 250 ml of sterilized medium. Mediums prepared by this method were distributed in 25 ml amounts per Petri dish. After cooling down, the agar medium was added the soil suspensions (in 10^{-4}-10^{-7} dilution) in 0.1 ml volume amounts. Petri dishes with soil suspension on the surface were incubated at 28ºC for 3-9 days. We counted only colonies that had zones of calcium phosphate dissolution around them.

To evaluate phosphate solubilizing microorganisms' influence on seed germination, we used wheat seeds. Laboratory research was conducted according to the Schroth, Hancock method 1982 [9]. The surface of the seeds was sterilized with 10% sodium hypochloride solution for 20 minutes, after which the seeds were washed with 70% ethanol and triple sterile distilled water.

Cultures of microorganisms under the study were incubated in 250 ml flasks, containing 100 ml of medium for cultivation (beef extract broth) at 28ºC until they reached steady stage of growth (titer is 1×10^6 cells/mL). Culture-containing liquid was obtained by centrifuging bacterial suspension for 10 minutes at 5000 RPM. Bacterial biomass sediment was washed three times with physiological saline solution, later diluted with sterile distilled water. We used 10 ml of test subculture per 20 seeds for 2 hours in each seed treatment round.

In accordance with aseptic regulations, inoculated seeds were placed onto dampened filter paper in Petri dishes. For control specimens, we used seeds treated with sterile water and sterile medium used for bacteria cultivation. Incubation was done at 28ºC.

Phosphate solubilizing activity of bacterial strains was determined using the Novogrudsky medium [10]. We added 1% suspension of phosphate-solubilizing bacterial (PSB) strains into the flasks containing 100 ml of medium, and incubated the flasks on the shake flask propagator for 14 days at 180 RPM. After 14 days, we calculated the amount of labile phosphorus in the cell culture liquid by colorimetric method using blue phosphorus-molybdenum complex [11].

The active mass concentration was converted into PO_4^{3-} mg/L format using the following formula:

$X = (1000 \times a)/(V \times 1000)$ mkg/L = 0.1 ×a (mg/L),
where:

a―phosphate ion content in the sample, defined by calibration chart, mkg;

V―aliquot of a sample, 10 cubic centimeters.

3. RESULTS AND DISCUSSIONS

The form or type of phosphorus compounds in soil depends on oxidation-reduction conditions of the medium. The main component of mineral phosphates is tricalcium phosphate (calcium orthophosphate). In all of the soil samples assessed in our study using Muromcev medium, we observed visible zones of phosphate dissolution (**Figure 1**).

Inoculation of plants seeds by active strains of microorganisms is often beneficial to their growth and development. Such effect can be defined by different mechanisms: by intensification of nitrogen fixation and phosphate solubilization, by production of physiologically active substances, by an increase in root absorption capacity, or by improved solubility of highly immobile compounds of plant nutrients [12].

Table 1 and **Figure 2** illustrate the influence of phosphate solubilizing bacterial treatment on wheat seed germination. Our research demonstrates that applying PSB in seed treatment increases wheat germination capacity (see strains P3-P6) and stimulates root growth as observed in all specimens (P1-P6).

Strains that positively affected wheat seed germination were identified at the species level. **Table 2** presents morphological and biochemical characteristics of studied strains.

Based on the obtained data on strain characteristics, phosphate-solubilizing bacterial strains were identified as follows: **P1**–*Artrobacter sp.,* **P3**–*Bacillus sp.,* **P6**–*Bacterium sp.,* **P8**–*Aureobacterium sp.,* **Az 1**–Azotobacter sp. In order to evaluate PSB strains' ability to mobilize phosphorus from insoluble soil phosphates, a
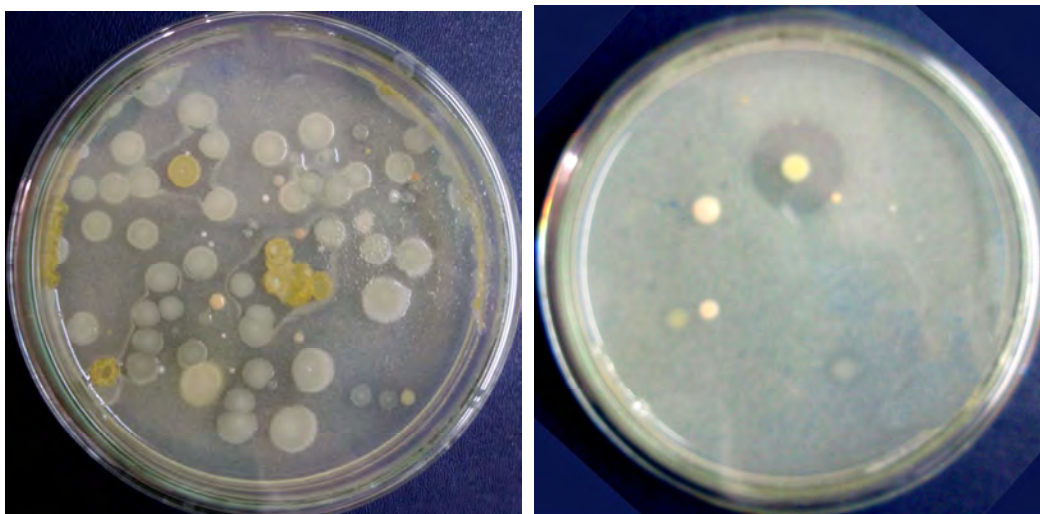
Figure 1. Phosphate dissolution zones around phosphate solubilizing bacteria colonies.

Figure 2. Germinated wheat seeds after treatment with PSB cell culture liquid. Left: control; Right: treatment with the P6 strain.

Table 1. The influence of phosphate solubilizing bacterial treatment on wheat seed germination.

Strain of PSB	Germination capacity , %	Average length of sprout, mm	Average length of root, mm
Control	65,00	40,69 ± 5,02	34,34 ± 3,93
P1	46,65	32,40 ± 3,03	40,88 ± 2,66
P2	61,65	43,25 ± 9,84	44,73 ± 7,52
P3	66,65	29,40 ± 8,79	43,15 ± 4,69
P4	68,35	20,63 ± 7,94	35,88 ± 5,99
P5	76,65	24,58 ± 17,55	38,92 ± 3,26
P6	66,65	32,76 ± 0,23	41,84 ± 9,16
P7	51,65	23,29 ± 8,12	33,63 ± 5,50
P8	60,00	25,79 ± 11,77	40,71 ± 7,49

further experiment was conducted using strains **P1, P3, P6, P8, Az1,** which were grown over a 14-day period. In the obtained cell culture liquid, the assessment of soluble (labile) phosphorus concentration was done.

The assessment of phosphate solubilization activity by PSB strains (**Table 3**) has demonstrated that phosphorus mobilization activity has increased more than 100 times in comparison to control sample. The most active strains

Table 2. Morphological, physiological, and biochemical characteristics of phosphate solubilizing bacteria strains in the study.

Characteristics	Strains				
	P-1	**P-3**	**P-6**	**P-8**	**Az1**
Morphology	rods	rods	rods	rods	rods
Gram Staining	+	-	–	+	–
Mobility	Immobile	Mobile	Mobile	Mobile	Mobile
Acid-Fastness	–	+	–	–	
Catalase	+	+	+	+	+
Oxidase	+	+	+	–	
Growth on Beef/Peptone Broth	+	+	+	+	
Relationship with oxygen	P.anaerobe	P.anaerobe	P.anaerobe	Aerobes	Aerobes
Dilution of gelatin	+	+	–	+	
Hydrogen sulphide formation	–	+	–	+	
Nitrate formation	–	+	+	–	
Starch Hydrolysis	+	–	–	–	+
Indole formation	–	+	–	–	
Ammonia formation	+	–	–	–	
Spore formation	–	+	–	–	–
Growth on Beef/Peptone Broth with NaCl					
3%	+	+	+	+	
6%	+	+	+	+	
Starch conversion	+	–	–	–	+
Carbohydrate uptake:					
Glucose	A	AG	A	A	
Galactose	As	AG	AG	As	
Glucose	A	AG	A	A	
Xylose	As	AG	A	As	
Lactose	As	AG	A	As	
Fructose	A	AG	A	A	
Arabinose	A	AG	A	As	
Saccharose	A	AG	A	A	
Maltose	A	AG	As	A	
Glycerin	As	AG	As	As	
Mannitol	A	AG	As	As	
Growth under different temperatures					
-3℃	+	–	+	+	
22℃	+	+	+	+	+
28℃	+	+	+	+	
30℃	+	+	+	+	+
37℃	+	+	–	+	
Comment: As-assimilates, A-acid formation, AG–acid and gas formation					

Table 3. Phosphate solubilization activity with the following PSB strains.

Strains:	Concentration of P_2O_5 in mkg per 1000 ml of medium/phosphate mobilization
P8	75 000/0,008
P1	70 000/0,007
P3	44 000/0,004
P6	20 000/0,002
Az 1	47 300/0,005
P1 + P8 + Az 1	146 000/0,015
Control	800/0,00008

were P8, P1 and Az1 strains, whereas strain P6 was least active. Growing three strains simultaneously (P1 + P8 + Az 1) allowed the highest level of phosphorus mobilization.

4. CONCLUSIONS

The results obtained over the course of this study let us theorize that phosphate solubilizing bacteria positively affect wheat seed germination in a multifaceted way. Identification of PSB in our study has demonstrated that

they belong to different taxonomic bacterial genera: *Azotobacter sp., Artrobacter sp., Bacterium sp., Bacillus sp., and Aerobacterium sp.* We believe that the strains obtained in samples P8, P1 and Az 1 are of particular interest for further research.

REFERENCES

[1] Corona, M.E.P., Klundert, I.V.D. and Verhoeven, J.T.A. (1996) Availability of organic and inorganic phosphorus compounds as phosphorus sources for carex species. *New Phytologist*, **133(2)**, 225-231.

[2] Pundarikakshudu, R. (1989) Studies of the phosphate dynamics in a vertisol in relation to the yield and nutrient uptake of rainfed cotton. *Experimental Agriculture*, **25(4)**, 39-45.

[3] Boronin, A.M. (1998) Rhizosphere bacteria of the genus Pseudomonas enabling plant growth and development. *Sorovsky Educational Magazine*, **10**, 25-31.

[4] Omar, S.A. (1998) The role of rock-phosphate-solubilizing fungi and vesicular-arbusular-mycorrhiza (VAM) in growth of wheat plants fertilized with rock phosphate. *World Journal of Microbiology and Biotechnology*, **14(2)**, 211-218.

[5] Gilbert, N. (2009) Environment: The disappearing nutrient. *Nature*, **461(7265)**, 716-718.

[6] Khan, M.S., Zaidi, A. and Wani, P.A. (2007) Role of phosphate-solubilizing microorganisms in sustainable agriculture—A review. *Agronomy for Sustainable Development*, **27(1)**, 29-43.

[7] Rimkevich, O.V. (2006) Environmental and functional roles of microorganisms in technogenically disturbed soils (based on samples from Dambukinsk gold-mining site). Dissertation Thesis for Ph.D. Degree, Blagoveshensk.

[8] Tepper, E.Z., Shilnikova, V.K. and Pereverzeva, G.I. (2004) Microbiology practicum: Study aid for universities. Drofa, Moscow.

[9] Schroth, M.N. and Hancock, J.G. (1982) Disease-suppressive soil and root-colonizing bacteria. *Science*, **216(4553)**, 1376-1381.

[10] Rodina, A.G. (1965) Aquatic microbiology methods. Nauka, Moscow; Leningrad.

[11] Namsaraev, B.B., Barkhutova, D.D. and Khakhinov, V.V. (2006) Field practicum in aquatic microbiology and aquatic chemistry. Ulan-Ude.

[12] Gromovyh, T.I., Litovka, Y.A., Sadykova, V.S. and Gabdulina, И.G.-M. (2005) Perspective for applicationincrop science/biological features of a new strain of streptomyces lateritius 19/97-M, promising for use in crop science. *Biotechnology*, **5**, 37-40.

Codon evolution in double-stranded organelle DNA: strong regulation of homonucleotides and their analog alternations

Kenji Sorimachi

Educational Support Center, Dokkyo Medical University, Tochigi, Japan; kenjis@dokkyomed.ac.jp

ABSTRACT

In our previous study, complete single DNA strands which were obtained from nuclei, chloroplasts and plant mitochondria obeyed Chargaff's second parity rule, although those which were obtained from animal mitochondria deviated from the rule. On the other hand, plant mitochondria obeyed another different rule after their classification. Complete single DNA strand sequences obtained from chloroplasts, plant mitochondria, and animal mitochondria, were divided into the coding and non-coding regions. The non-coding region, which was the complementary coding region on the reverse strand, was incorporated as a coding region in the forward strand. When the nucleotide contents of the coding region or non-coding regions were plotted against the composition of the four nucleotides in the complete single DNA strand, it was determined that chloroplast and plant mitochondrial DNA obeyed Chargaff's second parity rule in both the coding and non-coding regions. However, animal mitochondrial DNA deviated from this rule. In chloroplast and plant mitochondrial DNA, which obey Chargaff's second parity rule, the lines of regression for G (purine) and C (pyrimidine) intersected with regression lines for A (purine) and T (pyrimidines), respectively, at around 0.250 in all cases. On the other hand, in animal mitochondrial DNA, which deviates from Chargaff's second parity rule, only regression lines due to the content of homonucleotides or their analogs in the coding or non-coding region against those in the complete single DNA strand intersected at around 0.250 at the horizontal axis. Conversely, the intersection of the two lines of regression (G and A or C and T) against the contents of heteronucleotides or their analogs shifted from 0.25 in both coding and non-coding regions. Nucleo-tide alternations in chloroplasts and plant mitochondria are strictly regulated, not only by the proportion of homonucleotides and their analogs, but also by the heteronucleotides and their analogs. They are strictly regulated in animal mitochondria only by the content of homonucleotides and their analogs.

Keywords: Evolution; Chargaff's Parity Rules; Organelle; DNA; Genome; Coding and Non-Coding Regions

1. INTRODUCTION

"Chargaff's second parity rule" [1], G ≈ C, A ≈ T and [(G + A) ≈ (T + C)] is retained in single DNA stranded that is formed from double-stranded DNA; however, it is difficult to imagine how the G and C or A and T base pairs are formed in the single DNA strand, or why G ≈ C and A ≈ T. Therefore, the biological significance of Chargaff's second parity rule (first described 40 years ago) has not yet been elucidated because of its unclear fundamental reasoning. In fact, it is unclear whether Chargaff's second parity rule is even linked to biological evolution. However, recently, this historic puzzle [2], has been solved, based on the fact that genome nucleotide composition is homogeneous [3] and that both the forward and reverse strand compositions are very similar [4]. The second parity rule derives the similarities of nucleotide composition found between the forward and reverse strands. On the other hand, nucleotide contents represented by Chargaff's first parity rule [5], G = C, A = T and [(A + G) = (T + C)], excludes biological significance, and this rule is mathematically definitive and independent of biological significance. Under this rule, the nucleotide contents in nuclei are defined by these equations in any organism from bacteria to *Homo sapiens*.

The existence of deviations from Chargaff's second rule was reported by other groups [6,7]. Only single

DNA strands that form double-stranded genomic DNA obey Chargaff's second parity rule, whereas organelle DNA does not obey this rule [8]. Nikolaou and Almirantis reported that mitochondrial DNA might be classified into three groups based on GC and AT skews, and that their DNA deviated from Chargaff's second parity rule [7]. They also reported that chloroplasts shared the patterns of bacterial genomes [7]. Mitochondrial gene sequences support the view that the evolutionary antecedents of mitochondria are a subgroup of the alpha-Protobacteria [9], such as *Rickettsia, Anaplasma,* and *Ehrlichia* [10]. In addition, molecular phylogenetic studies showed that the closest bacterial homologs of chloroplasts are cyanobacteria [11]. Recently, deviations from Chargaff's second parity rule in animal mitochondrial DNA were attributed to a different rule, and a single origin of species was derived from these mathematical genomic analyses [12]. We have also examined nuclear and organelle DNA and shown that the nucleotide compositions are correlated with each other, and are correlated within the coding region of nuclear DNA [4]. Additionally, only homonucleotide contents are correlated to each other between the coding or non- coding regions and the single DNA strand in organelles [13]. These analyses indicate that biological evolution is expressed by linear formulae [4]. In the present study, we have investigated the precise nucleotide relationships between the coding or non-coding regions and the complete single DNA that forms the double-stranded DNA. These analyses included not only homonucleotides, but also heteronucleotides, as Chargaff's second parity rule is linked to the double-stranded DNA structure [2,8]. In fact, it would be interesting to determine whether Chargaff's second parity rule is preserved, not only in the complete genome, but also in the separated coding and non-coding regions, to understand biological evolution.

2. MATERIALS AND METHODS

Genome data were obtained from the National Center for Biotechnology Information (NCBI; http://www.ncbi.nlm.nih.gov/sites), and the list of organelles examined has been described in our previous paper [13]. The same species which were examined in our previous study were used to compare the present result with the previous data [13]. To evaluate the biological evolution of whole organelles, the coding region in the reverse strand was incorporated into the coding region in the forward strand as the complement [2]. Calculations were performed using Microsoft Excel (version 2003).

3. RESULTS

3.1. Codon Evolution in Chloroplasts

The coding and non-coding regions were separated be-

cause their nucleotide alternations differ [4]. In the present study, however, the coding region in the reverse strand was incorporated into the forward strand as the complement, and the nucleotide content in the coding region was plotted against the complete single DNA strand to understand whole genome evolution [2]. According to this process, each of the four nucleotide components are expressed by four equations, and the homonucleotide content is expressed by a regression line whose regression coefficient is close to 1.0 in normalized values. Similarly, when the nucleotide content of the coding region were plotted against the total G content in the complete single DNA strand, the lines for both G and C completely overlapped in chloroplasts. Similarly, the lines for T and A also overlapped (**Figure 1**, upper panel). This suggests that G ≈ C and T ≈ A in the coding region. Similar results were obtained for the non-coding region (**Figure 1**, lower panel).
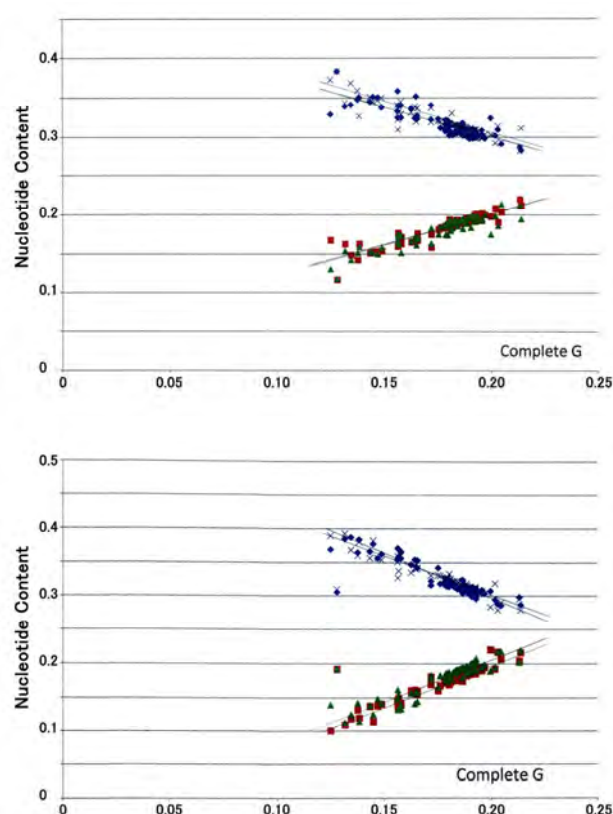
Figure 1. Nucleotide relationships in normalized chloroplast values. Upper panel, coding region; lower panel, non-coding region. Red squares, G; green triangles, C; blue diamonds, A; and shallow blue crosses, T. The composition of each nucleotide in the coding or non-coding region was plotted against the G content in the complete single DNA strand. The vertical axis represents the composition of the four nucleotides; the horizontal axis represents the G content in the complete single DNA strand.

Each line was computationally characterized and the results are shown in **Table 1**. Using normalized values in the four equations, as the summation of the four nucleotides is 1, the summation of the four equation slopes is 0 and that of the constant values at the vertical intercept is 1.0 in all cases [4]. This fact is based on mathematical rule using normalized values. As shown in **Figure 1**, the absolute values of the slopes of the lines for G and C or the lines for T and A were mathematically similar for both coding and non-coding regions, while the former two slopes were positive but the latter two were negative. That is, the G and C lines are symmetrical to the A and T lines in both the coding and non-coding regions. In addition, the slopes differed between the coding and non-coding regions, where the absolute values of the slopes were 0.760 ± 0.049 and 1.192 ± 0.078 in the coding and non-coding regions, respectively. Thus, the compositions of the four nucleotides correlated well with the nucleotide compositions in the complete single DNA strand. Regression coefficients were more than 0.9 or close to 0.9, except those for the A and T contents against the total T and A contents, which were 0.79 and 0.77, respectively, in the coding region.

Based on **Figure 1**, the overlapped lines for G and C clearly intersected with the overlapped lines for T and A. The points of intersection for the overlapped lines of regression were calculated based on the regression line equations presented in **Table 1**. The combinations of the two lines for calculations were either lines for G and A (purines) or lines for C and T (pyrimidines). All combinations were approximately 0.25 at the point of intersection for both the coding and non-coding regions in chloroplasts (**Table 2**).

3.2. Codon Evolution in Plant Mitochondria

The nucleotide contents in the coding and non-coding regions were plotted against those in the complete single DNA strand for DNA obtained from plant mitochondria (**Figure 2**). The G line overlapped with the C line, whereas the T line slightly diverged from the A line in the coding region compared (**Figure 2**, upper panel). Scattering of the sample points was observed for each of the four nucleotides, particularly in the high G content region of the complete single DNA strand. In the non-coding region, the G line differed significantly from the C line (**Figure 2**).

Furthermore, the C line was parallel to the G line. Scattering of sample points was observed in the complete genome, and was likely due to the small genome sizes [12]. Both the G and C lines were almost symmetrical with to both the A and T lines, respectively, for both the coding and non-coding regions.

Each line was computationally characterized and the results are shown in **Table 3**. The absolute values of the

Table 1. Regression lines representing nucleotide contents in the coding and non-coding regions against the nucleotide contents in the complete single strand DNA based on 97 chloroplasts.

Coding	R	Non-coding	R
Gc = 0.781 G + 0.045	0.93	Gn = 1.247 G – 0.050	0.97
Cc = 0.792 G + 0.042	0.91	Cn = 1.221 G – 0.039	0.94
Tc = –0.795 G + 0.461	0.90	Tn = –1.304 G + 0.556	0.95
Ac = –0.778 G + 0.453	0.86	An = –1.164 G + 0.533	0.95
Gc = 0.720 C + 0.054	0.88	Gn = 1.156 C – 0.037	0.93
Cc = 0.809 C + 0.037	0.96	Cn = 1.236 C – 0.046	0.97
Tc = –0.735 C + 0.452	0.85	Tn = –1.101 C + 0.525	0.92
Ac= –0.795 C + 0.458	0.90	A n= –1.291 C + 0.558	0.97
Gc = –0.742 T + 0.423	0.88	Gn = –1.220 T + 0.565	0.95
Cc = –0.786 T + 0.436	0.90	Cn = –1.206 T + 0.567	0.92
Tc = 0.831 T + 0.051	0.93	Tn = 1.181 T – 0.054	0.96
Ac = 0.697 T + 0.090	0.77	An = 1.246 T – 0.077	0.90
Gc = –0.700 A + 0.407	0.90	Gn = –1.093 A + 0.520	0.92
Cc = –0.753 A + 0.423	0.93	Cn = –1.156 A + 0.547	0.95
Tc = 0.650 A + 0.112	0.79	Tn = 1.005 A + 0.006	0.88
Ac = 0.804 A + 0.058	0.96	An = 1.244 A – 0.073	0.97

Xc and Xn mean the nucleotide content in the coding and non-coding regions, respectively.

Table 2. Crossing points obtained from two regression lines based on 97 chloroplasts.

Vs.	Lines	Coding	Non-coding
G	G-A	0.262	0.242
	C-T	0.264	0.236
C	G-A	0.267	0.243
	C-T	0.269	0.244
T	G-A	0.231	0.260
	C-T	0.238	0.260
A	G-A	0.232	0.254
	C-T	0.222	0.250
Av.	G-A	0.248 ± 0.019	0.250 ± 0.009
	C-T	0.248 ± 0.022	0.248 ± 0.010

slopes were 0.857 ± 0.168 and 0.840 ± 0.131 in the coding and non-coding regions, respectively, and the values similar between the both regions. The summation of the four equation slopes is 0, and that of the constant values at the vertical axis is 1 in all cases, as explained in **Figure 1**. The regression coefficients were around 0.9, except for low regression coefficients of 0.57 and 0.45 from the T and A contents in the coding region.

The point of intersection of the two regression lines was calculated based on the regression line equations

the other hand, C and T compositions were not correlated with G content in the complete single DNA strand (R-values of 0.24 and 0.01). Similar results were obtained in the non-coding region (**Figure 3**, lower panel and **Table 5**).

When nucleotide contents in the coding region or non-coding region were plotted against nucleotide contents in the complete single DNA strand, homonucleotides and their analogs (purines or pyrimidines) showed good correlations. However, heteronucleotides and their

Figure 2. Nucleotide relationships in normalized plant mitochondrial values. Upper, coding region; lower, non-coding region. Red squares, G; green triangles, C; blue diamonds, A; and shallow blue crosses, T. The composition of each nucleotide in the coding or non-coding region was plotted against the G content in the complete single DNA strand. The vertical axis represents the composition of the four nucleotides; the horizontal axis represents the G content in the complete single DNA strand.

presented in **Table 3**. All combinations due to G and A lines or C and T lines were approximately 0.24 in both the coding and non-coding regions for DNA obtained from plant mitochondria (**Table 4**).

3.3. Codon Evolution in Vertebrate Mitochondria

Nucleotide contents of the coding and non-coding regions were plotted against nucleotide contents in the complete single DNA strand (**Figure 3**). When the four nucleotide compositions in the coding region we plotted against the G content in the complete single DNA strand, the G content in the coding region was expressed by a linear regression line with a high regression coefficient (**Figure 3**, upper panel). The nucleotide A content could also be expressed by a linear regression line with a relatively high regression coefficient (0.82) (**Table 5**). On

Table 3. Regression lines representing nucleotide contents in the coding and non-coding regions against the nucleotide contents in the complete single strand DNA based on 47 plant mitochondria.

Coding	R	Non-coding	R
Gc = 0.993 G – 0.005	0.97	Gn = 0.839 G + 0.040	0.90
Cc = 0.904 G – 0.002	0.86	Cn = 0.981 G – 0.003	0.92
Tc = –0.770 G + 0.480	0.69	Tn = –0.803 G + 0.457	0.91
Ac = –1.127 G + 0.527	0.87	An = –1.018 G + 0.506	0.96
Gc = 0.808 C + 0.039	0.85	Gn = 0.663 C + 0.081	0.77
Cc = 0.955 C + 0.002	0.98	Cn = 0.956 C + 0.014	0.97
Tc = –0.797 C + 0.474	0.77	Tn = –0.749 C + 0.437	0.92
Ac = –0.966 C + 0.484	0.81	An = –0.870 C + 0.467	0.88
Gc = –0.793 T + 0.434	0.82	Gn = –0.560 T + 0.375	0.64
Cc = –0.890 T + 0.454	0.90	Cn = –0.916 T + 0.474	0.91
Tc = 0.984 T + 0.018	0.93	Tn = 0.685 T + 0.088	0.83
Ac = 0.699 T + 0.094	0.57	An = 0.790 T + 0.063	0.79
Gc = –0.767 A + 0.423	0.87	Gn = –0.722 A + 0.426	0.91
Cc = –0.746 A + 0.404	0.83	Cn = –0.784 A + 0.428	0.86
Tc = 0.435 A + 0.200	0.45	Tn = 0.666 A + 0.096	0.88
Ac = 1.078 A– 0.027	0.98	An = 0.840 A + 0.049	0.92

Xc and Xn mean the nucleotide content in the coding and non-coding regions, respectively.

Table 4. Crossing points obtained from two regression lines based on 47 plant mitochlondria.

Vs.	Lines	Coding	Non-coding
G	G-A	0.251	0.251
	C-T	0.288	0.258
C	G-A	0.251	0.252
	C-T	0.269	0.248
T	G-A	0.228	0.231
	C-T	0.233	0.241
A	G-A	0.244	0.241
	C-T	0.173	0.229
Av.	G-A	0.244 ± 0.011	0.244 ± 0.009
	C-T	0.241 ± 0.051	0.244± 0.012
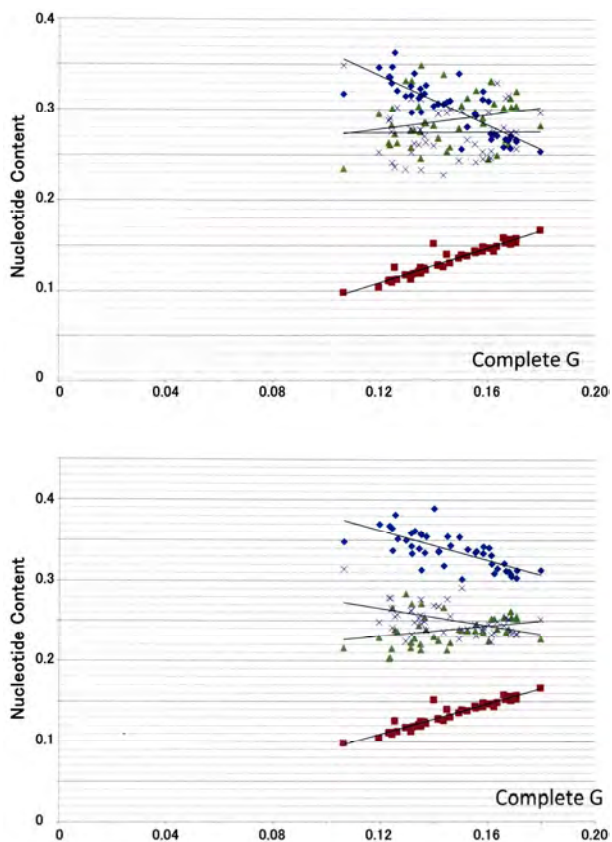
Figure 3. Nucleotide relationships in normalized vertebrate mitochondrial values. Upper, coding region; lower, non-coding region. Red squares, G; green triangles, C; blue diamonds, A; and shallow blue crosses, T. The composition of each nucleotide in the coding or non-coding region was plotted against the G content in the complete single DNA strand. The vertical axis represents the composition of the four nucleotides; the horizontal axis represents the G content in the complete single DNA strand.

analog relationships (*i.e.*, G vs. C or T and A vs. C or T) showed no correlation for vertebrate mitochondria (**Table 5**). This rule was observed in all cases in vertebrate mitochondria.

The calculated points of intersection of two regression line equations are presented in **Table 6**. The G and A (purines) lines intersected at 0.219 and 0.227 in the coding region and non-coding region, respectively, against the G (purine) content in the complete single DNA strand; while the C and T (pyrimidines) lines intersected at 0.106 and 0.160 in the coding and non-coding regions, respectively, against the G (purine) content (**Table 6**). The former values were close to 0.250, whereas the latter were relatively far from this value. On the other hand, the G and A (purines) lines intersected at 0.565 and 0.506 in the coding and non-coding regions, respectively, against the C (pyrimidine) content in the complete single

Table 5. Regression lines representing nucleotide contents in the coding and non-coding regions against the nucleotide contents in the complete single strand DNA based on 45 vertebrate mitochondria.

Coding	R	Non-coding	R
Gc = 0.948 G – 0.004	0.96	Gn = 1.133 G + 0.007	0.87
Cc = 0.386 G + 0.233	0.24	Cn = 0.322 G + 0.192	0.30
Tc = 0.019 G + 0.272	0.01	Tn = –0.542 G + 0.330	0.50
Ac = –1.353 G + 0.500	0.82	An = –0.913 G + 0.471	0.73
Gc = 0.148 C + 0.093	0.21	Gn = 0.295 C + 0.091	0.31
Cc = 1.165 C – 0.029	0.99	Cn = 0.681 C + 0.053	0.87
Tc = –0.882 C + 0.516	0.76	Tn = –0.562 C + 0.405	0.71
Ac = –0.431 C + 0.420	0.36	An = –0.414 C + 0.452	0.45
Gc = –0.068 T + 0.152	0.26	Gn = –0.120 T + 0.203	0.12
Cc = –0.960 T + 0.546	0.80	Cn = –0.533 T + 0.381	0.66
Tc = 1.167 T – 0.037	0.98	Tn = 0.647 T + 0.078	0.80
Ac = –0.139 T + 0.340	0.11	An = 0.006 T + 0.337	0.07
Gc = –0.505 A + 0.292	0.75	Gn = –0.674 A + 0.383	0.76
Cc = –0.388 A + 0.411	0.36	Cn = –0.295 A + 0.332	0.40
Tc = –0.212 A + 0.342	0.20	T = 0.198 A + 0.189	0.27
Ac = 1.106 A – 0.045	0.99	An = 0.771 A + 0.096	0.90

Xc and Xn mean the nucleotide content in the coding and non-coding regions, respectively.

Table 6. Crossing points obtained from two regression lines based on 45 vertebrates.

Vs.	Lines	Coding	Non-coding
G	G-A	0.219	0.227
	C-T	0.106	0.160
C	G-A	0.565	0.509
	C-T	0.266	0.283
T	G-A	2.648	1.063
	C-T	0.274	0.257
A	G-A	0.209	0.199
	C-T	0.115	0.290

DNA strand. The C and T (pyrimidines) lines crossed at 0.266 and 0.283 in the coding and non-coding regions, respectively, against the C (pyrimidine) content in the complete single DNA strand (**Table 6**). The former two values were significantly different from 0.250, whereas the latter two values were close to 0.250.

When the A (purine) and T (pyrimidine) contents in the complete single DNA strand were used instead of the G (purine) and C (pyrimidine) contents, consistently similar results were obtained (**Table 6**). Combinations of regression line equations (G and A or C and T) against heteronucleotide content in the complete single DNA strand rarely attained 0.250 as a point of intersection.

## 3.4. Codon Evolution in Invertebrate Mitochondria

As determined in a previous study [12], although nucleotide content relationships in the complete invertebrate mitochondrial genome were heteroskedastic, they were classified into two groups, I and II, based on their distributions on the graph. Plotting the C content of the coding region against the G content in the complete single DNA strand in invertebrate mitochondria, it showed that mitochondria could be clearly classified into two groups (denoted by a dotted line on **Figure 4**). This is consistent with the result obtained from the complete genome [12].

Nucleotide content relationships were also investigated in the classified invertebrate I mitochondria. Plotting the four nucleotide compositions in the coding region against the G content in the complete single DNA strand produced four lines of regression (**Figure 5**, upper panel); however, all four lines differed from each other. Similar results were obtained for the non-coding region (**Figure 5**, lower panel). The values of their regression coefficients, the slope, and constants for each equation are shown in **Table 7**. Relationships between the coding or non-coding region, the complete single DNA strand, and the homonucleotides and their analogs contents, correlated well for invertebrate I mitochondria (**Table 7**).

As shown in **Figure 5**, the lines for C and T against the G content in the complete single DNA strand intersected at around 0.250 for both the coding and non-coding regions. The points of intersection of two lines of regression equations are presented in **Table 7** and were calculated and tabulated in **Table 8**. The points
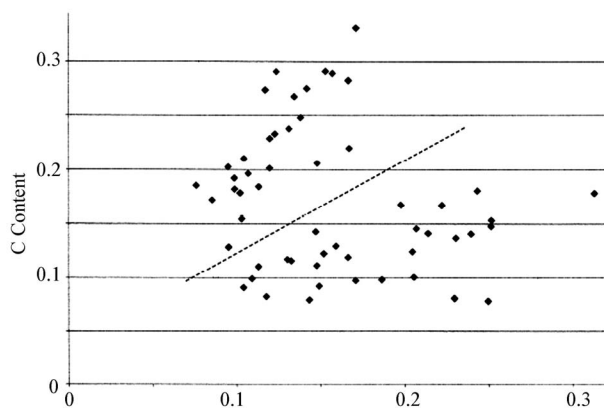
Figure 4. Nucleotide relationships in invertebrate mitochondria. Nucleotide contents were normalized, and the C content in the coding region was plotted against the G content in the complete single DNA strand. The vertical axis represents the G and C compositions and the horizontal axis represents the G content in the complete single DNA strand. The dotted line represents the G content in the coding region against the G content in the complete single DNA strand.
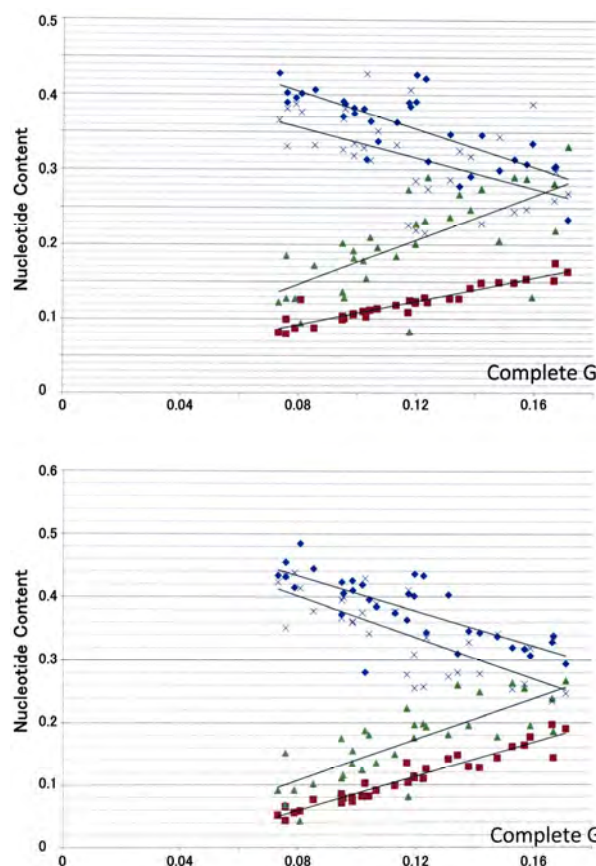
Figure 5. Nucleotide relationships in normalized invertebrate I mitochondrial values. Upper, coding region; lower, non-coding region. Red squares, G; green triangles, C; blue diamonds, A; and shallow blue crosses, T. The composition of each nucleotide in the coding or non-coding region was plotted against the G content in the complete single DNA strand. The vertical axis represents the composition of each of the four nucleotides, the horizontal axis represents the G content in the complete single DNA strand.

of intersection from the two lines of regression equations (G and A or C and T) against homonucleotides or their analog contents in the complete single DNA strand were close to 0.250, while those against heteronucleotides or their analogs contents were rarely 0.250 for invertebrate I mitochondria (**Table 8**).

Additionally, the nucleotide composition relationships observed between the coding or non-coding region and the complete single DNA strand were also examined for invertebrate II mitochondria. The characteristics of the lines of regression are shown in **Table 9**. The points of intersection for two lines of regression equations are shown in **Table 10**. The results obtained from invertebrate II mitochondria were similar to those of invertebrate I mitochondria.

Table 7. Regression lines representing nucleotide contents in the coding and non-coding regions against the nucleotide contents in the complete single strand DNA based on 31 invertebrate I mitochondria.

Coding	R	Non-coding	R
Gc = 0.781 G + 0.030	0.94	Gn = 1.364 G − 0.050	0.96
Cc = 1.496 G + 0.027	0.68	Cn = 1.645 G − 0.024	0.79
Tc = −1.014 G + 0.437	0.51	Tn = −1.628 G + 0.531	0.77
Ac = −1.263 G + 0.506	0.76	An = −1.380 G + 0.543	0.77
Gc = 0.229 C + 0.078	0.59	Gn = 0.513 C + 0.011	0.78
Cc = 1.006 C + 0.009	0.99	Cn = 0.916 C − 0.008	0.95
Tc = −0.740 C + 0.461	0.80	Tn = −0.866 C + 0.507	0.88
Ac = −0.495 C + 0.453	0.64	An = −0.562 C + 0.489	0.67
Gc = −0.224 T + 0.194	0.53	Gn = −0.459 T + 0.259	0.64
Cc = −0.961 T + 0.515	0.87	Gn = −0.825 T + 0.437	0.79
Tc = 0.984 T − 0.002	0.98	Tn = 1.016 T + 0.010	0.94
Ac = 0.201 T + 0.292	0.24	An = 0.268 T + 0.294	0.29
Gc = −0.327 A + 0.241	0.67	Gn = −0.659 A + 0.351	0.80
Cc = −0.809 A + 0.498	0.63	Cn = −0.899 A + 0.497	0.75
Tc = 0.197 A + 0.247	0.17	Tn = 0.563 A + 0.135	0.45
Ac = 0.939 A + 0.015	0.97	An = 0.995 A + 0.018	0.95

Xc and Xn mean the nucleotide content in the coding and non-coding regions, respectively.

Table 8. Crossing points obtained from two regression lines based on 31 invertebrate mitochondria.

Vs.	Lines	Coding	Non-coding
G	G-A	0.233	0.216
	C-T	0.163	0.170
C	G-A	0.518	0.445
	C-T	0.259	0.289
T	G-A	0.231	0.048
	C-T	0.266	0.232
A	G-A	0.157	0.201
	C-T	0.250	0.248

Table 9. Regression lines representing nucleotide contents in the coding and non-coding regions against the nucleotide contents in the complete single strand DNA based on 28 invertebrate II mitochondria.

Coding	R	Non-coding	R
Gc = 1.004 G − 0.002	0.96	Gn = 0.904 G + 0.018	0.89
Cc = 0.306 G + 0.066	0.54	Cn = 0.190 G + 0.096	0.26
Tc = −0.041 G + 0.396	0.05	Tn = −0.355 G + 0.413	0.35
Ac = −1.269 G + 0.539	0.85	An = −0.740 G + 0.472	0.77
Gc = 0.485 C + 0.126	0.30	Gn = 0.839 C + 0.083	0.53
Cc = 0.835 C + 0.017	0.94	Cn = 1.087 C − 0.006	0.93
Tc = −0.763 C + 0.486	0.57	Tn = −1.169 C + 0.495	0.74
Ac = −0.558 C + 0.371	0.24	An = −0.757 C + 0.429	0.50
Gc = −0.055 T + 0.209	0.05	Gn = −0.400 T + 0.339	0.35
Cc = −0.401 T + 0.274	0.63	Cn = −0.640 T + 0.372	0.76
Tc = 0.913 T + 0.047	0.94	Tn = 1.033 T − 0.041	0.91
Ac = −0.457 T + 0.470	0.27	An = 0.007 T + 0.330	0.02
Gc = −0.727 A + 0.413	0.88	Gn = −0.585 A + 0.370	0.73
Cc = −0.208 A + 0.188	0.46	Cn = −0.081 A + 0.157	0.14
Tc = −0.230 A + 0.460	0.34	Tn = 0.011 A + 0.343	0.88
Ac = 1.165 A − 0.061	0.98	An = 0.654 A + 0.130	0.86

Xc and Xn mean the nucleotide content in the coding and non-coding regions, respectively.

Table 10. Crossing points obtained from two regression lines based on 28 invertebrate II mitochondria.

Vs.	Lines	Coding	Non-coding
G	G-A	0.238	0.276
	C-T	0.951	0.934
C	G-A	0.235	0.217
	C-T	0.293	0.222
T	G-A	0.510	0.022
	C-T	0.173	0.247
A	G-A	0.251	0.194
	C-T	0.621	−2.022

4. DISCUSSION

The slopes for the lines of regression representing nucleotide contents differ between the coding and non-coding regions in nuclear DNA [4]. Comparing chloroplasts DNA with mitochondrial DNA, the slopes of the regression lines were the same in the coding region, although those values differed in the non-coding region (**Tables 1** and **3**). Thus, the evolutionary differences observed between chloroplasts and mitochondria are controlled in the non-coding region. In fact, mitochondria and chloroplasts have been proposed to be derived from proteobacteria [9,10] and cyanobacteria [11]. A comparison of the human genome [14,15] with the sea urchin genome [16] has revealed that the number of protein coding genes is similar between the two species, while the non-coding region of the former is much larger than that of the latter. This fact also suggests that the non-coding region plays an important role in developmental biology. In chloroplasts and plant mitochondria, the rule that G ≈ C, T ≈ A and [(G + A) ≈ (C + T)] is not only observed in the complete genome, but also in the coding or non-coding region in plant organelles, based on nucleotide content relationships between the coding or non-coding region and the complete single DNA strand.

On the other hand, the nucleotide content relationships for either the coding or non-coding regions did not obey Chargaff's second parity rule in nuclear genomes [4], instead, (G + A) > (C + T) in the coding region [17]. In addition, animal mitochondrial evolution seems to differ, not only from nuclear, but also from plant organelles. Plasmids, which are not compartmentalized from the nucleus, showed codon frequencies that resemble those of the host [18]. Thus, the compartmentalization of cellular organelles is likely to strongly influence organelle evolution.

To understand the establishment of Chargaff's second parity rule, the existence of both forward and reverse strands is necessary [2,8]. Namely, it is clear that the second parity rule is based on the double helical structure of DNA [19], where the complementary relationship between the two strands plays a role. Primitive genomes might be constructed by double-stranded DNA and mutations that occur synchronously over the genome [20] are governed by linear formulae [4]. In addition, Chargaff's parity rules are alternated to four linear formulae based on single nucleotide content, as shown above. Thus, biological evolution is likely to be based on the nucleotide contents expressed by linear formulae.

Chargaff's first parity rule [5], G = C, A = T, and [(G + A) = (C + T)], is well known and uses the four nucleotide contents that are normalized as follows: G + C + A + T = 1. Therefore, 2G + 2T = 1 or 2G + 2A = 1. Finally, T = 0.5 − G or A = 0.5 − G. Eventually, four nucleotide contents are expressed by just G content: G = G, C = G, T = 0.5 − G, and A = 0.5 − G. Namely, each of the four nucleotide contents are expressed by linear formulae based on just one nucleotide content (G). Thus lines for G and C or for lines T and A overlap. In addition, the G line intersects the A line at 0.250 and the C line crosses the T line at 0.250. Thus, the four regression lines obtained from the sample that obeys Chargaff's first parity rule cross exactly at 0.250. In addition, the four regression lines based on a sample that obeys Chargaff's second parity rule will intersect at around 0.250. In the present study, four regression lines based on chloroplasts (**Figure 1** and **Table 1**) and plant mitochondria (**Figure 2** and **Table 3**), which both obey Chargaff's second parity rule, intersect at around 0.250 (**Tables 2** and **4**). On the other hand, for animal mitochondria, only two regression lines due to homonucleotides or their analogs in the complete single DNA strand intersect around 0.250, while the other two regression lines due to heteronucleotides or their analogs in the complete single DNA strand rarely intersect at 0.250. Thus, nucleotide alternations, not only in homonucleotides and their analogs but also in heteronucleotides and their analogs, are strictly regulated against the complete single DNA strand in samples that obey Chargaff's second parity rule; namely, chloro-

plasts and plant mitochondria. However, only alternations of homonucleotides and their analogs are strictly regulated in both coding and non-coding regions against the complete single DNA strand in animal mitochondria. These results indicate that the evolutionary process of animal mitochondria differs from that of chloroplasts and plant mitochondria, possibly due to deviations from Chargaff's second parity rule. This is consistent with the previous conclusion that provided evidence for a single origin of life [12].

REFERENCES

[1] Rudner, R., Karkas, J.D. and Chargaff, E. (1968) Separation of B. subtilis DNA into complementary strands. 3. Direct analysis. *Proceedings of the National Academy Sciences*, **60(3)**, 921-922.

[2] Sorimachi, K. (2009) A proposed solution to the historic puzzle of Chargaff's second parity rule. *The Open Genomics Journal*, **2(3)**, 12-14.

[3] Sorimachi, K. and Okayasu, T. (2004) An evaluation of evolutionary theories based on genomic structures in Saccharomyces cerevisiae and Encephalitozoon cuniculi. *Mycoscience*, **45(5)**, 345-350.

[4] Sorimachi, K. and Okayasu, T. (2008) Codon evolution is governed by linear formulas. *Amino Acids*, **34(4)**, 661-668.

[5] Chargaff, E. (1950) Chemical specificity of nucleic acids and mechanism of their enzymatic degradation. *Experimentia*, **6(6)**, 201-209.

[6] Bell, S.J. and Forsdyke, D.R. (1999) Deviations from Chargaff's second parity rule with direction of transcription. *The Journal of Theoretical Biology*, **197(1)**, 63-76.

[7] Nikolaou, C. and Almirantis, Y. (2006) Deviations from Chargaff's second parity rule in organelle DNA insights into the evolution of organelle genomes. *Gene*, **381**, 34-41.

[8] Mitchell, D. and Bridge, R. (2006) A test of Chargaff's second rule. *Biochemical and Biophysical Research Communications*, **340(1)**, 90-94.

[9] Yang, D., Oyaizu, Y., Oyaizu, H., Olsen, G.J. and Woese, C.R. (1985) Mitochondrial origins. *Proceedings of National Academy Sciences*, **82(13)**, 4443-4447.

[10] Lang, B.F., Burger, G., O'Kelly, C.J., Cedergren, R., Golding, B., Lemieux, C., *et al*. (1997) An ancestral mitochondrial DNA resembling a eubacterial genome in miniature. *Nature*, **387(6632)**, 493-497.

[11] Raven, J.A. and Douglas, A.E. (2003) Genomes at the interface between bacteria and organelles. *Philosophical Transactions of Royal Society London. Series B*, *Biological Science*, **358(1429)**, 5-18.

[12] Sorimachi, K. (2010) Genomic data provides simple evidence for a single origin of life. *Natural Science*, **2(5)**, 521-527.

[13] Sorimachi, K. and Okayasu, T. (2008) Universal rules governing genome evolution expressed by linear formulas. *The Open Genomics Journal*, **1(11)**, 33-43.

[14] Lander, E.S., Linton, L.M., Birren, B., Nusbaum, C., Zody, M.C., Baldwin, J., Devon, K., *et al*. (2001) Initial

sequencing and analysis of the human genome. *Nature*, **409(6822)**, 860-921.

[15] Venter, J.C., Adams, M.D., Myers, E.W., Li, P.W., Mural, R.J., Sutton, G.G., *et al*. (2001) The sequence of the human genome. *Science*, **291(5507)**, 1304-1351.

[16] Sea urchin genome sequencing consortium. (2006) The genome of the sea urchin strongylocentrotus purpuratus. *Science*, **314(5801)**, 941-952.

[17] Szybalski, W., Kubinski, H. and Sheldrick, P. (1966) Pyrimidine clusters on the transcribing strand of DNA and their possible role in the initiation of RNA synthesis. *Cold Spring Harbor Symposia on Quantitative Biology*, **31**, 123-127.

[18] Sorimachi, K. and Okayasu, T. (2004) Classification of eubacteria based on their complete genome: Where does mycoplasmataceae belong? *Proceedings of the Royal Society of London. B* (*Supplement*), **271(4)**, S127-S130.

[19] Watson, J.D. and Crick, F.H.C. (1953) Genetical implications of the structure of deoxyribonucleic acid. *Nature*, **171(4361)**, 964-967.

[20] Sorimachi, K. and Okayasu, T. (2003) Gene assembly consisting of small units with similar amino acid composition in the Saacharomyces cerevisiae genome. *Mycoscience*, **44(5)**, 415-417.

Do male and female beetles (Tenebrio molitor) respond differently to rat feces containing eggs from the tapeworm, Hymenolepis diminuta?

John F. Shea

Department of Biology, Gonzaga University, Spokane, USA; shea@gonzaga.edu

ABSTRACT

Males and females often differ in their suscepti-bility and exposure to infection. Thus, they may also differ in their ability to avoid infection. The beetle, *Tenebrio molitor*, risks infection with cysticercoids when ingesting rat feces con-taining eggs of the tapeworm, *Hymenolepis di-minuta*. Previous studies demonstrated that beetles sometimes prefer infective feces sug-gesting that the tapeworm influences the for-aging behavior of beetles. After recording beetle movement in an arena containing infective and uninfective feces for one hour, sex main effects were not significant, but the effect of sex asked in trials was significant for males. Specifically, more male beetles occurred on the uninfective bait than on the infective bait. This observation suggests that male beetles avoid infective feces, which decreases their probability of infection with *H. diminuta*. If the cost of infection is higher in males, then selection to avoid infective feces may act more strongly on males.

Keywords: Hymenolepis diminuta; Cysticercoid; Tenebrio molitor; Behavior; Coprophagy; Parasite Manipulation

1. INTRODUCTION

In general, male vertebrates tend to show a greater in-tensity and prevalence of parasites than females [1-3], while the same pattern is not observed as commonly in invertebrates [4]. However, there are some exceptions in which experimentally infected arthropods result in a male infection bias [5-7]. This male infection bias in invertebrates may be linked to differences in infection susceptibility that are immunological [8-9], differences in infection exposure that are behavioral [10-11], or some combination [12]. If susceptibility and exposure to infection differs by sex, then does avoidance of infection also differ by sex? The beetle-tapeworm system lends itself to the study of this question.

In the tapeworm Hymenolepis diminuta, adults live in the small intestines of rodents, the definitive host. Eggs pass out of the rodents in their feces. The cysticercoid, or larval stage, occurs in an insect (the intermediate host, most often a beetle) that becomes infected by feeding upon infective feces. The rodent completes the cycle when it ingests an infected beetle. Thus, the success of this parasite depends on rodent-to-beetle transmission, which depends upon consumption of the egg stage by the beetle.

Prior studies [13,14] tested the fecal preference of groups of beetles, but did not examine unisex groups of beetles. One study [15] tested the fecal preference of tapeworm-infected male and female beetles (Tenebrio molitor) both in groups and as individuals. Only one study [5] examined unisex groups of uninfected beetles (T. molitor), which allows for sex comparisons while eliminating potentially confounding interactions between the sexes during the preference trial. The purpose of this study is to assess the relative importance of sex in fecal preference by recording beetle movement in an arena containing infective and uninfective feces at one-minute intervals for one hour.

2. MATERIALS AND METHODS

The "OSU Strain" [16] of H. diminuta was maintained in male Sprague-Dawley rats and beetles (T. molitor). Three rats were infected with 30 cysticercoids and maintained on commercial rodent chow and water. Three additional rats, obtained from the same commercial source, of identical age and from the same litter, were maintained under the same conditions as the infected rats to serve as the source of control (uninfective) feces. On the morning of the trials, rat cages were checked every 10 minutes, and fecal pellets were collected with forceps

to minimize contamination by rat urine. After each trial, the infective fecal pellets were examined to verify the presence of H. diminuta eggs.

Beetles were maintained on wheat bran, and small pieces of potato were added to the cultures on a regular basis. Pupae were removed from the cultures, and male and female pupae [17] were placed in separate dishes containing wheat bran. Beetles that emerged during a 24 h period were collected such that a daily cohort of beetles was maintained for both sexes.

Before the trial, seven to ten day-old male and female beetles (starved for two to three days) were placed in unisex groups of ten. To mitigate pseudo-replication, twelve groups of each sex were used in the preference trial in an alternating sequence. Each group was placed under a glass bowl in the center of a plastic arena under red light conditions. Beetles were provided with two types of bait: uninfective (control) or infective feces both of which had been collected within 10 minutes of defecation and randomly paired. Control feces were positioned randomly either in areas 1 and 3 or 2 and 4 (**Figure 1**) and infective feces were positioned in the opposing areas. A paper towel was used to mash the fecal pellets on the squares to prevent their displacement by beetles during the trial. Each bait area (25 mm^2) was large enough for all beetles to occur simultaneously and was located in a quadrant containing no bait (defined as a non-bait area). After 15 minutes, the bowl was removed and the beetles' movements were videotaped for 60 minutes under red light conditions. During video play back, the number of beetles observed at each bait area (square) and non-bait area (quadrant) was recorded at one-minute intervals. These occurrences were then summed over the 60 minute trial to obtain the total number of beetle occurrences at infective and control baits as well as non-bait areas.

Preference was measured as the difference between the number of beetles occurring at infective and control baits at each minute of the 60 minute trial. The same calculation was performed for the number of beetles occurring in non-bait areas. These differences in the number of beetle occurrences in the bait and non-bait areas were analyzed with the Mixed procedure in SAS (v.8, Cary, NC) with sex and trial as class variables and sex nested in trial as a random effect. The response variable was defined as the number of beetles at control bait/non-bait minus the number of beetles at infected bait/non-bait. Thus, a difference of zero indicates no preference.

The maximum proportion of female and male beetles occurring at the bait areas for each 60-minute trial was plotted against the average proportion of beetles at the bait areas (after an arcsine square root transformation for both proportions), and the slopes were compared. The

same was done for the maximum proportion of female and male beetles occurring in the non-bait areas.

3. RESULTS

The number of beetle occurrences did not differ between males and females in bait (**Table 1**; Mixed procedure, $P = 0.159$) or non-bait areas ($P = 0.873$). However, more males occurred at the uninfective bait than at the infective bait ($X \pm \text{SE} = 1.58 \pm 0.54$, $P = 0.008$), while females did not differ in the number of occurrences at either bait ($X \pm \text{SE} = 0.46 \pm 0.54$, $P = 0.412$). The number of beetle occurrences in the non-bait areas did not differ between infected and control halves of the arena for males (**Table 1**; $X \pm \text{SE} = 0.30 \pm 0.28$, $P = 0.292$) or for females ($X \pm \text{SE} = 0.24 \pm 0.28$, $P = 0.403$).

In a plot of the maximum number of beetles at each bait area against the average number of beetles at each bait area (data from **Table 2**), the slopes did not differ between males and females at the infective ($F_{1, 20} = 0.045$, $P = 0.834$) or the control bait areas ($F_{1, 20} = 2.75$, $P = 0.113$). In a plot of the maximum number of beetles in each non-bait area against the average number of beetles in each non-bait area (data from **Table 3**), the slopes
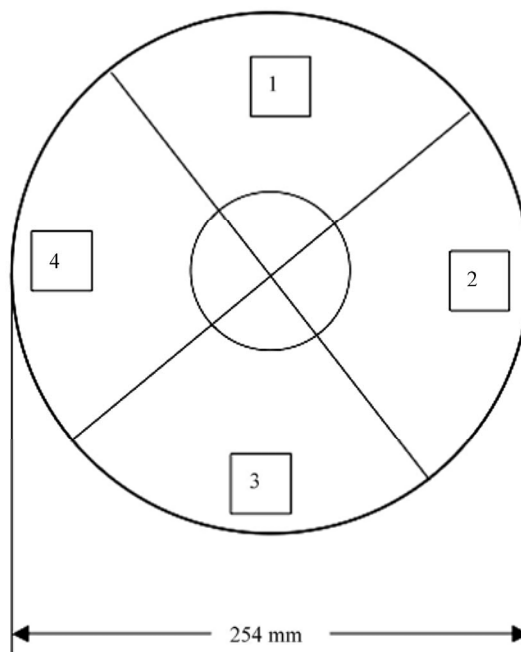
Figure 1. Diagram of the test arena for groups of beetles. Alternative baits were placed in the square bait areas located in four quadrants. Position of the control feces was determined randomly (e.g., either squares 1 and 3, or 2 and 4). Each bait area was 25 mm² and located in a quadrant containing no bait defined as a non-bait area. The diameter of the center circle was 64 mm and the distance from its center to the edge of a square was 75 mm.

Table 1. Results of the mixed procedure (SAS v.8) for beetle preference by sex for the bait area (top), and for the non-bait (beetles in quadrant–beetles on bait) area (bottom) in group trials.

Effect	Mean difference estimate[1,2]	s.e.	t	p
Sex	-1.12	0.77	-1.46	0.159
Trial (males)	1.58	0.54	2.90	0.008
Trial (females)	0.46	0.54	0.84	0.412
Sex	-0.06	0.40	-0.16	0.873
Trial (males)	0.30	0.28	1.08	0.292
Trial (females)	0.24	0.28	0.85	0.403

[1]For males and females, the mean difference equals total number of beetles at control bait/non-bait area minus total number of beetles at infected bait/non-bait area such that a positive value indicates preference for uninfective feces.

[2]$n_\male = 12$, $n_\female = 12$, d.f. = 22 in all cases; data from **Tables 2** and **3**.

Table 2. Total number of beetles occurring at each bait type (infected or control) summed over the entire 60 minute trial (range in parenthesis) with mean number of beetles (standard errors in parenthesis).

	Males		Females	
Trial	Infected	Control	Infected	Control
1.	34 (0-3)	299 (0-8)	26 (0-4)	22 (0-1)
2.	3 (0-1)	0 (0-0)	54 (0-3)	12 (0-2)
3.	36 (0-3)	243 (0-7)	22 (0-3)	45 (0-3)
4.	33 (0-3)	198 (0-7)	24 (0-3)	161 (0-8)
5.	73 (0-7)	173 (0-7)	36 (0-2)	71 (0-5)
6.	42 (0-4)	245 (0-8)	18 (0-2)	38 (0-2)
7.	192 (0-7)	34 (0-2)	9 (0-1)	90 (0-5)
8.	10 (0-2)	276 (0-8)	43 (0-3)	272 (0-9)
9.	34 (0-3)	1 (0-1)	202 (0-6)	71 (0-4)
10.	2 (0-1)	8 (0-6)	19 (0-2)	37 (0-3)
11.	141 (0-5)	182 (0-6)	20 (0-2)	36 (0-2)
12.	27 (0-2)	104 (0-6)	69 (0-8)	15 (0-2)
Mean	52.3 (16.7)	146.9 (32.6)	45.2 (16.7)	72.5 (21.7)

Table 3. Total number of beetles occurring in the non-bait area for each half of the arena (infected or control) summed over the entire 60 minute trial (range in parenthesis) with mean number of beetles (standard errors in parenthesis).

	Males		Females	
Trial	Infected	Control	Infected	Control
1.	150 (0-8)	117 (0-5)	254 (0-10)	298 (0-9)
2.	238 (1-10)	359 (0-9)	265 (1-8)	269 (1-8)
3.	179 (0-7)	142 (0-6)	244 (0-7)	289 (2-9)
4.	163 (0-6)	206 (0-7)	208 (0-8)	207 (0-7)
5.	164 (0-8)	190 (0-7)	215 (0-8)	278 (1-8)
6.	158 (0-7)	155 (0-5)	301 (0-10)	243 (0-9)
7.	208 (0-8)	166 (0-9)	204 (0-7)	297 (2-9)
8.	136 (0-6)	178 (0-8)	124 (0-5)	161 (0-8)
9.	206 (1-6)	359 (4-8)	160 (0-7)	167 (0-6)
10.	324 (1-9)	266 (1-9)	315 (3-8)	229 (0-7)
11.	153 (0-7)	126 (0-6)	265 (0-9)	279 (0-10)
12.	217 (0-7)	252 (0-9)	253 (1-8)	263 (1-9)
Mean	191.3 (15.1)	209.6 (24)	234 (16)	248.3 (13.9)

did not differ between males and females at the infective ($F_{1, 20} = 0.211$, $P = 0.651$) or the control non-bait areas ($F_{1, 20} = 0.748$, $P = 0.397$).

4. DISCUSSION

The presence of parasites often restricts host movement [18,19]. In this study, male and female beetles did not differ in the number of occurrences in the non-bait regions suggesting that beetle movement is not restricted by the presence of feces or tapeworm eggs. Thus, fewer beetles at the infective feces suggest that male beetles avoid infective feces rather than feces in general. It is unlikely that the control bait repels males since the total number of males in the non-bait regions did not differ between infected and control halves of the arena. Also, male and females did not differ in the maximum number of occurrences at either the infective or control baits. This indicates that both sexes behave similarly when foraging in unisex groups, minimizing concern about the confounding influence of social interactions. Overall, these data indicate that male beetles avoid infective feces while females show no preference.

Two experiments with *T. molitor* examined the costs of infection on fertility. In the first, males mated singly with infected females produced an average ($n = 30$) of 115.2 ovulated eggs, while males mated with uninfected females produced an average ($n = 30$) of 127.9 ovulated eggs [20]. In the second, females mated singly with infected males produce an average ($n = 7$) of 37 larvae while females mated with uninfected males produce an average ($n = 13$) of 63.7 larvae [21]. Additionally, infected male *T. molitor* are less attractive to females [21] and exhibit a lowered response to pheromone produced by uninfected females [22]. Thus, infection in males not only results in less reproductive success, but infected males are less likely to mate with a female.

Further, experimental infections of *T. molitor* indicate that males are more susceptible to infection than females [5], although this may not be true in some strains of *Tribolium confusum* and *Tribolium castaneum* [23]. In addition, males are more exposed to infection when they consume more food [24]. If males are more susceptible and exposed to infection and incur a greater reproductive cost once infected, then selection to avoid infective feces may act stronger on males than on females. Females also incur a cost when infected [20] and so may also avoid infective feces, but this behavior was not detected in this experiment.

Beetle age may factor into the relative cost of infection. The finding that starved male beetles avoid infective feces only partially agrees with Pappas *et al.* who found that fed male beetles avoid infective feces while more fed and starved females fed upon infective feces [5]. Pappas *et al.* tested 14-18 day old beetles whereas this study tested seven to ten day old beetles. Repeating this experiment with recently emerged beetles could yield different results. This is because greater reproductive output occurs when female beetles are mated with males infected two days post-emergence, suggesting an example of fecundity compensation [25]. Further both males and females experience increased survivorship when infected two days post-emergence [26]. Thus, recently emerged beetles may experience less selective pressure to avoid infective feces.

Although the results suggest that males avoid infective feces, the effectiveness of this avoidance behavior in natural settings needs examination because one study of natural populations of *Tenebrio molitor* found that 51% of males were infected as opposed to 41% of infected females [27]. Also, beetles produce both sex and aggregation pheromones [28,29], which could influence individual foraging behavior, suggesting a need for experiments that track marked individual beetles.

5. AKNOWLEDGEMENTS

REFERENCES

[1] Zuk, M. and McKean, K.A. (1996) Sex differences in parasitic infections: Patterns and processes. *International Journal for Parasitology*, **26(10)**, 1009-1024.

[2] Poulin, R. (1996) Sexual inequalities in helminth infections: A cost of being a male? *The American Naturalist*, **147(2)**, 287-295.

[3] Schalk, G. and Forbes, M.R. (1997) Male biases in parasitism of mammals: Effects of study type, host, age, and parasite taxon. *Oikos*, **78(1)**, 67-74.

[4] Sheridan, L.A., Poulin, R., Ward, D.F. and Zuk, M. (2000) Sex differences in parasitic infections among arthropod hosts: Is there is a male bias? *Oikos*, **88(2)**, 327-334.

[5] Pappas, P.W., Marschall, E.A., Morrison, S.E., Durka, G.M. and Daniel, C.S. (1995) Increased coprophagic activity of the beetle, tenebrio molitor, on feces containing eggs of the tapeworm, hymenolepis diminuta. *International Journal for Parasitology*, **25(10)**, 1179-1184.

[6] Gray, D.A. (1998) Sex differences in susceptibility of house crickets, acheta domesticus, to experimental infection with serratia liquefaciens. *Journal of Invertebrate Pathology*, **71(3)**, 288-289.

[7] Wedekind, C. and Jakobsen, P.J. (1998) Male-biased susceptibility to helminth infection: An experimental test with a copepod. *Oikos*, **81(3)**, 458-462.

[8] Kurtz, J., Wiesner, A., Götz, P. and Sauer, K.P. (2000) Gender differences and individual variation in the immune system of the scorpionfly panorpa vulgaris (Insecta: Mecoptera). *Developmental and Comparative Immunology*, **24(1)**, 1-12.

[9] Adamo, S.A., Jensen, M. and Younger, M. (2001) Changes in lifetime immunocompetence in male and female gryllus texensis (formerly G. integer): Trade-offs between immunity and reproduction. *Animal Behaviour*, **62(3)**, 417-425.

[10] Reimchen, T.E. and Nosil, P. (2001) Ecological causes of sex-biased parasitism in threespine stickleback. *Biological Journal of the Linnean Society*, **73(1)**, 51-63.

[11] Hecker, K.R., Forbes, M.R. and Leonard, N.J. (2002) Parasitism of damselflies (Enallagma boreale) by gregarines: sex biases and relations to adult survivorship. *Canadian Journal of Zoology*, **80(1)**, 162-168.

[12] Klein, S.L. (2000) The effects of hormones on sex differences in infection: From genes to behavior. *Neuroscience and Biobehavioral Reviews*, **24(6)**, 627-638.

[13] Evans, W.S., Hardy, M.C., Singh, R., Moodie, G.E. and Cote, J.J. (1992) Effect of the rat tapeworm, hymenolepis diminuta, on the coprophagic activity of its intermediate host, tribolium confusum. *Canadian Journal of Zoology*, **70(12)**, 2311-2314.

[14] Shostak, A.W. and Smyth, K.A. (1998) Activity of flour beetles (Tribolium confusum) in the presence of feces from rats infected with rat tapeworm (Hymenolepis diminuta). *Canadian Journal of Zoology*, **76(8)**, 1472-1479.

[15] Shea, J.F. (2007) Lack of preference for infective faeces in Hymenolepis diminuta-infected beetles (Tenebrio molitor). *Journal of Helminthology*, **81(3)**, 293-299.

[16] Pappas, P.W. and Leiby, D.A. (1986) Variation in the sizes of eggs and oncospheres and the numbers and distributions of testes in the tapeworm, hymenolepis diminuta. Journal of Parasitology, **72(3)**, 383-391.

[17] Bhattacharya, A.K., Ameel, J.J. and Waldebauer, G.P. (1970) A method for sexing living pupal and adult yellow mealworms. *Annals of the Entomological Society of America*, **63**, 1783-1785.

[18] Van der Wal, R., Irvine, J., Stien, A., Shepherd, N. and Albon, S.D. (2000) Faecal avoidance and the risk of infection by nematodes in a natural population of reindeer. *Oecologica*, **124(1)**, 19-25.

[19] Hutchings, M.R., Kryriazakis, I., Anderson, D.H., Gordon, I.J. and Coop, R.L. (1998) Behavioural strategies used by parasitized and non-parasitized sheep to avoid ingestion of gastro-intestinal nematodes associated with faeces. *Animal Science*, **67**, 97-106.

[20] Hurd, H. and Arme, C. (1986) Hymenolepis diminuta: The effects of metacestodes upon egg production and viability in the intermediate host tenebrio molitor. *Journal of Invertebrate Pathology*, **47(2)**, 225-230.

[21] Worden, B.D., Parker, P.G. and Pappas, P.W. (2000) Parasites reduce the attractiveness and reproductive success in male grain beetles. *Animal Behaviour*, **59(3)**, 543-550.

[22] Hurd, H. and Parry, G. (1991) Metacestode-induced depression of the production of, and response to, sex pheromone in the intermediate host tenebrio molitor. *Journal of Invertebrate Pathology*, **58(1)**, 82-87.

[23] Yan, G. and Norman, S. (1995) Infection of tribolium beetles with a tapeworm: Variation in susceptibility within and between beetle species and among genetic strains. *The Journal of Parasitology*, **81(1)**, 37-42.

[24] Shea, J.F. (2005) The effect of Hymenolepis diminuta (Cestoda) cysticercoids on the weight change, frass production, and food intake of the intermediate host, tenebrio molitor (Coleoptera). *Parasitology Research*, **98(1)**, 1-4.

[25] Hurd, H. and Ardin, R. (2003) Infection increases the value of nuptial gifts, and hence male reproductive success, in the hymenolepis diminuta-tenebrio molitor association. *Proceedings of the Royal Society of London B,* **270**, S172-S174.

[26] Hurd, H., Warr, E. and Polwart, A. (2001) A parasite that increases host lifespan. *Proceedings of the Royal Society of London B*, **268(1477)**, 1749-1753.

[27] Rau, M.E. (1979) The frequency distribution of Hymenolepis diminuta cysticercoids in natural, sympatric populations of Tenebrio molitor and T. obscurus. *International Journal for Parasitology*, **9(2)**, 85-87.

[28] Tschinkel, W., Willson, C. and Bern, H. (1967) Sex pheromone of the mealworm beetle. (Tenebrio molitor). *Journal of Experimental Zoology*, **164(1)**, 81-85.

[29] Hurd, H. and Fogo, S. (1991) Changes induced by Hymenolepis diminuta (Cestoda) in the behaviour of the intermediate host Tenebrio molitor (Coleoptera). *Canadian Journal of Zoology*, **69(9)**, 2291-2294.

Openly accessible at http://www.scirp.org/journal/NS/

Spatial and temporal distribution of the gastropod *Heleobia australis* in an eutrophic estuarine system suggests a metapopulation dynamics

Carlos Alejandro Echeverría[1]*, Raquel A. F. Neves[1], Leandro A. Pessoa[1], Paulo C. Paiva[2]

[1]Coastal and Estuarine Research Laboratory (Laboratório de Pesquisas Costeiras e Estuarinas-LABCOEST), UFRJmar, CT, Federal University of Rio de Janeiro, Rio de Janeiro, Brazil; *Corresponding Author: labcoest@gmail.com
[2]Polychaeta Laboratory, Zoology Department, Institute of Biology, Federal Univeristy of Rio de Janeiro, Rio de Janeiro, Brazil

ABSTRACT

Hydrobiidae is one of the most diverse taxa among limnic and estuarine mollusks. Patterns of spatial and seasonal distribution of *Heleobia australis* were studied in ten stations over two years, in the urban eutrophic bay of Guanabara, Rio de Janeiro, Brazil. Spatial dispersal strategies in adults of this species, analyzed in the laboratory, revealed three patterns: 1) mobility on soft sediments; 2) mobility on hard substrata; and 3) the ability to lift from the bottom to the surface, to again sink down. This facilitate species movement from one location to another by surface currents or attached to floating debris. Thus, individuals are able to escape from an impacted area and further re-colonize other patches after recovering from local impacts. The hypothesis of metapopulation dynamics (source–sink) was analyzed. Two stations with high and constant numbers of individuals were grouped and tested as possible 'sources'. The number of specimens in the remaining stations was highly variable, even with the complete disappearance and posterior highly dense re-occurrence of the mollusk, whereby these were tested as possible 'sinks'. Results derived from nested ANOVA supported the hypothesis of metapopulation dynamics in the case of *H. australis* adults, ex-pressed through opportunistic-species domination of a highly impacted estuarine system, such as Guanabara Bay.

Keywords: Metapopulation; Benthic Macrofauna; Population Dynamics; Heleobia Australis; Guanabara Bay

1. INTRODUCTION

The family Hydrobiidae contains the largest diversity among limnic and estuarine mollusks, wherein *Heleobia australis* is a dominant species in several degraded aquatic habitats [1], with a wide distribution in mixohaline environments [2], therein consuming deposited organic-material, including their own fecal pellets (autocoprophagy), especially when submitted to pronounced intra-specific competition [3]. This species is capable of re-settling on a soft-sediment surface, thereby acting as a bioturbator, as well as hard-substrata, besides being able to float away from the sediment itself by creating a gas bubble inside its shell. In this way, adults can temporarily enter the water column, whereat they are carried along by the tide and wind driven currents [4-7]. This dispersion strategy in adults, together with opportunistic behavior [8,9], facilitates both escape from excessively stressful situations and invasion of fresh or unpopulated areas thereby attesting to the success of this species in polluted and highly impacted places.

The spatial and seasonal distribution of *Heleobia australis* were studied in ten stations over two years in Guanabara Bay, (Rio de Janeiro, Brazil), a highly eutrophic urban bay. Two different patterns were observed: 1) the number of individuals was high and constant in two of the sampling stations, whereas 2) in the remainder there was considerable variation, to the point of complete disappearance and posterior highly dense recurrence. These patterns suggest that adults of the species are able to very quickly re-colonize depopulated areas, thereby recovering from mayor impacting events. This gave rise to the proposal of testing a metapopulation dynamics hypothesis to explain temporal variations in distribution patterns. In a metapopulation model, patches or groups of the population persist on a balance between local extinction and colonization [10]. Metapopulation may conform to its classical concept, in which all the sub-populations have a realistic chance of becoming extinct, but in other cases

there may be significant variation in either size or quality of the individual patches [11]. Thus, patches may be divided into sources (donor patches) and sinks (receiver patches) [12]. In this study, we considered as "colonization" within the metapopulation model, the reinvasion of depopulated areas by adult individuals [13] of *H. australis*, mainly due to its floating/sinking mechanism, thereby allowing for dispersal over relatively long distances, albeit subject to currents.

The studied area (Guanabara Bay, **Figure 1**) is a semi-enclosed water-body surrounded by large urban zones, and is characterized as one of the most degraded estuarine systems along the Brazilian coast [14,15]. The pollution is caused by untreated domestic sewage, besides incoming petroleum derivates and heavy metals, all of which accumulating in bottom sediments [16]. This accumulation substantially contributes to the disappearance, substitution or emergence of specific benthic in-vertebrates, an expression of population dynamics which can be used as environmental bio-indicators [17,18].

Herein we propose using a source-sink metapopulation model to explain the success of the species *Heleobia australis* in a eutrophic and highly impacted estuarine system, supported by its own dispersal strategies, opportunistic behavior and spatial and temporal distribution.

2. MATERIALS AND METHODS

2.1. Study Area

This study was undertaken in Guanabara Bay (**Figure 1**), an urban bay located in Rio de Janeiro, Brazil (22º40' and 23º00'S; 43º00' and 43º20'W). Circulation herein is essentially induced by semi-diurnal tidal currents, with a complex interaction of cold saline water input from the central (deeper) channel on the rising tide, and the warmer freshwater discharged from the surrounding rivers [14,16]. As to pollution and water exchange, three macro-regions have been defined by [19]: 1—a southern area undergoing pronounced oceanic influence, close to the opening of the bay (outer sector corresponding to BG 02, BG 03 and BG 09; **Figure 1**); 2—an intermediary sector, with heavily polluted waters adjacent to an over-populated island (Governador Island), (BG 10, BG 13, BG 14 and BG 18; **Figure 1**); the highest concentrations of sewage are located immediately south of this island, in waters close to the adjacent continent. 3—an inner sector, (BG 18, BG 25 and BG 28), with stations influenced by fringe mangroves, and presenting local peak concentrations of domestic and industrial pollutants, and recurring oil-leaks from the local petroleum industry. Several rivers which discharge into the bay receive huge
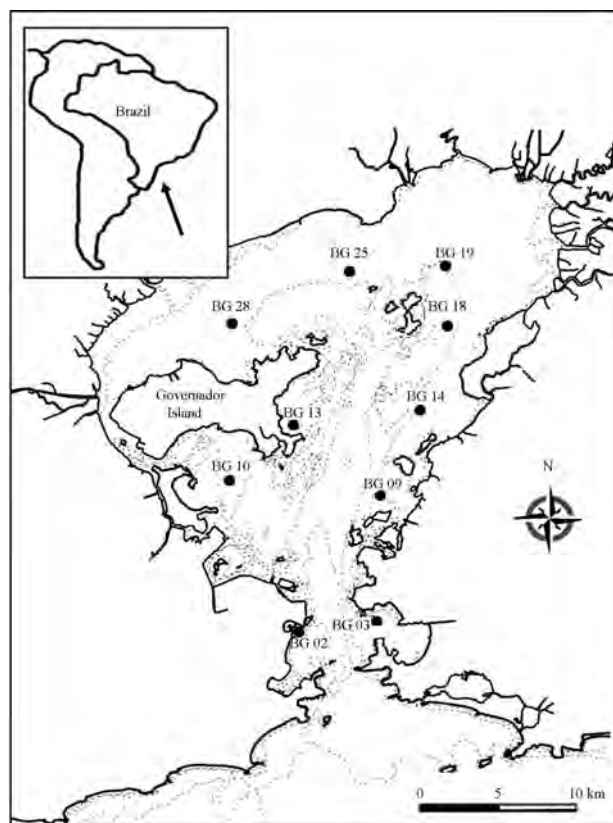

Figure 1. Guanabara Bay and indications of the surveyed stations (BG).

amounts of domestic sewage and industrial inputs. These rivers directly discharge large amounts of suspended solids, organic matter, heavy metals and hydrocarbons [16,20]. The climate in the region is humid tropical with a seasonal pattern of heavy summer rains (December to March) and a comparatively dry winter (July-August [21]; **Figure 2**).

2.2. Sampling

In order to study spatial and seasonal distribution of the local *H. australis* population, samples were collected at ten stations distributed on an embayment gradient, at depths between 4 and 7 meters (**Figure 1**). A Gravity corer, capable of bottom-sampling 0.008 m^{-2} with minimum sediment disturbance, was developed for this study.

Stations were sampled in six surveys throughout two consecutive years, which were defined according to regional seasonal patterns (rainfall): Year 1: C1—(First survey), July, 2005—dry season; C2—December, 2005—before the rainy season; C3—April, 2006—after the rainy season. Year 2: C4—July, 2006—dry season; C5— December, 2006—before the rainy season; and C6— April, 2007—after the rainy season (**Figure 2**; [21]). All sam-
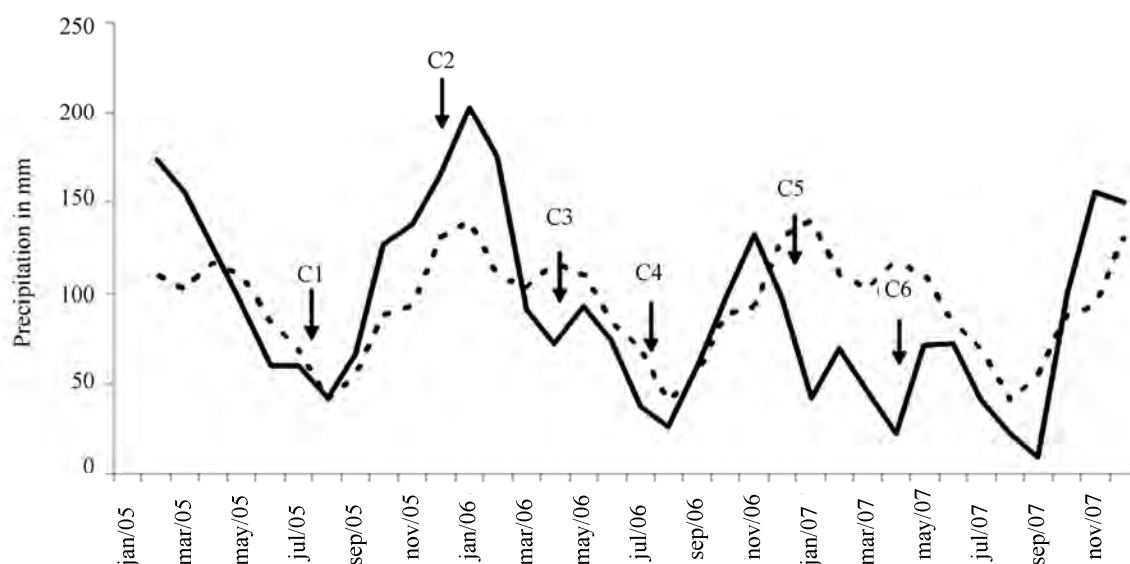
Figure 2. Historic mean-normal 61-90-(dotted line) and monthly accumulated rainfall (continuous line) in Rio de Janeiro, during the study. Surveys are shown by C1,C2,C3,C4,C5,C6. (modified from INMET, 2005-2007).

pling was carried out using the Research aluminium boat "Sizígia", from the Laboratório de Pesquisas Costeiras e Estuarinas (LABCOEST-UFRJmar-UFRJ).

Sediments of the seven inner and intermediate stations are predominantly silt-clay, where the Gravity corer per-formed satisfactorily. Of the remainder, two are located in sandy bottom sites (BG 02 and BG 03) and one (BG 09) a mixture of fine sand and clay [22]. The latter three stations were sampled by divers using a Gravity-like corer. Ten replicates were taken for each station per survey. Samples were sieved through a 0.5 mm mesh. Specimens were fixed and preserved in alcohol 70% for posterior analysis.

2.3. Laboratory Experiment

Heleobia australis adults were collected with a van Veen grab at station BG 10 (an intermediary station; **Figure 1**), in order to observe dispersal strategies and tolerance to hypoxic/anoxic bottoms. Specimens were maintained in aquaria with sea water and sediment collected from the very sampling station in the bay, both with and without continued aeration (aquarium-pump system). At least 30 specimens were monitored in both treatments their behavior and relative mortality being observed daily and weekly, respectively, during 30 days. Three dispersal strategies were taken into consideration, viz., mobility on the soft-sediment surface, flotation through the water column and mobility on hard substrata. The mortality rate was estimated by sampling approximately 40 ml of sediment from each aquarium. After stabilization in a Petri dish for ten minutes, moving (living) and non-

moving (dead) specimens were counted under a stereoscopic microscope.

In order to assess the hypothesis of long distance dispersal through adult flotation, a 30 cm diameter surface net with a 0.5 mm mesh was towed by the research boat "Sizígia", for five minutes in the area of source station BG 10 (**Figure 1**). The net was designed mainly for water surface sampling, with half of the opening out of the water. Organisms collected were transported to the laboratory and observed in Petry dishes for at least 12 hours, so as to check whether they were alive and in adequate conditions to colonize fresh areas.

A metapopulation dynamics model was proposed to assess temporal distribution of *H. australis* throughout the ten studied stations. The model was adapted to the manner in which specimens were considered able to "colonize" empty patches, and their way of shifting from the source patches, and was chosen as a way of explaining the observed patterns of rapid re-colonization with dense populations in previously empty patches in the bay. Source and sink patches were selected by sampling stations, taking into consideration the diverse observed patterns in density variation. Highly variable stations were assigned to sink patches, *i.e.*, spots where either population densities were mainly maintained by the input of specimens from other areas, or areas that showed a local disappearance of the mollusk, probably due to the lengthy duration of anoxic bottom water events. Stations with constantly high densities were assigned to sources, *i.e.*, sites propitious for maintaining an extremely high population, and thus scatter individuals to other areas in the bay.

2.4. Data Analysis

Population data were log-transformed (log (x + 1)) before statistical analysis [23]. Temporal and spatial variation in species density were tested by means of variance analysis (Two-way ANOVA), considering as fixed factors sampling stations and survey period, and as dependent variables, the number of individuals per square meter in each sample. Density data were calculated using the average of the ten replicate corers expressed per square. In order to test the metapopulation hypothesis, two sampling stations were considered as possible 'sources', due to their high densities and low variability over time, viz., BG 10 and BG 28 (**Figure 1**). The other seven were assigned as 'sinks', mainly due to their high density variation over time, even, according to surveys, reaching the point of local extinction followed by recovery. Stations BG 02, BG 03 and BG 09 were excluded from statistical analyses, due to the lack of specimens in several surveys. In order to test the hypothesis of a metapopulation model, data were submitted to mixed-model ANOVA [24-27], with two fixed orthogonal factors, areas with two levels (source and sink) and time with 6 levels (each survey), besides stations as a random nested factor within areas.

3. RESULTS

3.1. Spatial and Temporal Variation in Population Densities

Population densities throughout the bay increased (**Figure 4**) after the rainy season (C3 and C6; **Figure 2**). These differences in *H. australis* abundance were highly significant, both in space and time, p < 0,001 (**Figure 4**).

Population densities followed three distinguishable patterns (**Figure 3**): 1) stations with constant and high numbers of *H. australis* throughout all the studied period (BG 10 and BG 28); 2) those with highly variable numbers of the mollusk, and even with peaks of abundance (BG 13) and local disappearance (BG 13 and BG 19, C3) and: 3) those mainly without the species, but with episodic events of occurrence, even in considerable numbers (BG 02, BG 03 and BG 09, C2, C3 and C6).

These patterns gave to understand that densities were liable to change in a very quick and extensive manner throughout the stations, thereby implying the re-colonization capacity of the species. From observations, metapopulation dynamics is thereby suggested as an adaptation procedure for its survival in extremely impacted
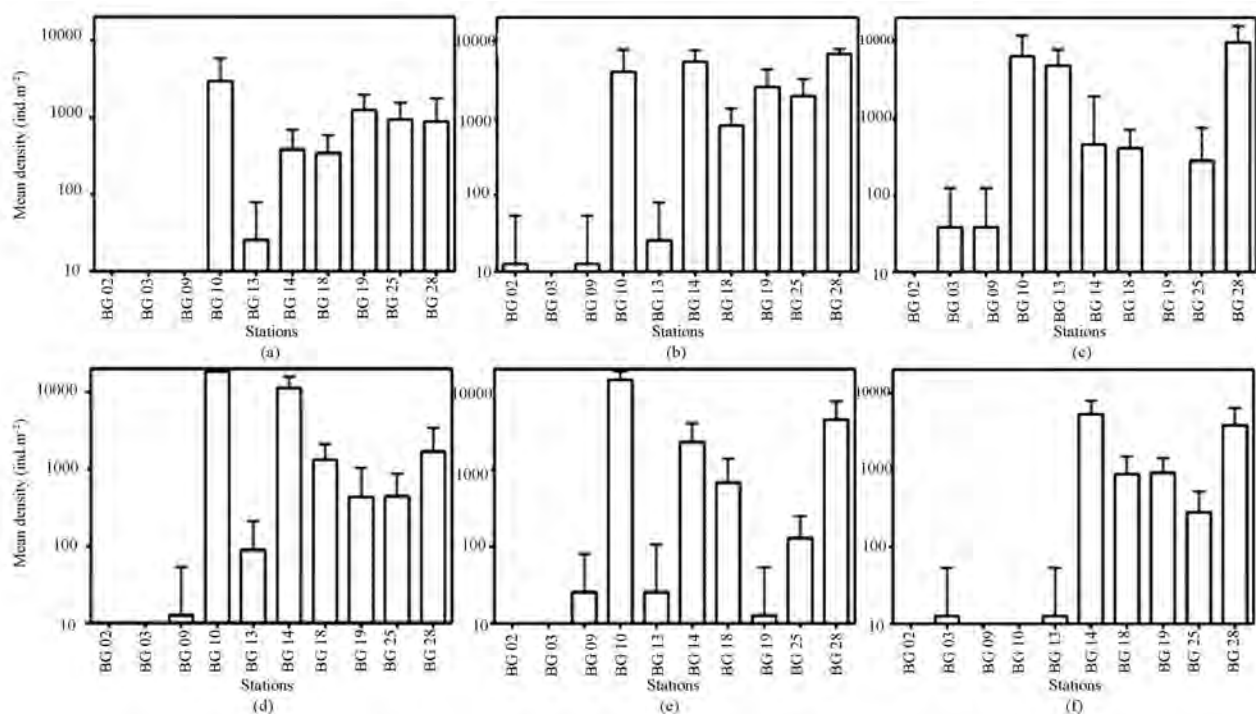

Figure 3. Mean density (Ind. m^{-2}; Logarithmic scale) of *Heleobia australis* in the sampling stations (BG 02, BG 03, BG 09, BG 10, BG 13, BG 14, BG 18, BG19, BG 25 and BG 28) for the surveyed period. a) C1, July/2005, dry season; b) C2, December/2005, before the rainy season; c) C3, April/2006, after the rainy season; d) C4, July/2006, dry season; e) C5, December/2006, before the rainy season; f) C6, April/2007, after the rainy season.

environments, evident as a notable instance of opportunistic behavior.

In order to test this hypothesis, stations with continuous high densities (BG 10 and BG 28) were selected as potential source-patches (**Figure 4(a)**), whereas stations with significant temporal variations in densities were selected as potential sink-patches (**Figure 4(b)**). The remainder was excluded from analysis, mainly due to their low densities (too many zeros in the matrix).

A comparison between source and sink stations revealed significant temporal and spatial variation (**Table 1**). Temporal patterns were significantly different between the two types, as indicated by the interaction between time and areas (time × areas; **Table 1**). Source stations appear to act as large patches in the meta-population model, by constantly supplying individuals to smaller patches (sink stations). This confirms the possibility that *H. australis* adults may take part in meta-population dynamics, through their capacity for relatively long distance loco-motion (see below) throughout
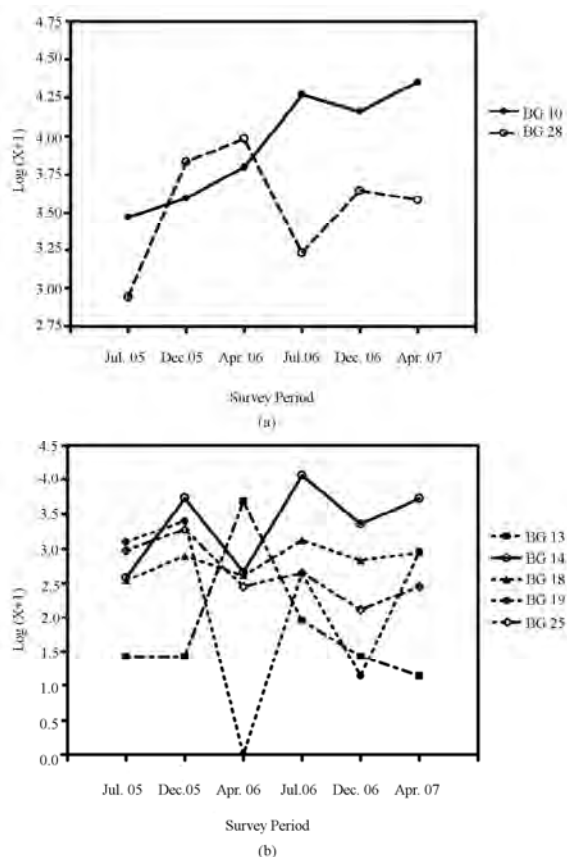
Table 1. Mixed-model ANOVA results, factors: time, arrears (source-sink), interaction (time × areas) and stations (areas).

Factor	S.S.	D.F.	MS.	F	P
Time	55.293	5	11.059	9.532	0.000
Areas	315.156	1	315.15	6.979	0.046
Time × Arear	46.514	5	9.303	8.019	0.000
Stations (Areas)	225.794	5	45.159	38.926	0.000
Error	467.527	403	1.160		

an enclosed bay, as part of a species opportunistic strategy, thereby assuring success in an extremely impacted environment.

3.2. Laboratory Experiments

Under aquarium experimental conditions, with aeration lead to 100% mortality, whereas without all survived till the end of the experiment (30 days). This suggests that distribution at the outer stations could be limited, among other factors, by the concentration of dissolved oxygen in the water, Dispersal strategies were observed in both treatments, except for flotation, which was not observed under continued aeration.
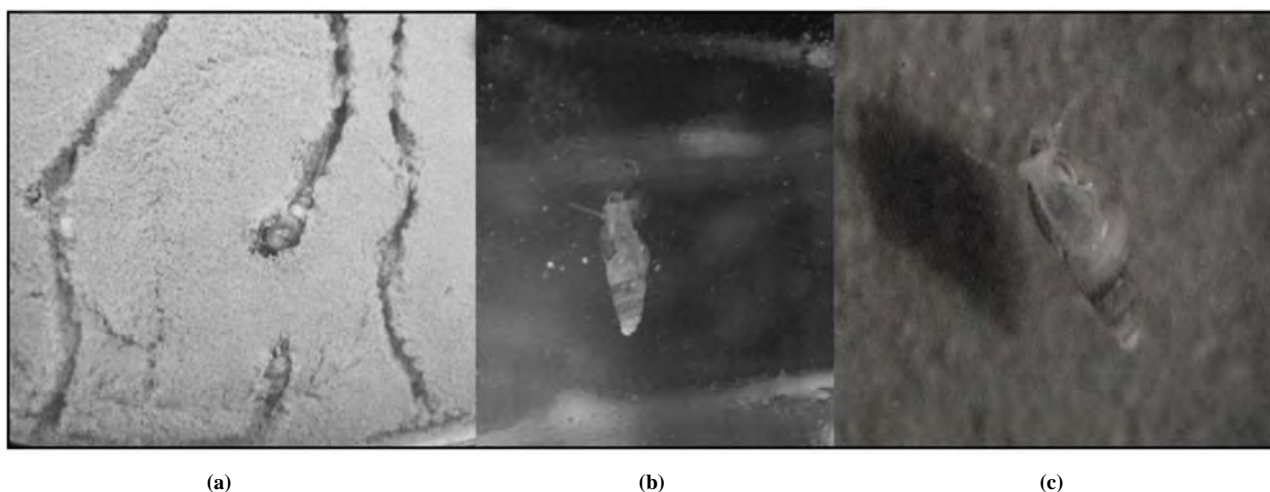
The observed mobility patterns on soft-sediment, through leaving trails, is characteristic of a surface crawler, (paths; **Figure 5(a)**), and suggests depositfeeding behavior. Nevertheless, the species was also able to move over hard substrata, as demonstrated by their dispersal when adhering to the wall of an aquarium (**Figure 3(b)**). Adult flotation behavior may result in a relatively long distance and fast dispersion strategy, thereby facilitating the re-colonization of new or depopulated (post-impact) habitats (**Figure 5(c)**), thus implying a possible meta-population scenario concerning the distribution pattern of a population in a semi-enclosed environment.

In five minutes of towing a surface net in the area of BG-10 station (considered as a possible source station), 60 alive and undamaged specimens of *H. australis* were collected, which were still alive after 12 hours of observation. Several specimens were also seen in situ attached to floating debris, as leaves, plastic bags, etc., all of which corroborating the possibility of long distance dispersal in adult specimens.

4. DISCUSSION

4.1. Patterns of Spatial and Temporal Variation in Population Density

The low densities observed at the outer stations could be related to environmental features, e.g. sediment type, since the predominant aspect was sandy bottoms un-

Figure 4. Mean density (Ind. m⁻²; log-linear scale) of *Heleobia australis*, grouped according the function of the patches; a) stations BG 10 and BG 28, source patches; b) Remaining stations, sink patches; except for BG 02, BG 03 and BG 09.

| (a) | (b) | (c) |

Figure 5. Dispersal strategies observed in the *Heleobia australis* during the manipulative experiments; a) mobility on a soft-sediment surface (trails); b) mobility on hard substrata (aquarium walls); c) flotation in the water column.

der-going strong oceanic water influence [22]. On the other hand, field measurements and laboratory experiments with Hydrobiidae in muddy and sandy habitats [28,29] refuted the hypothesis of greater body size and density in the former [30]. Furthermore, when considering fine and coarse-grained sediments, no difference in growth rate was observed.

In our study, mortality was 100% in experimentally aerated aquariums, a possible indication that distribution, among other factors, could be limited by OD content, thereby implying that *H. australis* is a typical estuarine species, wherein bottom OD contents are likely to be lower. Furthermore, bottom water oxygen depletion over a long period could be an impacting factor, thereby probably causing the observed local disappearance of the mollusk at intermediate stations. Since, in this event, there were few dead organisms, and considering the species capacity of floating from the sediment into the water column, it is suggested that adult specimens are thereby able to avoid stressful environment situations.

Intermediate and inner sector stations are heavily affected by sewage pollution [31]. Oscillation in *H. australis* density in the latter was likely to be associated to variations in organic matter inputs and the resulting bottom water dissolved oxygen concentrations [32].

Higher densities of the mollusk in more degraded areas [16] is in agreement with opportunistic behavior, through the capacity in taking advantage of high organic metal levels and tolerating moderate or high habitat contamination, both in metals and organic compounds [33], besides a tolerance for hypoxic/anoxic bottom conditions [34]. Population increment after the rainy season (for example, stations C3 and C6; **Figure 2**) could be associated to increased continental input (organic matter)

from the neighboring rivers [16] (**Figure 4**).

4.2. Dispersion and Mobility

The specimens used in lab experiments were collected from station BG 10, where bottom conditions are anoxic and concentrations of heavy metals, chlorophyll a and faecal coliforms high [35]. According to our experiments when dealing with aeration treatments, relatively higher levels of dissolved oxygen seemed to constitute a negative factor for this species. Aeration of originally anoxic sediments leads to the oxidation of reduced sulphur forms [36], usually, due to the high production of acids and a significant decrease in pH [37]. On studying the effects of acidification in freshwater gastropods, Okland [38] discovered that the group was completely absent in lakes with a pH lower than 5.2. The author mentioned the disappearance of three species during a pH-reduction event (5.2-4.2), and considered that this was related to damage to their calcareous shells. Sediments with low pH seemed to be deleterious to *H. australis* under experimental conditions (microcosms). Thus, the increase in dissolved oxygen in bottom waters of impacted areas could have a negative effect on the mollusk. Nevertheless, under field conditions, individuals are capable of floating away from bottom areas with acid pH [39]. The opportunistic behavior in *Heleobia australis* is presumed through its adaptation to hypoxic/anoxic conditions, quick growth and colonization. Resiliency of benthic communities to short term hypoxic events depends on species composition, differential life cycle, reproduction period and pattern of larval dispersal [40]. Species mobility strategies are very important not only for self dispersal, but also for that of planktonic larvae, the observed adult flotation capability facilitating even wider

dispersion [41,42].

The dispersion tactics of *H. australis* give support to the proposed source-sink metapopulation strategy as observed in the eutrophic Guanabara Bay. Similar distribution patterns had been observed in Hydrobiidae species in Limfjord (Denmark) [34] and benthic communities in Botany Bay (Australia) [24]. The persistence of patches in a metapopulation depends on factors affecting extinction and colonization rates, such as inter-patch distances, species dispersal abilities and the number of patches [10]. The source-stations BG 10 and BG 28, and probably other patches in the bay, seem to sustain several sink-population patches. The persistence of this metapopulation is dependent not only on the overall balance between local mortality and re-colonization, but also on the transport balance between source and sink areas. Patchiness in distribution of benthic species exists at different spatial scales [24,43]. In the case of *H. australis*, these patterns were observed by Neto and Lana [44] as small-scale aggregates (decimetric scale) within larger homogenous patches in Paranaguá Bay (Brazil).

Further studies on the dynamics of these populations of *H. australis* are necessary in order to establish an idea of transport intensity among patches and also to assess the spatial organization and flux between sink and source areas within the bay.

5. ACKNOWLEDGEMENTS

REFERENCES

[1] Senra, M.C.E. (2003) Análise preliminar e caracterização da malacofauna em sedimentos da Baía de Guanabara. *Anuario do Instituto de Geociências da UFRJ*, **26**, 149-151.

[2] Bemvenuti, C.E., Capitoli, R.R. and Gianuca, N.M. (1978) Estudos de ecologia bentônica na região estuarial da Lagoa dos Patos. II Distribuição quantitativa do macrobentos infralitoral. *Atlantica*, **3**, 23-32.

[3] Lopez-Figueroa, F. and Niell, F.X. (1988) Feeding behavior of Hydrobia ulvae (Pennant) in microcosms. *Journal of Experimental Marine Biology and Ecology*, **114(2-3)**, 153-167.

[4] Little, C. and Nix, W. (1976) The burrowing and floating behavior of the gastropod Hydrobia ulvae. *Estuarine, Coastal and Marine Science*, **4(5)**, 537-544.

[5] Bemvenuti, C.E. (1998) Fundos não vegetados. In: Seeliger, U., Odebrecht, C. and Castello, J. Eds., *Os ecossistemas costeiro e marinho do extremo sul do Brasil*, Ecoscientia, Rio Grande, Brazil, 87-92.

[6] Norkko, J., Bonsdorff, E. and Norkko, A. (2000) Drifting algal mats as an alternative habitat for benthic invertebrates: Species specific responses to transient resource. *Journal of Experimental Marine Biology and Ecology*, **248(1)**, 79-104.

[7] Orvain, F. and Sauriau, P.G. (2002) Environmental and behavioural factors affecting activity in the intertidal gastropod Hydrobia ulvae. *Journal of Experimental Marine Biology and Ecology*, **272(2)**, 191-216.

[8] Lana, P.C. (1986) Macrofauna bêntica de fundos sublitorais não consolidados da Baía de Paranaguá (Paraná). *Neritica*, **1(3)**, 79-89.

[9] Bemvenuti, C.E., Cattaneo, A.S. and Netto, S.A. (1992) Características estruturais da macrofauna bentônica em dois pontos da região estuarial da Lagoa dos Patos, RS, Brasil. *Atlantica*, **14(4)**, 5-28.

[10] Stiling, P. (1996) Ecology: Theories and applications. 2nd Edition, Prentice-Hall Inc, New Jersey.

[11] Holyoak, M., Leibold, M.A. and Holt, R.D. (2005) Me-tacommunities: Spatial dynamics and ecological communities. University of Chicago Press, Chicago.

[12] Pulliam, H.R. (1988) Sources, sinks and population regulation. *American Naturalist*, **132(5)**, 652-661.

[13] Junkins, R., Kelaher, B. and Levinton, J. (2006) Contribution of adult oligochaete emigration and immigration in a dynamic soft-sediment community. *Journal of Experimental Marine Biology and Ecology*, **330(1)**, 208-220.

[14] Amador, E.S. (1997) Baía de Guanabara e ecossistemas periféricos: Homem e natureza. Reporte Gráfica e Editora LTDA, Rio de Janeiro.

[15] Valentin, J.L., Tenenbaum, D.R., Bonecker, A.C.T., Bo-necker, S.L.C., Nogueira, C.R. and Villac, M.C. (1999) Osistema planctônico da Baía de Guanabara: Síntese do conhecimento. In: Silva, S.H.G. and Lavrado, H.P. Eds., Ecologia dos ecossistemas costeiros do estado do Rio de Janeiro, Série Oecologia Brasiliensis, Rio de Janeiro, 35-39.

[16] Kjerfve, B., Ribeiro, C.H.A., Dias, G.T.M., Filippo, A.M. and Quaresma, V.S. (1997) Oceanographic characteristics of an impacted coastal bay: Baía de Guanabara, Rio de Janeiro, Brazil. *Continental Shelf Research*, **17(13)**, 1609-1643.

[17] Underwood, A.J. (1991) Beyond BACI: Experimental designs for detecting human environmental impacts on temporal variations in natural populations. *Australian Journal of Marine and Freshwater Research*, **42(5)**, 569-587.

[18] Underwood, A.J. (1992) Beyond BACI:The detection of environmental impact on populations in the real, but variable, world. *Journal of Experimental Marine Biology and Ecology*, **161(2)**, 145-178.

[19] Wandeness, A.P., Mattos, M.A.R. and Nogueira, C.S.R. (1997) Copepoda (Crustacea) of Guanabara bay, R.J.I. specific composition. *Brazilian Archives of Biology and Technology*, **40**, 377-381.

[20] Geraldes, M.C., Paula, A.H., Godoy, J.M. and Valeriano, C.M. (2006) Pb isotope signatures of sediments from Guanabara Bay, SE Brazil: Evidence for multiple anthro-pogenic sources. *Journal of Geochemical Exploration*, **88(1-3)**, 384-388.

[21] INMET. (2005-2007). Rain precipitation data of the re-

gion and years of study, Meteorology National Institute. (Meteorology National Institute data center, RJ, BR) on-line. http://www.inmet.gov.br

[22] Quaresma, V.S., Dias, G.T.M. and Baptista Neto, J.A. (2000) Caracterização da ocorrência de padrões de sonar de varredura lateral e sísmica de alta freqüência (3,5 e 7,0 kHz) na porção sul da Baía de Guanabara-RJ. *Brazilian Journal of Geophysics*, **18(2)**, 201-214.

[23] Quinn, G.P. and Keough, M.J. (2003) Experimental design and data analysis for biologists. Cambridge University Press, Cambridge.

[24] Morrisey, D.J., Howitt, L., Underwood, A.J. and Stark, J.S. (1992) Spatial variation in soft-sediment benthos. *Marine Ecology Progress Series*, **81**, 197-204.

[25] Sokal, R.R. and Rohlf, F.J. (1995) Biometry: The principles and practice of statistics in biological research. 3rd Edition, W. H. Freeman and Co, New York.

[26] Underwood, A.J. (1997) Experiments in ecology: Their logical design and interpretation using analysis of variance. Cambridge University Press, Cambridge.

[27] Paiva, P.C. (2001) Spatial and temporal variation of a nearshore benthic community in Southern Brazil: Implications for the design of monitoring programs. *Estuarine, Coastal and Shelf Science*, **52(4)**, 423-433.

[28] Forbes, V.E. and Lopez, G.R. (1990) The role of sediment type in growth and fecundity of mud snails (Hidrobiidae). *Oecologia*, **83**, 53-61.

[29] Grudemo, J. and Bohlin, T. (2000) Effects of sediment type and intra- and interspecific competition on growth rate of the marine snails Hydrobia ulvae and Hydrobia ventrosa. *Journal of Experimental Marine Biology and Ecology*, **253**, 115-127.

[30] Fish, J.D. and Fish, S. (1974) The breeding cycle and growth of Hydrobia ulvae in the Dovey Estuary. *Journal of the Marine Biology Association UK*, **54(3)**, 685-697.

[31] Paranhos, R., Pereira, A.P. and Mayr, L.M. (1998) Diel variability of water quality in a tropical polluted bay. *Environmental Monitoring and Assessment*, **50(2)**, 131-141.

[32] Mayr, L.M., Tenenbaum, D.R., Villac, M.C., Paranhos, R., Nogueira, C.R., Bonecker, S.L.C. and Bonecker, A.C.T. (1989) Hydrobiological characterization of Guanabara Bay. In: Magoon, O. and Neves, C. Eds., Coastlines of Brazil, American Society of Civil Engineers, New York, 124-138.

[33] Rakocinski, C.F., Brown, S.S., Gaston, G.R., Heard, R.W.,

Walker, W.W. and Summers, J.K. (2000) Species-abundance-biomass responses by estuarine macrobenthos to sediment chemical contamination. *Journal of Aquatic Ecosystem Stress and Recovery*, **7(3)**, 201-214.

[34] Fenchel, T. (1975) Factors determining the distribution patterns of mud snails (Hydrobiidae). *Oecologia*, **20(1)**, 1-17.

[35] Lacerda, L.D., Souza, C.M.M. and Pestana, M.H.D. (1988) Geochemical distribution of Cd, Cu, Cr and Pb in sediments along the southeastern Brazilian coast. In: Seeliger, U., Lacerda, L.D. and Patchineelam, R. Eds., Metals in Coastal Environments of Latin America, Springer, Berlin, 86-89.

[36] Davis, A.P., Hao, O.J. and Chen, J.M. (1994) Kinetics of heavy metal reactions with ferrous sulphide. *Chemosphere*, **28(6)**, 1147-1164.

[37] Ivanov, M.V. (1983) Major fluxes of the global biogeo-chemical cycle of sulphur. In: Ivanov, M.V. and Freney, J.R. Eds., The Global Biogeochemical Sulphur Cycle, Wiley, Chichester, 449-463.

[38] Okland, J. (1992) Effects of acidic water on freshwater snails: Results from a study of 1000 lakes throughout Norway. *Environmental Pollution*, **78(1-3)**, 127-130.

[39] Bemvenuti, C.E., Rosa-Filho, J.S. and Elliot, M. (2003) Changes in soft-bottom macrobenthic assemblages after a sulphuric acid spill in the Harbour of Rio Grande (RS-Brazil). *Brazilian Journal of Biology*, **63(2)**, 183-194.

[40] Rosenberg, R. (2001) Marine benthic faunal successional stages and related sedimentary activity. *Scientia Marina*, **65(2)**, 107-119.

[41] Santos, S.L. and Simon, J.L. (1980) Marine soft-bottom community establishment following annual defaunation: Larval or adult recruitment? *Marine Ecology Progress Series*, **2**, 235-241.

[42] Little, C. (2000) The biology of soft shores and estuaries. Oxford University Press, New York.

[43] Thrush, S.F., Hewitt, J.E. and Pridmore, R.D. (1989) Patterns in the spatial arrangement of polychaetes and bivalves in intertidal sandflats. *Marine Biology*, **102(4)**, 529-535.

[44] Neto, A.S. and Lana, P.C. (1994) Effects of sediment disturbance on the structure of benthic fauna in a sub-tropical tidal creek of southeastern Brazil. *Marine Ecology Progress Series*, **106**, 239-247.

Polymeric microelement on the top of the fiber formation and optical loss in this element analysis

Maria I. Fokina, Nina O. Sobeshuk, Igor Y. Denisyuk*

Saint-Petersburg State University of Informational Technologies, Mechanics and Optics, Saint-Petersburg, Russia;
*Corresponding Author: denisiuk@mail.ifmo.ru

ABSTRACT

This paper describes the formation technology of polymeric microlenses self-organized on the fiber top in the limited reaction volume. The loss inserted to the optical coupling channel and their sources was investigated.

Keywords: Self-Focusing; Microlens; Optical Fiber; Photopolymer; Coupling

1. INTRODUCTION

Currently one of the important problems of fiber optics is the coupling of optical fibers with light sources and the introduction of light into the fiber with minimal losses. Direct welding of two fibers is optimal only for fibers with the same diameter and the aperture, while in other cases losses increasing require the use of focusing and collimating external systems. Loss of the light at fiber coupling whit LED laser or diode is too large, because emitting area, as the laser and the diode, always larger then diameter of fiber core. One solution to this problem is the use of focusing microelements on the top of the fiber.

A numerous effective technologies for microelements preparation, including microlenses made directly at the fiber top now are developed. Creating elements immediately at the fiber top is preferred because provides a self-alignment (coaxiality of axes) microlens and the fiber and no need for further manual assembly.

There are several well known methods for optical microelements preparation on the top of the fiber such as: laser fusion, or a gas burner (microoptical elements of various forms and purposes) [1], chemical etching (light coneconcentrator) [2], ion beam engraving (diffractive microlensese) [3]. The first two methods have found wide application, but the disadvantage is the possible misalignment of the microelement and core, and the de-

fect of a second—the unavoidable chemical contamination of the surface. Technology of ion beam engraving allows to obtain micro-relief of very high quality and small size, but this method is technically difficult in expensive [3].
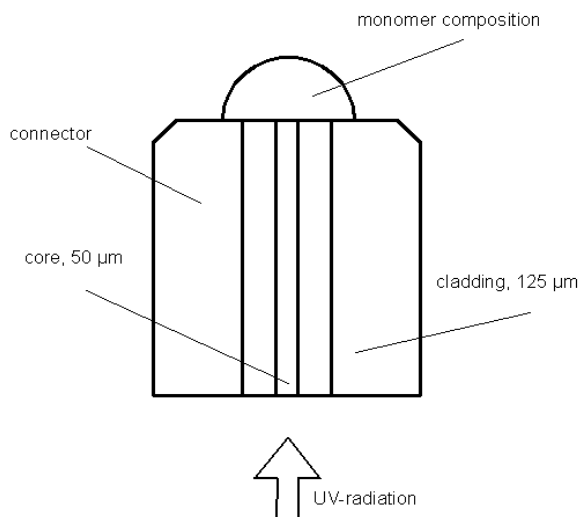
In recent years carried out many researches in the field of preparation of the polymeric optical microelements on the top of fiber [4-6]. The method is based on monomer composition polymerization deposited on the fiber top by laser radiation coming from the fiber. This technology allows obtaining high-quality microelements, as well as to control their size and profile [6]. However, all developments in this, of course, promising area, are at the stage of laboratory research, and experimental results depend from many different conditions such as type of monomer, initiator concentration, polymerization volume and differ in different works. In this work we prolong our experiments with microlens in fiber top self-writing made previously [7-9]. We find that processes of photopolymerization depend from speed of oxygen diffusion from monomers surface to polymerized area and so it depend from monomer volume. In this work we accomplish self-writing photopolymerization process in small monomer drop placed in fiber top in condition of fast oxygen diffusion from it surface. As oxygen will inhibit acrylate photopolymerization process [10].

2. EXPERIMENT

This work is devoted to investigation of the polymeric microelements formation processes at the end of optical fiber using laser radiation coming from the fiber at conditions of oxygen high speed diffusion to polymerization area. **Figure 1** shows the scheme of "growing" elements.

Into the one end of the fiber 50/125 was introduced a N2 laser irradiation ($\lambda = 337$ nm), on the other, vertically mounted end, a drop of the liquid monomer composition was deposited. The height of the drop was controlled

Figure 1. Scheme of the formation a polymeric element on the top of the fiber.

Figure 2. Element at the fiber top with the minimum exposure. Line of 50 μm is shown in the photo.

Figure 3. Polymeric element at the top of the fiber, exposure—10 sec.

Figure 4. Polymeric element at the top of the fiber, exposure—15 sec.

Figure 5. Polymeric element on the top of the fiber, exposure—45 sec.

visually over microscope. A mixture of acrylates was used: 2-carboxyethyl acrylate (50%), Bisphenol A glycerolate (20%), 1,6-hexanediol diacrylate (10%) and Trimethylolpropane ethoxylate (1 EO/OH) methyl ether diacrylate (20%). All reagents were purchased from Aldrich. As the initiator dimetoksifenilatsetofenon (0.1%) with absorption maximum at 250 nm was used. At 337 nm its absorption length was few millimeters. The refractive index of the mixture is –1.48. Exposure ranged from 3 up to 45 seconds (t = 3, 5, 10, 15, 25, 45 sec).

The elements formation process can be divided into following stages:

1) The process of polymerization doesn't begin immediately, but from the moment when the absorbed by monomer energy reaches a certain threshold. Delay appears because of the fact that the first impulses burn the oxygen in the monomer, which is the inhibitor of the process, after that only formation of free radicals from initiator molecules begin.

2) With a minimum exposure the formation of small, quasi-lens is observed, **Figure 2**.
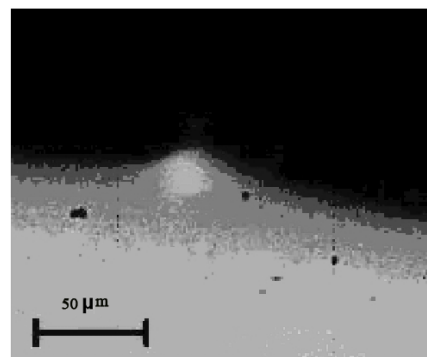
This stage is the most difficult to reproduce because polymerization process takes place very rapidly and continuously.

3) Formation of cylindrical/conical shape element with rounded top, **Figure 3**.
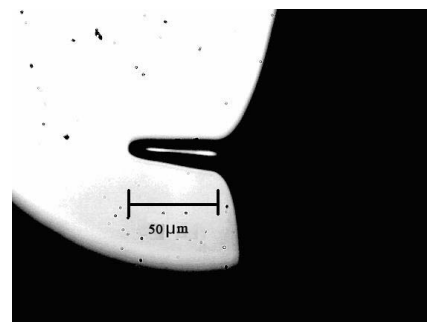
4) The formation of the narrowing structure is possible (**Figure 4**).

5) There is an alignment of profile of the element while increasing exposure. Experiments have shown that this form (**Figure 5**) has a high repeatability (the probability of almost 100%) when exposure element is sufficient.
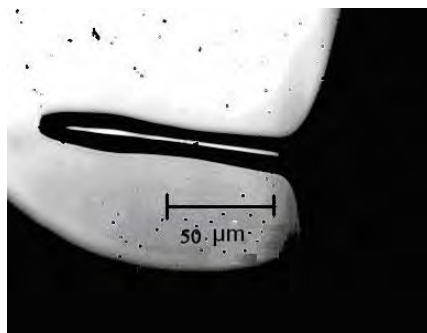
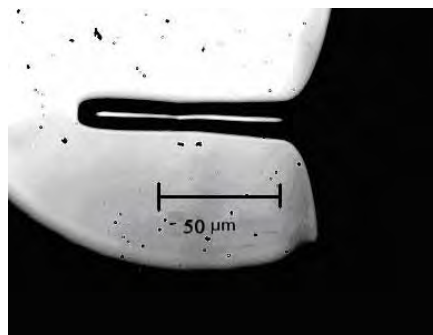After that visible light passing through microelements

was investigated. The experimental scheme is shown on **Figure 6**.

The dependence of the radiation intensity on the distance between the fiber end without microelement and a scanning fiber connected to a photodetector was measured in the first part of the experiment. In the second—the dependence of intensity on the distance between the scanning fiber and the fiber with polymeric microelement is on the end. As the scanning fiber 9/125 μm was used, because most interesting is efficiency of using microelements in the coupling of fibers of different core diameters (single mode with multimode).

Figure 7 shows the results of measurements (dependence of the photodetector signal on the distance between the fibers). Line 1 corresponds to the first part of the experiment, the line 2—the second.
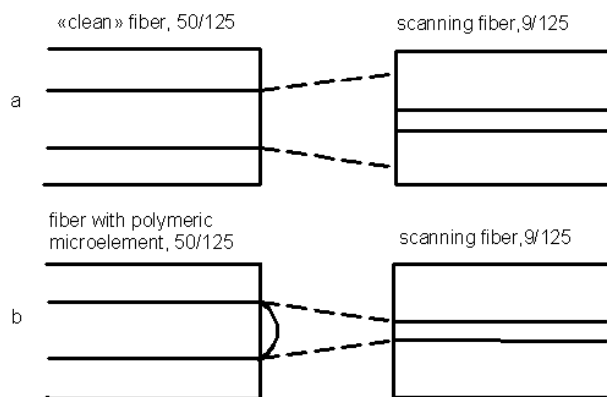
Figure 6. a) Measurement using fiber without microlens, b) Measurement using the fiber with polymeric microelement on the end.
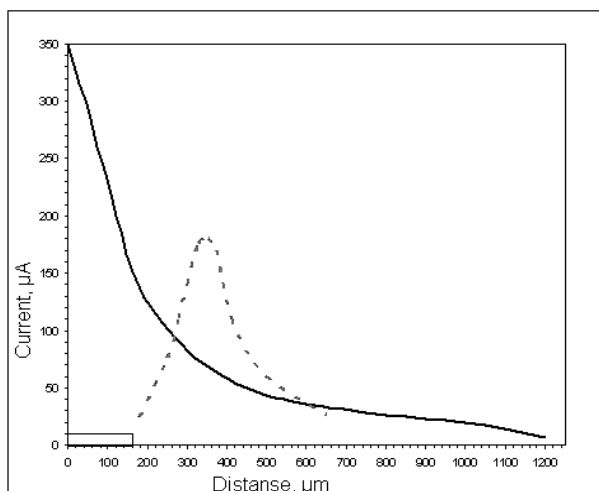

Figure 7. Dependence of the photodetector signal from the distance between the fibers: 1 (full line)—fiber without microlens; 2 (dashed line)—polymeric microelement on the end of the fiber.

Curve 2 has a clearly defined maximum, which confirms that the microelement focuses light. However, the graph shows that even at the maximum signal, consequently the intensity of radiation is lower than when fibers connected back to back. To clarify the source of the losses the following experiment was made: radiation of He-Ne laser was introduced into the fiber with microlens at its end. **Figure 8** shows the obtained result: element remains dark, but there are significant losses at the interface polymer-fiber.

3. RESULTS DISCUSSION

The dynamics of growth of self writing waveguide and formation of polymeric microelements at the end of the optical fiber was investigated in this work. Micro-photos made in series during formation of self-writing waveguide in the top of the fiber. The main stages of element formation are shown in **Figure 9** (in the left—exposition time for each photo). One of the features of obtained samples is that the width of all elements, starting from the third formation phase, is approximately equal to the half-width of fiber core. This can be explained in the following way: after reaching the threshold energy
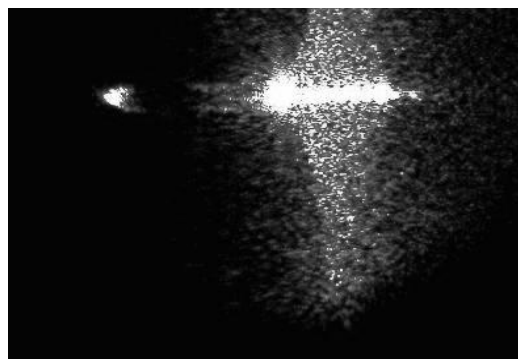
Figure 8. Passage of light through the fiber with a polymeric element at the end.
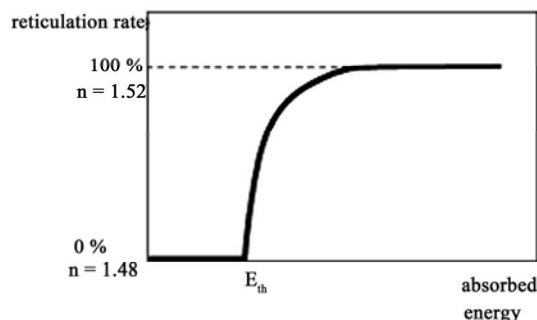
Figure 9. Empirical reticulation rate of the formulation versus absorbed energy. E_{th} is the threshold energy (achieved when the polymerization starts) and n the refraction index of the formulation.

the polymerization process takes place continuously and is accompanied by increasing of the refractive index **Figure 9** [5].

For this composition increasing of the refractive indices is 0.04 (the monomer composition—1.48, the polymer—1.52). As a result, we see the effect of self-focusing of the light in the polymer, *i.e.* formation of the waveguide, the core of which is a polymer, and the cladding—unpolymerized monomer. It is known that even with full internal reflection light goes abroad the substance to the distance equal to half the wavelength, and, therefore, slow growth element in wide might be expected. However, this does not happen, because energy of emergent radiation is insufficient to burn oxygen and initiate the polymerization.

One of the components of monomer composition 2-carboxyethyl acrylate having a linear structure also provides directional growth of element from fiber glass surface. 2-carboxyethyl acrylate contains acid groups chemically active with quartz, which provide reaction of monomer with fiber top and beginning of element grown from fiber top away.

Also it was found that element length will stop in some moment and the radius of curvature of the drop increases when increasing exposure. **Figure 10** shows photographs illustrating this effect.

We think that stopping of micro-element grown is a result of approaching of polymerized area to surface of monomer drop and, therefore, stopping of photopolymerization in result of oxygen inhibition influence.

Our investigation results showed that the fabrication method requires improving and optimization: significant losses in the microelement aren't observed, which confirms its waveguide structure, but there are significant losses at the interface between microelement and optical fiber. In fact is it the main component of optical losses and its removing will result on diminishing of optical losses to appropriate value.

Certainly, optical losses at interface: optical fiber/self writing waveguide resulting from narrowing of element in comparison to fiber core (fiber core 50 um; waveguide 25 um). Stepped transformation of waveguide core from 50 to 25 um will result on radiation going away at this interface.

In our opinion narrowing of polymerized area is a result of photo polymerization reaction inhibition by oxygen diffused from monomer drop volume to exposed area and slowing down of polymerization in surface of waveguide. Certainly this effect is negative and can be more powerful for single mode optical fiber having core diameter 7 um.

To overcome or reduce effect of waveguide narrowing according to our opinion are needed to diminish oxygen diffusion speed in monomer mixture, so are needed to

Photos of element	Exposure, seconds
	3
	10
	15
	45
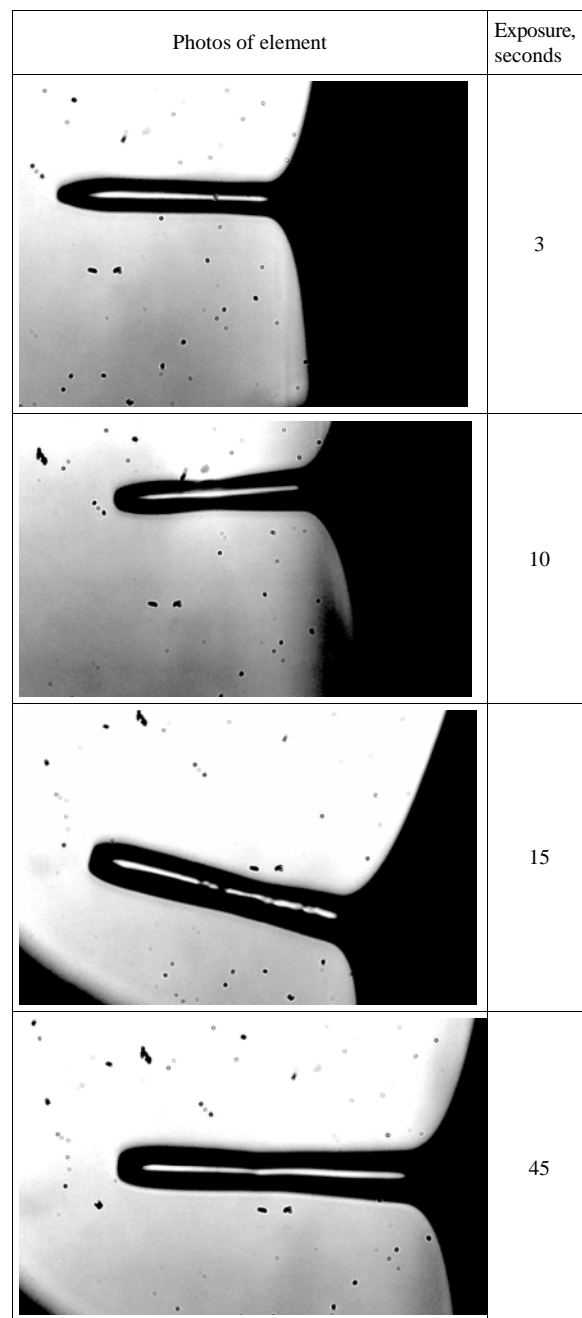
Figure 10. Dependence the radius of curvature of element from exposure.

change monomer composition to increase its viscosity or add traps for oxygen.

Now we prepare series of monomers composition with increased viscosity and with addition of nanoparticles as possible traps for oxygen diffusion. First experiments show improvement of waveguide formation.

Results obtained with these new UV-curable nanocomposite materials will be subject of next publication.

4. CONCLUSIONS

In this work the processes of microelement self-writing by photopolymerization of composition drop deposited at the top of the optical fiber by laser radiation coming from the fiber are analyzed. Experimental investigation of focusing light by obtained microlenses was made, this study shows possibility of coupling microlens preparation with focal length of about 400 um.

It was shown that the observed loss of light in the microlenses formed by this method are determined by difference of diameters of self-organized light concentrator and fiber core, the losses directly in the microelement almost are not.

REFERENCES

[1] Veiko, V.P., Berezin, S.D. and Chuiko, V.A. (1997) Laser technlogies for producing fiber-optical components. *Bulletin of the Russian Academy of Sciences-Physics*, **61(8)**, 1627-1631.

[2] Yang, Y., Lee, J., Reichard, K., Ruffin, P. and Liang, F. (2005) Fabrication and implementation of a multi-to-single mode converter based on a tapered multimode fiber. *Optic Communications*, **249(1-3)**, 129-137.

[3] Schiapelli, A., Kumar, R., Prasciolu, M., Cojoc, D. and Cabrini, S. (2004) Efficient fiber-to-waveguide coupling by a lens on the end of the optical fiber fabricated by focused ion beam milling. *Microelectronic Engineering*, **73-74**(1), 397-404.

[4] Hocinea, M., Bachelotb, R., Ecoffetc, C., Fressengeasa, N., Royerb, P. and Kugel, G. (2002) End-of-fiber polymer tip: Manufacturing and modeling. *Syhthetic Metals*, **127(1-3)**, 313-318.

[5] Barchelot, R., Ecoffet, C., Deloiel, D. and Royer, P. (2001) Integration of micrometer-sized polymer elements at the end of optical fibers by free-radical photopolymerization. *Applied Optics*, **40(32)**, 5860-5871.

[6] Plekhanov, A.I. and Shelkovnikov, V.V. (2006) Optical fibers with photopolymeric microlenses in the top. *Nanotechnologies in Russia*, **1(1-2)**, 240-244.

[7] Fokina, M. (2007) Optical surface making by UV-curing of monomeric compositions in near field of coherent light source. *Molecular Crystals and Liquid Crystals*, **468**, 385-394.

[8] Fokina, M.I., Burunkova, J.E. and Denisuk, I.Y. (2007) Influence of photoactive additive on growth of polymer microelements on the top of optical fiber. *SPIE Paper Number*, **6732**, 673215.

[9] Fokina, M.I., Kaporskiy, L.N. and Denisyuk, I.Y. (2008) Nature of microelements self writing in fiber tips in UV-Curable composites. *Molecular Crystals and Liquid Crystals*, **497**, 236-240.

[10] Andrzejewska, E. (2001) Photopolymerization kinetics of multifunctional monomers. *Progress in Polymer Science*, **26(4)**, 605-665.

Self-repairing material systems—a dream or a reality?

Hartmut Fischer[1,2]

[1]TNO Science and Industry, Eindhoven, The Netherlands;
[2]CSIRO Material Science and Engineering, Clayton South, Australia; hartmut.fischer@tno.nl

ABSTRACT

Currently, most industrial materials rely entirely on passive protection mechanisms; such mechanisms are readily applicable and universal for many different materials systems. However, they will always stay passive, and therefore their lifetime and functionality is limited and related to the amount of protective additives and the intensity of their consumption. Therefore, better, and preferentially active process for the protection/repair of damaged materials—self-repairing-processes—were developed and need to be developed further. Although it sounds futuristic or like a fiction in the modern, trendy times, which in many ways affects also directions of research; self healing of material systems exists already for a long time in all sorts of systems of materials or functionalities. The aim of this work is to go beyond the scope of a classical review the ones published recently in this field which almost entirely focused only onto polymeric systems. In this work, an analysis of the underlying functional and constructional principles of existing natural and synthetically self-healing systems spanning over a range of classes of materials is given leading to general rules and principles for the design of new and application tailored self-healing material systems.

Keywords: Self Healing; Systems; Sensors

1. INTRODUCTION

Self-healing is an intrinsic property of living organisms, enabling them to cope with all sorts of damage or injury they experience during their lifetime. This repair occurs with essentially no external intervention. Thus, wounds heal, broken bones heal, and even lost parts of living bodies (lizard tails etc.) can be replaced in some cases. Some natural self-healing composite systems such as bones go beyond simple healing to the extent that they remodel themselves continuously. Damaged material is removed and replaced by new material and over-designed material is also removed and structures under stress are enhanced by additional material. To enable this process, specific cells entrapped in the bone tissues act as strain sensors and feel large deformations. Subsequently, signals are sent to cells responsible for removing or forming material (bone) [1].

In order to deal with the phenomenon and the connected principles of self-healing in general, and even further to design and construct artificial self-healing functionalities for systems and devices, it is important to understand the nature and the consequences of damage and of degradation processes first.

Damage in general terms can be described as changes introduced to a system that affect its function and/or performance. That means that damage is not meaningful without a comparison of two different states of the system in question, one of which is assumed to be the initial (and often un-damaged) state. The term damage does not necessarily imply a total loss of system functionality, but rather a departure in level of system operation from optimal. A fundamental challenge is the fact, that damage is typically a local phenomenon and may be therefore difficult to detect (in time) [2].

Most materials (systems) lose their integrity, their value, operation or usefulness over time due to degradation processes where defects grow and coalesce to cause component and finally system level damage (e.g. fatigue or corrosion damage accumulation). On a relatively short time scale, damage can also result from scheduled discrete events such as aircraft landing and from unscheduled discrete events such as an impact. As damage grows, it will reach a point where it affects the system operation to a level, which is not any longer acceptable for a user; this point is referred to failure.

The main causes of deterioration of materials may be summarised as:

1) Harmful materials, substances and agents such as oxygen, oxidizing agents, water, salts, poisons, active materials, and living bodies such as virus, bacteria, fungi,

insects, animals, human beings and others,

2) Factors from the surroundings such as heat, visible light, external mechanical force e.g. strong wind, radiation, pressure, rain, collapse of the adjacent structure, a sudden impact and others.

Such deterioration (or damage) are in general irreversible, they occur progressively and exponentially in time until a certain threshold is reached where either significantly high costs for repairs are necessary or a (fatal) failure is going to occur. Increased lifetime and reliability of materials systems and devices can be critical requirements in traffic, construction, information transfer, medicine, military, space missions as well as in ordinary daily life.

In order to prevent such detorioration the following response mechanisms are known:

PASSIVE (Built-in damage prevention): by protection agents, that are directly attacked by the deterioration and the concentration of the agent is directly related to the amount of protection and that provide no repairability and hence no memory of the inherent structure.

ACTIVE (Autonomous or self-repair): here the deterioration attacks directly atoms and molecules of the material itself instead of protection agents. The amount of repairing agents needed depends on the concentration of damaged sites and the accumulation of damage in time and at certain locations as well as on the repair rate; a transfer of material is needed and a memory of the original structure is preferable.

The pictures in **Figure 1** show schematically the described mechanisms applied to the case of polymers matrices as damaged material.

Currently, most industrial materials rely entirely on passive protection mechanisms; such mechanisms are readily applicable and universal for many different materials systems. However, they will always stay passive, and therefore their lifetime and functionality is limited and related to the amount of protective additives and the intensity of their consumption.

Therefore, better, and preferentially active processes for the protection/repair of damaged materials—self-repairing-processes—were developed and need to be developed further. Although it sounds futuristic or like a fiction in the modern, trendy times, which in many ways affects also directions of research; self healing of material systems exists already for a long time in all sorts of systems of materials or functionalities.

The aim of this work is to go beyond the scope of a classical review which almost entirely focused only onto polymeric systems like the ones published recently in this field [4-6]. In this work, an analysis of the underlying functional and constructional principles of existing natural and synthetically self-healing systems spanning over a range of classes of materials is given leading to general rules and principles for the design of new and application tailored self-healing material systems. Therefore, specific choices from the existing literature
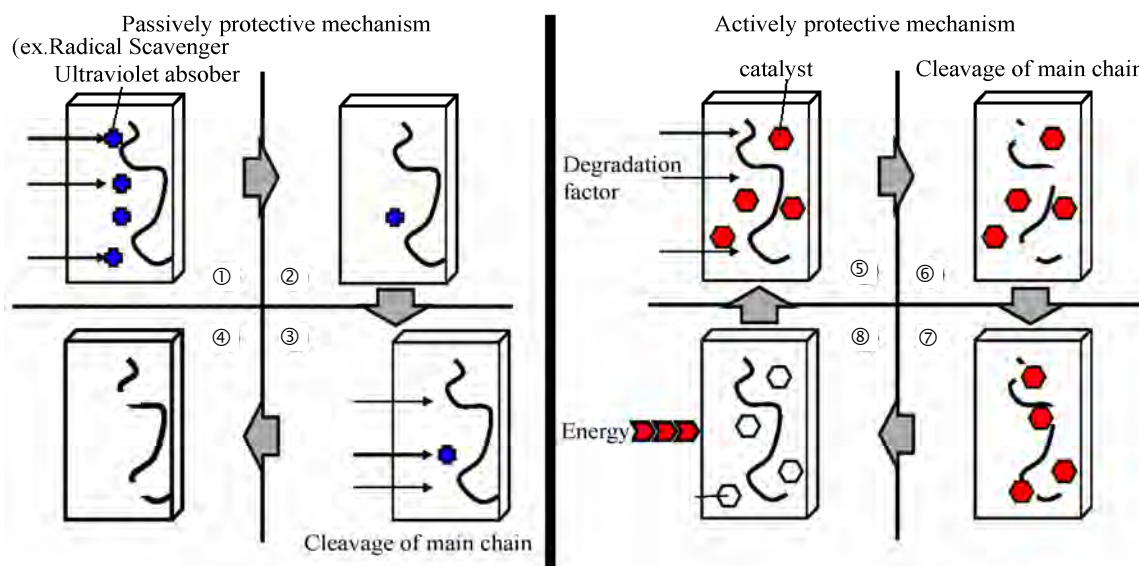
Figure 1. Passively protective mechanism versus active protective mechanism. Reference [3]: 1) Degradation factors are prevented from interacting with polymer chains, 2) Concentration of stabilizer deteriorates, 3) Degradation factors interact directly with polymer chains, 4) Degradation of polymeric chains, 5) Degradation factors directly interact with polymer chains and degradation occurs temporarily, 6) Cleavage of main chain, 7) Catalytic re-bonding reaction occurs, 8) Catalyst becomes reactivated.

have been made for this analysis, which either show new principles or contribute to this aim without repeating already existing systems in a similar or slightly different way.

In the next section, a discussion of the phenomenon of repair and especially self-repair is presented, together with the principal design features and requirements that enable a self-repair to take place.

Examples of self-repairing systems in material and life science starting with assisted (stimulated) repairing and of self repairing systems already known or currently under development are discussed in Section 3. This is followed by a discussion of the sensors and triggers employed or potentially employable in self-healing systems in Sections 4 and 5. Finally, conclusions are drawn with respect to requirements for the design of self-healing systems and working areas necessary to concentrate on are presented (in the Sections 6 and 7).

2. WHAT IS SELF REPAIR?

Repair itself is a process which can be initiated after damage on a local or global scale of a given functional system with the aim, to reduce the local or global level of damage and to extend or to renew the functionality and life-time of the damaged part, system or device.

Self-repair is then in principle an *autonomically* initiated response to damage or failure. In order to perform this repair, any self-repair system must be capable of 1) identifying and 2) repairing failures. If failure is classified as '*any occurrence, which results in the system deviating from its original task or not being any more able to fulfil its function*', what is than ultimately classified as '*repair*'? (Self) repair can be classified under two significant approaches:

Attributive repair and
Functional repair

Attributive repair are attempts to restore the attributes of the system to their original state, the full capacity of the system.

Functional repair are attempts to restore the function of the system. If full functionality cannot be restored, this strategy attempts to focus the remaining available resources to maximise the available functionality.

Attributive repair is the optimal solution. If the attempt to restore the system to its complete original condition fails, there is still significant benefit to be gained in most instances if the system continues to operate, even with reduced functionality.

Attributive self-repair is an intrinsic property of nature. **Figure 2** shows a schematic example of the steps in a self-repair cycle in nature, in this case bone failure due to fracture. This autonomic healing is initiated by the

(a)   (b)   (c)   (d)   (e)
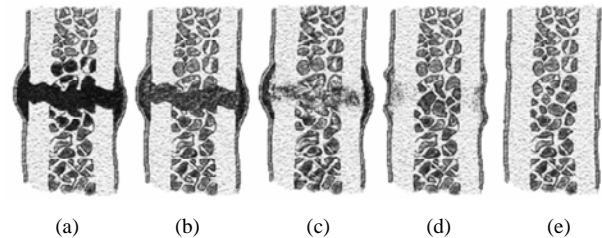
Figure 2. Schematic picture of the healing stages of bone: a) internal bleeding (sensor), forming of a fibroin cloth; b) unorganized fiber mesh develops (first step of (primitive) repair); c) calcinations of the fibrocartilage (second step of repair); d) calcification converted into fibrous bone (structural repair); e) transformation into lamellar bone (complete recovery of intrinsic structure and functionality) [7].

local damage of the vascular blood system. Healing a bone requires energy in the form of nutrition together with the delivery of cell material to the fracture site by the network of blood vessels; for healing a sufficient healing time must elapse. The healing process consists of multiple stages of deposition and assembly of material.

Mimicking nature is the ultimate goal for materials designers and developers.

There are essentially two design approaches to realize self-repairing systems:

1) a conventional design modifying existent design philosophies by incorporating intelligent techniques at the design stage to obtain a system with sufficient autonomous capabilities to initiate and effect a functional and in ideal cases an attributive repair.

2) a radically new design philosophy, where the system is designed in a cellular structure such that each cell contains a (genetic) code, which defines and determines its functionality. This term is called embryonics and it attempts to replicate the cellular structure of organisms in nature and their inherent self-replicating and thus self-healing capabilities resulting mostly in attributive repair.

Although both strategies will certainly lead to new self-repairing systems, the conventional process will be easier to implement in the short term.

Generally, self-repair processes in smart systems should not only replace any passive protection mechanism but should finally lead to structures, which are able to sense its internal state, to monitor the healthiness of the material/functionality/system/device at any time and at any location and respond in a manner that fulfils its functional requirements based on the gained information—sensing/detection, diagnosis of failure and activating of repair!

In order to perform properly, a smart system must have incorporated (embedded or surface mounted) ac-

tuation and sensor elements which offer the capacity of health monitoring (to be able to diagnose, interpret and correct structural faults in situ as they occur) by measurement of physical quantities such as vibration, permeability, current flow, strain, acoustic emission, impedance, pH-changes, colour tracers, etc., that are informative with respect to the state of structural health. Methods and instruments are X-ray tomography, ultrasonic methods and eddy current methods and strain- gauges, optical fibres, piezos and in general "smart tagged" composites.

Specifically, information relating to the severity, significance and location of damage is required. Therefore, a detection of:

1) Damage occurrence,

2) Damage location,

3) Damage type

4) Damage force magnitude and consequently

5) The remaining lifetime of the structure is necessary for maintaining the functionality of the material/structure/device. The information obtained has to be fed into the recovery cycle as sketched in **Figure 3**.

The interpretation and operational evaluation of the obtained data may include on top of the data acquisition a normalisation and filtering process, a feature selection and information condensation and finally a statistical model development for feature discrimination. This diagnosis will lead to an eventual initiation of the repair action.

Finally, to perform a repair action, mobile parts are needed to be transported to the location of the damage. This can be realised using a liquid either locally available or available via a vascular network system like the blood system in living organisms but also a transport via the gas phase is possible, in case material for the repair action is needed.

Self-healing or self-repair can therefore in summary be defined as "the ability to substantially return to an initial, proper operating state or condition prior exposure to a dynamic environment by making the necessary adjustments to restore to normality and/or the ability to resist the formation of irregularities and/or defects". It is a much more effective damage management decreasing damage level during certain stages of life time than passive prevention, since it is only applied in cases, times and locations of real need—damage which jeopardizes the functionality of a given system. Ideally, a self-healing system will therefore display an unlimited lifetime since the rate of damage formation is negative or zero.
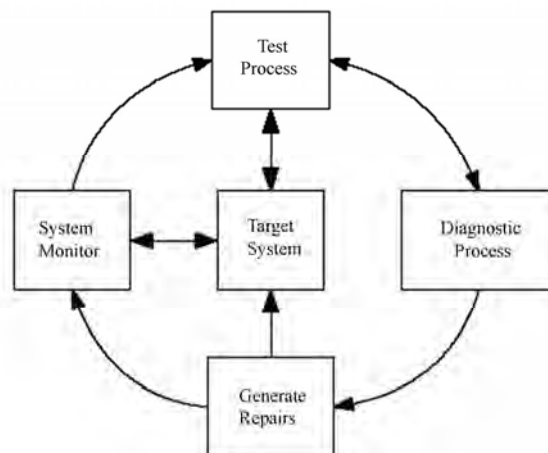
Figure 3. Health monitoring and repair cycle for an active smart self-repairing system [8]. The system monitor must be able to analyse system performance against predefined performance benchmarks in order to continuously verify correct operation of the process. The testing process also must have bi-directional communication to activate specific test sequences and receive results. This process should exploit any built -in self-test ability, and the testing results are forwarded to the diagnostic process. Automating the fault diagnosis process inherently demands the application of intelligent techniques. Finally, the self-repair process must be able to affect a repair based on the reduction in resources available, following isolation of the faulty components. If the original level of performance cannot be restored, the monitoring system must be modified to reflect the changes in system characteristics. This feature demands an optimisation capability. Reprinted from Engineering Applications of Artificial Intelligence, Self-repair of embedded systems, 17, E. A. Coyle, L. P. Maguire, T. M. McGinnity, 1-9, Copyright (2004), with permission from Elsevier.

3. EXAMPLES OF SELF REPAIRING SYSTEMS IN MATERIAL AND LIFE SCIENCE

In this section a number of existing self-repair systems is critically analysed with respect to its design, functional units/modules and their action/performance.

Within all classes of materials, the self-repair potential of polymers is probably the largest of all materials, since the polymeric nature offers more possibilities of developing and displaying molecular mobility than any other material. However, and as discussed below, this does not exclude other materials from a participation in functional self-healing systems.

The different options for the design of the repair action of a polymeric based system connected with examples of how this can be realized are illustrated in **Figure**

4 [9] and will be discussed in the following paragraphs.

Essentially a differentiation between nature-analogous true autonomous self-repairing systems and other systems, which may be only able to react onto damage and to make the necessary adjustments to restore itself to normality with human intervention, and may be therefore better called assisted healing systems, can be made. Assisted (local) healing can be achieved, e.g. by an increase of temperature, by irradiation or by other stimuli.

3.1. Thermally Stimulated Repair

A repair of accumulated damage may be triggered by thermal stimulation where the system allows the flow of material, wetting of the crack surfaces and gluing them together in a heating-cooling cycle.

This can be most easily achieved in a system containing polymeric chains, which during the transition from the glassy to the rubbery state experience a huge increase in mobility and hence the possibility to re-entangle after physical separation.

The model to explain the movement of a polymer molecule in a snake-like fashion inside a cross-linked polymeric gel, also known as the reptation model as proposed by de Gennes [10] implies also a possibility of polymeric chains to repair damage. Prager and Tirell [11], Jud and Kausch [12] and later Wool and O'Connor [13] used the same reptation model to determine the time required for healing caused by the inter-diffusion of

molecules between crack faces and thus re-gaining strength by annealing just above the T_g. Kim and Wool [14] predicted theoretically the recovery process as a function of healing time confirming existing experimentaldata [15]. Also, it has been shown that, if amorphous bulk samples of high-molecular-weight polystyrene (PS) were brought into contact with themselves in a lap-shear joint geometry *below* the bulk glass transition temperature, an increase in lap-shear strength and fracture occurred [16,17]. This can be attributed to the *time–temperature shift of the glass transition*, as well as to the possible enhanced surface molecular mobility of polymer chains leading to a lower T_g at free polymer surfaces compared to the bulk T_g which enables inter-diffusion of chains and self-healing even below T_g! At the present time, a decrease in density and a decrease in the entanglement density close to the polymer surface can be considered as the factors contributing to the increased molecular mobility at polymeric surfaces in comparison with that in the bulk [18]. In addition to these factors, a "jump" in the conformational entropy of the chain segments located at the surface (these segments have a decreased entropy imposed by the polymer-air interface [19] upon the contact of the surfaces) may be considered as one of the driving forces of inter-diffusion across the interface.

In principle, self-repairing polymers can therefore be realized essentially attributed to molecular inter-diffusion. Polymer networks with dangling chains can there-
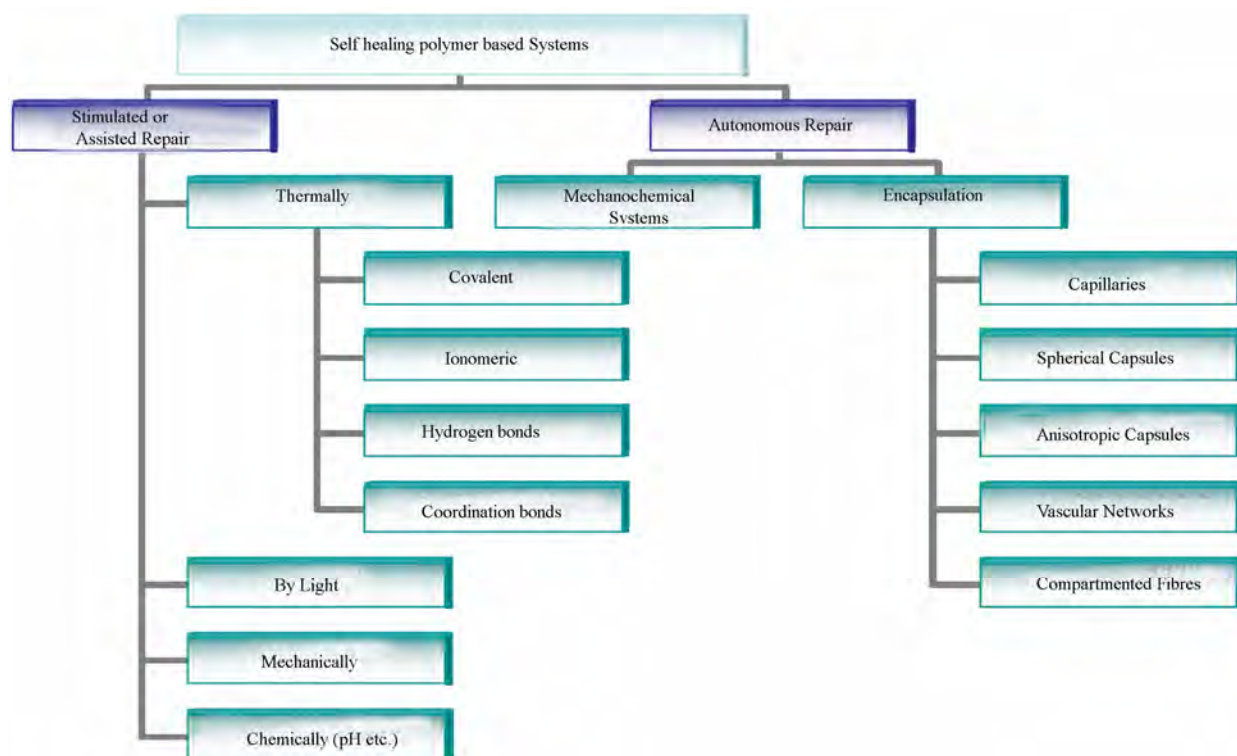

Figure 4. Organization of self-healing polymer based material systems according to the different principles employed adapted from [9].

fore be employed to heal cleavages at room temperature without any manual intervention [20].

However, self-repair needs time and rest. In a later study, the concept of re-entanglement of polymeric chains by reptation has been applied in thermoset composite materials where a linear thermoplastic polymer material was inserted into an epoxy matrix leading to a recovery of up 70% of the fracture toughness [21]. In this case as in the previous cases, multiple repairs are possible [22].

Alternatively, Zako and Tanako embedded small grain-particle adhesives in a glass epoxy composite laminate [23] an Meure, Wu and Furman polyethylene-co-methacrylic acid particles in an epoxy resin [24] to act as repair agents. The 50 micron sized particles consisted of thermosetting type epoxy; the matrix was a cold-setting epoxy. Damage can be repaired by the particles acting as repairing actuator when melted by heat. A similar mechanism can be used for the thermally stimulated self-repair of glass-ceramic composites, here heals the flow of the viscoelastic glass matrix at higher temperatures aging induced micro-voids in the composite material [25].

A very efficient and fast assisted repairing system by external stimulation consist just of one material capable of fulfilling all functions (structural properties, sensor and providing of mobility) by reversible formation of covalent or non-covalent bonds (ionic or H-bonds). Thermally controlled covalent bond formation is already long known in organic chemistry and may be applied to the formation of linear polymers as well as to the formation of polymer networks. Besides thermally reversible urea [26], alkoxyamine units incorporated in the main chain [27], nitroso-dimerisation and ester formation under presence of cyclic anhydrides [28], the (4 + 2) Diels-Alder reaction is by far the most important reaction. It was already discovered in 1928 [29] and honoured with the Nobel Prize in 1950 and generally considered the "Mona Lisa" of reactions in organic chemistry since it requires very little energy for the formation of a covalently connected ring-structure. This reaction enables step polymerizations and cross-linking reactions together with a thermally reversibility and is therefore ideally

suited for thermally stimulated polymer repair and potentially, recycling. Mostly, but not exclusively, the reaction between furane and maleimide derivatives is used for the generation of a thermally reversible bond. This has been applied already in 1969 for the synthesis of reversibly cross-linked networks, which yielded a tough rubbery film at 100ºC and returned to a re-mouldable polymer at 140ºC [30]. Subsequently, this principle has been further developed and the suitability of the system for self-healing bulk materials demonstrated [31-33]. These thermally reversible bond (cross-link) formations leading to self-healing properties upon thermal stimulation using the Diels-Alder reaction (see **Scheme 1**) can be used in application areas like coating systems [34].

Using this concept, powder coatings can be applied in their cross-linked state, which has distinct advantages with respect to their storage stability. When heated above the threshold temperature flow should be sufficient to enable proper film formation. As soon as the surface is of sufficient quality, cross-linking can be started—simply by cooling down! In a fully cross-linked state of a powder coating system, *i.e.*, below a certain threshold temperature, the coating will exhibit its essential properties with respect to mechanical strength, etc., but in its (partly) de-cross-linked state, above the threshold temperature, it will show a certain level of plasticity and flow. This plasticity will decrease problems in the area of film formation of powder coatings, will enable repair of the coating using their self-healing properties (see **Figure 5**).
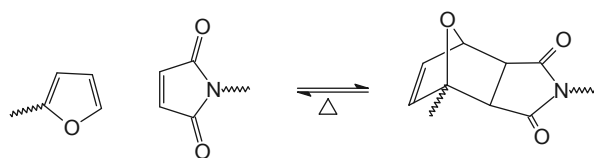
Scheme 1. Schematic representation of the Diels-Alder reaction used for thermally stimulated repair.

(a)   (b)   (c)   (d)   (e)
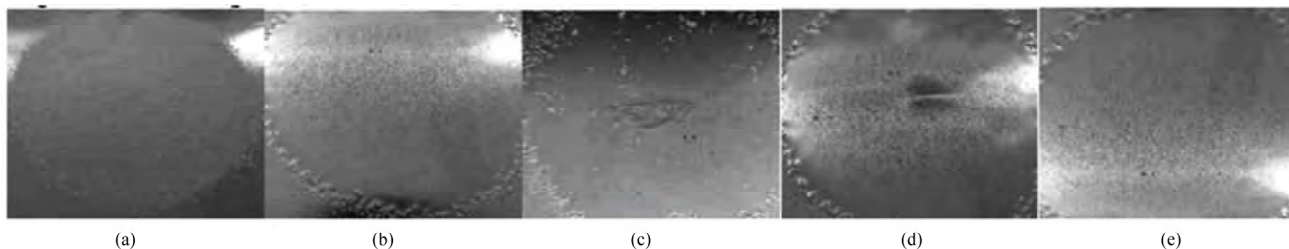
Figure 5. Visualisation of the self-healing of a cross-linked powder coating based on the acrylate copolymers: a) crosslinked powder, b) molten powder, c) damaged coating, d) re-flow, e) repaired coating [34], scale bar = 5 mm.

Besides application in coatings [35-38], reversibly cross-linkable materials are of interest for several areas of applications including thermally reversible bonding [39], thermally reversible solubility of polymers [40], processes connected with the recycling of plastics [37], encapsulates which open at elevated temperatures, reversible data storage medium [41] and also as matrix material in composites [42,43]. Here, polymeric materials with dicyclopentadiene units in the polymer backbone were used as a matrix for re-mending composites reinforced with graphite fibers [42]. The graphite fibers are used as electrical conductors to provide the necessary heat to the polymer. Microcracks, introduced by bending the substrate were healed by applying electric currents. Alternatively, arrays of conductive, electromagnetic scattering elements such as copper wires and coils were incorporated together with reinforcing fibres into a matrix consisting of a thermally reversible crosslinked networked base on a retro-Diels-Alder mechanism [43]. Since the wires are uniformly distributed within the matrix they can be used to heat the composite quick and uniformly by absorption of electromagnetic radiation. Furthermore, the reinforcing fibres are also contributing to the healing mechanisms, since they display a negative coefficient of thermal expansion (Kevlar: –2 to –6 ppm/K) and ensure therefore a mechanical closure of cracks while raising the temperature and increasing the healing efficiency in such a way to a great deal.

In a similar way, embedded shape-memory alloy wires [44] as well as a syntactic shape memory polystyrene foam [45] have been used to improve the performance of an existing self healing system. The improvement in performance due to crack closure enables multiple self-healing actions and increases crack fill factors during the repair action.

Non-covalently bonded polymeric systems are also known to heal upon thermal treatment. For example a supramolecular network can be established by thermally reversible H-bonds leading to rearrangements of the molecules in the non-bonded, heated state and reformation of the network in the "cold" state [46,47].

A reversible formation of ionomeric "cross-links"—clusters, which are formed by phase separation of the charged parts of macromolecules from the neutral chain segments can be used also as a self-repair mechanism being repeatable many times depending primarily on the stability of the polymer. Although it is not an autonomic process, it is activated when thermal energy is transferred to the polymer. During high-speed impact, energy is absorbed which is elastically stored and dissipated as heat. This increases the local temperature of the impacted polymer above the melting point (disrupting the physical cross-links) while having little effect upon the

temperature of the surrounding matrix. The ionic domains persist in the melt so that the polymer can be elongated to high levels of strain and rebound elastically when the stored energy is released at failure. The level of stretching enables the polymer to seal the cavity as it returns to its original position, but it is the viscoelastic properties and the capacity of physical cross-links to reform that determines the final level and strength of healing. The structural integrity of the polymer provides sufficient strength in the melt to prevent other deleterious effects from polymer flow [48,49].

3.2. Non-Thermal Stimulation of Self Repair

In a similar manner to the retro-Diels-Alder compounds, reversible cross-links can be established by photo induced cross-linking, which can be reversed by irradiation with a different wavelength to heal cracks, such as with cinnamic acid derivatives [50].

A covalently cross-linked network containing ally sulfides is able to undergo photomediated, reversible cleavage of its backbone to allow chain rearrangement for rapid stress relief at ambient conditions without mechanical property degradation [51]. The key to this reversible backbone cleavage is addition-fragmentation chain transfer. A reaction diffusion of radicals through the cross-linked matrix occurs initially by reaction of a radical with an in-chain functionality, forming an intermediate, which in turn fragments, reforming the initial functionality and radical. This addition-fragmentation process alters the topology of the network, but the polymer chemistry and network connectivity remain unchanged.

Alternatively, also an electrical current run through a conductive material system may be used to assist healing [52]. By imparting conductive properties into these materials, one may obtain 'real-time' status of a material's structural integrity through electric feedback mechanisms. This feature could lead to new approaches for detecting and quantifying microcracks which further could lead to materials capable of recording their stress/load histories. Other possibilities include using electric fields or currents as healing function. Upon the formation of a microcrack, the total number of electron percolation pathways within the material should decrease. As a result, its inherent electrical resistance should increase accordingly. If the material is integrated into a circuit, the drop in conductivity could be used to trigger a simultaneous increase in the applied electric field. Considering that the microcrack is the source of the increased resistance, this voltage bias should result in the generation of heat localized at the microcrack. By harnessing the generated thermal energy to overcome kinetic barriers, the system may be electrically driven

back to its original (*i.e.* a low resistance/high-current) state. This has been shown using N-heterocyclic carbines and transition metals [52].

It is well known that "crack healing" of polymers is observed via stimulation using a specific solvent. This phenomenon is called "solvent healing". In this healing process, the solvent is applied onto the fractured polymer until healing has occurred and then removed. The observed crack healing is a superposition of two different mechanisms: firstly, the formation of a close contact of the crack surfaces initiated by internal compression induced by surface swelling, and secondly, the self-diffusion of polymer chains across the interface forming the physical links (entanglements) between polymer chains coming from different sides of the interface promoted by the action of the solvent lowering locally the T_g [53,54]. This concept can also be used for a built-in self-healing system, as described below.

3.3. Synthetically Designed Autonomously Self-Repairing Systems

3.3.1. Ceramic Systems

An existing self-healing material or system can be found in the layers applied in barrier systems (liners) to ensure security of deposits of dangerous waste. Here, geo-synthetic clay liners (GCLs), which contain natural sodium bentonite encapsulated between geo-textile components, are the sealing elements [55]. Desiccation cracks, which cause a significant increase of the permeability, can be repaired by the self-sealing properties of calcium and sodium bentonite.

Alternatively, self-healing sealing elements based on the principle that two or more parent materials (for example pozzolanic material and lime containing material)

placed in vertical or horizontal layers, are described. These materials will react at their interfaces to form insoluble, barrier reaction products and heal themselves after being fractured (see **Figure 6** [56]).

Curiously, the same strategy has been operating in the construction for centuries. Many ancient Roman constructions made from limestone survived only because of the self-healing capacity of limestone in interaction with moisture/water. The phenomenon of self-healing in concrete has been known for many years [57-62]. Cracks in reinforced concrete are unavoidable and the corrosion of reinforcing steel due to de-icing salts or sea water is a major course of deterioration of reinforced concrete structures while disrupting the naturally formed corrosion protective passivation film. It has been observed that some cracks in old concrete structures are lined with white crystalline material suggesting the ability of concrete to self-seal the cracks with chemical products ($CaCO_3$), most likely with the aid of rainwater and carbon dioxide (see **Figure 7**). The healing of cement results in the voids being filled with hydration products which have a bulk volume approximately 2.1 times the original volume [63], an effect which is discussed below. However, efficient self-healing occurs only for cracks not exceeding a certain width (ca 135 microns) [64].

Unfortunately, this mechanism not always work in normal concrete because the width of the tensile cracks cannot be easily controlled or tuned. Localized fracture leads to continued increases in crack width under decreasing tensile load, and rapidly exhausts the amount of chemicals available for crack sealing and composite re-healing. Thus, it is critical that the tensile crack width is controlled and must be limited to a few tens of microns. Again, the success of the repair action depends

(a)	(b)
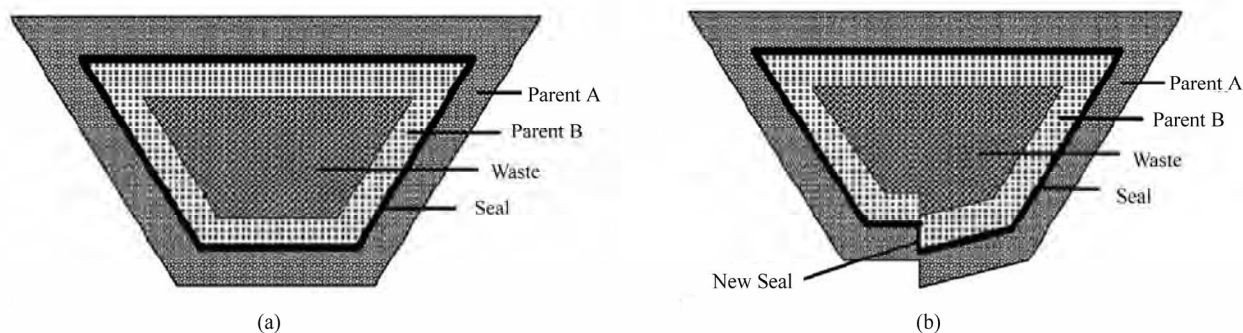
Figure 6. Schematic illustration of the self-sealing/self-healing feature of a pozzolanic and lime containing barrier material system: a) before fracture; b) after fracture. Reprinted from Waste Management, Laboratory development and field demonstration of self-sealing/self-healing landfill liner, 25, C. Shi, R. Booth, 231-238, Copyright (2005), with permission from Elsevier.

strongly on the damage degree accumulated. When the damage degree is less than the threshold, the self-healing ratio of concrete is increased with the increase in damage degree; once the damage degree exceeds the threshold, the self-healing ratio is decreased with the increase in damage degree [65].

In recent years, fiber-reinforced cement-based composites optimized for ultra high tensile ductility with a minimized amount of fibres have been designed based on micromechanics design tools [66]. Such materials, defined as Engineered Cementitious Composites (ECC), display "plastically yield" under excessive loading through controlled micro-cracking while suppressing brittle fracture localization and thus enabling self-repair actions.

The potential of calcite-precipitating bacteria for concrete or limestone surface remediation or durability improvement has only recently been investigated and is a possible alternative to repair cracks in concrete [67].

In the case of composite materials, it is also possible to use an inorganic phase to perform the self-repairing process, as demonstrated in the case of decalcification-hydration reactions of hydraulic (CA) fillers in poly-phenylenesulfide (PPS) coatings used in geothermal applications. The hydraulic fillers, which can heal and repair micro-sized cracks appearing on the surfaces of corrosion protection coatings, are embedded into the matrix material (PPS) [68]. The decalcification-hydration reactions of the $CaO\text{-}Al_2O_3$ and $CaO\text{-}2\,Al_2O_3$ reactants present and exposed in the cracks lead to the rapid growth of boehmite crystals, densely filling and sealing the cracks, while the calcite leaches out of cracks because of the formation of water-soluble calcium bicarbonate (see **Figure 8**).

Healing and repairing of micro-sized cracks generated on the surfaces of the PPS coating was observed after exposure of the cleaved coatings to a simulated geothermal environment (200°C, CO_2-loaded brine). During exposure for 24 h block-like boehmite crystals (ca. 4 μm in size) filled and sealed the open cracks. This was reflected in an increase in pore resistance up to two orders of its magnitude compared with that of cleaved coatings without fillers [68].

3.3.2. Viscoelastic Recovery and Healing

Micro-damage self-healing also exists in asphalt mixtures. After the removal of external load, two processes occur: the first is viscoelastic recovery in the bulk of the material and the second is healing in a fracture process zone [69]. Viscoelastic recovery occurs in the bulk of the material only after a stress or strain is induced which is sufficiently large to generate damage. The phenomenological difference between viscoelastic recovery and

healing is that the former is due to the rearrangement of molecules within the bulk of the material, whereas the latter is due to the wetting and inter-diffusion of material between the two faces of a micro-crack to achieve properties of the original material. The three primary steps in the healing process are:

1) Wetting of the two faces of a micro-crack

2) Diffusion of molecules from one face to the other

3) Randomization of the diffused molecules to reach the level of strength of the original material

Again, especially rest periods introduced at certain damage levels increase the fatigue life of asphalt binders [69].

A very recent example of self-healing via reformation of weak, fracture interrupted bonds has been demonstrated on a supramolecular rubber employing molecules that associate together to form both chains and cross-links via hydrogen bonds [70] (see **Figure 9**).

By mixing ditopic and multitopic molecules, which are able to associate with more than two other molecules, a network could be formed. The system shows recoverable extensibility up to several hundred per cent and very little creep under load. In contrast to conventional cross-linked or thermo-reversible rubbers, these systems, when broken or cut, can be simply repaired by bringing together fractured surfaces in contact—an example of autonomous self-healing at room temperature. The process of breaking and healing can be repeated many
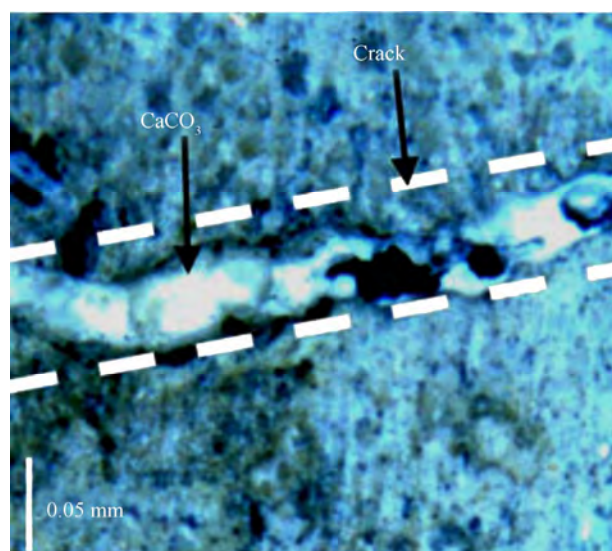

Figure 7. Crack blockage in mortar specimen by $CaCO_3$ after NaCl solution exposure, crack width = 49 microns. Reprinted from Cement and Concrete Research, Permeability and self-healing of cracked concrete as a function of temperature and crack width, 33, H.-W. Reinhardt, M. Jooss, 9131-9136, Copyright (2003), with permission from Elsevier.
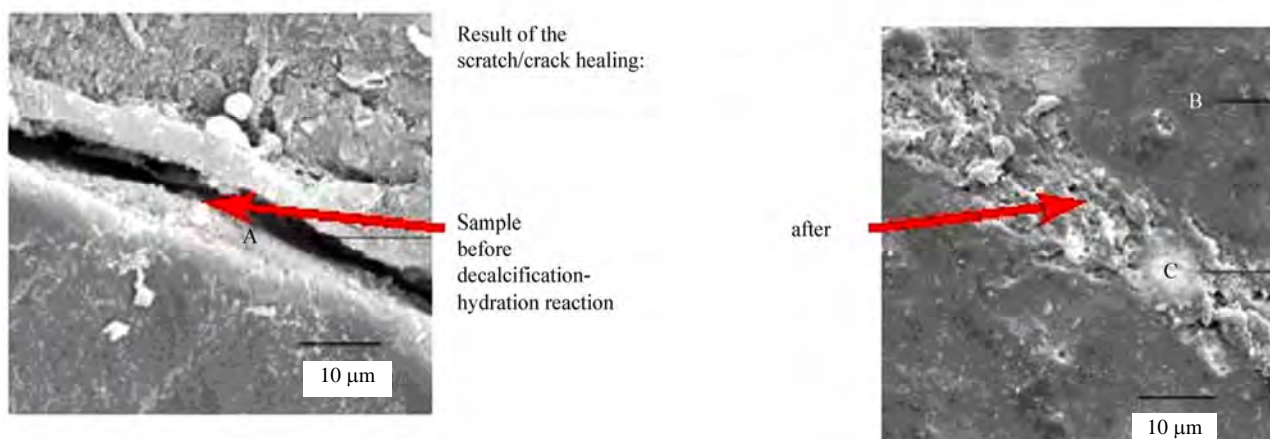
Figure 8. Self-repair action of a decalcification-hydration reaction on a polymer composite surface [68].
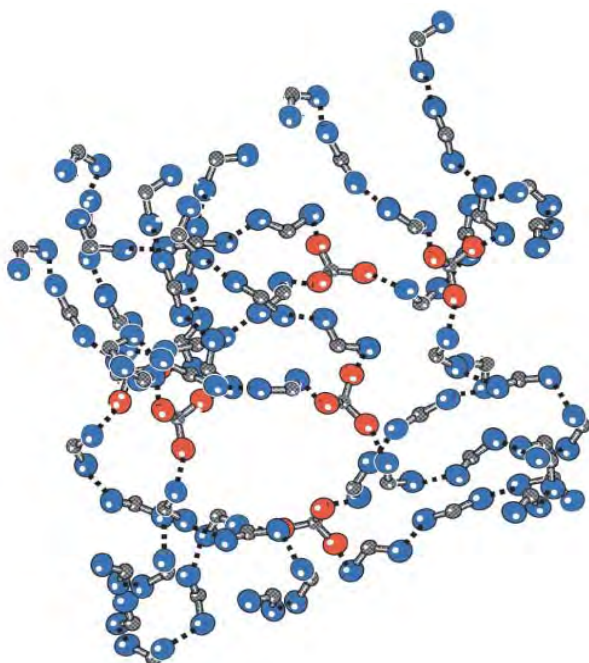
Figure 9. Schematic view of the Supramolecular reversible network formed by mixtures of ditopic (blue) and tritopic (red) molecules associated by directional H-bonds (represented by dotted lines) as employed for the self-healing rubber. Reprinted by permission from Macmillan Publishers Ltd: [Nature] (Self-healing and thermoreversible rubber from supramolecular assembly, P. Cordier , F. Tournilhac , C. Soulie-Ziakov, L. Leibler, 451, 977-980), copyright (2008).

times. However, the time needed to establish a contact of the fractured surfaces determines the healing efficiency. Longer healing times lead to better healing, but even when contact time is as short as fifteen minutes a repaired sample can be deformed up to about 200% without breaking.

In order to be self-mending, the supramolecular rubber has to be made from small molecules and the supramolecular associations have to be strong and long-lived so that at equilibrium, the fraction of non-associated groups in the network is low. However, the strength of the associations has to be lower than that of covalent bonds so that, when broken, many non-associated groups are present near the fracture surface. Self-healing is efficient because a large number of groups 'eager' to link is available. At shorter healing times, fewer bridges across the interface are formed and the elongation at break is lower. When the sample is not mended immediately after being broken, the number of non-associated groups available for healing progressively decreases as they find other partners for H-bonds and become unavailable for a re-formation of the entangled network.

3.3.3. Self-Healing by Phase Changes and Volume Expansion

The self-healing potential in metals and metal alloys is connected with a dynamic precipitation of atoms and the consequent potential to delay crack initiation and crack propagation as observed in Al alloys similar to a plasticity-induced crack closure. When a dislocation interacts with a precipitate, solute atoms will be transferred to the precipitate, causing Ostwald ripening, if their binding energy to the precipitate exceeds that to the dislocation. Conversely, solute atoms will be removed from the precipitate if their binding energy to the dislocation is greater. Dynamic precipitation tends to compensate for micro structural damage, with the result that a higher integrity structure is maintained for an extended lifetime [71]. Alternatively, the precipitation of dissolved atoms like B and N under formation of BN on creep cavity surfaces (in for example austenitic steel) leads to a self-healing of the creep cavitations together with an

increase in creep rupture strength and ductility [72].

Oxidative self-recovery of surface damaged ceramics and ceramic composites may also be a useful self-repair mechanism (**Figure 10**). Oxidation of NiAl/α-Al$_2$O$_3$ composites provides the metamorphic surface layers consisting of NiAl$_2$O$_4$ and Al$_2$O$_3$ with compressive stress to improve the mechanical properties [73]. The peculiarity of this material is the dominant formation of NiAl$_2$O$_4$ along with the grain boundary of the matrix Al$_2$O$_3$ by the reaction,

$$2NiAl + Al_2O_3 (boundary) + 5/2O_2 = 2NiAl_2O_4$$

The rapid diffusion of the reaction product through the grain boundary results in the repair of surface defects (see **Figure 10**).

This concept has been further developed for thermal barrier coatings with a composition of NiCrAlY, again with Al as reactive element. This enables a reaction with oxygen to form a protective barrier layer under volume expansion in response to damage due to thermal mismatch during thermal cycling. Here, an addition of 0.1-0.2% Zr leads to an optimisation of the self-repair process [74]. Similar concepts were reported for the systems ZrB$_2$/SiC [75], SiC/Al$_2$O$_3$ [76], SiC/Si$_3$N$_4$ [77], BN/SiC, B$_4$C, SiC/B$_4$C, MoSiC$_2$ containing ceramics and Ti$_3$AlC$_2$ [78], where the surface crack oxidation leads to an effec-

tive volume expansion and, thus, to a filling of the crack opening.

Volume-expanding phases are of course most suited to be applied in self-healing systems, since they offer the possibility to fill the empty crack volume completely and to re-generate the structural integrity of the system. This requires a material identically or similar in properties to the damaged matrix material. Examples include phase transition *tetragonal-monoclinic* (e.g. in ZrO$_2$) phase transitions, α–β–γ phase transitions as seen in sulphur, TRIP transformation, piezo-effects, curie-transitions and others which induce a volume change of 1-4%, sufficient to fill cracks and to perform a healing operation. Those changes are mostly triggered by a critical strain $\tilde{\sigma}$ or/and by temperature. More simply is the healing of zirconia and especially yttria-stabilized zirconia (YSZ) where an efficient damage recovery in large-scale molecular dynamics simulations has been observed [79]. Dynamic annealing is highly effective in zirconias during the first 5 ps of damage evolution, especially in and due to the presence of oxygen structural vacancies. The number of anion displacements in YSZ keeps increasing with time instead of reaching a steady value as in ZrO$_2$. This demonstrates the role played by structural vacancies in the migration of O^{2-}. Defect diffusion plays an importantrole in the dynamic recovery of radiation damage. Espe-
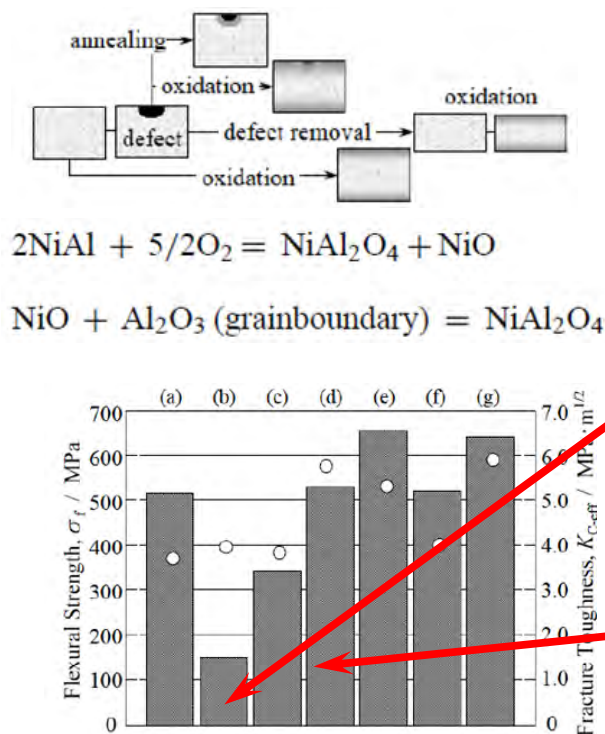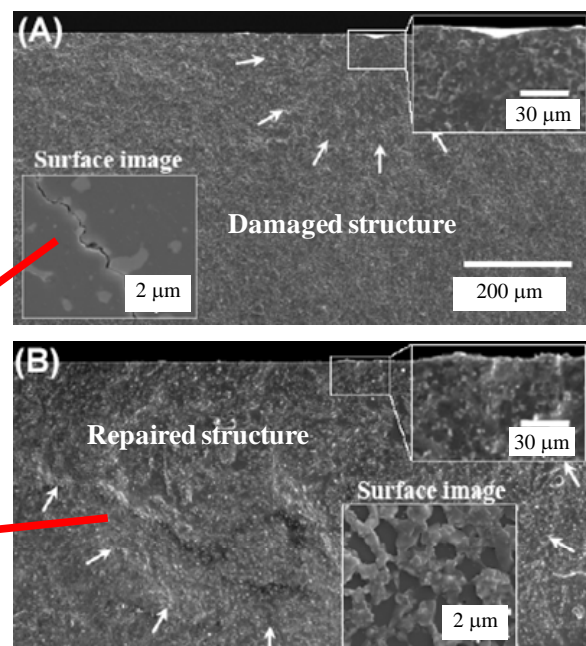
Figure 10. Crack healing of ceramics due to oxidative self-recovery of ceramics [73]. Flexural strength (a) without defect, (b) with defects, (c) annealed, (d) repaired, (e) removal of defect, (f) oxidized without defect, and (g) oxidized after removal and fracture surface of (A) with defects and (B) repaired materials, the symbol o corresponds to the right axis.

cially in YSZ, the anion interstitials almost completely annihilate with structural vacancies, resulting in no residual radiation-induced defects on the anion sublattice (see **Figure 11**).

This results in near-complete recovery of damage. Damage recovery on the cation sublattice is assisted by the anion sublattice recovery, which explains the remarkable radiation tolerance of stabilized zirconia.

If those concepts are not applicable, a possible reaction with components provided by the environment using transport via the gas phase might be an option for a self-repair action. This principle is especially useful in coatings where dimension constraints prevent the use of other options for self-repairing design (see below). Coatings should not only protect a surface from a possible damage and/or corrosion but should also provide additional properties like anti-reflection, gas barrier etc. However, if coatings are damaged and/or pinholes formed, serious damage could occur due to corrosion on and in the substrate. To fill such damage areas and/or pinholes and to restore the passive corrosion protection or other functionalities, the coating can be loaded with nanoparticles, which react upon volume expansion with moisture or oxygen. In a practical example, raw smectic clay has been used as the phase being able to absorb moisture under volume expansion [80]. In a later study, this concept has been developed further leading to a true recovery of damaged surfaces [81]. There, the option of healing surface scratches in multi layer coatings consisting of a polysiloxane film on top of a thin montmorillonite layer as expandable phase was studied (see **Figure 12**). Filling of cracks in the polymeric topcoat occurred primarily within the first two hours of exposure to moisture-saturated air and resulted in a good restoration of the surface flatness [81].

3.3.4. Mimicking Nature

Mimicking nature has resulted in a variety of self-healing systems. One of the first synthetically design systems developed, tested and used in ceramics (concrete) and subsequently in polymeric matrices compromising all three functionalities (damage sensor, healing mobile materials, structurally integer functioning system) are resin filled glass capillaries incorporated in the matrix material [82-90]. Upon damage or fracture, the glass capillaries act as a strain sensor, releasing the encapsulated adhesive components (epoxy and hardener, cyanoacrylate etc.) into the composite structure to perform the repair action while (partially) filling the crack. The damage can be sensed/visualized by adding a fluorescent dye to the components (see **Figure 13**); the capsules (glass capillaries) also serve as part of the (reinforcing) composite structure.

This 'bleeding composites' approach thus combines

damage detection with a high sensitivity due to the continuity of the hollow fibres and self-repair, however, also with two draw-backs: 1) they will release an excess of healing liquid since the volume of the compartments is often much larger than the damage volume and 2) they will display a tendency to clotting since the propagation of the repairing reaction of the stored agent within the hollow fibre can still occur thus preventing the chance of multiple repair.

Systems following a similar idea were developed for an application in thermosets (epoxy); the approach has been applied to other matrix materials as well [91-94].

Here, the resin containing containers are hollow polymeric capsules (see **Figures 14**,**15**).

The fragile capsules act as sensor and as reservoir of the resin. Upon fracture the released monomer reacts with the catalyst distributed within the matrix forming a cross-linked polymer network and repairing the damage.
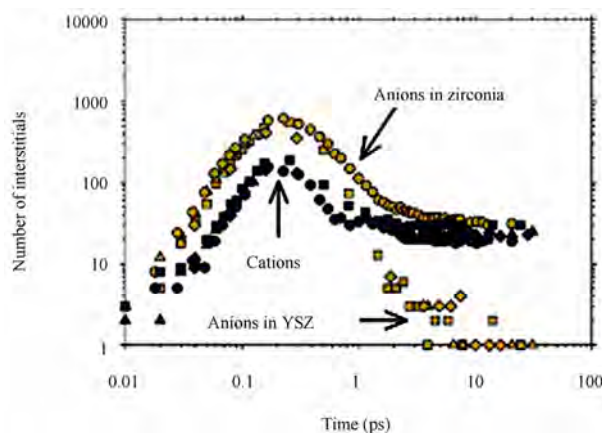

Figure 11. Evolution of the number of interstitials in YSZ and pure ZrO_2 following 30-keV Zr recoils. The numbers of cation and anion interstitials in ZrO_2 and YSZ peak at about 0.2 ps and then decline sharply. Subsequently, in YSZ, the anion interstitials almost completely annihilate with structural vacancies, resulting in no residual radiation-induced defects on the anion sublattice. The difference in anion sublattice damage between ZrO_2 and YSZ is due to the presence of structural vacancies in YSZ. (squares, triangles, and diamonds represent [001], [110], and [111] recoils, respectively) and pure ZrO_2 (circles) [79].
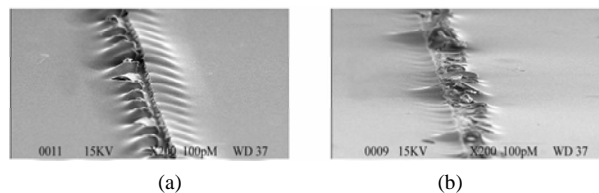

Figure 12. Crack-healing of multilayer coatings due to phase expansion upon moisture absorption before (a) and after 21 h of healing (b) in wet atmospheric conditions [81]. Scale bar = 10 microns.

The healing efficiency of this concept is high (see **Figure 16**) [95-97].

However, since a significant load of microcapsules is required to get efficient self-healing due to the small
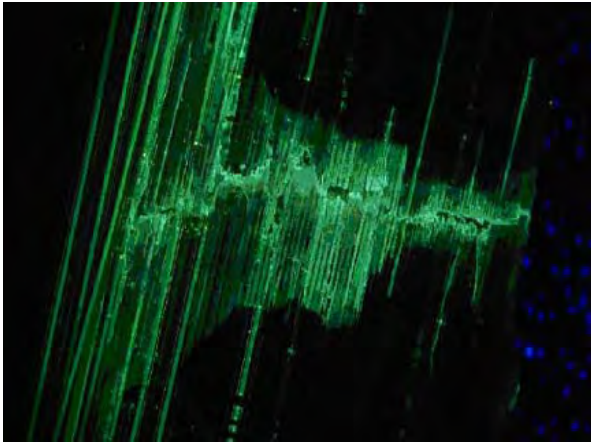

Figure 13. Fracture of a hybrid solid/hollow fibre reinforced plastic showing bleeding of UV fluorescent dye along crack paths(x 45 magnification) [88].
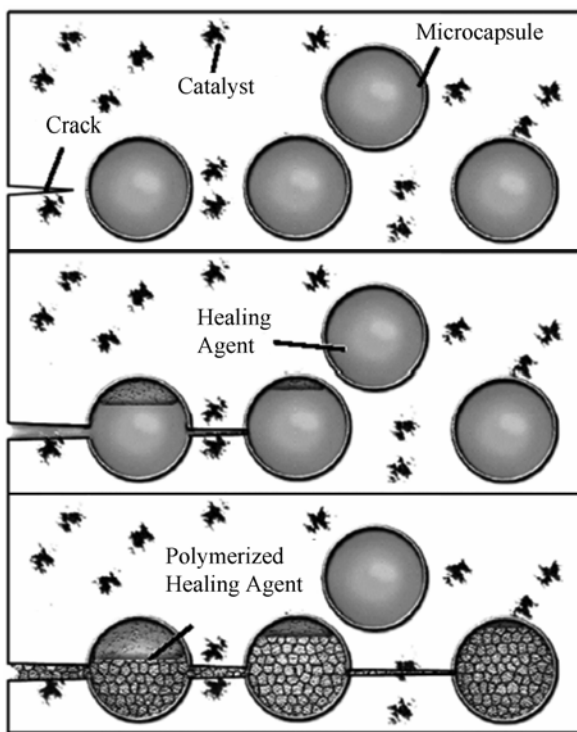
Figure 14. Schematic picture of the self-healing action of a in spherical capsules embedded resin upon damage/fracture of the matrix material. Reprinted by permission from Macmillan Publishers Ltd: [Nature] (Autonomic healing of polymer composites, S. R. White, N. R. Sottos, P. H. Geubelle, J. S. Moore, M. R. Kessler, 409, 794-797), copyright (2001).
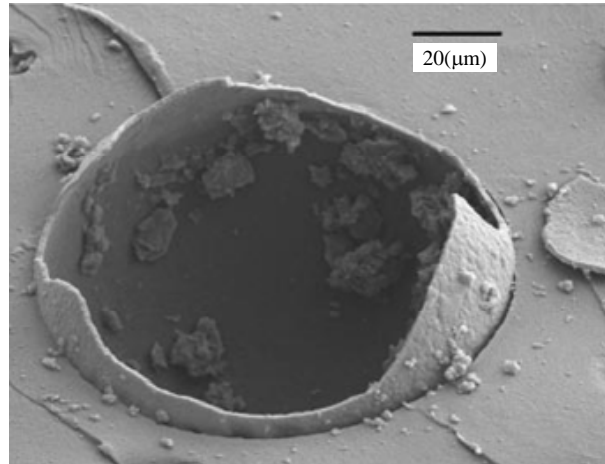
Figure 15. SEM picture of a broken capsule. Reprinted by permission from Macmillan Publishers Ltd: [Nature] (Autonomic healing of polymer composites, S. R. White, N. R. Sottos, P. H. Geubelle, J. S. Moore, M. R. Kessler, 409, 794-797), copyright (2001).

(a)

(b)
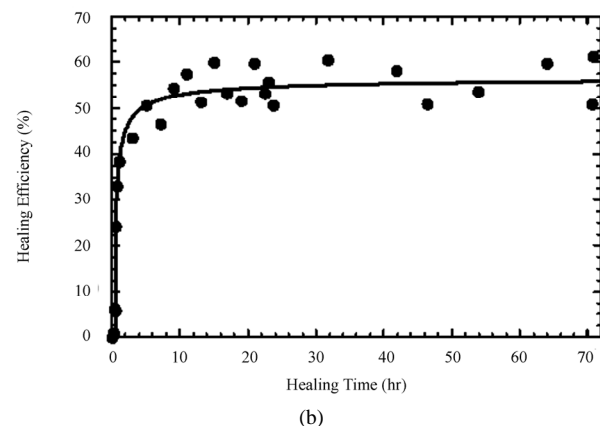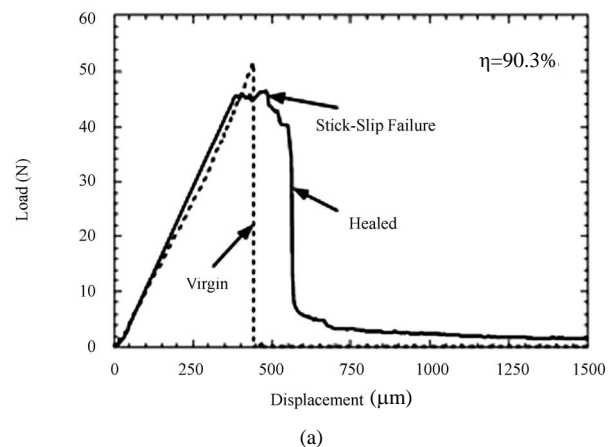
Figure 16. a) Healing efficiency of the capsule strategy in a single experiment and b) in time [95].

amount of liquid depleted upon fracture and the limited probability of fracture during damage, the mechanical

properties of the matrix material are substantially weakened and limit the application of this concept. Furthermore several material processing aspects are also not favourable. Anyway, these systems have been further developed and optimized for coating applications [98-101] since they offer an autonomic self-repair for anti-corrosion protective coatings.

The latest developments of autonomous systems combine the concept of the incorporation of a self-healing liquid with the increase in mobility of macromolecules via solvent stimulation [102-104]. Here, solvent-containing micro-capsules were either embedded in an epoxy matrix or in a matrix of thermoplastic polymers. In the case of the thermoset, the presence of the solvent increases the mobility in the system and healing efficiencies of up to 82% was observed due to molecular diffusion and reaction of residual functionality [102, 103]. The healing performance appears to be inversely related to cross-link density. Healing with epoxy-solvent microcapsules is superior to capsules that contain solvent alone (up to 120% healing efficiency), and data showing multiple healing events are reported for this system. In the case of the thermoplastic matrix, the mobility of the macromolecules increases due to the lowering of the glass transition temperature via solvent chain interactions leading to the possibility of re-entanglement formation and complete crack closure (see **Figure 17**) [104].

In order to combine the advantages of the two existing concepts for the storage of a self-healing liquid (the hollow fibre container and the spherical capsule concept), experiments have been carried out to develop anisotropic capsules [105]. Such particles offer a better probability of being fractured upon damage than spheres. Thus a substantial lower load of capsules (up to five times less) is needed for a realisation of self-healing properties and the initial mechanical properties of the system will be preserved [105]. On the other hand, they offer the same advantages with respect to processing and preparation as the spherical capsules compared to the hollow fibres.

Ultimately, a mimic of the blood vessel system capable of a repeated, autonomic repair of damaging events seems a perfect self-healing material system. Healing in such systems is accomplished by a vascular network system supplying the necessary components at the damage site. A vascular system permits a continuously and repeatable repair of all types of failure modes at any point in the structure since it renews the supply of the healing part of the system during the lifetime of the structure at any location and any time.

A skin structure exhibiting flexibility, self-healing and damage sensing is the simplest system realizing a network-like supply of an active self-healing liquid [106].

The skin is fabricated on a substrate of copper-clad polyimide sheets in a layer-by-layer technique using polyimide sheets and an ultraviolet (UV)-curable epoxy. The UV-curable epoxy is used as both a structural adhesive and as the self-healing fill material (see **Figure 18**). The skin structure is integrated with an array of inductor-capacitor (LC) circuits, where each circuit is characterized by a unique resonant frequency. If the skin is damaged, the UV-curable epoxy is released and is cured by ambient sunlight. Further, damage affects one or more of the LC circuits, altering its resonant frequency. An integrated antenna coil is used to detect and locate the damaged portion of the skin; so far tests indicated a good performance with respect to self-healing of the skin and fault isolation.

Other examples of such a system have been described by Toohey *et al*. [107,108] and by Williams *et al*. [109, 110]. Here, a 3-dimensional micro-vascular network system, either manufactured by a direct write assembly procedure using a fugitive ink or by connection of glass capillaries via risers has been embedded in an epoxy
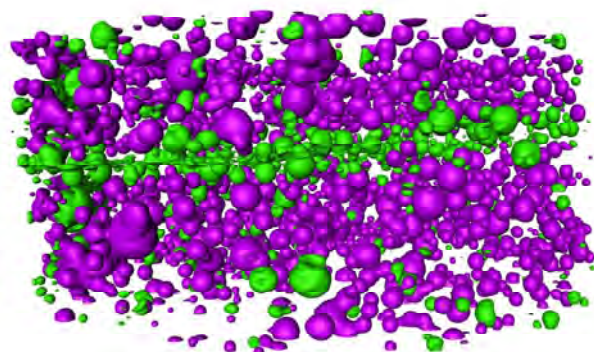
Figure 17. MRI tomogram of a healed thermoplastic containing solvent filled capsules. The green capsules are empty. The majority of the empty capsules are located at the fracture plane as intended, healing is obtained, and no empty space of the original fracture plain is observable [104].
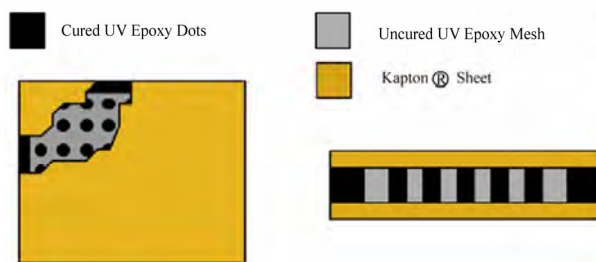
Figure 18. Basic diagram of self-healing skin, top view with cutaway and cross-section. Reprinted by permission from IOP Publishing Ltd: [Smart Mater. Struct.] (A flexible, self-healing sensor skin, J. A. Carlson *et al*, 15, N129), copyright (2006).

matrix system and tested upon bending. These systems show repeatedly crack healing upon damage.

Alternatively, 3D microvasular networks can be realized simply by loading the hollow micro-fibres of a free-standing paper manufactured by electro-spinning with a healing agent displaying a rapid reactivity, volatility and ability to propagate repair triggered e.g. by the influx of moisture [111]. The self-healing agent used is TiCl₄ blocking the pores of the hollow micro-fibres as well as sealing possible cracks by the formation of ceramic particles of TiO_2 after hydrolytic decomposition in contact with water vapour.

The natural blood vessel system works, however, in a slightly different way [112]. In this case, a temporary repair as response of a physical damage is achieved in the form of a clot that plugs the defect. During subsequent days steps to regenerate the missing parts are initiated. The healing of a skin wound is a complex process requiring the collaborative efforts of many different tissues and cell lineages. Inflammatory cells and then fibroblasts and capillaries invade the clot to form a contractile granulation tissue that draws the wound margins together; meanwhile, the cut epidermal edges migrate forward to cover the denuded wound surface. The formation of a clot then serves as a temporary shield protecting the denuded wound tissues and provides a provisional matrix over and through which cells can migrate during the repair process. The clot consists of platelets embedded in a mesh of crosslinked fibrin fibers derived by thrombin cleavage of fibrinogen, together with smaller amounts of plasma fibronectin, vitronectin, and thrombospondin.

An interesting analogy to the process uses nanoparticles dispersed in polymer films and shows in simulations and experiments a preferred coagulation of nanoparticles at areas of stress concentration similar to the clotting of blood platelets at zones of damage [113-116]. This is because the mobility of the filler particles at the length scales present in nanocomposites is controlled by the conformational entropy of polymer chains. Polymer chains close to nanoparticles are stretched and extended, which results in an entropy penalty. This decrease in polymer conformational entropy is greater than the decrease in nanoparticle translational entropy; thus, nanoparticle-polymer interactions are minimized by segregation of the nanoparticles in areas of stress concentration such as a crack tip. For particles comparable to the radius of gyration of the polymeric chain, the decrease in conformational entropy of the respective polymer sub-chains upon particle sequestration is dominant; the chains gain conformational entropy while repelling the particles because they do not have to stretch around particles [113-115]. The system can relieve the entropic cost of chain stretching by allowing the particles to self-assemble to the solid walls. In the presence of a notch, the nanoparticles are driven to localize in the notch. The driving force for this localization is a polymer-induced depletion attraction; the confined polymers in the melt gain conformational entropy by "pushing" the fillers to the surfaces and into the notch (**Figure 19**).

The time required for the particles to migrate to the notch is comparable to the time needed for the chains to move by approximately four radii of gyrations. The morphology obtained from the simulation allowed a determination of the mechanical properties of the nanocomposite-coated surface. The calculations show that the nanoparticle fillers significantly reduce the stress concentration at the notch tip relative to the case where the notched surface is just coated with a pure polymer layer (see **Figure 20**).

As a consequence, load transfer from the matrix to the agglomerated nanoparticles is predicted and the mechanical properties can recover to 75% of their original value [114]. The calculations on the crack tip opening displacement indicate that the presence of the nanocomposite in the notch would inhibit the system from undergoing further damage (crack propagation from this notch) when an external load is applied to the system. It is important to realize that some fractions of the polymer are also localized in this damaged region. If the macromolecules and the particles are chemically compatible, the chains provide cohesion between the fillers and the polymer coating.

The application of such nanocomposite coatings could thus constitute an important step in the production of components with defect-free surfaces. Upon appearance of a defect, the coating effectively senses its presence and then causes the repair of the damaged area.

In a practical example, nanoparticles are added to a high viscous liquid polymer that is sandwiched between two brittle, glassy layers (see schematically in **Figure 21**).

This architecture is common in multi-layer composites that are used in optical and anticorrosion coatings, mi-
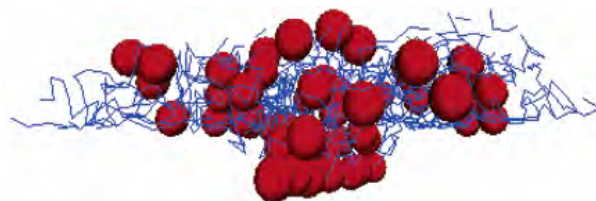

Figure 19. An instantaneous molecular configuration showing a surface notch filled with nanoparticles due to a depletion attraction between the particles and the surface. Particle beads are shown as spheres and polymer chains as lines [115].

(a)

(b)
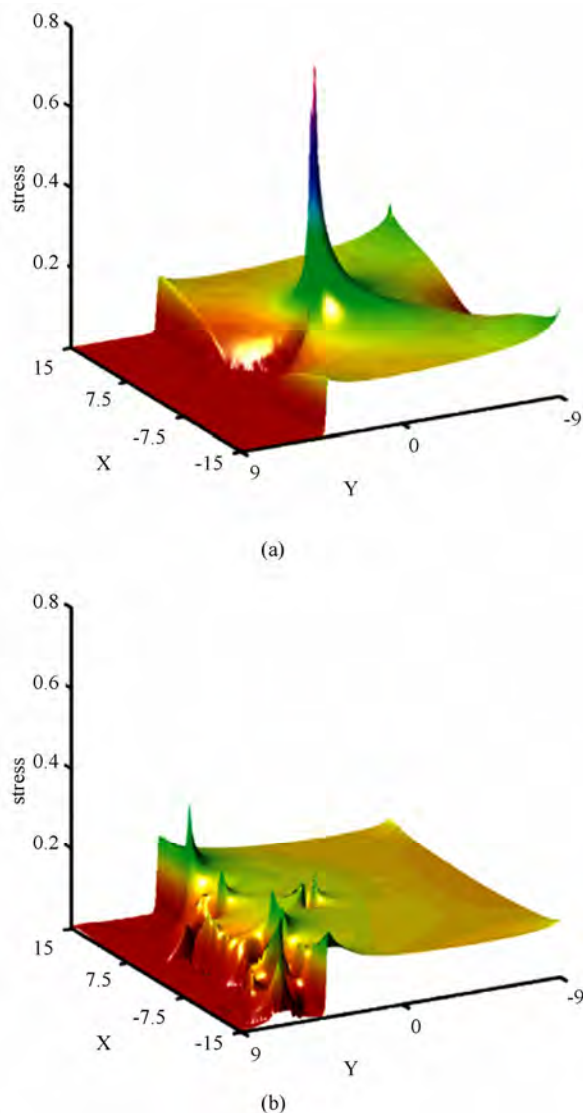
Figure 20. Results of the calculation of the stress distribution using a lattice-spring model for (a) a polymer coating not containing nanoparticles. The stress reaches a maximum at the notch tip. (b) The polymer coating contains nanoparticles and the stress at the notch tip is significantly reduced. The colour bar indicates the magnitude of the stress [114].

croelectronics packaging, and solid-state devices. Such films are susceptible to failure through the formation of cracks, which propagate vertically to the polymer layer. Since the polymer is fluid-like it expels the nanoparticles to the brittle surfaces, where some of the particles pack into the cracks, effectively mending the brittle surface. In the experimental study [117], the particles were fluorescent and could readily be visualized in the cracks (see **Figure 22**).

In this example, the polymers and particles provide the healing mechanism without any external intervention.
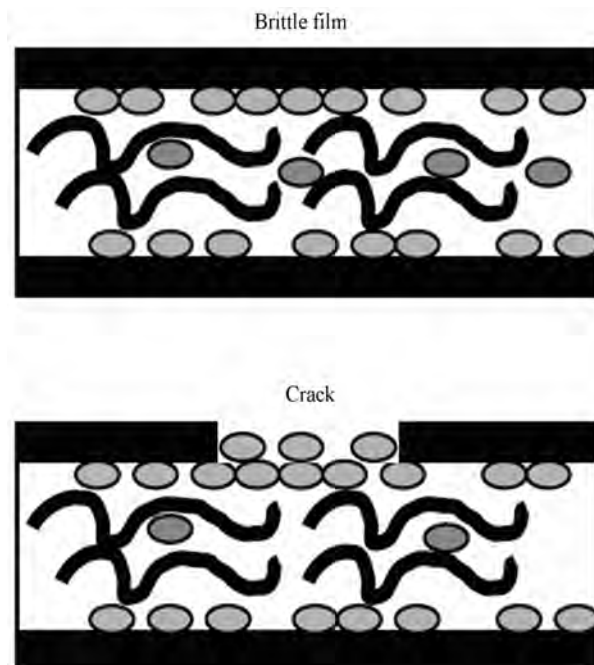
Figure 21. Scheme of a multilayer composite (coating). A polymer layer (represented by the black chains) containing nanoparticles is sandwiched between two intact, brittle layers. Upon appearance of, a crack in the top surface and due to the particle-polymer interactions, the particles become localized in the crack and effectively mend the damage.
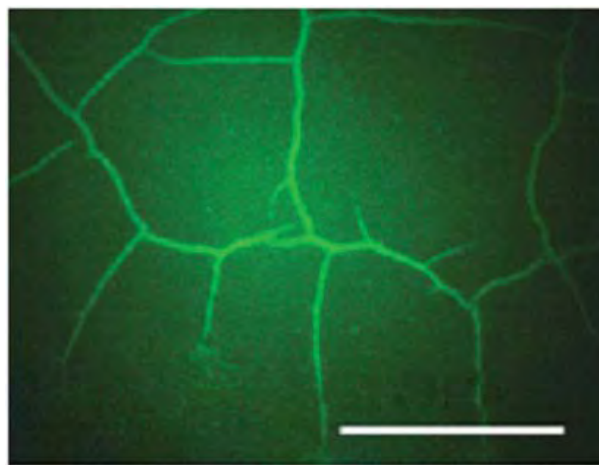
Figure 22. Fluorescence microscope image of a crack in a 60 nm SiOx layer on a mixture of PMMA with PEO-covered 3.8-nm-diameter CdSe/ZnS nanoparticles. The cracked film is viewed with a fluorescence microscope, in which the segregation of the CdSe nanoparticles to the cracks is highlighted by the fluorescence of the nanoparticle. [117], scale bar = 50 microns. Reprinted by permission from Macmillan Publishers Ltd: [Nature Materials] (Entropy-driven segregation of nanoparticles to cracks in multilayered composite polymer structures, S. Gupta , Q. Zhang , T. Emrick, A. C. Balazs, T. P. Russell, 5, 229-233), copyright (2006).

The approach has the advantage of being "re-usable"; when new cracks appear, the polymers again drive the particles to the damaged site and thereby continue the repair. In principle, this process can continue until essentially all the particles in the polymer layer are expelled and localized in the cracks.

Finally, since the particles can potentially be made out of the same materials as the brittle walls, the system will resemble the initial, undamaged materials. Additionally, the fluorescing particles provide a useful diagnostic tool, pinpointing the location of the cracks and revealing the mechanical state of the material.

A model has been published describing the rolling motion of a fluid-driven, particle-filled microcapsule along a heterogeneous, adhesive substrate to show how the release of the encapsulated nanoparticles can be harnessed to repair damage on the underlying surface [118]. The microcapsules that could act as 'artificial leukocytes' are driven by an imposed flow to move along an adhesive surface, which represents the wall of a microchannel (either in the synthetic microvasculature, or more generally, in a microfluidic device). The microcapsules enclose a solution of nanoparticles and these nanoparticles can diffuse from the interior of the capsule into the host fluid. When the capsule is trapped at the leading edge of the damaged region, a relatively high fraction of the released particles are now localized near this region and can more effectively cover this damaged site. Once the damage is repaired, the capsule can again be driven by the imposed flow to move along the surface where they could potentially sense and perform the repair action at another damage site.

So far, all self healing mechanisms and discussed systems tried to mimic nature by filling or re-filling cavities of damaged materials just like it is the case in nature. However, nature has more than one strategy to deal with threads. Continuously re-shaping, metabolic cycles as well as isolation of sub-critical thread concentrations (bacteria) are also healing strategies in nature.

Such metabolic reactions can also be used in polymeric systems to accompany a self-healing process as described for polycarbonate (PC, polyetherketone (PEK) and poly-p 2.6 dimehylphenylenether (PPE) [119]. In the last case e.g., the polymeric chains cut by heat, light, oxygen and external mechanical force will produce a radical on the end of the scission chain in the first step. Subsequently, a hydrogen donor stabilizes the radical. The Cu (II) catalyst added beforehand forms a complex with each end of the two different chains and withdraws two electrons from them. The chains combine, eliminating two protons from the ends and reducing the copper Cu (II) to Cu (I). The Cu (I) migrates in the polymer and reacts with an oxygen molecule in an oxidation step to Cu (II). The oxygen ion then reacts with two protons to form a water molecule which leaves the system. Key factors for the speed of the self-repair action are the concentration of the chain ends and the mobility of the chains (the recovery rate increases with decreasing initial molecular weight and increasing amount of dimethylphthalate as plasticizer), the oxygen partial pressure in the surroundings and the speed of emission of water (see **Figure 23**) [119].

The isolation of subcritical damage and the stop of further growth is the strategy applied while introducing
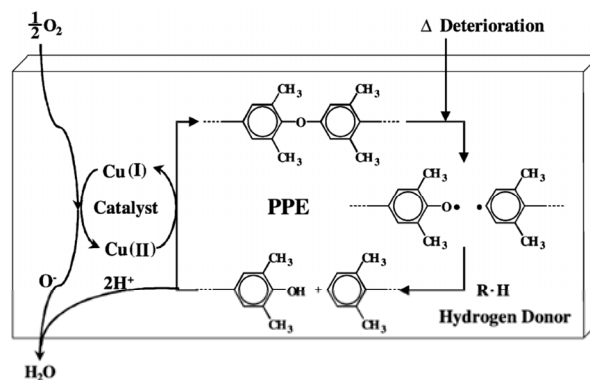
Figure 23. Scheme of the self-repairing metabolism in PPE. Reprinted by permission from IOP Publishing Ltd: [Sci. Technol. Adv. Mater.] (Self-repairing mechanism of plastics, K. Takeda *et al*, 4, 435), copyright (2003).
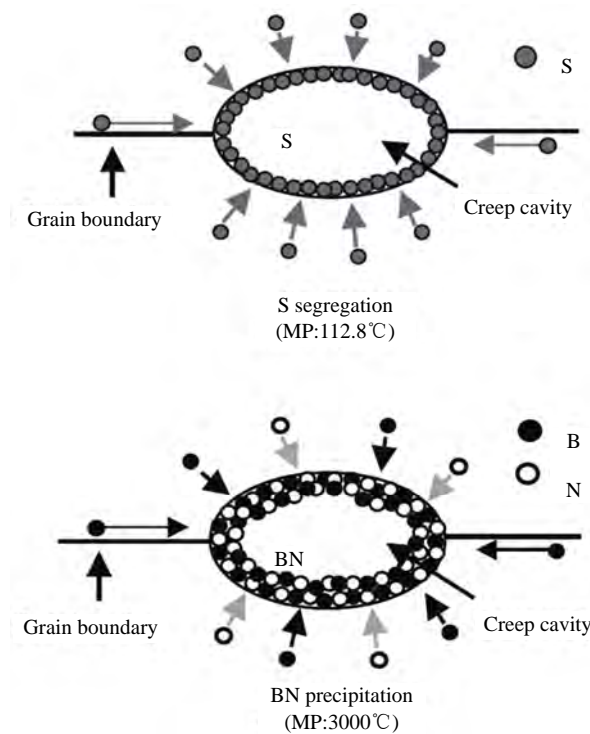
Figure 24. An illustration of S segregation and BN precipitation on creep cavity surface [120].

self-repair to austenic stainless steel [120] (see **Figure 24**). High temperatures during use of austenic steels leads to low ductility creep fracture in long timescales caused by the nucleation, growth and coalescence of grain boundary cavities. Dissolved sulphur segregates on cavity surfaces easily, and enhances the creep cavitation remarkably most likely due to a lowering the creep cavity surface energy and increasing the surface diffusion rate. The additions of Ce (0.016 wt%) is highly effective in removing the traces of soluble S in the steel through the formation of Ce_2O_2S. In the absence of S segregation, B (0.07 wt%) and N (0.007 wt%) can segregate due to their small atomic diameter efficiently to the creep cavity surface and form boron nitride (BN) compound on the surface during creep. As BN is very stable at high temperatures, the precipitation of BN film on the creep cavity surface suppresses the creep cavitation in steel by reducing the creep cavity growth rate. The BN precipitation continues during creep exposure and heals the creep damage. The creep cavities are self-healed by a continuous precipitation of BN on creep cavity surface during creep exposure, and the growth of the self healed creep cavities is suppressed almost completely. The function of self-healing for creep cavitation provides the steel with a longer rupture life and higher rupture ductility.

4. SENSORS AND TRIGGERS FOR SELF-HEALING SYSTEMS

Fundamental to the understanding and implementation of self-healing systems is the detection of damage and a trigger mechanism which initiates the repair action. This is done in nature efficiently e.g. in the case of wound-healing by growth factors and matrix components that are available to provide these "start" signals, triggering relatively sedentary cell lineages at the wound margin to proliferate, to become invasive, and then to lay down a new matrix in the wound gap [112].

However, the tricky part is really the distinction between the healthy and the damage status of a given system. Here, a decision between acceptable damage and unacceptably changed behaviour of the system has to be made, or in other words an indication of the time of the usual transition from a normal state to a degraded state when attacks become successful and/or faults begin to take effect. In the end, any system should detect failure in a timely manner and must be smart enough to compute the degree of malfunction in the system and to asses finally whether the system actually needs the intervention by a "recovery program".

As stated above, sensor elements are essential for the design and functionality of self-healing systems. In the case of the hollow glass capillaries or the urea-formal-dehyde capsules used for the storage and delivery of a liquid performing the self-healing action, the shell of the capsule or the glass capillary itself act as strain sensor. They are tuned by their mechanical properties to break and to release the fluid in the event of damage.

The self-healing system based on re-formation of covalent bonds during a heating-cooling cycle fulfils in itself the sensor function. The low viscous system bridges the gaps of crack or damage due to the surface tension properties of the liquid.

However, it is certainly preferable to get access to autonomic self-healing systems with a more sophisticated embedded structural health monitoring sensor unit enabling decision making about the place and time of the required repair action to be taken. There are a number of possible damage sensors available, which are discussed with respect to their advantages and performance in [121]. Most important is the size and/or the location of the damage that can be resolved by a certain sensor system (see **Figure 25**), the size of the sensor itself and the requirements to get a certain sensor functioning (power consumption).

A combination of vibration and wave propagation data has been used to determine the location and degree of damage in structural components in an automated damage identification technique requiring minimal operator intervention [122]. To build such a detection system, a structure had to be instrumented with an array of actuators and sensors to excite and record its dynamic response. In order to determine structural damage, a damage index, calculated from the measured dynamic response of the structure in a reference state (baseline) and the current state, was introduced.

While the vibration-based analysis was used to identify widespread damage within the structure, the analysis of the waveform signals provides detailed information on the location and nature of smaller defects. The unified computer-assisted automatic data analysis procedure can improve the reliability of the defects detection capability and aid in the development of in-situ health monitoring systems for defects-critical structures. In a similar way, electrical resistance measurements are applied to monitor the health situation of a certain system using a (percolated) conductive network or carbon fibres incorporated in a structure. The resistance changes irreversibly upon damage, as shown for damage inflicted by flexure, tension, fatigue, and impact. The oblique resistance, as measured at an angle between the longitudinal and through-thickness directions, is particularly sensitive. This enables the real-time monitoring of damage in form of fire breakage and delamination in the case of composites tested in tension fatigue, compression and impact and provides an estimate of the remaining fatigue
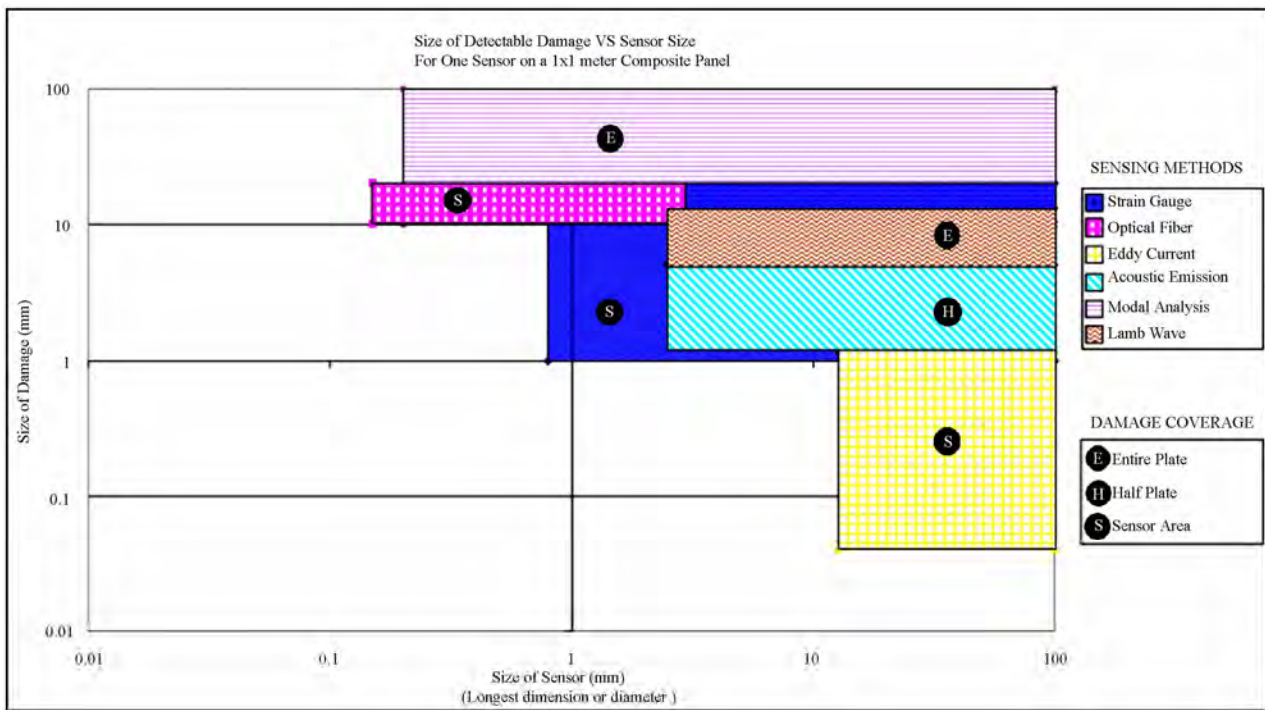
Figure 25. Sensor selection space comparing size of detectable damage with sensor size for various sensing methods [121].

life-time [123].

Also, carbon nanotube networks have been employed for sensing of distributed strain and damage and consequently for lifetime prediction and initiation of healing [124,125]. Under static load, changes in resistance with deformation and the initiation of microcracking during loading of the composite laminate can be monitored (see **Figure 26**).

On unloading, the resistance decreases to nearly the original value as the transverse cracks were closed by the stiff outer plies of the composite system. Upon reloading, the specimen show a sharp increase in resistance at much lower levels of deformation corresponding to reopening of the microcracks, indicative of permanent damage to the composite. This approach may be useful in self-healing systems.

In a recent study, the sensor possibilities of carbon nanotube networks incorporated in composite systems with respect to fatigue-induced damage was investigated with regard to impact on in-situ health monitoring, damage prognosis and the success of self-healing [126]. Monitoring of the volume and through-thickness resistance enabled a determination of the extent and propagation of fatigue-induced damage such as crack and delamination growth in the vicinity of stress concentrations. The conductive nanotube network also provides opportunities to repair damage by enabling fast heating of the crack interfaces; up to 70% recovery of the strength of

the undamaged composite has been achieved. Again, the repair action has been taken by an enhanced mobility of a resin at temperatures above T_g.

Anyway, the first step to autonomic self-repair is certainly structural health monitoring. Since all materials contain inherent defects, the detection of existence and location of damage requires a comparison between two system states. Sensors cannot measure damage directly, features need to be extracted through data processing and in a learning process type of damage and severity of damage can be identified.

Therefore, e.g. machine learning for structural health monitoring has to be applied. In general, there are two approaches to damage identification [127]. Model-driven methods establish a high-fidelity physical model of the structure, usually by finite element analysis, and then establish a comparison metric between the model and the measured data from the real structure. If the model is for a system or structure in normal (*i.e.* undamaged) condition, any departures indicate that the structure has deviated from normal condition and damage is inferred. Data-driven approaches also establish a model, but this is usually a statistical representation of the system, e.g. a probability density function of the normal condition. Any departures from normality are then signalled by measured data appearing in regions of very low density. The algorithms that have been developed over time for data-driven approaches are mainly drawn from the disci-
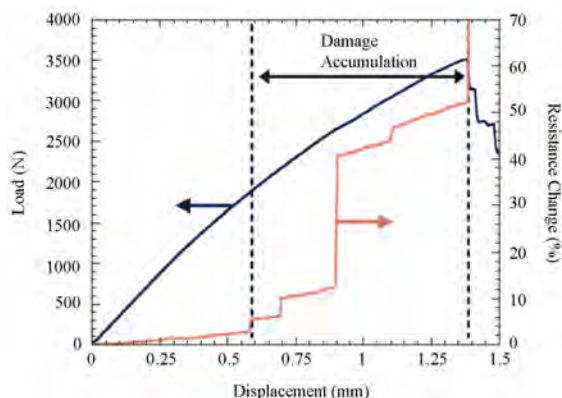
Figure 26. Load-displacement and resistance curves for a composite system with incorporated carbon nanotubes acting as strain sensors [124]. A linear increase in resistance with load is clearly seen. Upon the initiation of microcracking there is a sharp change in the resistance. In the progression from the first initiation of cracking to ultimate failure of the composite laminate the resistance changes drastically. Thostenson, E.T., Chou, T.-W., "Carbon nanotube networks: Sensing of distributed strain and damage for life prediction and self healing", Advanced Materials, (2006) 18 (21), pp. 2837-2841 Copyright Wiley-VCH Verlag GmbH & Co. KGaA. Reproduced with permission.

pline of pattern recognition, or more broadly, machine learning. Apart from the first step to structural health monitoring, the detection of damage including data capture, feature selection as a process of amplification and discarding of redundant information and novelty selection, the damage location and the damage assessment which need as additional part a network of novelty detectors the information is finally computed via a neuronal network prediction of damage severity. However, without a detailed knowledge of the underlying fatigue and e.g. fracture properties of the system it will not be possible to extrapolate to failure.

5. REQUIREMENTS AND CONSEQUENCES OF SELF-REPAIR

Self-healing is, in a sense, opposite to a degradation process, which as a dissipative process is connected with the production of entropy. In 1877, Boltzmann suggested a definition of entropy using the statistical thermodynamics approach and the concept of microstates as

$$S = k \ln \Omega$$

with k as the Boltzmannis constant and Ω as the number of microstates corresponding to a given macroscopic state of a system. Microstates are the arrangements of energy and matter in the system that are distinguishable at the atomic or molecular level, but are indistinguish-

able at the macroscopic level. Any system tends to evolve into a less-ordered and thus more random macrostate that has a larger number of corresponding microstates, and thus the "configurational" entropy S grows.

All processes that lead to degradation (wear, corrosion, fatigue, etc.) often involve interactions with different characteristic length scales. For example, friction and wear involve interactions of microscale and nanoscale asperities and wear particles, capillary interactions, adhesion, chemical molecular bonding. In most cases, these interactions lead to an irreversible energy dissipation and, therefore, to the production of entropy. In many cases, a system can be divided naturally into several scale levels with a limited interaction between hierarchical scales. The entropy production at the macroscale can be therefore compensated by the entropy consumption at another level. Since the entropy is an additive function and the levels of the hierarchy are separated, the net entropy can be presented as the sum of entropies associated with the structures and process at corresponding scale levels as

$$S_{\text{net}} = S_{\text{macro}} + S_{\text{meso}} + S_{\text{nano}} \tag{1}$$

where the indices "net", "macro", "meso" and "nano" correspond to the net entropy, macroscale, microscale (mesoscale), and nanoscale (atomic scale) components [128]. For most applications, is the integrity of the macroscale structure (e.g., the absence of cracks, appearance etc.) of predominant interest whereas the mesoscale and nanoscale structure is of lower interest. The integrity of the macroscale structure may be therefore repaired or restored at the expense of the micro- and atomic scale structures.

In the case of the autonomous self-healing using fluid systems as applied while using capsules or capillaries filed with a glue [82-104] excess entropy, $\triangle S_{\text{macro}}$ associated with the macroscale defects, such as cracks or voids is compensated by affecting the mesoscale structure, e.g., by fracture of microcapsules and the release of the fluid, which decreases the degree of order of the microstructure and thus increases the entropy for $\triangle S_{\text{meso}}$. Crack propagation is an irreversible process, because when intermolecular bonds are broken, the energy γ is released irreversibly, so the entropy amount $S_{\text{crack}} = \gamma KA/T$ is produced to create a crack with area A. The coefficient $0 < K < 1$ is the fraction of the dissipated energy Q that is consumed for the creation of the crack, whereas the rest of the energy is dissipated. The ideal state without cracks corresponds to the minimum number of microstates and thus to the lowest possible configurational entropy. The crack can be formed in many different ways and the cracked macrostate corresponds to a number of microstates producing excess configurational entropy, $\triangle S_{\text{macro}}$. In a similar manner, when a capsule ruptures and

its content is released, the configurational entropy grows because mixing occurs. The configurational entropy growth of mixing of two substances is given by

$$\triangle S_{\text{mixing}} = -R\left(n_1\ln X_1 + n_2\ln X_2\right) \qquad (2)$$

where n_1 and n_2 are the amounts in moles of two pure substances, X_1 and X_2 are mole fraction in the solution, and R is the gas constant. Part of this excess entropy can be consumed for healing the bonds at the crack. The net configurational entropy grows, however the growth is not due to the cracking but due to microcapsule rupture and an irreversible decrease of their number.

If N capsules are ruptured to heal the crack with the area A, the net entropy production is given by the mesoscale entropy of mixing minus the macroscale entropy of crack healing

$$\Delta S_{net} = \Delta S_{meso} + \Delta S_{macro} = N\Delta S_{mixing} - K\frac{\gamma L}{T} > 0 \qquad (3)$$

In case $\Delta S_{macro} < \Delta S_{meso}$, the healing is done by decreasing the macroscale component of entropy at the expense of the mesoscale component [128]. Crack healing decreases then disorder (and entropy) as observed at the macroscale, while fracture of the microcapsules increases disorder (and entropy) when observed at the mesoscale. Self healing occurs thus autonomically if the net entropy of the system is increasing and if the rate of healing is higher than the rate of degradation; the effectiveness of the healing mechanism can be influenced or perhaps measured using relating microstructure parameters to the entropy.

It is important to stress that self-repair is not simply a material property, but rather a **system property**. Therefore, it is not realistic to develop universal self-repairing systems being applicable in all sorts of applications. Consequently, it is important to develop new concepts of self-repairing systems with additional values compared to the existing one, which are focused on a well-defined area/field of applications. However, the self-repair mechanisms used in most current systems and devices are not yet as developed as in the complex functional systems as existing in nature.

Existing autonomic self-healing processes need time (rest periods) and energy. However, the end product is neither aesthetically nor functionally perfect. Defects on a nanoscale size are randomly distributed in any material, mechanical loads during the use cause the formation of cracks initiated by the nanoscaled defects, which cause, in time, degradation of the material up to a possible catastrophic failure.

A self-healing mechanism already initiated at a nanoscale offer many advantages for a more effective prevention of further propagation and growth of micro-cracks as has been shown in a recent modelling

study [129]. There, the self-healing process of materials with embedded "glue"-carrying cells, in the regime of the onset of the initial fatigue has been studied by three-dimensional numerical simulations within the percolation- model approach. The onset of material fatigue is delayed in such a system by development of a plateaulike time dependence of the material quality. In this low-damage regime, the changes in the conductance and thus in similar transport and response properties of the material can be used as measures of the material quality degradation. A feature found for three dimensions being much more profound than in earlier-studied two-dimensional systems, is the competition between the healing cells. Even for low initial densities of the healing cells, they interfere with each other and reduce each other's effective healing efficiency. Short-range healing means that cells affect their neighbourhood approximately within a distance equal to their size. Thus, in order not to interfere literally, not to waste glue, other healing cells should not be healing this whole neighbourhood; thus they must be about two "shells of influence" away. The exclusion radius is thus at least three times the cell radius, in terms of the center-to-center separation, it is likely even larger, depending on the specific geometry.

Any architecture for self-healing systems should satisfy essential properties like adaptability, dynamicity, awareness, autonomy, robustness and distribution. From this analysis and discussions of the currently active and explored principles of self-repair the following requirements for the design of an ultimate self-healing structure/material can be formulated:

- A **reflection mechanism** to detect internal or external conditions for which the system should respond to **sensing** function of damage
- A **reasoning mechanism** to determine which actions should be taken in order to response to an input from the reflection mechanism—**the feedback** to repair mechanism, **signal transport**
- A **configuration mechanism** to perform necessary changes to repair or optimize the system as directed by reasoning mechanism and activation of the repair mechanism (*repair-on-demand*)—**transport of energy and/or material**, repair with the ability to "heal/fill" damage (e.g. volume increase!)
- *Repair has to be either attributive or functional, may be single repair (only one time) or repeating repair*
- **Detection of success and of the status of the structure, recovery of the initial status**
- No reduction of the performance of the matrix material by the self-repair functionality; good adhesion and bonding and sufficient thermo-mechanical

properties of the repair material

- Sufficient high stability of the self-repair functionality during processing and storage

Such systems have been already constructed and will be discussed at two examples:

5.1. Self-Repairing Strategies and Structures Used in Current Electronic Devices

One method of self-healing is to design a multiply redundant system that can reconfigure itself when damaged. Re-configurable control systems require three separate functions: failure detection and isolation to determine which components are no longer useful; parameter identification to provide a model of the damaged structure, and online control design that uses information from the other two to re-establish control of the modified structure. This approach has been applied for some time already in re-configurable circuit hardware. This is particularly the case for DRAM. As a typical industry case, the original yield before a built-in self repair (BISR) using redundant elements for repair for a 256-Mbit commodity DRAM in a 0.11-micron CMOS process is almost 0, yet the yield of the same product after repair can

increase to more than 60%, and even to 80%. Here, the BISR consists of three main blocks: built-in self test (BIST), built-in redundancy analysis (BIRA), and address reconfiguration (AR) [130]. Typically, a BIST circuit consists of a controller, a test pattern generator (TPG), a data comparator, and interface logic. The controller executes the test algorithm and issues commands for the TPG. One of the algorithms used is testing is the Syndrome identification algorithm. This method identifies fail patterns during the test process to increase spare allocation efficiency. After analysis, the AR circuit repairs the memory; e.g. it replaces the faulty memory elements with the fault-free, spare ones. This typically involves address remapping or address decoder reconfiguration. When the memory size increases, the total benefit as a combination of early-market entry benefit, test benefit, development cost and cost for the redundant memory grows quickly, because the yield decreases exponentially when the memory size increases, and thus the BISR design shows its effectiveness in enhancing the yield. Development costs become negligible when production volume is high, because they are constant for the product. Self-repair systems are currently well known and in use in several electronic structures to maintain
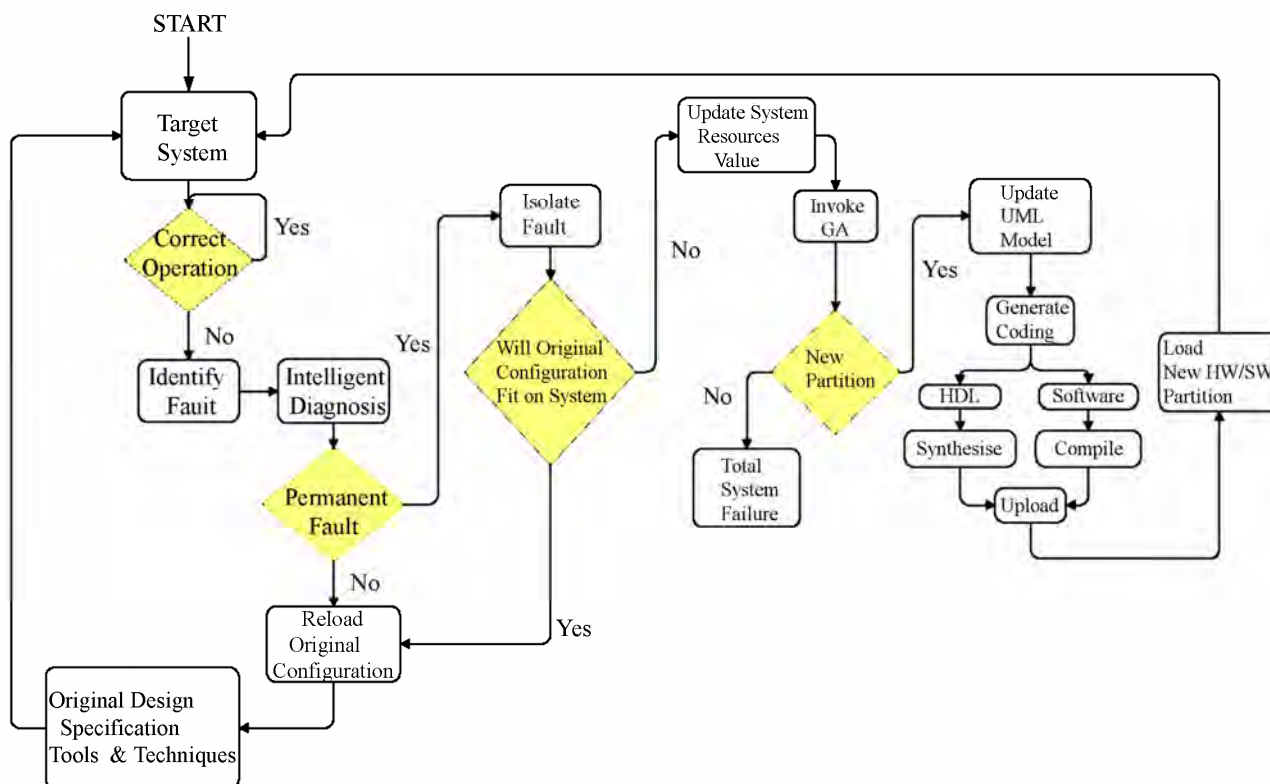
Figure 27. Flow diagram typical for a self-repairing structure used in electronic devices. Reprinted from Engineering Applications of Artificial Intelligence, Self-repair of embedded systems, 17, E. A. Coyle, L. P. Maguire, T. M. McGinnity, 1-9, Copyright (2004), with permission from Elsevier.

their reliability for a long time. In fact, embedded systems are increasingly entrusted with critical tasks and it becomes crucial that these systems exhibit a high level of reliability. The increasing complexity of such systems makes production of defect-free systems extremely difficult. Therefore, self-repair methodologies were introduced employing a unified modelling language and genetic algorithms and increasing the flexibility and reliability of such systems by enabling the transfer of functionalities between hardware and software. A flow diagram of the processes in such a system is shown in **Figure 27**.

In contrast to the majority of the already covered systems, this system is an example where the functionality is related to information flow and not to mechanical or aesthetic or other main functionalities. Hence, also the flow of information is used as the signal in the diagnostic process and as the mobile part of the system, able to perform the repair action. The diagnostic circle addresses the functionality during operation of the target system and decides whether the current configuration is able to deal with the isolated fault and to update the system resource value on demand resulting in new partitions, compilation and upload of the new partitions onto the system information. Industrial leaders like Microsoft, Sun Microsystems and IBM are carrying out research on autonomic self-healing systems, grid computing, software agents and middleware computing are typically strategies and software systems and hardware architecture are being developed with self-healing properties. A summary of the developments in this area is given recently by Gosh (2007) [131].

5.2. Self-Repairing Bolted Joints

Bolted joint, as one of the most common mechanical components in all types of engineering structures, are critical to the function of the structure and their failure could have huge costs or endanger lives. Unfortunately, bolted joints are subject to a variety of common modes of failure. These include self-loosening, shaking apart, breaking because of corrosion, stress cracking or fatigue, slippage (which can change the way a structure absorbs load, leakage of corrosive substances in the joint), and separation leading to rapid fatigue. One of the most frequent modes of failure for bolted joints is self-loosening. To reduce this mode of failure a concept of a self-sensing and self-healing bolted joint has been developed, consisting of structural members joined together by bolt and nut combinations equipped with piezoceramic and shape memory alloy elements [132] (see **Figure 28(a)**). This concept combines an impedance-based health- monitoring technique (monitoring of bolt tension and connection damage) together with

actuators to restore tension in the system. The actuators are included in the joint as shape memory alloy (SMA) washers. The most common SMA is nickel-titanium, often referred to NiTi or Nitinol, a material that has the ability to convert heat to mechanical energy through a phase transition.

The actuation ability of smart materials should also provide force to a smart structure to counteract damage once it is detected, introducing the possibility of self-healing structures as demonstrated on this example. The impedance method detects and inspects whether the damage threshold value has been reached or not, and provides a signal to activate the SMA actuator if needed. When damage occurs, temporary adjustments of the bolt tension can be achieved actively and remotely in order to restore lost torque for continued operation (see **Figure 28(b)**). Thus, this is an example for the construction of a self-monitoring and self-healing system that could be added to existing structures, and provides both condition monitoring and self repair.

(a)

(b)
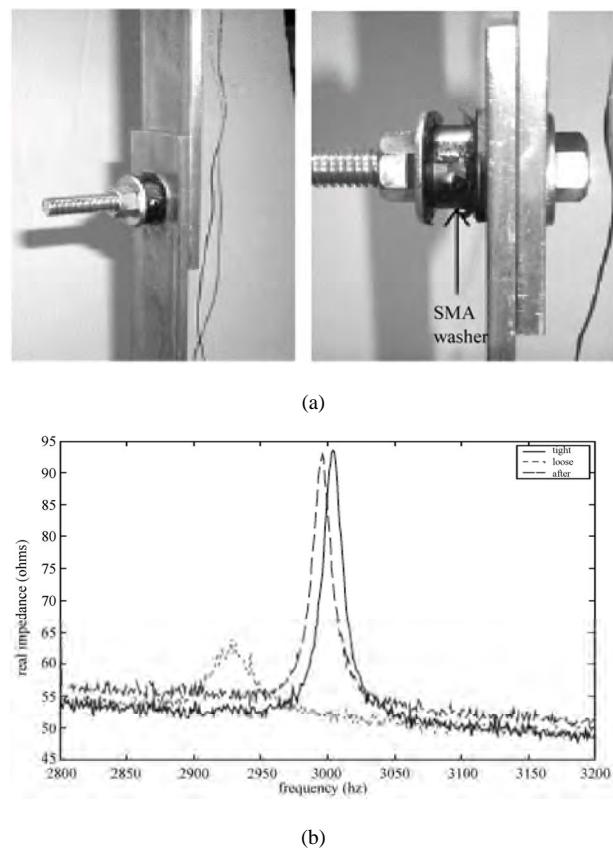
Figure 28. a) Bolted Joint Configuration with SMA washer and PZT impedance sensor, b) Part of the impedance spectrum of a tight, loose and by SMA actuation fastened bolt connection. Reprinted by permission from IOP Publishing Ltd: [Smart Mater. Struct.] (Practical issues of activating self-repairing bolted joints, D. M. Peairs *et al*, 13, 1414), copyright (2004).

6. TOWARDS A NEW GENERATION OF SELF-HEALING SYSTEMS

In order to develop a new generation of self-healing devices-smart structures, the following working areas need particular effort:

1) Development/design of sensing elements to be incorporated within structures/surfaces which are able to trigger the self-repair process (signal transport, activation of the repair mechanism). This means that, contrary to most of the model systems, the sensor function has to be further developed and extended with an active learning functionality, able to differentiate and to detect damage, to interpret the obtained information and to trigger/stimulate the repair action on demand. These sensoric elements should be ideally structural parts of the system and should not detoriate the general functionality of the system.

2) Development of transport/repair mechanisms for different activation energies/materials and different circumstances (speed, temperature, amount of recovery). This is especially needed to widen the area of applications of self-healing systems to more materials and systems. Up to now, only a limited number of solutions are existing (encapsulated glues etc.), however, new principles have to be developed and employed to cover a broader range of performance demands.

3) Development of multiple repair processes applicable and sufficient for the purpose. This relates especially to the speed of the repair action, which has to be adjusted to the needs and rest time periods available. Another need is the development of the action-on-demand-only, strongly coupled with the development of sensor/trigger mechanism. If an action-on-demand-only can be realized, then it will be easier to ensure the capability of multiple repair actions. Such an action could be triggered by a concentration of stress which initiates the repair action while activating an initiator. Materials that anticipate damage and increase their strength where damage probability is largest like the system developed by nature for the maintenance of our skeleton are virtually damage free, if enough energy and time for the constant maintenance actions is supplied and given. Alternatively, continuously active materials like present in a living polymerization will realize a perfect restoration of the undamaged state if more reactive monomers are supplied after damage, e.g. via capsules [133].

4) Finally, methods must be developed to test and characterise the structures/devices and to quantify the success of the self-repair action. Up to now, there is only a minor understanding of quantification of the success of self-healing, mostly by measurement of mechanical performance, however, since self-healing is not necessarily only connected to mechanical damage, some measure of the quality of the self-repair has to be developed.

If these requirements are met, then it will be possible to create truly smart structures, which sense their internal state and external environment and based on the information gained respond in a manner that fulfils their functional requirements. The primary advantage of moving towards smart structures technology is the potential cost benefit of condition-based maintenance strategies and the prospective life extension that may be achieved through *in-situ* health monitoring.

7. CONCLUDING REMARKS

Implementation of self-healing is not intended to deal with poor or inadequate application design, development flaws, and problems with the quality of materials or operational errors of systems and devices. However, it should respond to damage caused by external deterioration factors. Thus, self-healing should offer great opportunities for increases in durability and reliability, reduced maintenance and overall costs. This includes reduced material resources, since the usual over-design of materials is no longer required. Repair will be addressed at the very position of first appearance of damage, minimizing the need to have self-repairing functionality throughout the whole system.

Autonomic self-repair should be intrinsically connected with a minimization of the free energy of the system after experiencing damage (e.g. fracture would create additional surfaces and hence enhance the overall energy level of the system). However, this is not as easy and autonomic as it may seem, damage may only lead to another local minimum of the overall free energy and this would be in some cases difficult to detect for a given system. It is for example extremely difficult to detect the energy changes connected with a change in pure appearance of a coating without having scratches and even more difficult to react with a repair action on such changes, however the changes would account for a damage of the esthetical function of the coating. As for now, most of the introduced synthetic self-healing systems have still substantial short-comes, such as the liquid based capsule system, which requires a large amount of capsules to fulfil the function thereby reducing the mechanics of the system in a way that it can only be treated as a model system for fundamental studies [91] or the difficulty in filling and sealing of the liquid based capillary systems which limits applicability [82-90]. Fully autonomous systems need to provide currently a level of mobility which makes them rather unattractive as constructive materials [70]. However, the latest developments show ways for possible solutions such as the application of liquid filled capsules in coating systems or flexible laminates [134,135], here enabling a functional

repair of a system as corrosion protection which has not the same constraints as a structural material or the use of the same strategy while deploying conductive particles in liquids and as such repairing conductive pathways [136]. The design principles of a self-healing system are universal, however the synthetic system solutions developed so far are mostly special for the very circumstances of the material system and the application (conditions), no universal solution exists applicable for all material systems.

At the most basic level, a self-repairing system requires redundant capacity and the ability to use it effectively. The system must be capable of modifying the configuration of the target system in order to affect a repair. New design principles and strategies will be applied, and finally self-repairing potential will only be incorporated where it is needed or where damage of the material, system or device is going to start. Self-repair will be universal in terms of materials and will follow universal design principles and hence can be applied anywhere. The overall capabilities required for a self-repairing system extend the application functionality specified by the system designers. The additional elements required include monitoring, test, diagnosis, and repair capabilities. The system monitor must be able to analyse high-level system performance of the system against predefined performance benchmarks, continuously verifying the correctness of the operation of the process and bi-directionally communicating with the target system. The testing process also must have bi-directional communication to activate specific test sequences and receive results. This process should exploit any built-in self-test (BIST) ability, and the testing results are forwarded to the diagnostic process. Automating the fault diagnosis process inherently demands the application of intelligent techniques. Finally, the self-repair process must be able to affect a repair based on the reduction in resources available, following isolation of the faulty components. If the original level of performance cannot be restored, the monitoring system must be modified to reflect the changes in system characteristics. This feature demands an optimisation capability. Providing these additional capabilities impose a significant burden on the system, there is a trade-off between the additional cost of the system to facilitate self-repair and the potential cost of failure.

The purpose of this reflection is not to provide a review of the knowledge on self-healing systems; therefore, it is by far not covering all work on this subject. The analysis of the systems as discussed in this work shows that the creation of self-healing systems is and is becoming reality. Although a number of synthetically designed self-healing systems are developed and still under development, they mostly fulfil only partially all requirements of an ideal self-healing system as produced by nature.

The knowledge of the system complexity enables the design of a self-healing system for a given application and possible damage. The introduction of self-healing properties into materials systems is with this knowledge and an interdisciplinary approach of design combining all disciplines of science is a growing reality, which has been already demonstrated for a number of synthetic model systems and will have a great future in materials technology especially for systems used in maintenance critical applications such as areas with limited accessibility, high demands of reliability, a guaranteed long life or in areas where repairs cause a lot of hindrance/ annoyance/costs.

8. AKNOWLEDGEMENTS

REFERENCES

[1] Fratzl, P. and Weinkamer, R. (2007) Hierarchical structure and repair of bone: Deformation, remodeling, healing. *Self Healing Materials*, *An Alternative Approach to* 20 *Centuries of Materials Science*, *Series*: *Springer Series in Materials Science*, **100**, 323-335.

[2] Farrar, C.R. and Worden, K. (2007) An introduction to structural health monitoring. *Philosophical Transactions of the Royal Society A*, **365(1851)**, 303-315.

[3] Asai, S., Koumoto, K., Matsushita, Y., Yashima, E., Morinaga, M., Takeda, K., Iritani, E., Tagawa, T., Tanahashi, M. and Miyazawa, K.-I. (2003) Advances in nature-guided materials processing. *Science and Technology of Advanced Materials*, **4(5)**, 421-433.

[4] Bergman, S.D. and Wudl, F. (2008) Mendable polymers. *Journal of Materials Chemistry*, **18(1)**, 41-62.

[5] Wool, R.P. (2008) Self-healing materials: A review. *Soft Matter*, **4(3)**, 400-418.

[6] Wu, D.Y., Meure, S. and Solomon, D. (2008) Self-healing polymeric materials: A review of recent developments. *Progress in Polymer Science*, **33(5)**, 479-522.

[7] Albert, S.F. (1981) Electrical stimulation of bone repair. *Clinical Podiatric Medical Surgery*, **8(4)**, 923-935.

[8] Coyle, E.A., Maguire, L.P. and McGinnity, T.M. (2004) Self repair of embedded systems. *Engineering Applications of Artificial Intelligence*, **17(1)**, 1-9.

[9] Williams, K.A., Dreyer, D.R. and Bielawski, C.W. (2008) The underlying chemistry of self-healing materials. *MRS Bulletin*, **33(8)**, 759-765.

[10] de Gennes, P.G. (1971) Reptation of a polymer chain in the presence of fixed obstacles. *Journal of Chemical Physics*, **55(2)**, 572-579.

[11] Prager, S. and Tirell, M. (1981) The healing process at polymer-polymer interfaces. *Journal of Chemical Physics*, **75(10)**, 5194-5198.

[12] Jud, K. and Kausch, H.H. (1979) Load transfer through chain molecules after interpenetration at interfaces. *Polymer Bulletin*, **1(1)**, 697-707.

[13] Wool, R.P. and O'Connor, K.M. (1981) A theory of crack healing in polymers. *Journal of Applied Physics*, **52(10)**, 5953-5963.

[14] Kim, Y.H. and Wool, R.P. (1983) A theory of healing at a polymer-polymer interface. *Macromolecules*, **16(7)**, 1115-1120.

[15] Jud, K., Kausch, H.H. and Williams, J.G. (1981) Fracture mechanics studies of crack healing and welding of polymers. *Journal of Material Science*, **16(1)**, 204-210.

[16] Boiko, Y. M. and Lyngaae-Jørgensen, J. (2004) Healing of interfaces of high- and ultra-high-molecular-weight polystyrene below the bulk Tg. *Polymer*, **45(25)**, 8541-8549.

[17] Guerin, G., Mauger, F. and Prud'homme, R.E. (2003) The adhesion of amorphous polystyrene surfaces below Tg. *Polymer*, **44(24)**, 7477-7784.

[18] Brown, H.R. and Russell, T.P. (1996) Entanglements at polymer interfaces. *Macromolecules*, **29(2)**, 798-800.

[19] Silberberg, A. (1988) Distribution of segments near the surface of a melt of linear flexible macromolecules: Effect on surface tension. *Journal of Colloid and Interface Science*, **125(1)**, 14-22.

[20] Yamaguchi, M., Ono, S. and Terano, M. (2007) Self-repairing property of polymer network with dangling chains. *Materials Letters*, **61(6)**, 1396-1399.

[21] Hayes, S.A., Jones, F.R., Marshiya, K. and Zhang, W. (2007) A self-healing thermosetting composite material. *Composites Part A*: *Applied Science and Manufacturing*, **38(4)**, 1116-1120.

[22] Hayes, S.A., Zhang, W., Branthwaite, M. and Jones, F.R. (2007) Self-healing of damage in fibre-reinforced polymer-matrix composites. *Journal of the Royal Society Interface*, **4(13)**, 381-387.

[23] Zako, M. and Takano, N. (1999) Intelligent material systems using epoxy particles to repair microcracks and delamination in GFRP. *Journal of Intelligent Material Systems and Structures*, **10(10)**, 836-841.

[24] Meure, S., Wu, D.Y. and Furman, S. (2009) Polyethylene-co-mathacrylic acid healing agents for mendable epoxy resins. *Acta Materialia*, **57(14)**, 4312-4320.

[25] Liu, W., Sun, X. and Khaleel, M.A. (2008) Predicting Young's modulus of glass/ceramic sealant for solid oxide fuel cell considering the combined effects of aging, micro-voids and self-healing. *Journal of Power Sources*, **185(2)**, 1193-1200.

[26] Seo, S.H., Kim, Y.-W. and Chang, J.Y. (2005) Smectic layered polymer networks based on side chain liquid crystalline polymers having thermally reversible urea bonds. *Macromolecules*, **38(5)**, 1525-1527.

[27] Otsuka, H., Aotani, K., Amamoto, Y. and Takahara, A.

(2007) Thermal reorganization and molecular weight control of dynamic covalent polymers containing alkoxyamines in their main chains. *Macromolecules*, **40(5)**, 1429-1434.

[28] Mee, M.A.J., Goossens, J.G.P. and v. Duin, M. (2008) Thermoreversible cross-linking of maleated ethylene/propylene copolymers with diamines and amino-alcohols. *Polymer*, **49(5)**, 1239-1248.

[29] Diels, O. and Alder, K. (1928). Synthesen in der hydroaromatischen Reihe. *Liebigs Annalen der Chemie*, **460(1)**, 98-122.

[30] Craven, J. M., US patent 3.435.003 (1969).

[31] Chen, X., Dam, M.A., Ono, K., Mal, A., Shen, H., Nutt, S.R., Sheran, K. and Wudl, F., (2002) A thermally re-mendable cross-linked polymeric material. *Science*, **295(5560)**, 1698-1702.

[32] Chen, X., Wudl, F., Mal, A., Shen, H. and Nutt, S.R. (2003) New thermally remendable highly cross-linked polymeric materials. *Macromolecules*, **36(6)**, 1802-1807.

[33] Murphy, E.B., Bolanos, E., Schaffner-Hamann, C., Wudl, F., Nutt, S.R. and Auad, M.L. (2008) Synthesis and characterization of a single-component thermally remendable polymer network: Staudinger and stille revisited. *Macromolecules*, **41(14)**, 5203-5209.

[34] Wouters, M., Craenmehr, E., Tempelaars, K., Fischer, H., Stroeks, N. and van Zanten, J. (2008) Preparation and properties of a novel remendable coating concept. *Progress in Organic Coatings*, **64(2-3)**, 156-162.

[35] Schuman T.P. (2007) Smart corrosion inhibition strategies: Substrate, coating, and inhibitors. *JCT Coatings Tech*, **4(2)**, 60-70.

[36] Wang, Y., Bolanos, E., Wudl, F., Hahn, T. and Kwok, N. (2007) Self-healing polymers and composites based on thermal activation. *Proceedings of SPIE—The International Society for Optical Engineering*, **6526**, 1-12.

[37] Liu, Y.-L. and Hsieh, C.-Y. (2006) Crosslinked epoxy materials exhibiting thermal remendablility and removability from multifunctional maleimide and furan compounds. *Journal of Polymer Science*: *Part A*: *Polymer Chemistry*, **44(2)**, 905-913.

[38] Liu, Y.-L. and Chen, Y.-W. (2007) Thermally reversible cross-linked polyamides with high toughness and self-repairing ability from maleimide- and furan-functionalized aromatic polyamides. *Macromolecular Chemistry and Physics*, **208(2)**, 224-232.

[39] Aubert, J.H. (2003) Thermally removable epoxy adhesives incorporating thermally reversible Diels-Alder adducts. *The Journal of Adhesion*, **79(6)**, 609-616.

[40] Liu, Y.-L., Hsieh, C.-Y. and Chen, Y.-W. (2006) Thermally reversible cross-linked polyamides and thermoresponsive gels by means of Diels-Alder reaction. *Polymer*, **47(8)**, 2581-2586.

[41] Gotsmann, B., Duerig, U., Frommer, J. and Hawker, C.J. (2006) Exploiting chemical switching in a diels-alder polymer for nanoscale probe lithography and data storage. *Advanced Functional Materials*, **16(11)**, 1499-1505.

[42] Park, J.S., Takahashi, K., Guo, Z., Wang, Y., Bolanos, E., Hamann-Schaffner, C., Murphy, E., Wudl, F. and Hahn, H.T. (2008) Towards development of a self-healing composite using a mendable polymer and resistive heating. *Journal of Composite Materials*, **42(26)**, 2869-2881.

[43] Plaisted, T.A., Amirkhizi, A.V., Arbelaez, D., Nemat-

Nasser, S.C. and Nemat-Nasser, S. (2003) Self-healing structural composites with electromagnetic functionality. *Proceedings of SPIE—The International Society for Optical Engineering*, **5054**, 372-381.

[44] Kirkby, E.L., Rule, J.D., Michaud, V.J., Sottos, N.R., White, S.R. and Månson, J.-A.E. (2008) Embedded shape-memory alloy wires for improved performance of self-healing polymers. *Advanced Functional Materials*, **18(15)**, 2253-2260.

[45] Li, G. and John, M. (2008) A self-healing smart syntactic foam under multiple impacts. *Composites Science and Technology*, **68(15-16)**, 3337-3343.

[46] Brunsveld, L., Folmer, B.J.B., Meijer, E.W. and Sijbesma, R.P. (2001) Supramolecular polymers. *Chemical Reviews*, **101(12)**, 4071-4098.

[47] Chino, K. and Ashiura, M. (2001) Thermoreversible cross-linking rubber using supramolecular hydrogen-bonding networks. *Macromolecules*, **34(26)**, 9201-9204.

[48] Kalista, S.J.Jr. and Ward, T.C. (2007) Thermal characteristics of the self-healing response in poly(ethylene-co-methacrylic acid) copolymers. *Journal of the Royal Society Interface*, **4(13)**, 405-411.

[49] Varley, R.J. and v.d. Zwaag, S. (2008) Towards an understanding of thermally activated self-healing of an ionomer system during ballistic penetration. *Acta Materialica*, **56(19)**, 5737-5750.

[50] Chung, C.M., Roh, S.Y., Cho, S.Y. and Kim, J.G. (2004) Crack healing in polymeric materials via photochemical [2+2] cycloaddition. *Chemistry of Materials*, **16(21)**, 3982-3984.

[51] Scott, T.F., Schneider, A.D., Cook, W.D. and Bowmen, C.N. (2005) Chemistry: Photoinduced plasticity in cross-linked polymers. *Science*, **308(5728)**, 1615-1617.

[52] Williams, K.A., Boydston, A.J. and Bielawski, C.W. (2007) Towards electrically conductive, self-healing materials. *Journal of the Royal Society Interface*, **4(13)**, 359-362.

[53] Kawagoe, M., Nakanishi, M., Qui, J. and Morita, M. (1997) Growth and healing of a surface crack in poly (methyl methacrylate) under case II diffusion of methanol. *Polymer*, **38(24)**, 5969-5975.

[54] Hsieh, H.-C., Yang, T.-J. and Lee, S. (2001) Crack healing in poly(methyl methacrylate) induced by co-solvent of methanol and ethanol. *Polymer*, **42(3)**, 1227-1241.

[55] Egloffstein, T.A. (2001) Natural bentonites-Influence of the ion exchange and partial desiccation on permeability and self-healing capacity of bentonites used in GCL. *Geotextiles and Geomembranes*, **19(7)**, 427-444.

[56] Shi, C. and Booth, R. (2005) Laboratory Development and field demonstration of self-sealing/self-healing landfill liner. *Waste Management*, **25(3)**, 231-238.

[57] Edvardsen, C. (1999) Water permeability and autogenous healing of cracks in concrete. *Materials Journal*, **96(4)**, 448-454.

[58] Hearn, N. (1998) Self-sealing, autogenous healing and continued hydration: What is the difference? *Materials and Structures/Materiaux et Constructions*, **31(8)**, 563-567,

[59] Loving, N.W. (1968) Autogenous healing of concrete. *American Concrete Pipe Association*, *Bulletin*, **13**, 3.

[60] Wagner, E.F. (1974) Autogenous healing of cracks in cement-mortar linings for gray-iron and ductile-iron wa-

ter pipe. *Journal of American Water Works Association*, **66(6)**, 358-360.

[61] Soroker, V.J. and Denson, A.J. (1926) Autogenous healing of concrete. *Zement*, **25**, 30.

[62] Brandeis, F. (1937) Autogenous healing of concrete. *Beton und Eisen*, **36**, 12.

[63] Powe, T.C., Copeland, L.E., Hayes, J.C. and Mann, H.M. (1954) Permeability of Portland cement pastes. *Journal of the American Concrete Institute*, **51(3)**, 285-298.

[64] Sahmaran, M. (2007) Effect of flexure induced transverse crack and self-healing on chloride diffusivity of reinforced mortar. *Journal of Materials Science*, **42(22)**, 9131-9136.

[65] Zhong, W. and Yao, W. (2008) Influence of damage degree on self-healing of concrete. *Construction and Building Materials*, **22(6)**, 1137-1142.

[66] Li, V.C. and Yang, E.-H. (2007) Self healing in concrete materials. *Self Healing Materials*, *An Alternative Approach to* 20 *Centuries of Materials Science*, *Series*: *Springer Series in Materials Science*, **100**, 161-193.

[67] Jonker, H. (2007) Self healing in concrete materials. *Self Healing Materials*, *An Alternative Approach to* 20 *Centuries of Materials Science*, *Series*: *Springer Series in Materials Science*, **100**, 195-204.

[68] Sugama, T. and Gawlik, K. (2003) Self-repairing poly (phenylenesulfide) coatings in hydrothermal environments at 200ºC. *Materials Letters*, **57(26-27)**, 4282-4290.

[69] Kim, Y.R., Little, D.N. and Lytton, R.L. (2003) Fatigue and healing characterization of asphalt mixes. *Journal of Materials in Civil Engineering* (*ASCE*), **15(1)**, 75-83.

[70] Cordier, P., Tournilhac, F., Soulié-Ziakovic, C. and Leibler, L. (2008) Self-healing and thermoreversible rubber from supramolecular assembly. *Nature*, **451(7181)**, 977-980.

[71] Lumley, R.N., O'Donnell, R.G., Polmear, I.J. and Griffiths, J.R. (2005) Enhanced fatigue resistance by under-ageing an Al-Cu-Mg-Ag alloy. *Matererials Science Forum*, **29**, 256-261.

[72] Shiya, N., Kyono, J. and Laha, K. (2006) Self-healing effect of boron nitride precipitation on creep cavitation in austenitic stainless steel. *Journal of Intelligent Material Systems and Structures*, **17(12)**, 1127-1133.

[73] Abe, O., Ohwa, Y. and Kuranobu, Y.-I. (2006) Possibility of enhanced strength and self-recovery of surface damages of ceramics composites under oxidative conditions. *Journal of the European Ceramic Society*, **26(4-5)**, 689-695.

[74] Bennett I.J. and Sloof, W.G. (2006) Modeling the influence of reactive elements on the work of adhesion between a thermally grown oxide and a bond coat alloy. *Materials and Corrosion*, **57(3)**, 223-229.

[75] Zhang, X., Xu, L., Du, S., Han, W. and Han, J. (2008) Crack-healing behavior of zirconium diboride composite reinforced with silicon carbide whiskers. *Scripta Materialia*, **59(11)**, 1222-1225.

[76] Ando, K., Kim, B.-S., Chu, M.-C., Saito, S., Takahashi, K. (2004) Crack-healing and mechanical behaviour of Al2O3/SiC composites at elevated temperature. *Fatigue and Fracture of Engineering Materials and Structures*, **27(7)**, 533-541.

[77] Ando, K., Chu, M.-C. and Mastusita, S. (2003) Effect of crack-healing and proof-testing procedures on fatigue

strength and reliability of Si3N4/SiC composites. *Journal of the European Ceramic Society*, **23(6)**, 977-984.

[78] Song, G.M., Pei, Y.T., Sloof, W.G., Li, S.B., De Hosson, J.Th.M. and van der Zwaag, S. (2008) Oxidation-induced crack healing in Ti3AlC2 ceramics. *Scripta Materialia*, **58(1)**, 13-16.

[79] Devanathan, R. and Weber, W.J. (2008) Dynamic annealing of defects in irradiated zirconia-based ceramics. *Journal of Materials Research*, **23(3)**, 593-595.

[80] Hikasa, A., Sekino, T., Hayashi, Y., Rajagopalan, R. and Niihara, K. (2004) Preparation and corrosion studies of self-healing multi-layered nano coatings of silica and swelling clay. *Materials Research Innovations*, **8(2)**, 84-88.

[81] Miccichè, F., Fischer, H., Varley, R. and van der Zwaag, S. (2007) Moisture induced crack filling in barrier coatings containing montmorillonite as an expandable phase. *Surface & Coatings Technology*, **202(14)**, 3346-3353.

[82] Dry, C. (1994) Matrix cracking repair and filling using active and passive modes for smart timed release of chemicals from fibers into cement matrices. *Smart Marterials and Structures*, **3(2)**, 118-123.

[83] Dry, C., Dry, C. and McMillan, W. (1996) Three-part methylmethacrylate adhesive system as an internal delivery system for smart responsive concrete. *Smart Marterials and Structures*, **5(3)**, 297-300.

[84] Dry, C., (2000) Three designs for the internal release of sealants, adhesives, and waterproofing chemicals into concrete to reduce permeability. *Cement and Concrete Research*, **30(12)**, 1969-1977.

[85] Dry, C., Corsaw, M. and Bayer, E. (2003) A comparison of internal self-repair with resin injection in repair of concrete. *Journal of Adhesion Science and Technology*, **17(1)**, 79-89.

[86] Dry, C. (1996) Procedure developed for self-repair of polymeric matrix composite materials. *Composite Structures*, **35(3)**, 263-269.

[87] Bleay, S.M., Loader, C.B., Hawyes, V.J., Humberstone, L. and Curtis, P.T. (2001) A smart repair system for polymer matrix composites. *Composites—Part A*: *Applied Science and Manufacturing*, **32(12)**, 1767-1776.

[88] Pang, J.W.C. and Bond, I.P. (2005) 'Bleeding composites'—Damage detection and self-repair using a biomimetic approach. *Composites Part A*: *Applied Science and Manufacturing*, **36(2)**, 183-188.

[89] Motuku, M., Vaidya, U.K. and Janowski, G.M. (1999) Parametric studies on self-repairing approaches for resin infused composites subjected to low velocity impact. *Smart Materials and Structures*, **8(5)**, 623-638.

[90] Trask, R.S. and Bond, I.P. (2006) Self-healing composite sandwich structures. *Smart Materials and Structures*, **15(3)**, 704-710.

[91] White, S.R., Sottos, N.R., Geubelle, P.H., Moore, J.S., Kessler, M.R., Sriram, S.R., Brown, E.N. and Viswanathan, S. (2001) Autonomic healing of polymer composites. *Nature*, **409(6822)**, 794-779.

[92] Yan, C.Y., Min, Z.R., Ming, Q.Z., Chen, J., Gui, C.Y. and Xue, M.L. (2008) Self-healing polymeric materials using epoxy/mercaptan as the healant. *Macromolecules*, **41(14)**, 5197-5202.

[93] Jones, A.S., Rule, J.D., Moore, J.S., Sottos, N.R. and White, S.R. (2007) Self-healing of damage in fi-

bre-reinforced polymer-matrix composites. *Journal of the Royal Society Interface*, **4(13)**, 395-403.

[94] Cho, S.H., Andersson, H.M., White, S.R., Sottos, N.R. and Brun, P.V. (2006) Polydiniethylsiloxane-based self-healing materials. *Advanced Materials*, **18**, 997-1000.

[95] Brown, E.N., Sottos, N.R. and White, S.R. (2002) Fracture testing of a self-healing polymer composite. *Experimental Mechanics*, **42(4)**, 372-379.

[96] Blaiszik, B.J., Sottos, N.R. and White, S.R. (2008) Nanocapsules for self-healing materials. *Composites Science and Technology*, **68(3-4)**, 978-986.

[97] Yin, T., Rong, M.Z., Zhang, M.Q. and Yang, G.C. (2007) Self-healing epoxy composites—preparation and effect of the healant consisting of microencapsulated epoxy and latent curing agent. *Composites Science and Technology*, **67(2)**, 201-212.

[98] Kumar, A., Stephenson, L.D. and Murray, J.N. (2006) Self-healing coatings for steel. *Progress in Organic Coatings*, **55(3)**, 244-253.

[99] He, X. and Shi, X. (2009) Self-repairing coating for corrosion protection of aluminum alloys. *Progress in Organic Coatings*, **65(1)**, 37-43.

[100] Suryanarayana, C., Rao, K.C. and Kumar, D. (2008) Preparation and characterization of microcapsules containing linseed oil and its use in self-healing coatings. *Progress in Organic Coatings*, **63**(1), 72-78.

[101] Sauvant-Moynot, V., Gonzalez, S. and Kittel, J. (2008) Self-healing coatings: An alternative route for anticorrosion protection. *Progress in Organic Coatings*, **63(3)**, 307-315.

[102] Caruso, M.M., Blaiszik, B.J., White, S.R., Sottos, N.R. and Moore, J.S. (2008) Full recovery of fracture toughness using a nontoxic solvent-based self-healing system. *Advanced Functional Materials*, **18(13)**, 1898-1904.

[103] Caruso, M.M., Delafuente, D.A., Ho, V., Sottos, N.R., Moore, J.S. and White, S.R. (2007) Solvent-promoted self- healing epoxy materials. *Macromolecules*, **40(25)**, 8830-8832.

[104] Mookhoek, S.D., Mayo, S.C., Hughes, A.E., Fischer, H.R. and Zwaag, v.d.S. (2010) Applying SEM-based X-ray microtomography to observe self-healing in solvent encapsulated thermoplastic materials. *Advanced Engineering Materials*, **12(3)**, 228

[105] Bon, S.A.F., Mookhoek, S.D., Colver, P.J., Fischer, H.R. and van der Zwaag, S. (2007) Route to stable non-spherical emulsion droplets. *European Polymer Journal*, **43(11)**, 4839-4842

[106] Carlson, J.A., English, J.M. and Coe, D.J. (2006) A flexible, self-healing sensor skin. *Smart Materials and Structures*, **15(5)**, N129-N135.

[107] Toohey, K.S., Sottos, N.R., Lewis, J.A., Moore, J.S. and White, S.R. (2007) Self-healing materials with microvascular networks. *Nature Materials*, **6(8)**, 581-585.

[108] Toohey, K.S., Sottos, N.R. and White, S.R. (2009) Characterization of microvascular-based self-healing coatings. *Experimental Mechanics*, **49(5)**, 707-717.

[109] Williams, H.R., Trask, R.S., Knights, A.C., Williams, E.R. and Bond, I.P. (2008) Biomimetic reliability strategies for self-healing vascular networks in engineering materials. *Journal of the Royal Society Interface*, **5(24)**, 735-747.

[110] Williams, H.R., Trask, R.S., Weaver, P.M. and Bond, I.P.

(2008) Minimum mass vascular networks in multifunctional materials. *Journal of the Royal Society Interface*, **5(18)**, 55-65.

[111] Liu, H.A., Gnade, B.E. and Baalkus, Jr.K.J. (2008) A delivery system for self-healing inorganic films. *Advanced Functional Materials*, **18(22)**, 1-10.

[112] Martin, P. (1997) Wound healing—aiming for a perfect skin regeneration. *Science*, **276(5309)**, 75-81.

[113] Lee, J.Y., Buxton, G. and Balazs, A.C. (2004) Using nanoparticles to create self-healing composites. *Journal of Chemical Physics*, **121(11)**, 5531-5540.

[114] Tyagi, S., Lee, J.Y., Buxton, G.A. and Balazs, A.C. (2004) Using nanocomposite coatings to heal surfacebdefects. *Macromolecules*, **37(24)**, 9160-9168.

[115] Smith, K.A., Tyagi, S. and Balazs, A. (2005) Healing surface defects with polymer nanocomposites containing spheres. *AIChE Annual Meeting, Conference Proceedings*, 4717.

[116] Smith, K.A., Tyagi, S. and Balazs, A.C. (2005) Healing surface defects with nanoparticle filled polymer coatings: Effect of particle geometry. *Macromolecules*, **38(24)**, 10138-10147.

[117] Gupta, S., Zhang, Q., Emrick, T., Balazs, A.C. and Russell, T.P. (2006) Entropy-driven segregation of nanoparticles to cracks in multilayered composite polymer structures. *Nature Materials*, **5(3)**, 229-233.

[118] Verberg, R., Dale, A.T., Kumar, P., Alexeev, A. and Balazs, A.C. (2007) Healing substrates with mobile, particle-filled microcapsules: Designing a 'repair and go' system. *Journal of the Royal Society Interface*, **4(13)**, 349-357.

[119] Takeda, K., Tanahashi, M. and Unno, H. (2003) Self-repairing mechanism of plastics. *Science and Technology of Advanced Materials*, **4(5)**, 435-444.

[120] Shinya, N., Kyono, J. and Laha, K. (2006) Self-healing effect of boron nitride precipitation on creep cavitation in austenitic stainless steel. *Journal of Intelligent Material Systems and Structures*, **17(12)**, 1127-1133.

[121] Kessler, S.S. and Spearing, S.M. (2003) Selection of materials and sensors for health monitoring of composite structures. *Proceedings of Materials Research Society Symposium*, **785**, 365-375.

[122] Mal, A., Banerjee, S. and Ricci, F. (2007) An automated damage identification technique based on vibration and wave propagation data. *Philosophical Transactions of the Royal Society A*, **365(1851)**, 479-491.

[123] Hayes, S.A. and Hue, L. (2002) A resistance-based damage location sensor for carbon-fibre composites. *Smart Materials and Structures*, **11(6)**, 966-969.

[124] Thostenson, E.T. and Chou, T.-W. (2006) Carbon nanotube networks: Sensing of distributed strain and damage for life prediction and self healing. *Advanced Materials*, **18(21)**, 2837-2841.

[125] Thostenson, E.T. and Chou, T.-W. (2008) Carbon nanotube-based health monitoring of mechanically fastened composite joints. *Composites Science Technology*, **68(12)**, 2557-2561.

[126] Zhang, W., Sakalkar, V. and Koratkar, N. (2007) In situ health monitoring and repair in composites using carbon nanotube additives. *Applied Physics Letters*, **91(13)**, 133102-133104.

[127] Worden, K. and Manson G. (2007) The application of machine learning to structural health monitoring. *Philosophical Transactions of the Royal Society A*, **365(1851)**, 515-537.

[128] Nosonovsky, M., Amano, R., Lucci, J.M. and Rohatgi, P.K. (2009) Physical chemistry of self-organization and self-healing in metals. *Physical Chemistry Chemical Physics*, **11(41)**, 9530-9536.

[129] Dementsov, A. and Privman, V. (2008) Three-dimensional percolation modeling of self-healing composites. *Physical Review E—Statistical*, *Nonlinear*, *and Soft Matter Physics*, **78(2)**, 021104.

[130] Huang, R.-F., Chen, C.-H. and Wu, C.-W. (2007) Economic aspects of memory built-in self-repair. *IEEE Design & Test of Computers*, **24(2)**, 164-172.

[131] Gosh, D., Sharman, R., Rao, H.R. and Upadhaya, S. (2007) Self-healing systems—survey and synthesis. *Decision*, *Support Systems*, **42(4)**, 2164-2185

[132] Peairs, D.M., Park, G. and Inman, D.J. (2004) Practical issues of activating self-repairing bolted joints. *Smart Materials and Structures*, **13(6)**, 1414-1423.

[133] Wang, H.-W., Yuan, Y.C., Rong, M.Z. and Zhang, M.Q. (2010) Self-Healing of thermoplastics via living polymerisation. *Macromolecules*, **43(2)**, 595-598.

[134] Cho, S.H., White, S.R. and Braun, P.V. (2009) Self-Healing polymer coatings. *Advanced Materials*, **21(6)**, 645-649.

[135] Beiermann, B.A., Keller, M.W. and Sottos, N.R. (2009) Self-Healing flexible laminates for resealing of puncture damage. *Smart Materials and Structures*, **18(8)**, 1-7.

[136] Caruso, M.M., Schelkopf, S.R., Jackson, A.C., Landry, A.M., Braun, P.V. and Moore, J.S. (2009) Microcapsules containing suspensions of carbon nanotubes. *Journal of Materials Chemistry*, **19(34)**, 6093-6096.

Molecular dynamics simulations of the interaction of carbon nanotube and a carbon disulfide solvent

Kholmirzo Kholmurodov[1,2]*, Guzel Aru[1], Kenji Yasuoka[3]

[1]Laboratory of Radiation Biology, Joint Institute for Nuclear Research, Dubna, Russia; *Corresponding Author: mirzo@jinr.ru
[2]International University "Dubna", Dubna, Russia
[3]Department of Mechanical Engineering, Keio University, Yokohama, Japan

ABSTRACT

An analysis of the molecular dynamics (MD) of the interaction between a carbon nanotube (CNT) and a carbon disulfide active solvent (CS$_2$) has been carried out. The aim of the present work is to estimate the dynamical and structural behavior of the CNT-CS$_2$ system at different relative atomic concentrations and under temperature changes. The structural radial distribution functions and the dynamical configurations have been built for a CNT interacting with a CS$_2$ solvent. A nontrivial observation for the CNT-CS$_2$ system is that the solvent carbon disulfide atoms make up a patterned (layered) formation around the carbon nanotube.
Keywords: Molecular Dynamics; Carbon Nanotube; Carbon Disulfide Solvent

1. INTRODUCTION

Among the organic materials, carbon Nanotubes (CNTs) are unique for their electrical and chemical properties. They are very interesting in terms of material research and electronic applications. Depending on their chemical structure, carbon nanotubes (CNTs) can be used as an alternative to organic or inorganic semiconductors as well as conductors. The chemical bonding of nanotubes is composed entirely of sp^2 bonds, similar to those of graphite. This bonding structure, which is stronger than the sp^3 bonds found in diamonds, provides the molecules with their unique strength. Nanotubes naturally align themselves into "ropes" held together by van der Waals forces. The nature of the bonding of a nanotube is described by quantum chemistry—specifically, orbital hybridization. Solvents in which the CNTs can be solubilized include chlorobenzene, chloroform, methylene chloride, carbon disulfide, benzene, etc. The solubilities

of the carbon nanotubes in these solvents range from about 0.01 to 5.0 mg/ml [1-4].

The aim of the present paper is to simulate the dynamical and structural properties of a CNT interacting with a carbon disulfide (CS$_2$) solvent taking into account the Van der Waals forces only. For the CNT-CS$_2$ system, we simulate different relative CNT solvent concentrations and temperature scales. In the description of the physical properties of the CNT, we employ the Tersoff potential [5]. It is a special case of a density-dependent potential, which reproduces the properties of the covalent bonding in systems containing carbon, silicon, germanium, etc, and alloys of these elements. A special feature of the potential is that it allows bond breaking and associated changes in bond hybridization. The energy is modelled as a sum of pair-like interactions where, however, the coefficient of the attractive term in the pair-like potential (which plays the role of the bond order) depends on the local environment giving a many-body potential.

The Tersoff potential has 11 atomic and 2 bi-atomic parameters (see, formulas 1-9):

$$U_{ij} = f_C(r_{ij})[f_R(r_{ij}) - \gamma_{ij} f_A(r_{ij})], \tag{1}$$

where the potential parameters have the following forms:

$$f_R(r_{ij}) = A_{ij} \exp(-a_{ij} r_{ij}), \tag{2}$$

$$f_A(r_{ij}) = B_{ij} \exp(-b_{ij} r_{ij}), \tag{3}$$

$$f_C(r_{ij}) = \frac{1}{2} + \frac{1}{2}\cos[\pi(r_{ij} - R_{ij})/(r_{ij} - R_{ij})], \ R_{ij} < r_{ij} < S_{ij}, \tag{4}$$

In (1) $f_R(r_{ij})$ and $f_A(r_{ij})$ mean repulsive and attractive, $f_C(r_{ij})$ —potential cutoff functions ($f_C(r_{ij}) = f_C(r_{ij}) = 1$ for $r_{ij} < R_{ij}$ and $f_C(r_{ij}) = 0$ for $r_{ij} > S_{ij}$).

It is worth noting that the main feasure of the Tersoff potential is that the coefficients in (1) reflect many-body

nature of the interactions. The basic means of the coefficients is that the strenth of each bond depends on the local environment and is lowered when the number of neighboors is relatively high. This dependence can accentuate or diminish the attractive force relative to the repulsive force, according to the environment, such that:

$$\gamma_{ij} = \chi_{ij}(1 + \beta_i^{\eta_i} L_{ij}^{\eta_i})^{-1/2\eta_i}, \qquad (5)$$

$$L_{ij} = \sum_{k \neq i, j} f_C(r_{ik})\omega_{ik} g(\theta_{ijk}), \qquad (6)$$

$$g(\theta_{ijk}) = 1 + c_i^2 / d_i^2 - c_i^2 / [d_i^2 + (h_i - \cos\theta_{ijk})^2], \qquad (7)$$

$$a_{ij} = (a_i + a_j)/2, \quad b_{ij} = (b_i + b_j)/2, \qquad (8)$$

$$A_{ij} = (A_i A_j)^{1/2}, \quad B_{ij} = (B_i B_j)^{1/2}, \quad A_{ij} = (A_i A_j)^{1/2},$$
$$R_{ij} = (R_i R_j)^{1/2}, \quad S_{ij} = (S_i S_j)^{1/2}. \qquad (9)$$

We have accepted the following values: $\chi_{ii} = 1$, $\chi_{ij} = \chi_{ji}$, $\omega_{ii} = 1$, $\omega_{ij} = \omega_{ji}$.

The carbon disulfide (CS_2) solvent has a comparatively high solubility (~7.9 mg/ml). Several earlier papers considered interaction between the CS_2 solvent and a fullerene (C_{60}) solution [6-12]. The C_{60}-CS_2 system belongs to a class of solutions where a peak in the temperature dependence of solubility is observed (T_{max}~280 K). The structural features of the fullerene in a solution, as well as the fullerene—solvent (C_{60}–CS_2) interaction mechanism have been investigated in detail in [6-12] by different methods (small-angle neutron scattering (SANS) and others). As was noted in [12], the characteristic size of the CS_2 molecule (~0.3 nm) is comparable to that of the C_{60} fullerene (~ 1 nm); so, any interface organization of the CS_2 molecules different from that in bulk must result in a significant difference between the interface and bulk molecular density of the solvent, and, hence, affect the visible size of the fullerene.

2. MATERIALS AND METHODS

We performed the molecular dynamics (MD) simulation of several CNT-CS_2 model systems. The MD simulation was based on the DL_POLY general-purpose code [13-15]. The MD cell is orthorhombic and square in the XY plane ($30.7 \times 30.7 \times 41.7$). The integration algorithm is an NPT Berendsen 'ensemble'.

The CNT (carbon nanotube) consists of 800 carbon atoms in a nanotube of 41.7 angstrom in length (see **Figure 1**). For the CNT, we used the Tersoff potential parameters of the DL_POLY software database [13-14]:

$A = 1393.6$, $a = 3.4879$, $B = 346.74$, $b = 2.2119$, $R = 1.8$, $S = 2.1$,
$\beta = 1.5724 \times 10^{-7}$, $\eta = 0.72751$, $c = 38049$, $d = 4.3484$, $h = -0.57058$.

The CS_2 molecules were treated as rigid with the bond length of 1.55 angstrom between carbon and sulfide atoms (**Figure 2**). Throughout the computation, only the Lennard-Jones (LJ) interactions were taken into account. The number of the CS_2 solvent molecules was varied, so we simulated CNT-solvent model systems of different relative atomic concentrations: x = 0.2, 0.4, …, 1.0 (**Figure 3**). The LJ potential was also used for the CNT—solvent interactions; the potential and parameteres are shown in **Table 1**, where C denotes the CNT carbon
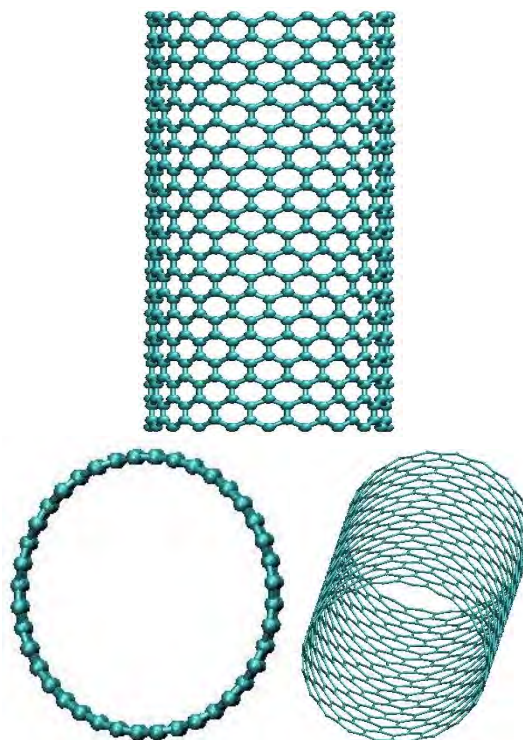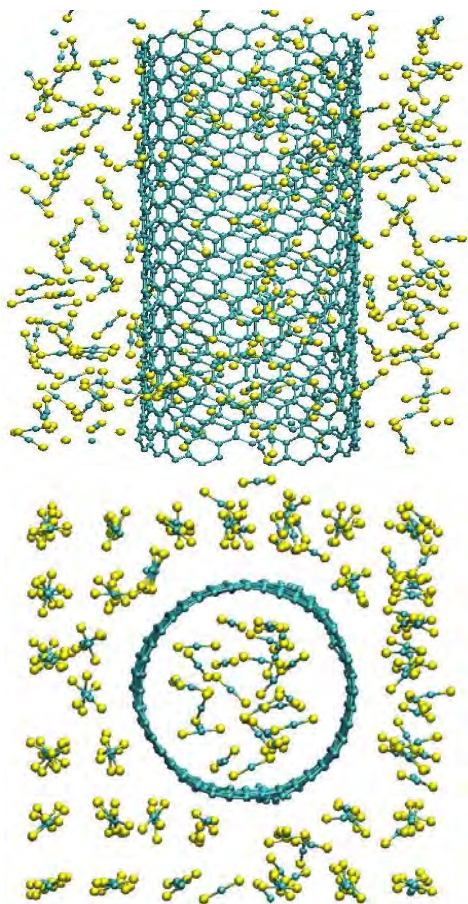

Figure 1. Structural presentations of the carbon nanotube (CNT) (top and bottom).

Table 1. Potential parameters of the CNT-CS_2 model.

Atomic pair	Potential	Functional form	Parameters	ε, eV	σ, Å
C-C $_S$	Lj	$U(r) = 4\varepsilon\left[\left(\frac{\sigma}{r}\right)^{12} - \left(\frac{\sigma}{r}\right)^{6}\right]$	ε, σ	0.0044	3.35
C-S	Lj	…	ε, σ	0.0082	3.44
S-S	Lj	…	ε, σ	0.0153	3.52

Figure 2. Structural presentations of the CS_2 solvent (top and bottom).

Figure 3. Structural presentations of the CNT-CS_2 system (top and bottom).

atoms and C_s—the carbon atoms of the CS_2 solvent.

3. RESULTS AND DISCUSSIONS

The dynamics of the interaction between the CNT (carbon nanotube) and the CS_2 solvent has been studied at different ratios of the CNT-solvent atomic concentrations:

$$x = \frac{N_S}{N_{CNT}}$$

where N_s is the number of the solvent atoms and N_{CNT} is the number of the CNT atoms. We have simulated five CNT-CS_2 systems with $x = 0.2$, 0.4, 0.6, 0.8 and 1. We call the systems with $x = 0.2$ and $x = 1$ low- and high-density systems, respectively. The CNT consists of 800 carbon (C) atoms. Further, we denote the carbon atoms of the CS_2 solvent as C_s.

3.1. Structural RDFs for the CNT-Solvent Atomic Pairs

In **Figure 4**, we present the behavior of the radial
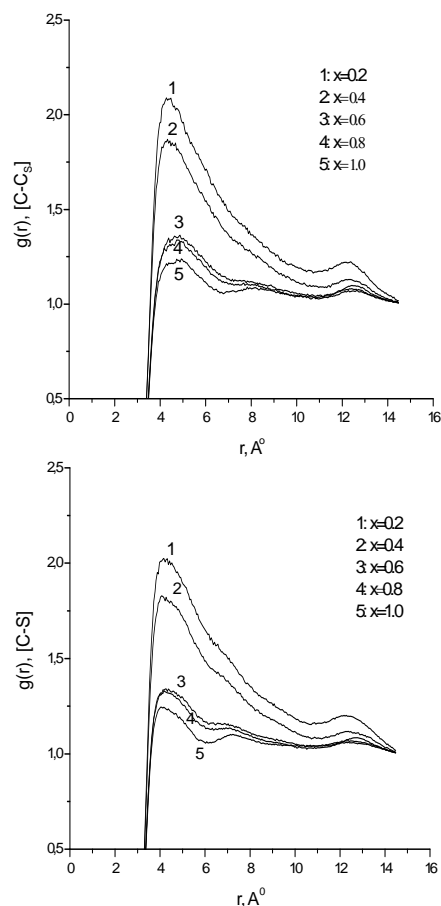
Figure 4. Structural RDFs for the atomic pairs C-Cs and C-S at different ratios of the CNT–solvent atomic concentration x.

distribution function (RDF) for the CNT-solvent atomic pairs C-C_s and C-S at different values of x. It can be seen that the RDF of the CNT-CS_2 system at x > 0.4 obeys a similar law. For all values of x, we have clearly observed two peaks in the RDF graphs. However, for x > 0.4, **Figure 4** shows an additional small RDF peak between the first two ones. This behavior of the RDF points to a structural rearrangement of the CNT-CS_2 system, which is going from the low density phase (x = 0.2) into the high density phase (x = 1). The additional (third) peak in the RDF curve has also been observed on the temperature dependence (part III below).

3.2. Structural RDFs for the Solvent-Solvent Atomic Pairs

In **Figures 5** and **6**, the radial distribution functions (RDFs) are presented for the solvent-solvent atomic pairs (C_s-C_s, C_s-S, and S-S) at different values of x. It is seen that the RDFs of the solvent atoms differ from each other by their first peaks only; the secondary peaks for all solvent-solvent atomic pairs (CS_2-CS_2) are similar. The RDF for the S-S atoms has a comparably large first
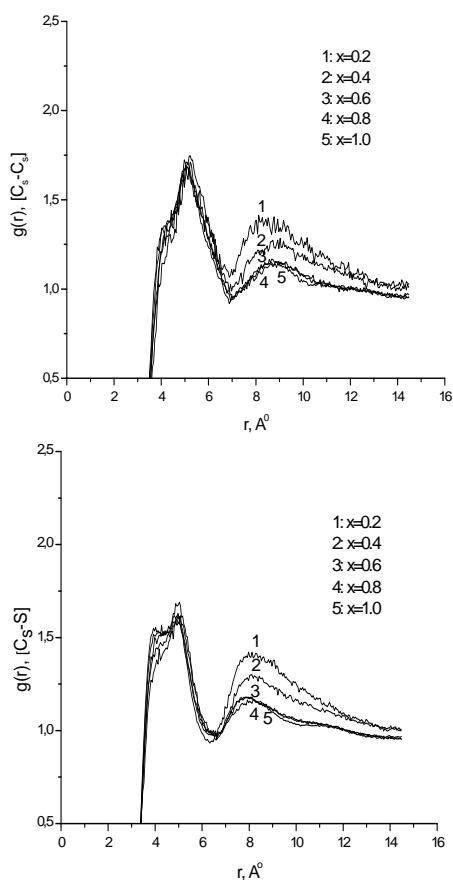
Figure 5. Structural RDF for the atomic pairs Cs-Cs and Cs-S at different ratios of the CNT—solvent atomic concentration x.
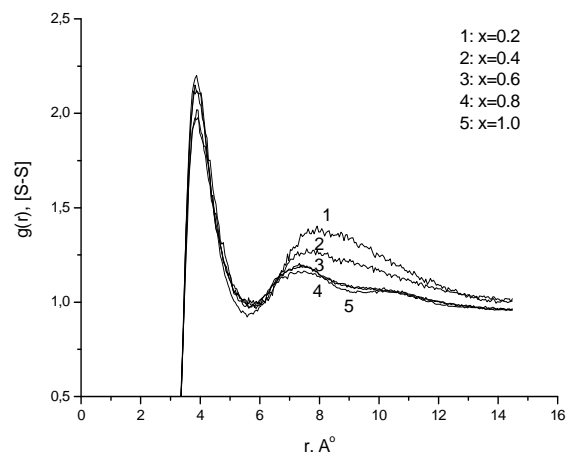
Figure 6. Structural RDF for the atomic pair S-S at different ratios of the CNT–solvent atomic concentration x.

peak (**Figure 6**). This indicates that in the solvent media, the atomic pair S-S has a relatively high ordering in comparison with the C_s-C_s one. The RDF first peak for the C_s-S atomic pair (**Figure 5**, below) is low as compared with S-S ones. We attribute such behavior to an influence of CNT's carbon (C) atoms on the CNT—solvent interaction process and ordering.

3.3. MD-Simulated Structural CNT-CS_2 Configurations

We have compared the MD structural configurations of the CNT-CS_2 system for the low-density (x = 0.2) and high-density (x = 1) phases. In **Figure 7**, MD-simulated snapshots are presented for x = 0.2. **Figure 7** shows the side and top views (left and righr, respectively) of the CNT-CS_2 system; the snapshots correspond to the moments of t = 0 (top), 10 ps (middle), and 80 ps (bottom). It is seen that starting from arbitrarily distributed positions at the initial (t = 0) state, the solvent (CS_2) atoms become more structured in the later states of the dynamics around and inside the CNT.

The CS_2 structuring behavior around the CNT has also been observed during temperature variation in the CNT-CS_2 system. In **Figure 8**, the RDF curves are displayed for the low density phase (x = 0.2) depending on temperature: T = 200 K (1), T = 250 K (2), and T = 300 K (3). **Figure 8** shows the RDF results for CNT-solvent atomic pairs C-C_s (left) and C-S (right). The RDFs in **Figure 8** show some RDF changes (only for the first peaks).

Figure 9 shows RDF curves for the solvent-solvent atomic pairs C_s-C_s (left) and C_s-S (right). A visible change in the RDF graph is seen for the atomic pair C_s-S. During the temperature variation, we observe   changes for C_s-S both in the first and secondary peaks.
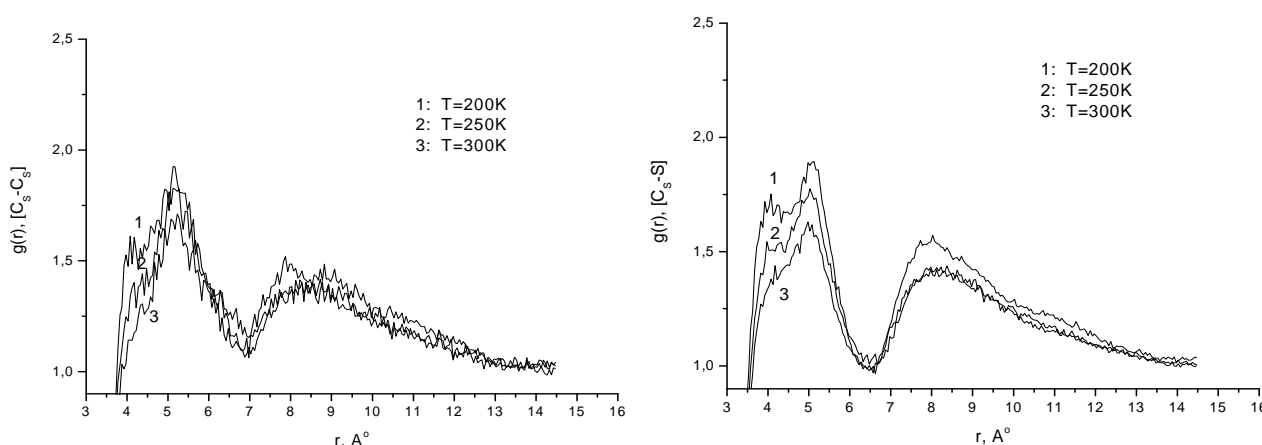
A is seen in the RDF graph in **Figure 10**, the atomic

(a) Low-density phase (x = 0.2)

t = 0   t = 0

t = 10 ps   t = 10 ps

t = 80 ps   t = 80 ps
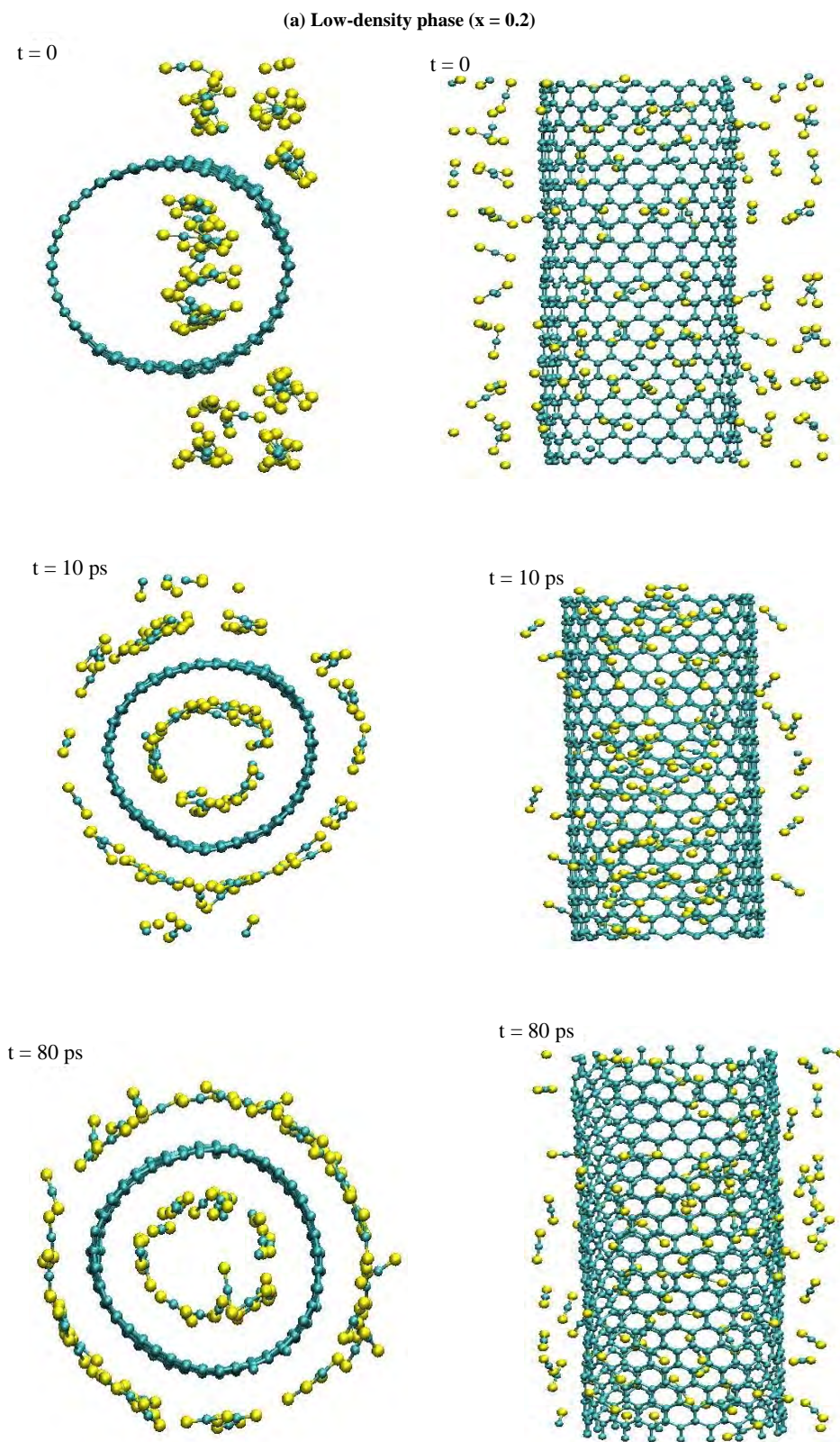
Figure 7. Snapshots of the CNT―solvent configurations at a low density (relative atomic concentration x = 0.2).

Openly accessible at http://www.scirp.org/journal/NS/
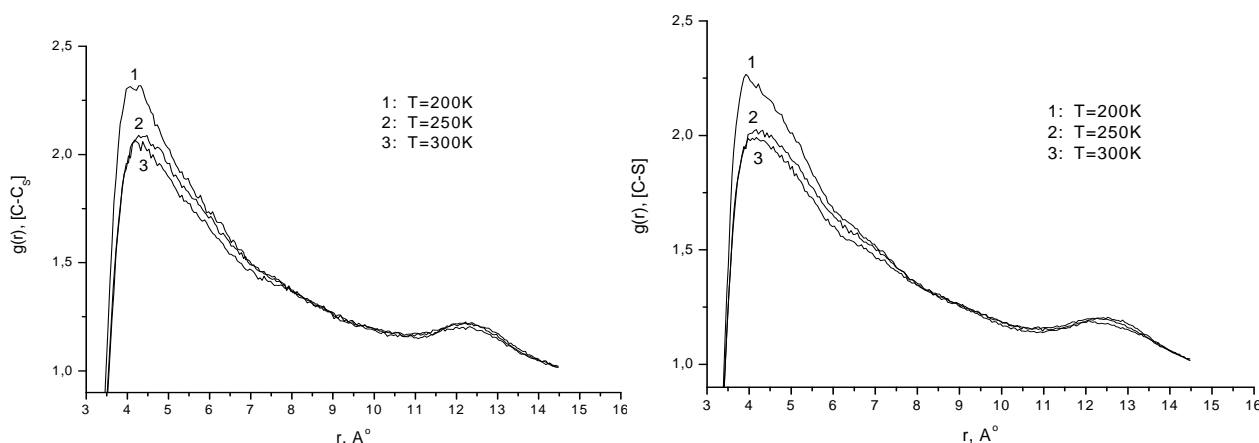
Figure 8. Structural RDFs for the atomic pairs C-Cs and C-S at x = 0.2 with temperature.

Figure 9. Structural RDF for the atomic pairs Cs-Cs and Cs-S at x = 0.2 with temperature.
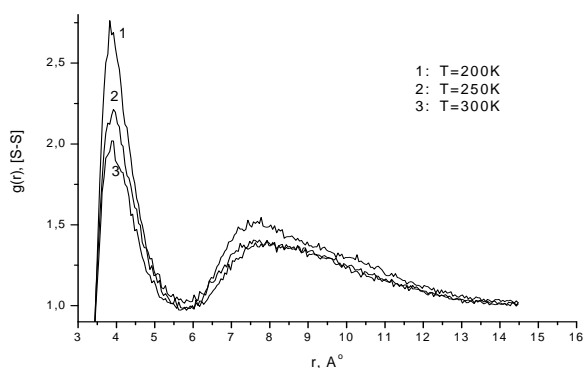
Figure 10. The structural RDF for the atomic pair S-S at x = 0.2 with temperature.

pair S-S has a relatively high ordering in the solvent media. Also, the RDF for the S-S pair shows a strong temperature dependence. We see that the amplitude of the first peak decreases twice as the temperature increases from T = 200 K to 300 K.

In **Figure 11**, the MD snapshots are presented for the high density phase (x = 1).

Comparing these results with those of the low density phase (x = 0.2, **Figure 7**), we observe a similar structural formation of the CS_2 solvent atoms around the CNT. However, the RDFs of the high-density phase are strongly specific against the low-density phase RDFs. A comparison of **Figures 12-14** with **Figures 8-10** is straightforward.

3.4. Patterned Structure Formation in the CNT-CS$_2$ System

One of the nontrivial observations for the CNT-CS$_2$ system is that the solvent carbon disulfide atoms make up a patterned (layered) formation around the carbon nanotube. In **Figure 15**, we present a CNT-CS$_2$ resultant structure where the atomic distributions are compared in three regions (marked by the circles 1, 2, and 3). It is seen that in regions 1 and 2, the solvent CS$_2$ atoms have to be configured similarly to CNT's shape. The solvent atoms inside and outside the CNT are regularly distributed within the spheres of the same radii off the CNT. In contrast, for region 3 we observe an

(b) High density phase (x = 1)

t = 0

t = 0

t = 10 ps

t = 10 ps

t = 80 ps

t = 80 ps
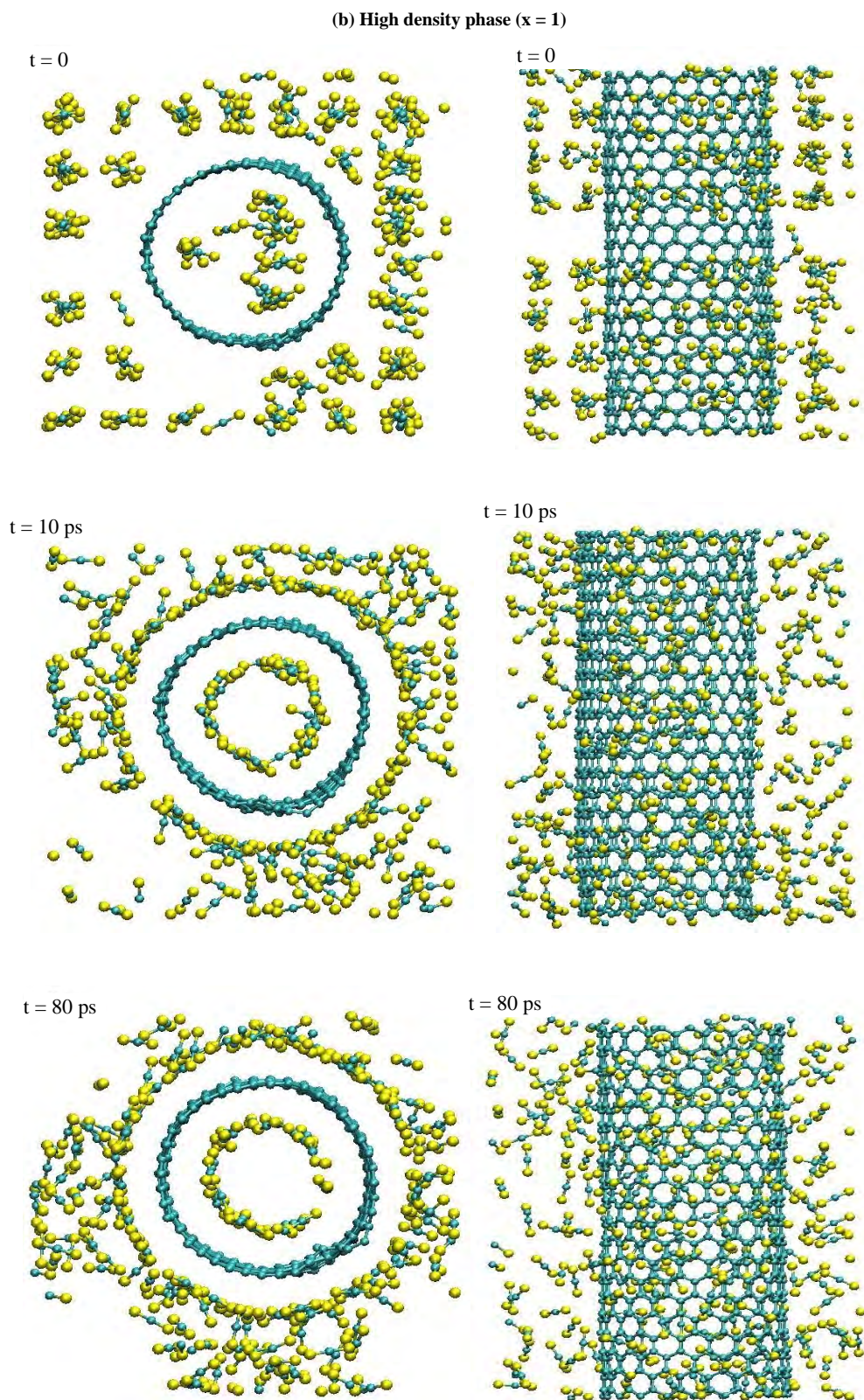
Figure 11. Snapshots of the CNT―solvent configurations at a high density (relative atomic concentration x = 1).

　　　　　　　　　　　Openly accessible at http://www.scirp.org/journal/NS/
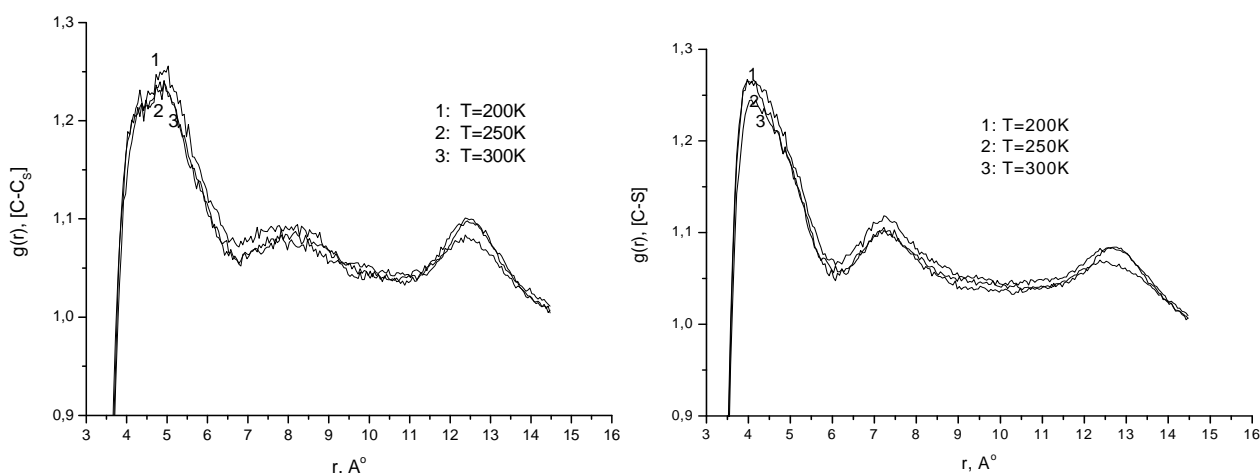
Figure 12. Structural RDFs for the atomic pairs C-Cs and C-S at x = 1 with temperature.
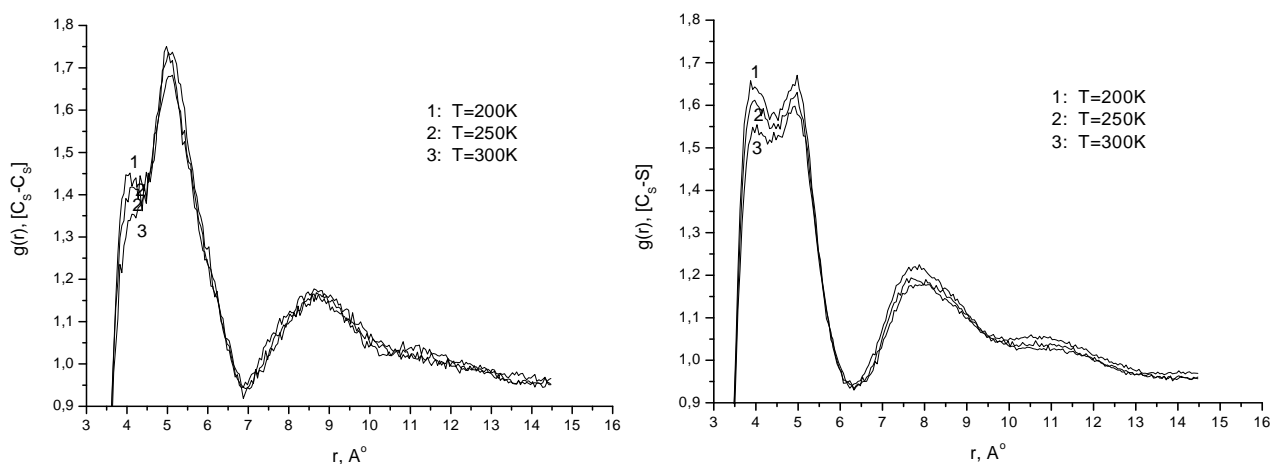
Figure 13. Structural RDFs for the atomic pairs Cs-Cs and Cs-S at x = 1 with temperature.
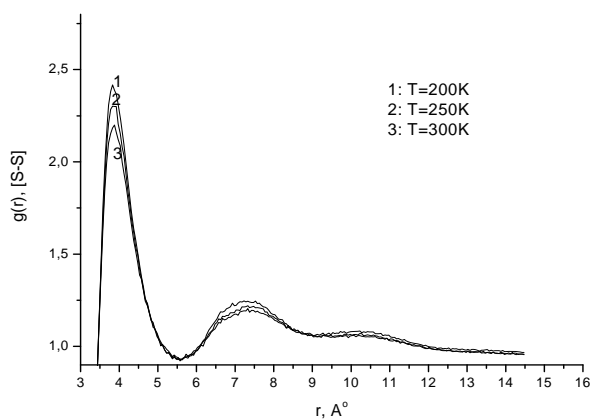
Figure 14. Structural RDF for the atomic pair S-S at x = 1 with temperature.

irregular structure of the same atoms that results from solvent-solvent ineraction. It should be noted that **Figure 15** shows an important example of a graphene-
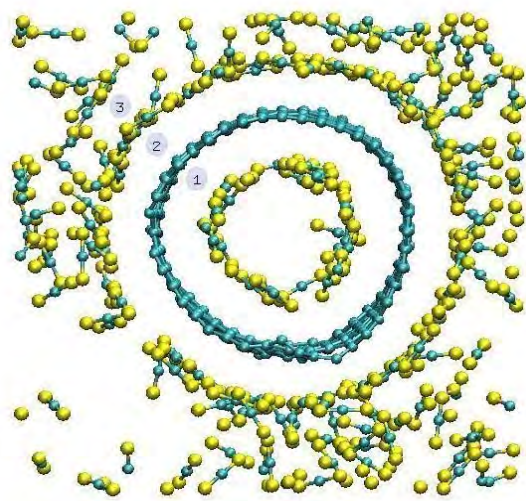
Figure 15. The CNT-CS2 atomic distributions for three regions shown as circles 1, 2, and 3.

like (patterned, layered) behavior. Such formations are of great importance for the applications and technological uses of the CNT-CS$_2$ systems [1-12].

4. ACKNOWLEDGEMENTS

REFERENCES

[1] Zheng, L.X., O'Connell, M.J., Doorn, S.K., Liao, X.Z., Zhao, Y.H., Akhadov, E.A., Hoffbauer, M.A., Roop, B.J., *et al*. (2003) *Nature Materials*, **3(10)**, 673-676.

[2] Mintmire, J.W., Dunlap, B.I. and White, C.T. (1992) *Physical Review Letters*, **68(5)**, 631-634.

[3] Dekker, C. (1999) Carbon nanotubes as molecular quantum wires. *Physics Today*, **52(5)**, 22-28. http://www.physicstoday.org/vol-56/iss-2/pdf/Vol52no5p22-28.pdf

[4] Martel, R., Derycke, V., Lavoie, C., Appenzeller, J., Chan, K.K., Tersoff, J. and Avouris, Ph. (2001) Ambipolar electrical transport in semiconducting single-wall carbon nanotubes. *Physical Review Letters*, **87(25)**, 256805.

[5] Tersoff, J. (1989) *Modeling solid-state chemistry*: *Interatomic potentials for multicomponent systems. Physical Review B*, **39(8)**, 5566-5568.

[6] Affholter, K.A., Henderson, S.J., Wignall, G.D., Bunick, G.J., Haufler, R.E. and Compton, R.N. (1993) Structural characterization of C$_{60}$ and C$_{70}$ fullerenes by small-angle neutron scattering. *Journal of Chemical Physics*, **99(11)**, 9224-9229.

[7] Melnichenko, Y.B., Wignall, G.D., Compton, R.N. and Bakale, G. (1999) Characterization of fullerenes and fullerene derivatives by small-angle neutron scattering and transmission measurements. *Journal of Chemical Physics*, **111(10)**, 4724.

[8] Smorenburg, H.E., Crevecoeur, R.M., de Schepper, I.M. and de Graaf, L.A. (1995) Structure and dynamics of C$_{60}$ molecules in liquid CS$_2$ from neutron scattering. *Physical Review E*, **52(3)**, 2742-2752.

[9] Migliardo, F., Magazu, V. and Migliardo, M. (2004) Structural properties of C$_{60}$ in solution. *Journal of Molecular Liquids*, **110(1-3)**, 3-6.

[10] Tomiyami, T., Uchiyama, S. and Shinohara, H. (1997) Solubility and partial spartial volume of C$_{60}$ and C$_{70}$. *Chemical Physics Letters*, **264**, 143-148.

[11] Bokare, A.D. and Patnaik, A. (2003) Microscopic diffusion model applied to C$_{60}$ fullerene fractals in carbon disulphide solution. *Journal of Chemical Physics*, **119(8)**, 4529-4538.

[12] Teterev, Yu., Aksenov, V.L., Avdeev, M.V. and Kholmurodov, Kh.T. (2007) Organization of solvent at interface with fullerene in solution C60/carbon disulfide by molecular bynamics simulations. In: Kholmurodov, K., Ed., *Molecular Simulation Studies in Materials and Biological Sciences*, Nova Science Publishers, New York, 129-134.

[13] Smith, W. and Forester, T.R. (1996) The DL_POLY molecular simulation package. *Journal of Molecular Graphics*, **14(3)**, 136-141.

[14] Smith, W., Forester, T.R. and Todorov, I.T. (2008) The DL poly 2 user manual. Version 2.19, STFC Daresbury Laboratory Daresbury, Warrington WA4 4AD Cheshire, UK.

[15] Kholmurodov, K., Smith, W., Yasuoka, K. and Ebisuzaki, T. (2000) Highly vectorised "link-cell" Fortran code for the DL_POLY molecular dynamics simulation package. *Computer Physics Communications*, **125(1-3)**, 167-192.

North pacific cool-down: 1940s-1960s

Kern E. Kenyon

4632 North Lane, Del Mar, USA; kernken@aol.com

ABSTRACT

Between the 1940s and the 1960s there was a significant lowering of the surface temperatures of the central North Pacific. This cool-down is discussed on the basis of analyses of a very large surface temperature data base, covering most of the North Pacific, which began in 1947 and continued for at least 30 years afterwards. A surface area more than 20 degrees of latitude by approximately 70 degrees of longitude, centered on 40°N, cooled down within about a ten year period by typically 0.5℃ and by as much as 1.0℃. Previously a permanent surface and near surface circulation was proposed in which a shallow very broad warm surface layer flows northeastward at mid-latitudes on the eastern side of the North Pacific while colder water returns southward to the east, west and underneath the warm surface current. It is suggested that variations in this hypothesized circulation, due to natural causes not yet completely understood, potentially provide a mechanism for producing a cooling down (or warming up) of a large region of the central North Pacific at mid-latitudes in a relatively short period of time (ten years or less).

Keywords: Climate Change; Cool-Down; North Pacific; Sea Surface Temperatures

1. INTRODUCTION

"The earth's average surface temperature has increased by about 1.2°F in the past century, with most of the increase occurring from about 1920 to 1950, and again beginning around 1975" [1]. A curious reader will want to know what happened between 1950 and 1975. One might infer from this quote that the earth's average surface temperature also increased from 1950 to 1975, only at a slower rate. But since 1982 it has been established that a "confusing" cooling trend occurred from around 1940 to the 1960s as illustrated by the average surface temperatures of the Northern Hemisphere [2]. More specifically, though not explained either, is the fact that the annual mean temperature of the United States as a whole lowered between about 1953 and 1968 by roughly 0.7℃ [3]. It is shown below, through analyzing an extensive set of sea surface temperature data, involving millions of ship injection temperatures [4], that the temperature of most of the North Pacific Ocean's surface waters dropped, in the mean, by around 0.5℃ within a ten year span between about 1949 and 1959.

From data analyses published earlier [5,**Figure 1**] comes the educated guess that a large slice of the North Pacific was cooling down simultaneously with the US within about a 30 year period starting in 1947. The figure shows sea surface temperatures, averaged over a month and 5 degree latitude/longitude squares, plotted against longitude, between California and Japan, along 35°N for six consecutive months. For each month and longitude three means are compared: 10, 20, and 29 years, all beginning with 1947. Over most of the interior of the ocean the three curves are nested with the 29 year mean lying on the bottom, the 10 year mean on top and the 20 year mean in between these two. Temperature gaps separating the curves are small, in the 0.1℃ range, but systematic over a large band of longitudes (about 70 degrees), implying a consistent mean cooling from 1947-1975 (This cool-down was noticed by the author at the time the figure was made but not mentioned explicitly in that paper because it was not relevant to the purpose at hand).

Here an examination of the cool-down is presented which is expanded from a single latitude line (35°N) to a band of latitudes (30-50°N) but at the same time more narrowly focused in time: the most intense period of cooling is condensed from 30 to 10 years. It is not that the author is purposefully avoiding the currently popular subject of global warming; it is only that the data that are readily available to him happened to coincide with the cool-down of the North Pacific, which is sandwiched between two perhaps better known warming periods.

A characteristic of recent books and position papers
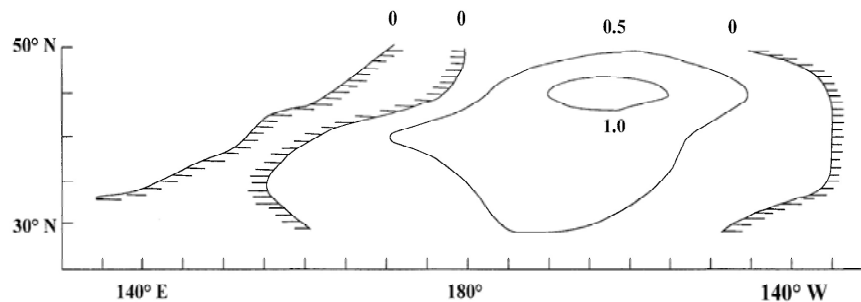
Figure 1. Temperature difference map for the surface of the mid-latitude central North Pacific. Monthly five degree temperatures from the Namias-Scripps data base were averaged over two separate five year periods: 1947-1951 and 1957-1961, after which the annual mean was taken over the twelve months for both periods. Then the 57-61 averages were subtracted from the 47-51 averages for each five degree latitude/longitude square and contours (℃) of surface temperature difference were drawn on the map. A cool-down occurred in a large region in the middle of the map. Hatch marks indicate smaller areas that warmed up between 47-51 and 57-61. Latitude on the vertical axis, longitude on the horizontal axis.

on global warming and climate change is that they are long on discussion but short on data presentation. In this brief journal article an effort is made to have a more balanced account. Also it appears that nobody has yet specifically studied the particular North Pacific SST data base in terms of short period climate variations in the way I have chosen to look at these observations here.

2. MAIN RESULT

Figure 1 shows the final product of the analysis: a map of sea surface temperature differences for the central area and mid-latitude region of the North Pacific. It is based on the Namias-Scripps sea surface temperatures, which extend from coast to coast and from 20-55°N. For a given month and five degree latitude/longitude square all reported injection temperatures from merchant ships were combined to get a single number. In my possession are computer printouts of the temperatures from January 1947 through December 1977. These printouts were used to make **Figure 1** by means of averaging and subtracting. I do not know if the one month five degree square average data set continued after 1977. If it did, somebody could easily use these data to study global warming as reflected in the surface temperatures of the North Pacific.

Construction of **Figure 1** was carried out as follows. For each five degree latitude/longitude square and month a straight five year average was computed starting in 1947 and ending in 1951. Then the annual mean was made by averaging over the twelve months. Exactly the same procedure was done for the interval 1957-1961. By subtracting one set of five-year means from the other a map of sea surface temperature differences was obtained.

What **Figure 1** shows is that between the 1947-1951 annual mean and the 1957-1961 annual mean the whole central mid-latitude region of the North Pacific cooled down by typically 0.5℃ and by as much as 1.0℃.

Although the cool-down may have started as early as about 1940, as mentioned above, there is no way I have to investigate any warming or cooling of the North Pacific before 1947, which is the start of the Namias-Scripps sea surface temperature data set. However, a systematic cooling was found to take place over the 29 year period 1947-1977 along 35°N [5]. Here the cooling period has been narrowed from the upper end of this 30 year period such that the most intense cooling occurred within the interval 1947-1961. If desired perhaps a further narrowing could be investigated in the time domain by taking running means instead of five year block averages, which was the simplest way to begin the investigation using the given temperature printouts. Also the map in **Figure 1** could be extended southward to 20°N and northward to 55°N, but then there are occasional gaps in the temperature record for some five degree squares and certain seasons which are outside the normal shipping lanes.

3. PROCEDURE

Figure 1 can be dissected in various ways, but what follows comes closest to the actual way it was put together in the first place. One intermediate step between the raw data and the final result is shown in **Figure 2**, which exhibits the five year annual mean surface temperatures as a function of longitude along 40°N: the solid curve is for 1947-1951, the dashed curve is for 1957-1961. If the dashed curve is subtracted from the solid one in **Figure 2**,
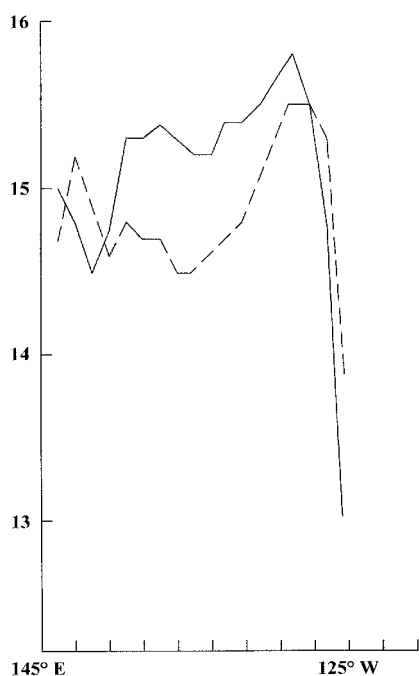
Figure 2. Five year annual mean surface temperatures (℃, vertical axis) as a function of longitude along $40°N$ (horizontal axis). Solid curve is for 1947-1951; dashed curve is for 1957-1961.

the temperature differences along $40°N$ in **Figure 1** are reproduced. It can be seen from Figure 2 that the averaged surface temperatures of 1957-1961 were significantly lower by about half a degree Centigrade than the corresponding ones of 1947-1951 over the entire central portion of the slice of the North Pacific Ocean at $40°N$.

A striking feature is revealed in **Figure 2**, but due to the subtraction involved **Figure 1** contains no hint of it. In the eastern half of the ocean there is a large-scale longitudinal maximum in surface temperature. Proceeding west from California the surface temperature rises to a maximum at around $145°W$ and then decreases again. The maximum occurs in both curves, and it is a real and permanent feature as documented previously [5]. Along $35°N$ there is an analogous maximum is surface temperature. It is interesting that the eastern maximum in **Figure 2** has already survived the annual mean plus five years of averaging. Were the averaging interval to extend over 10, 20 or even 30 years the maximum would still be there.

Figure 3 comes one step closer to the raw data in that it shows five year averages of surface temperature along $40°N$ but just for the month of January. Again the solid curve is for 1947-1951 and the dashed one is for 1957-1961. Here a much larger lowering of the temperature by almost $2℃$ between the two periods oc-

curred in the central North Pacific. Also prominent in both the solid and dashed curves of **Figure 3** is the longitudinal maximum temperature in the eastern Pacific.

Finally, two examples of the basic data are given along $40°N$ in **Figure 4** for January of two particular years: 1948 and 1958. A cool-down occurred between these two Januaries, ten years apart, but it is distributed mainly in the eastern side of the ocean. Very pronounced is the longitudinal maximum for January of 1948.

4. DISCUSSION

Although the question of the ocean's role in climate change has been forcefully raised [6], so far there are no answers coming back that can explain a significant surface temperature change ($0.5℃$) over a large area (70 degrees of longitude by more than 20 degrees of latitude) in a short time (10 years or less), outside of extreme conditions like the beginnings and endings of the ice ages, which are presumed to take place relatively quickly.

Consider the permanent longitudinal maximum in surface temperature on the eastern side of the ocean at mid-latitudes, examples of which are illustrated in **Figures 2-4** (and more in depth studies of which were carried out before [5]). What is the most reasonable inter-
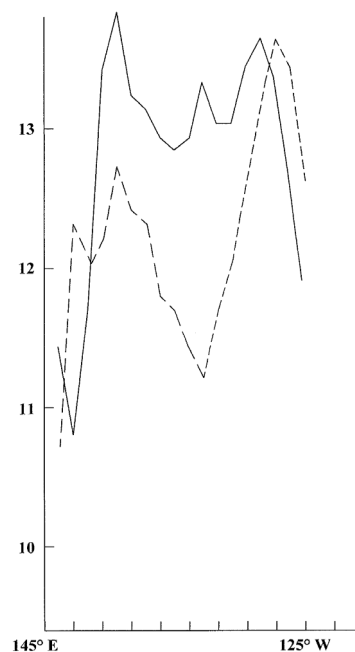
Figure 3. Five year mean temperatures (℃, vertical axis) for January as a function of longitude along $40°N$ (horizontal axis. Solid curve is for 1047-1951; dashed curve is for 1957-1961.
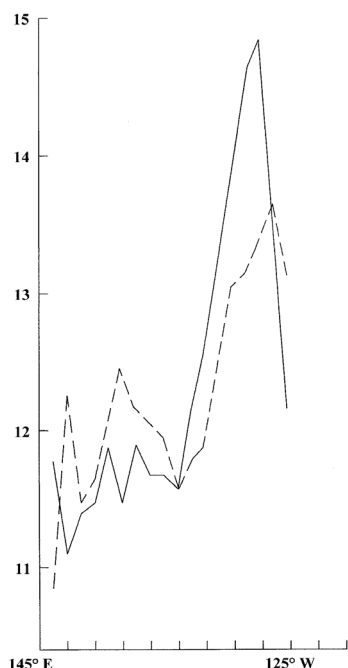
Figure 4. Monthly mean temperatures (℃, vertical axis) for January as a function of longitude along 40°N (horizontal axis). Solid curve is for 1948; dashed curve is for 1958.

pretation of this real feature? Since the water to the east, west and underneath the temperature maximum is colder, and the air temperature above it is colder too (estab-lished from meteorological data taken on individual cruises), a plausible explanation is that in order to sustain the permanent longitudinal temperature maximum, warm surface water must continually be brought in to the area of the maximum from lower latitudes. In other words, the longitudinal maximum temperature is the signature of a broad northward flow of warm surface water. A comprehensive hydrographic section along 35°N [7] strongly suggests that the broad warm current is also shallow, about 100 m at the most. Consistent with this idea is the notion that colder water returns south, crossing mid-latitudes, to the east and west of the longitudinal temperature maximum at the surface and under the surface maximum at about 100 m below the surface.

Such a broad surface current, hiding in plain sight until recently put forward [8], is potentially capable of changing the surface temperature of a large region of the North Pacific by about 1℃. For example, notice the variability displayed by the longitude and temperature scales of the temperature maximum in **Figures 2-4**. While existing in every month of every year so far studied along 35 and 40°N, there are month to month changes within a single year and year to year changes for a given month. Inquiries as to exactly how such changes in sea surface temperature are brought about by changes in the warm current are projects for the future. Also, although the reality of the permanent longitudinal temperature maximum feature itself at mid-latitudes on the eastern side of the ocean is not in any doubt, there have been no independent observational checks on the month to month changes in this feature that are revealed in the Namias-Scripps surface temperature data set. Nor have year to year changes of the longitudinal maximum for a given month been confirmed by separate means.

How quickly could a change in surface temperature of 1.0℃ be expected to occur over broad reaches of the North Pacific? If the warm current is indeed chiefly responsible, then one way to estimate a lower bound on the required time is the distance traveled by the warm water divided by its mean flow rate, *i.e.* an advective time-scale. Earlier analyses gave the flow rate in the ball park of 10 cm/sec or less [8] and the travel distance is in the range of 1,000 to 10,000 km, from which a rough time-scale of 3 years or less is computed.

Finally, one should add that all the conceivable causes of the North Pacific cool-down are still not known at this point, nor is it yet possible to definitely link the observed cool-down to the influences of man. Optimistically, if the cool-down were better understood, it may follow that an increase takes place in understanding the warmings that came before and after the cooling. Natural causes involving the proposed northward warm current and its colder southward return flow are suggested here for contributing to the cool-down, but this method could work equally well for the warmings. On the other hand, if a good fraction of the warmings is to be blamed on man's activities, then the question is: how can the cool-down in between two warming periods be accounted for in terms of the interference of man?

REFERENCES

[1] Emanuel, K. (2007) What we know about climate change. MIT Press, Cambridge, MA.

[2] Weart, S.R. (2003) The discovery of global warming. Harvard University Press, Boston.

[3] Moran, J.M. and Morgan, M.D. (1994) Meteorology. Macmillan College Publishing Company, New York.

[4] Namias, J. (1970) Macroscale variations in sea-surface temperatures in the North Pacific. *Journal of Geophysical Research*, **75(3)**, 565-582.

[5] Kenyon, K.E. (1977) A large-scale longitudinal variation in surface temperature in the North Pacific. *Journal of Physical Oceanography*, **7(2)**, 258-263.

[6] Murphy, D. (2007) To follow the water. Basic Books, New York.

[7] Kenyon, K.E. (1983) Sections along 35°N in the Pacific. *Deep-Sea Res.*, **30(4)**, 349-369.

[8] Kenyon, K.E. (1981) A shallow northeastward current in the North Pacific. *Journal of Geophysical Research*, **86(C7)**, 6529-6536.

Semantic model and optimization of creative processes at mathematical knowledge formation

Victor Egorovitch Firstov

Department of Mechanics and Mathematics, Saratov State University, Saratov, Russia; firstov1951@gmail.com

ABSTRACT

The aim of this work is mathematical education through the knowledge system and mathematical modeling. A net model of formation of mathematical knowledge as a deductive theory is suggested here. Within this model the formation of deductive theory is represented as the development of a certain informational space, the elements of which are structured in the form of the orientated semantic net. This net is properly metrized and characterized by a certain system of coverings. It allows injecting net optimization parameters, regulating qualitative aspects of knowledge system under consideration. To regulate the creative processes of the formation and realization of mathematical knowedge, stochastic model of formation deductive theory is suggested here in the form of branching Markovian process, which is realized in the corresponding informational space as a semantic net. According to this stochastic model we can get correct foundation of criterion of optimization creative processes that leads to "great main points" strategy (GMP-strategy) in the process of realization of the effective control in the research work in the sphere of mathematics and its applications.

1. INTRODUCTION

"The book of nature is written by the mathematical language" [1]. This Galilei`s manifesto determined the methodology of natural science development on the basis of observations and experiments, the result of these observations and experiments are interpreted within the frames of corresponding mathematical model. The latter implicitly assumes the mechanism of science integration thus, this methodology of development have been successfully realized during the last century beginning with famous Newton's "Mathematical Priciples of Natural Philosophy" (1687) [2]. The reason of this success is easily explained by L. Boltzmann′s assertion in his book [3]:" The theory is more practical, it is quantum-essence of experiment." One can understand in the sence that quantum-essence is the system of postulates, which is in the foundation of theoretical model of the object under consideration.

In 1948 N. Wiener [4] had stated main cybernetics' positions. He had done it on C. Shannon′s information theory (1948) [5]. According to this theory, any process of control system represents some transformation of systemic information. Information is basis notion of cybernetics and has an abstract quantitative measure. It allows to measure both material and non-material aspects of the object under consideration. Thus, possibilities of mathematical modelling have extended including processes in social and humanitarian fields [6].

With the appearance of computers in the middle of the XX$^{\text{th}}$ century, a separate direction connected with the realization of intellectual systems (IS) has been formed in cybernetics [7,8]. Accents in this case focused on learning of cognitive processes. In 1980s this led to the building of learning ACT-theory [9] and neural network associative model of J. Hopfild [10]. Modern level of IS development represents adaptive learning systems [11].

A half century experience of IS development shows that their possibilities are determined by mathematical model parameters, which are in the ground of IS. Thus, the questions of IS efficiency lead to the parameters op-

timization of corresponding mathematical models which describe given cognitive processes. Formally, it assumes the investigation of topology of semantic nets which realize given cognitive processes. This investigation allows determining the system of net parameters with the help of which one can influence the knowledge system. Thus, optimal control by cognitive processes is carried out, including creative search and interdisciplinary learning.

2. SEMANTIC MODEL OF INFORMAL AXIOMATIC THEORY

Let $S = (M; \Sigma)$ is a mathematical structure, where $M = \{M_1;...;M_k\}$ is a system of ground sets, representing main objects of structure S, and $\Sigma = \{\alpha_1;...;\alpha_s\}$ is a system of axiom, describing ground relations between them. The informal theory $Th(S)$ of the structure S represented denumerable set, the elements of which are ordered by definite rules of conclusion. One can speak of the theory $Th(S)$ as of the structural space information [12], which is formed within given concluded rules in the form of constructively infinite recursive procedure, that is to say, the space $Th(S)$ is some kind of Herbrand's universe analogue.

Theory space $Th(S)$ is given by the digraph $\vec{\Gamma}(S)$, representing the mathematical structure S in the form of semantic net, which realizes the passing of definite object information. At this, the set $Th(S)$ determines the nodes of the object net domain $\vec{\Gamma}(S)$, and its arcs (orientated edges) are given with the help of the commutator I – set of functions f of following type:

$$f: T_1;...;T_n \to T, \quad (1)$$

where $T; T_1;...: T_n \in Th(S)$, and symbol $\to$ means informal logical consequence of the statement T from $T_1;...;T_n$. Digraph $\vec{\Gamma}(S)$ is appeared by the pair $(V; E)$, where the set of nodes V and the set of arcs E is defined by the expressions:

$$V= Th(S) \cup I; \quad E \subset (Th(S) \times I) \cup (I \times \bar{\Sigma}), \quad (2)$$

where $\bar{\Sigma}$ is the complement of the system axioms Σ till $Th(S)$, and, without community restrict, the axiom system Σ may be considered independent. For a given digraph $\vec{\Gamma}(S)$, the system of nodes $\Sigma \subset Th(S)$ represents the sources and, thus, $\vec{\Gamma}(S)$ represents of the semantic net, which determines the information space structure of axiomatic theory $Th(S)$.

3. TOPOLOGICAL PROPERTIES OF THE SEMANTIC NET $\vec{\Gamma}(S)$

In order to investigate semantic net properties $\vec{\Gamma}(S)$,

topological presentations, realized according to two directions, are used [12].

The first direction determines routes, distances and connection between subject nodes of the semantic net $\vec{\Gamma}(S)$. Let on the digraph $\vec{\Gamma}(S)$ (2) the nodes are distinguished $v_0; v_1;...; v_n \in V$, which form the sequence of arcs

$$\vec{L}(v_0;...;v_n): (v_0; v_1)(v_1; v_2)...(v_{n-1}; v_n) \in E, \quad (3)$$

where $(v_i; v_{i+1}) = (v_i; f_i)(f_i; v_{i+1}); \quad f_i \in I; \quad i = \overline{0; n-1}$. Thus, the oriented route is given, connecting the node v_0 with v_n (it means, that the node v_n is reached from the node v_0), and the nodes v_i, $i = \overline{0; n-1}$, are called intermediate ones on the route (3), and this fact is expressed in the form of: $v_0 \prec v_i \prec v_n$. The route length (3) and the distance from the node v_0 to the node v_n are, correspondingly, determined by correlations:

$$|\vec{L}(v_0;...;v_n)| = n; \quad |\vec{r}(v_0; v_n)| = inf |\vec{L}(v_0; v_n)|, \quad (4)$$

where $|\vec{L}(v_0; v_n)|$ is the set of all route lengths, connecting the node v_0 with v_n.

The second direction of semantic net $\vec{\Gamma}(S)$ investigations is carried out with the help of special system of coverings, which is formed by the following way. For arbitrary node $T \in Th(S)$ the set is determined:

$$U(T) = \{T_i / T_i \prec T \lor T_i = T, T_i; T \in Th(S), i \in N\} \subset Th(S), \quad (5)$$

the elements of which represent the nodes, for which the node T is reached on the digraph $\vec{\Gamma}(S)$. The set $U(T)$ is called the sphere of dominating of the node T in the space $Th(S)$, and its power $|U(T)|$ determines the capacity of the dominating sphere U(T). Capacity $|U(T)|$ in given case represents topological of information quantity according to N. Rashevsky [13]. The following topological properties are set up for dominating spheres:

1) $T_1 \in U(T) \Leftrightarrow U(T_1) \subseteq U(T)$, (6)

moreover, the equality $U(T_1) = U(T)$ at $T \neq T_1$ is equivalent to the fact, that the nodes $T; T_1$ are linked by the cycle.

2) If $U(T_1) \cap U(T_2) \neq \varnothing$ and sets $U(T_1), U(T_2)$ are not linked by implication, then among nodes $T \in U(T_1) \cap U(T_2)$, at least one of them, is a point of net branching $\vec{\Gamma}(S)$.

Let $\vec{L}(\Sigma; T)$ is the set of routes, leading from axioms Σ to the node T. Then with the help of (4), the distance from Σ to T and the diameter of the sphere $U(T)$, are correspondently, determined:

$$|\vec{r}(\Sigma; T)| = \inf |\vec{L}(\Sigma; T)|, d(U(T)) = \sup |\vec{L}(\Sigma; T)|. \quad (7)$$

Within the conception capacity (5) and distance (7), a recursive procedure is determined, for forming the sys-

tem of inclusion coverings in the theory structure $Th(S)$.

Theorem 1. In the space $Th(S)$ one can always underline a denumerable assemblage of subsets, which form the chain

$$Th(S) \supset Th_1(S) \supset Th_2(S) \supset ..., \quad (8)$$

thus, the chain of inclusion coverings of the space $Th(S)$ is formed:

$$h(S) \subset h_1(S) \subset h_2(S) \subset ... , \quad (9)$$

where $h(S) = \{U(T) : T \in Th(S)\}$, $h_i(S) = \{U_i(T) : T \in Th_i(S)\}$,

$Th_i(S) = \{T : T \in Th(S), |\vec{r}(\Sigma;T)| \geq i\}, i = 1; 2; ...$

Thus, algorithm of knowledge generalization is given in the semantic net $\vec{\Gamma}(S)$: if a certain section $h_i(S)$ is chosen in chain (9), then an object sphere of knowledge $Th(S)$ is covered by the system of spheres $U_i(T) \in h_i(S)$ and in each of such sphere the dominated node $T \in U_i(T)$ presents the generalization of the rest elements of sphere $U_i(T)$. As a result, the spheres $U_i(T)$ are classified by some system of characteristics in order to form an appropriate conception. Accordingly, the property (9) in the process of generalization realizes the principle of "matryoshki", and as a result the level of abstraction′s conception is gradually increasing. It means that the process of getting knowledge is connected with the development of intellect.

4. OPTIMIZATION OF THE DEDUCTIVE CONCLUSION ON SEMANTIC NETS

Let among the statements $T \in Th(S)$ there is finite set of positions $T_{i_1}; ...; T_{i_k}$, for which in the net $\vec{\Gamma}(S)$ there is the only function $f_m \in I$ with the range of definition Dom $f_m = \{T_{i_1}; ...; T_{i_k}\}$. This function realizes the informal logical conclusion:

$$f_m : T_{i_1}; ...; T_{i_k} \longrightarrow T. \quad (10)$$

If Dom $f_m \not\subset \Sigma$, then each of the nodes $T_{i_1}; ...; T_{i_k} \in$ Dom $f_m \setminus \Sigma$ similarly (10) has a corresponding I-node and also occurs the result, one-valued following from corresponding positions of predicate universe $Th(S)$ and so on, till we come to the proofs:

$$f_{11} : \Sigma_1 \to T_1; f_{12} : \Sigma_2 \to T_2; ...; f_{1r} : \Sigma_r \to T_r, \quad (11)$$

where $\Sigma_1; ...; \Sigma_r \subseteq \Sigma$ 5. Thus, in general case, procedure's

proof of the statement $T \in Th(S)$ is a partially ordered set $B(T)$, which is made up of predicate nodes, structured through functions (10),(11). It is evident, that $B(T) \subseteq U(T)$ and, hence, the sphere of dominating $U(T)$ present a union of the all possible proofs` of the statement T.

Let $\overline{L}(\Sigma;T)$ is a set of routes from the axioms Σ to the node T in the proof $B(T)$ (10),(11). Then, the length $|\vec{b}(T)|$ of proof $B(T)$ presents critical way on $B(T)$ and is determined through recursion:

$$|\vec{b}(T)| = \max (|\vec{b}(T_{i_1})|; ...; |\overline{b}(T_{i_k})|)+1 = d(B(T)), \quad (12)$$

where $d(B(T))$—the diameter of the proof $B(T)$, which is determined similarly (7).

Apart from the length (12), the proof $B(T)$ is characterized by the capacity $|B(T)|$. Through regulation by these parameters of the conclusion the tasks of the optimization while forming the knowledge, in the form of the theory $Th(S)$ are considered in the net $\vec{\Gamma}(S)$. Let $B_1(T); ...; B_j(T)$ are different proofs of the statement $T \in Th(S)$, having the lengths $|\vec{b}_1(T)|; ...; |\vec{b}_j(T)|$ and capacities $|B_1(T)|; ...; |B_j(T)|$. Then, the following tasks of the optimization are determined on the net $\vec{\Gamma}(S)$:

$$B_0(T) = \text{opt}(B_1(T); ...; B_j(T)) \Longleftrightarrow |\vec{b}_0(T)| = \min(|\vec{b}_1(T)|; ...; |\vec{b}_j(T)|), \quad (13)$$

$$B_0(T) = \text{opt}(B_1(T); ...; B_1(T)) \Longleftrightarrow |B_0(T)| = \min(|B_1(T)|; ...; |B_j(T)|) \quad (14)$$

Each of the tasks (13), (14) present the optimization of the statement proof $T \in Th(S)$, accordingly, by the minimization of its length or capacity. On the whole, these tasks may be considered together. This statement of optimal tasks means the simplification of the proof through reducing the volume of the analysed information. On the whole, it is coordinated with the principles of the information theory.

For example, the optimization of Pythagorean theorem proofs was carried out according to criteria (13); (14), through the analysis of existing variants in school geometry: Euclidean classical proof, the proofs of indian mathematician Bhascara and vectorial method of proof with the help of scalar product [12]. The parameters of the proofs of Pythagorean theorem T in the Euclid's, Hillbert's and Weyl's axiomatics are given in the **Table 1**.

Table 1. Metric characteristics of main versions of proofs Pythagorean theorem in different axiom system.

Proof	Axiomatics	i	$|\vec{b}_i(T)|$	$|B_i(T)|$
Euclid	Euclid (IV B.C.)	0	10	36
Bhascara (proof-I, ~1150)		1	9	23
Bhascara (proof-II, ~1150)	D. Hilbert (1899)	2	12	35
vectorial method	H. Weyl (1918)	3	2	12

As it is seen from the **Table 1**, the optimization of proofs according to the criteria (13), (14) the preference is on the side of the vectorial proof in Weyl's axiomatics. However, the rise of abstraction level happens in the teaching process, which is in the inverse dependence with didactic principles of accessibility and visual teaching aids. This fact has its reflection in Russian teaching literature on elementary geometry. The analysis of this literature for the period of 1768-2000 shows, that in the second half of the XIX$^{\text{th}}$ century, Euclid's classical proof is practically nowhere met in school textbooks and Bhascara′s proofs are mostly used, because they are more vivid and accessable [12].

5. FORMALIZATION OF CREATIVE PROCESSES DURING THE ASSIMILATION OF THE SPACE *Th*(*S*) AND THE RANGE SIGNIFICANCE OF THE ELEMENTS IN THE NET $\vec{\Gamma}(S)$

One can regard creative processes in the training as the generalization of knowledge at the metalevel with the help of heuristics. The link between metalevel knowledge and the known object sphere of knowledge is formally expressed in the fact, that the space *Th*(*S*) is formed with the help of endless recursive procedure and, hence, one can say of current statement $Th_1(S)$, for which $\Sigma \subset Th_1(S) \subset Th(S)$, then knowledge metalevel is introduced with the help of partition

$$Th(S) = Th_1(S) \cup CTh_1(S), \qquad (15)$$

where $CTh_1(S)$ is the complement $Th_1(S)$ till $Th(S)$, which determines the knowledge metalevel in the form of nodes. To these nodes relation of incidence in the net $\vec{\Gamma}(S)$ is heuristically established. The partition (15) in the net $\vec{\Gamma}(S)$ induces set partition of functional nodes $I = I_1 \cup CI_1$, where CI_1 is the set of functions, realizing the conclusion to metalevel:

$$CI_1 : Th_1(S) \rightarrow CTh_1(S). \qquad (16)$$

Correlations (15) and (16) present a formalisational description of the knowledge generalization procedure to metalevel in the process of axsiomatical theory *Th*(*S*) formation. The optimization procedure of this process is forming in the range of presentation about node significance in the semantic net.

Let $U(T)$ is the sphere of dominating of the statement T and $B_1(T)$; …;$B_n(T)$ are possible proofs of this statement, having lengths $|\vec{b}_1(T)|;…;| \vec{b}_n(T)|$. Let us call the quantity

$$D(\Sigma;T) = \min (|\vec{b}_1(T)|;…;| \vec{b}_n(T)|) \qquad (17)$$

some logical distance from axiom`s $\Sigma \subset Th(S)$ to the statement *T*. In fact, logical distance $D(\Sigma;T)$ coincides with algorithmical determination of information quantity according to A.N. Kolmogorov [14].

Formally, any significance presents a partial order in the space *Th*(*S*) and it is given in the form of domination relation according to Pareto:

$$T_1 \lhd T \Leftrightarrow |U(T)| \geq |U(T_1)| \wedge D(\Sigma;T) \leq D(\Sigma;T_1), \quad (18)$$

where one of the inequalities is strictly done. In the case of defining (18), the statement T is considered to be significant than T_1 and it means that more important elements of the space *Th*(*S*) are more influential (the first inequality in (18)), and they are closer to the information system sources Σ (the second inequality in (18)). One can also interpret the significant elements as huge main points of the net $\vec{\Gamma}(S)$, which are closer to its sources.

6. GMP-OPTIMIZATION STRATEGY OF CREATIVE PROCESSES IN THE FORMATION OF MATHEMATICAL KNOWLEDGE

The reasons of relationships significance (18) is carried out in the language of theory′s random processes [15]. As in the process of creative searching the moments of revealing time t of new theory form statements *Th*(*S*) are not determined, then its creation presents a random process *Th*(*S*;*t*) with continuous time $t \geq 0$ and with denumerable set of the states, the moments of transitions between them are distributed in the interval $t > 0$ by chance.

<u>Theorem 2.</u> The random process *Th*(*S*;*t*) is a heterogeneous branching Markovian process.

Heterogeneous in time, the branching Markovian process Th(S;t) is determined as a process, the transition probability $P_{in}(\tau;t)$ of which satisfy the Kolmogorov-Chapman equation with branching condition:

$$P_{ik}(\tau;t) = \sum_{r_1+…+r_i=k+i(l\text{-}1)} P_{l r_1}(\tau;t)P_{l r_2}(\tau;t)...P_{l r_i}(\tau;t), (19)$$

where $P_{ik}(\tau;t)$ is the probability of the condition having *i* elements at the moment τ, to the moment *t* it will contain $k \geq i \geq l = |\Sigma|$ elements and the evolution $P_{ik}(\tau;t)$ is described by Kolmogorov system of differential equations for the heterogeneous branching Markovian process [16].

The reason of Pareto-optimization procedure by significance criterion (18) means that when the information space theory *Th*(*S*) is mastered by chance and is realized by branching Markovian process *Th*(*S*;*t*) then more significant theory statements *Th*(*S*) have higher probabilities of transitions between the process statements *Th*(*S*;*t*) and the result of this is as follows: let $P_{ik} = P_{ik}(\tau;t)$ is

the solution of Kolmogorov equations under condition (19). That will be enough to examine an example $k = i + 1$ and then from the branching condition (19) you will get:

$$P_{i,i+1} = iP_{l,l+1}P_{ll}^{i-1} = i(1-P_{ll})P_{ll}^{i-1}. \qquad (20)$$

With the increasing the length of the interval $(\tau; t)$, the meaning $P_{ll} \to 0$ and the function $P_{i,i+1}$ is increasing in the wide range $l \leq i < -\ln P_{ll}$. Since the meaning i in this case is linked with the quantity $Th(S)$, which corresponds to i-state of the process $Th(S;t)$, then it goes without saying, that, under other similar conditions, the dominating sphere $U(T)$ with more capacity $|U(T)|$ has more chances to widen, because the probability of proof of new statements at forming theory $Th(S)$ is increasing. Thus, the reason of the first inequality in the Pareto-optimization procedure (18) is given. However, the growth of transition`s probability $P_{ik}(\tau; t)$ in this model occurs not only with the growth i, but also with the decrease τ, because in this case the interval length $(\tau; t)$ is increasing. The τ decrease is equivalent to the decrease of logical distance (17) that leads to the reasons of second inequality in Pareto-optimization (18). Thus, the conception of the range significance of the statements` theory $Th(S)$ by means of Pareto-domination (18) has a sufficient reason. According to this reason, the optimum control by creative processes in training comes to effective control of definite random process according to the criterion of significance (18). In this case, the effective strategy of theory formation $Th(S)$ in the creative process leads to the conception of "great main points" in the net $\overrightarrow{\Gamma}(S)$ or GMP-strategy. This conception intends the investigation, coming out from significant statements $T_{01}; \ldots; T_{0k} \in Th(S)$, have been chosen according to the net criterion of the significance (18). The inductive hypothesis H, given on the base of these statements, has more chances "to be materialized" as a logical generalization of starting positions. The idea of existing "great main points" is in tune with the modern psychological conceptions in the field of intellectual theory [17]. According to these conceptions, "great main points", which have an increased sensitivity to certain semantic influence, can qualitatively change the character of understanding` problem situation.

7. GMP-STRATEGY AND HILBERT'S MATHEMATICAL PROBLEMS

A vivid illustration of optimization creative search within the framework of GMP-strategy presents the solution of well-known problems in the theory of numbers, and also Hilbert′s problems (1900) [18]. The chronology of their position and solution is exactly known (**Table 2**).

The analysis shows, if the period of decision Goldbach′s, Waring′s and Fermat′s problems in the theory of numbers makes up hundreds of years, then Hilbert′s problems has a unique result, which occurs by 1-2 less. It is important to say, that the choice of 23 problems from a wide manifold of mathematical ones, appearing in the XIX-XX$^{\text{th}}$ centuries according to Hilbert′s report at the II International Congress of Mathematicians (1900), supposed quite certain "rules of selection". The sense of them is the realization GMP-strategy. Those problems are interesting, the decision of which is possible at a given level of mathematical development. These problems can give a further progress to mathematics.

8. THE EXPERIMENT OF GMP-STRATEGY IN INTERDISCIPLINARY LEARNING

The possibilities of GMP-strategy are not limited only by the optimization of the mathematical researches but are spread over the interdisciplinary training level within the framework of morphism′s category. In this case, the author's experience shows, that the realization of GMP-strategy usually takes place on the basis of some

Table 2. The problematic optimization of the research work in mathematics.

Problems		Problem Decision		Period of problem decision, years
Name	Statement Time	Author(s)	Date	
Last Theorem of Fermat′s	$\sim$ 1630	A.Wiles	1995	365
Goldbach′s problem: $n=p_1+p_2+p_3$	1742	I.M. Vinogradov	1937	195
Waring′s problem: $n=p_1^s+\ldots+p_k^s$	1770	D. Hilbert	1909	139-172
		G.Hardy-J.Littlewood	1928	
		Ju.V. Linnik	1942	
Hilbert′s problems	1900	20 problems are solved during the period of 1901-2007		1-107

general scientific methodology for example, in the course of a canon or the conception of centrism.

The conception of canon development is often observed in social sciences for example, in the states theory. As a canon here, the ideals of a democracy state justice can be taken into consideration dating back to the republic of Ancient Rome (510/509 B.C.) and Platon′s dialogues (427-347 B.C.). In this case, GMP-strategy is started through the axiomatization of the justice canon, on the basis of which the deductive theory is formed.

Nowadays, this theory represents a separate sector in mathematics, known as cooperative games, within the framework of which, it became possible to explain the peculiarities of modern democracy [19].

The centrism conception represents a general principle of methodology, the grounds of which dates back to ancient times, having a reflection in antiquity doctrines, traditions and religions. According to Archimedean interpretation, this principle leads to the conception about center of gravity (barycenter) of a material corpse. On the ground of this principle, modern classical mechanics was formed. GMP-strategy on the basis of barycenter conception is formed by the following way. In 1827, A.Möbius gave mathematical grounds to the barycenter of the system′s material points, that is, he came to the grounds of barycenter′s coordinates, which turned out to be projection ones [20]. Thus, mechanic conception of barycenter acquired an abstract interpretation within projection geometry. Furthermore, GMP-strategy can have a lot of variations, for example:

1). With the help of barycenter′s coordinates is given the interpretation of Hardy- Weinberg′s law in the genetic population [21,22] and on this ground, a power interdisciplinary direction in the form of mathematical genetics has appeared [23];

2). In the end of the XXth century, a famous american specialist in the field of psychology of the arts R.Arnheim, propounded a thesis [24], according to which, the psychology of professional artists differs by rather intuitively sensitive color perception and as a result, they, anyhow, see the distribution of color shades on the pictorial field as a balanced one. This thesis is proved by the experience within the conception about the colorimetric barycenter of paintings, developed in the works [25-28], where it is introduced through mapping:

$$Im \times F \to W, \qquad (21)$$

which to every point of the pictorial image Im, depending on its color F, is brought to conformity with a non-negative number from W set, which is designated the colorimetric mass of this point. The mapping (21) determines structural colorimetric of a pictorial work. The colorimetric barycenter of the picture, with the position of which the compositional peculiarities of a given picture are connected, can then be calculated on the basis of the well-known mechanics formulas. As investigations have shown [25-28], the colorimetrical barycenter is a balancing color point of a pictorial work and this fact has been proved by the formation of barycenter ensemble for the large collection of paintings. For this, barycenter ensemble coordinates of pictures are mapped on the unit square and dotting image of ensemble received like this gives an idea about barycenter dispersion relatively to central position. **Figure 1** shows such colorimetric barycenter ensemble from 1174 pictures of painters of the XXth (white dot indicates the average position of the barycenter for the ensemble). It is evident, that artists representing a variety of compositional genres in many cases try to avoid significant deflections from equilibrium of colorimetric mass in the picture. This GMP-strategy within the conception of colorimetric barycenter represents an important component in teaching mathematics in the field of humanity education [29].

In pedagogics GMP-strategy is carried out on the basis of cybernetic conception [30]. Objectively, it is caused by the fact that in the field of didaktikos, pedagogics is based on the theory of cognitive processes, which realize transformation and transfer of information from generation to generation. Cybernetics promotes the development of pedagogical science helping solve arising contradictions between its content and form not only through experience, but also within the category of morphism with the help of modeling and optimization of pedagogical processes. The realization of cybernetic conception while making up the fundamental theory of mathematical models in order to regulate effectively cognitive processes in teaching comes from information nature of pedagogical processes. The control in this case can go on through aim influence on quantitative or qualitative aspects of information, realized in the teaching
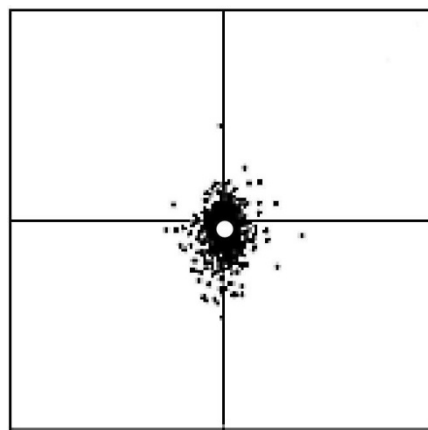
Figure 1. Colorimetric barycenter ensemble from 1174 pictures of painters of the XXth century.

process.

Models, describing the control by cognitive processes through aim influence on quantitative information aspect of corresponding educational content, are formed on the basis of metric functions, which, in this case, have an explicit mathematical form. The procedure of optimization in these models has a universe character, as abstract quantitative information measures are in its ground and the optimal control in this case leads to the improvement of the systems organization of the teaching process through the search of optimal configuration of information nets and flows in this process according to minimum criterion of information entropy. The class of basic models, the control of which is carried out according to the quantitative measures of information, includes: Socrat′s dialogue, testing, class-lesson system of teaching, organization of group cooperation during the teaching process and the procedure of subject planning of the teaching process [31-34]. Given models make up the basis of a number of information technologies, which have been approved in the teaching process. In particular, at optimization of group cooperation in the teaching process the observations have shown the rise of progress standards of education contingent up to 20-25%.

Models, describing the control of cognitive processes through aim influence on qualitative (semantic) information aspect of educational content, are formed within accepted model of knowledge interpretation. In accepted cognitological model (point 2) the system of knowledge is introduced within informal axiomatic theory in the form of semantic net. This net is properly metrized and is characterized by a definite system of coverings in point 3. It makes possible to introduce net parameters of optimization, controlling qualitative aspects of the knowledge system under consideration (points 3-6). To the class of basic models, the control of which is carried out by influence on information semantic aspect, models of formation of education content, creative pedagogics and realization of teaching on interdicipline level are included. The criteria of such control optimization are formulated in points 3;4 and at optimization of deductive conclusion leads to reducing of volume of analyzed information within criteria (13),(14), and at optimization of creative processes they are controlled by criterion of significance (18). These theoretical statements are confirmed not only by experienced data of **Tables 1**, **2**, but also are effectively realized by the author in his teaching work while training teachers of mathematics at Saratov State University after N.G. Chernyshevski (Russia) since 1997.

9. CONCLUSIONS

As a matter of fact, GMP-strategy based on Pare-

to-optimization (18) is treated as a control by definite random process $Th(S;t)$, modeling the creative search while developing the space $Th(S)$. This search turns to be more effective, if it comes from more significant positions. This thesis is acknowledged not only by theoretical premises (points 3-6) and by the success in solving Hilbert's problems (**Table 2**), but by the whole process of historical mathematical development. It is difficult to overrate Pithagor's theorem in Euclid's geometry, Desargues's and Pascal's theorems in projective geometry, Euclid's algorithm in the theory numbers, Viete's theorem in the algebra of polynomial, Cayley's theorem in the theory of groups and so on.

Nowadays the significance of specified states is actual as well. Recently, in the work [35] within the framework of GMP-strategy for determining of Pythagorean triples, a special matrix transformation semigroup's transformation of primitive pairs has been made up. Thus, a close link between Pithagor's theorem and Euclid's algorithm is stated and original approaches to the solution of the oldest mathematical problem about the power of a set of twin primes numbers. It is important to say that, except the original mathematical results, an effective training to the methods of the mathematical creation takes place within the framework of GMP-strategy.

The possibilities of GMP-strategy are not limited only by the control of creative processes in the sphere of mathematical education. In the morphism's category, GMP-strategy is spread on the level of interdisciplinary teaching. Thus, the integration of mathematical knowledge in the field of natural and humanitarian sciences takes place. In this case, GMP-strategy realizes a certain variant of common scientific methodology (for example, canon or centrism). This variant is axiomatized and then theoretical model of the object or phenomenon is formed. It is important to say, that in the process of interdisciplinary GMP-strategy, effective training to the methods of mathematical creation takes place. So, the original reflexive conception in the fields of creative pedagogics is realized on the basis of GMP-strategy.

10. ACKNOWLEDGMENTS

REFERENCES

[1]   Galilei, G. (1964) Il Saggiatore. Opere. Salani, Firenze.

[2]   Newton, I. (1946) Mathematical Principles of Natural Philosophy. The Universitet of California Press, Berkley.

[3]   Boltzmann, L. (1909) Wissenschaftliche abhandlungen. Leipzig.

[4]   Wiener, N. (1961) Cybernetics (or control and commu-

nication in the animal and machine). The MIT Press, New York.

[5] Shannon, C.E. (1948) A mathematical theory of communication. *Bell System Technical Journal*, **27(3)**, 379-423.

[6] Henry, P. and Lazarsfeld, N.W. (1966) Readings in mathematical social science. In: P. F. Lazarsfeld and N. W. Henry Eds., A Collection of Articles, Science Research Associates, Chicago.

[7] Rosenblatt, F. (1958) The perception: A probabilistic model for information storage and organization in the brain. *Psychological Review*, **65(6)**, 386-408.

[8] Feigenbaum, E.A. (1963) Computers and thought. In: E. A. Feigenbaum and J. Feldman Eds., A Collection of Articles, McGraw-Hill Book Co., New York, 477-523

[9] Anderson, J.R. (1983) The architecture of cognition. Harvard University Press, Cambridge, Massachusetts, USA.

[10] Hopfild, J.J. (1982) Neural networks and physical systems with emergent collective computational abilities. *Proceedings of the National Academy of Sciences of USA*, **79(8)**, 2554-2558.

[11] Brusilovsky, P. (1996) An intelligent tutoring system onWorld-Wide Web. *Proceedings of the 3th International WWW Conference*, Fraunhofer Institute for Computer Grafics, Darmstagt, 42-45.

[12] Firstov, V.E. (2006) The semantic model and optimization trough mathematical knowledge formation and propagation. *Vestnik Saratov State Technical University*, **3(14)**, 34-43.

[13] Rashevsky, N. (1955) Live, information theory and topology. *The Bulletin of Mathematical Biophysics*, **17(3)**, 25-78.

[14] Kolmogorov, A.N. [in Russian: Колмогоров А. Н. (1965) Три подхода к определению понятия "количество информации". *Проблмы передачи информации.* Т.1, вып.1, сс.3-11].

[15] Firstov, V.E. (2006) The stochastic model by the information space of deductive theory formation and optimization of the research work in mathematics. *Vestnik Saratov State Technical University*, **4(17)**, 13-21.

[16] Harris, T.E. (1963) The theory of branching processes. Springer-Verlag, Berlin-Göttingen-Heidelberg.

[17] Glaser, R. (1984) Education and thinking: The role of knowledge. *American Psychologist*, **39(2)**, 93-104.

[18] Hilbert, D. (1900) Mathematische probleme. *Nachr. Ges. Wiss. Göttingen*, 253-297.

[19] Moulin, H. (1988) Axioms of cooperative decision making. Cambridge University Press, Cambridge-New York-New Rochelle-Melbourne-Sydney.

[20] Möbius, A.F. (1885) Der barycentrische calcul. Bd. 1, Gesammelte Werke, Leipzig.

[21] Hardy, G.H. (1908) Mendelian proportions in a mixed population. *Science*, **28(706)**, 49-50.

[22] Weinberg, W. (1908) Über den Nachwies der Vererbung beim Menschen. *Jahreshefte des Vereins for Vater- landische Naturkunde in Würtemberg*, **64**, 368-382.

[23] Crow, J.F. and Kimura, M. (1970) An introduction in Population Genetics Theory. Harper and Row, New York.

[24] Arnheim, R. (1988) The power of the center. A study of composition in the visual arts. University of California Press, Berkeley.

[25] Firstov, V.V., Firstov, V.E. and Voloshinov, A.V. (2005) Conception of colorimetric barycenter in painting analysis. *Proceedings of the International Congress on Aesthetics*, *Creativity and Psychology of the Arts*, Moscow, 2005, 258-260.

[26] Firstov, V.V., Firstov, V.E. and Voloshinov, A.V. (2006) The concept of colorimetric barycenter in group analysis of painting. *Culture and Communication: Proceedings of the XIX Congress International Association of Empirical Aesthetics*, Avignon, France, 2006, 439-443.

[27] Firstov, V. V., Firstov, V. E., Voloshinov, A. V. and Locher, P. (2007) The Colorimetric Barycenter of Paintings. *Empirical Studies of the Arts*, **25(2)**, 209-217.

[28] Firstov, V.E., Firstov, V.V. and Voloshinov, A.V. (2008) The concept of colorimetric barycenter and visual perception of the color balance center in painting. *Proceedings of the XX Biennial Congress of the International Association of Empirical Aesthetics*, Chicago, USA, 2008, 273-277.

[29] Firstov, V.E. (2009) About teaching math in humanitarian specializations and occupations in IHE. *Higher Education Today*, **2**, 82-84.

[30] Firstov, V.E. (2009) Cybernetic concept of current educational process. *Higher Education Today*, **3**, 66-68.

[31] Firstov, V.E. (2007) Dialogue education: Cybernetic aspect. *Vestnik Saratov State Technical University*, **4(28)**, 135-145.

[32] Firstov, V.E. (2008) Informational conception of optimization of group cooperation in teaching. *Vestnik Saratov State Technical University*, **3(34)**, 105-109.

[33] Firstov, V.E. (2008) The concept of defeveloping training of L.S. Vygotsky, pedagogics of cooperation and cybernetics. *Yaroslavl Pedagogical Bulletin*, **3(56)**, 98- 104.

[34] Firstov, V.E. (2009) Expert systems and information conception in developing training. *Yaroslavl Pedagogical Bulletin*, **1(58)**, 69-73.

[35] Firstov, V.E. (2008) A special matrix trasformation semigroup of primitive pairs and the genealogy of pythagorean triples. *Mathematical Notes*, **84(2)**, 263-279.

Possible schemes of calculation modeling in a quantum computer

Vladimir Voronov

Irkutsk State Technical University, Irkutsk, Russia; voronov@istu.edu.ru

ABSTRACT

In the present work a possibility of computation modeling, which should be realized in a real quantum computer, is discussed. In this connection two models of a device, which work is determined by the structure and dynamics of real molecular systems are reported.

Keywords: Quantum Computers; Strong-Correlated Systems; Entanglement of States

1. INTRODUCTION

The present work deals with a possibility of computation modeling, which should be realized in a real quantum computer. In this connection, the models of a device, which work is determined by the structure and dynamics of real molecular systems are reported.

Recently [1,2] we have put forward an idea, which realization would allow one to overcome, at least, some problems related to the creation of quantum computers, *i.e.*, the idea of molecular Internet. According to this idea, every molecular system with its own set of degrees of freedom and (or) states represents a server having memory of certain volume. This server is used for storage and transmission of the information. The latter is further transformed in computational operations during the solution of specific mathematical task. If to assume that quantum computer has to perform the same operations as the classical one, the necessary memory volume of such a server could be achieved by two (at least, in principal) routes: 1) introduction of maximum amount of atoms playing the role of q-bits into the molecular system; 2) combination of separate molecules in a spatially ordered structure where physical and chemical interactions of any nature can be realized. These interactions will ensure the formation of superpositional coherent states needed for the performance of computational operations. The above approaches are quite reasonable from the viewpoint of the modern theoretical notions on quantum cal-

culation problem. But, in our opinion, the ways of this problem solution are beyond the frameworks of the conventional theory. Below we will discuss some general concepts, which can pave the road to new approaches to the problem of quantum computer creation.

2. MODELING PRESENTMENT OF QUANTUM COMPUTING

According to the Shor theory [3], a certain number of states remain free in the course pf information input. In principle, these states can be used for the performance of parallel calculations. Since a number of such states can be very large (relative to the corresponding number of q-bits), the tasks which previously seems insoluble become realistic. As applied to the molecular Internet idea, one can correlate the states of quantum particles (q-bits) with real molecular objects with all far-reaching consequences. Thus, keeping the idea of quantum calculations intact, it is possible to impart it a real content. Really, if the quantum states aforementioned are still virtual, the molecular states are manifested themselves in macroworld by many phenomena which reflect quite adequately these states. Therefore, these states become experimentally accessible. The problem is in the correlation of these states with the corresponding mathematical patterns. Hence, the application of these states for the solution of specific task should involve the usage of the information, which is already contained in the molecular structure.

Logic route to the realization of the molecular Internet idea is in combined application of the spatial molecular structure and spin values of q-bits constituting this molecular structure. Really, we have mentioned above that the problem is in the search for an approach which allows quantum systems (due to the peculiarities of structure and/or behavior) to be manifested in the macroworld. Therefore, if one can manage to correlate q-bit spins with molecular structure this will mean the realization of such an approach. Thus, the circle is closed, *i.e.* there is

a principal way to the organization of quantum states detection without any distortion of this state. Experimental realization of the approach becomes predictable: combined usage of the information on the molecular system state and spins (q-bits) contained in this system. Further problems of quantum calculations are the matter of technique to some degree, though not very simple.

The experimental investigations carried out by the present time are far from the realization of quantum calculation idea. Indeed, even though the elementary quantum algorithms have been already elaborated using the NMR method [4-6], the possibility of the creation of real quantum computers on the basis of this phenomenon is yet to be proved. The probable application of other physical methods for this purpose is under discussion. In this case, the approach based on the preliminary modeling the operation scheme, which should be realized in a quantum computer (followed with its embodiment in specific electronic schemes), seems to be intriguing. By the moment there are many essential prerequisites for such experiments. Really, the preparation of nano-sized heterostructures enables to obtain a wide range of properties for different kinds of device applications. In its turn, the development of physics and technologies of synthetic nanostructures makes it possible to prepare them in quite wide variety (see [7] and the references therein). That is way the above model route to the creation of quantum calculation processors may be considered as promising.

All the aforesaid allow one to propose the following variant to model the real quantum calculation. Preliminary it is worthwhile to note that according to the current theoretical notions, to reach the goal one should have such devises (as the starting universal logic block), which can perform repeatedly logic operations "NOR" and "controlled NOR". In other words, these devises (logic gates) must possess a property of reversibility. Among such devices is the Toffoli three-bit gate (see, for example, [8,9] and the references therein). If to stay further within the framework of the model proposed, one should create the elementary blocks: gates; each of them must incorporate three q-bits interacting with each other. At the same time, the environment of each q-bit must be suitable for the triggering the calculation procedure. These blocks can be formed by three nano-sized objects containing an electron with a specific spin state. Next, one should model the reversibility property of the three q-bit gate. This can be attained due to the multiple reproduction of the above block from three nanoobjects as well as the application of special commutating devices operating, for example, on the basis of femto-second laser.

This brings up the questions: "To what degree the pro-

posed method for the organization of quantum calculations is realistic and what are the dimensions of the devise capable of such operations as quantum calculations?" If one is limited here by the qualitative answers to the questions arisen it would be reasonable to pay the attention to the germanium and silicon nanostructures prepared recently using scanning tunnel microscope [7]. In this case, one can grow the nanoobjects (islands of approximately 10 nm size at the base and some nm in height) located in about 50 nm from each other. It is an easy to evaluate that every square centimeter will contain about 10^{10} of such islands. Therefore, from the nanoobjects mentioned one can create (at least, in principle) the appropriate number of the gates (by collecting the islands in groups) to make up the processor, capable of solving the real tasks.

3. MODELING OF QUANTUM CORRELATION

Another step of the quantum calculations needs to be modeled. We mean here the entanglement of states or quantum correlation of the q-bits system localized in nano-islands. This is a mandatory step preceding the calculations [8,9]. Therefore, one can speak about preparation of the entangled state. To model the above step, it is proposed to use the self-organization of quantum (molecular) systems. In other words, one should synthesize the molecules where the entanglement of states is provided due to the self-organization of atoms. Such a possibility could be evaluated as follows. Let the dependence of deviation amplitude $f(x)$ on the initial state x is defined by the expression:

$$f(x) = ax - bx^n, \qquad (1)$$

where a and $b -$ are constant positive coefficients, $n \geq 2$. If $x \ll 1$, then $bx^n \ll ax$, therefore

$$f(x) \approx ax \qquad (2)$$

Thus, in the case of (2), $f(x)$ grows linearly with growth of x. If x value is comparable with 1, it would be impossible to neglect the bx^n member, since for the description of the system behavior one should use the initial Equation (1). Hence, the growth of function deviation at the expense of ax member will cause nonlinear limitation owing to the deduction of bx^n value. Under several x values, the $f(x)$ function will be close again to zero and all starts from the beginning. The system will automatically regulate itself, as its properties depend on a current state (in this case—from x value). Therefore, it is reasonable to conclude that by somehow changing the given molecular system, it is

possible to achieve (in principle) the necessary values for the corresponding parameter (or parameters). Obviously, such changes could be carried out by three ways: 1) the introduction of new atoms to molecular structure; 2) the external action (for example, applying an electromagnetic field); 3) the combination of these two ways.

The fundamental problem is to understand what molecular objects can be suitable for similar manipulations. Based on the most general ideas, one can assume that here one should deal with the compounds where characteristic intramolecular interactions will ensure the realization of the required (from a position of a problem discussed here) quantum states. These are the compounds containing atoms with unfilled $3d-$, $4f-$ and $5f-$ shells. In solids, such atoms retain localized magnetic moments completely or partially. The strong interaction of electrons of these groups with each other or with collective electrons of outer shells represent a peculiarity imparting the unique properties to a variety of the compounds containing atoms of transition and rare-earth elements. The investigations carried out over the last fifteen – twenty years have shown that for these compounds the diverse physical phenomena are possible. Among them are phase transitions resulting in the magnet-ordered phases and superconductivity, dielectric and metal states; transitions with appearance and disappearance of the localized magnetic moments. The specified properties are the consequence of strong interactions of electronic and magnetic degrees of freedom. The systems with strong interaction of electrons are referred to as the strong-correlated systems [10].

Particularly, the functional dependence (1) can follow to any parameter, which is characteristic for the given molecular system. It is only necessary that the parameter would periodically undergo such changes that its limiting values would correspond to those quantum states which should be used for modeling the process of the quantum calculations. These states can be realized for the molecular systems which behavior at the macroworld level (in laboratory system of coordinates) is connected with the manifestations of heterogeneity of intra-molecular processes. Just due to the peculiarities of structure and dynamics of the molecular system, the nonlinearities, which will provide periodicity in change of a parameter characterizing its behavior, becomes possible. Apparently, a vivid illustration of the possibility of the specified process realization is the compounds belonging to a new class of polynuclear heterospin complexes containing the ligands with non-paired electron [11]. For example, this is tetranuclear nickel cluster [$Ni_2(OH)_3$ $(C_5H_9O_2)_5(C_5H_{10}O_2)_4$(L)]$1.5C_7H_8$ (I), where $L-$ is a nitroxide radical. The compound (I) is a representative of the aforementioned strongly correlated systems.

According to the data reported in the work [11],

spin-Hamiltonian, describing the exchange magnetic interactions in these compounds, looks as follows:

$$H = -2JJ_0S_1S_2 - 2J_1\left(S_1S_3 + S_2S_4\right) - 2J_2\left(S_1S_2 + S_2S_3\right),$$
(3)

where S with the corresponding index is a spin value of unpaired electrons localized on $Ni(II)$ atoms and nitroxyl groups, $J-$ is a parameter characterizing interaction between the mentioned groups. Naturally, in the case of other compounds which differ from compound (I) in structure, the right part of the expression (3) will look otherwise. However, it is important that by selecting the appropriate initial compounds one can obtain such heteronuclear complex where the interaction of groups having unpaired electron spins will provide the fulfillment of the condition (1).

The question is arisen: "What is nature of quantum object state allowing the model of entanglement to be realized?" To answer the question, one should take into account the following considerations. The description of quantum states, based on the application of spin-Hamiltonian (3) assumes the availability of free (real) quantum particles, spin carriers S. Meanwhile, the introduction of unpaired electron into the ligand molecule can lead to the appearance of states caused by the interaction of spin S with electrons of the ligand molecule. It is known that the description of such a collective behavior is often associated with the use of the quasi-particle concept. For example, the notions on magnetic polaron or ferron turned out to be fruitful for the explanation of different heterogeneous charge and spin states in magnets [12]. We will start from the established fact, *i.e.* from the localization of unpaired electron spins in two positions like in paramagnetic heterospin complexes of elements of the first transition group bearing stable iminoxyl radicals [11]. In the case of unpaired electron spins related to the central ion, with which the ligand molecules are coordinated, it is a common knowledge that the behavior of the spins mentioned can be unambiguously described accounting for $3d-$ orbitals of a metal. We will address therefore to unpaired electrons which are localized on ligands.

Let us consider a simple case: the presence of unpaired electron localized on a ligand. Obviously, this electron will somehow with an electronic subsystem of the ligand molecules. Indeed, the electronic structure of a specific ligand molecule was formed in the absence of unpaired electron. Therefore, the latter should be considered as a certain excitation. Further on, let us admit that that owing to peculiarities (in this case, the specification is not important) of spatial and electron structure of the complex and under the conditions of thermodynamic equilibrium (set by the sample temperature),

ferron-like states are realized in ligands. Here it is necessary to explain that full spin of ferron state is formed by the local spin and electron spin (see [12] and the references therein). As to the local spin is concerned, it is caused by magnetic (in particular, antiferromagnetic) state of the matrix, where the conductive electron moves. In other words, there is always specific information on the state of such a matrix.

Formally, in the case of heterospin complexes discussed here, a matrix, in which the unpaired electron with spin $S = 1/2$ is inserted, is a ligand molecule and not solid phase of microsample as it is observed in manganites [12]. The assumption on realization of ferron-like states should mean that the result of the interaction of unpaired electron with electron subsystem of the ligand will be the state with non-compensated electron spin which differs from the state of free electron. In our case, the quantum objects employed in the calculations are electrons. The emergence of ferron states allows one to distinguish electrons transferred to these states for a while. For a certain time, an electron is located on $d-$, or f-orbitals of the central ion (for example, nickel). Further, due to the specifics of intramolecular spin-spin interactions the electron is temporarily transferred to ferron state. In a certain period of time (typical for ferron), the electron is again located on metal orbitals. Then the cycle is repeated. Here, once should stress once again that the ferron state differs from the free electron state. Really, it is a common knowledge that a peculiar feature of the objects called quasi-particles is the difference of their mass from the mass of the corresponding free particle. So, the mass of polyaron is hundrets times higher than that of free electron. This feature is also inherits in ferrons [12]. As was mentioned above, the full spin of ferron state also differs from spin of free electron. Thus, the state of entanglement, needed for operation of a quantum computer, turns out to be modeled. The possible route to a large number of quantum objects has been described above.

One should explain why heterospin complexes can be considered as possible objects to model quantum calculations. These are paramagnetic systems containing as ligands the molecular systems having unpaired electron or unpaired electrons. The role of $d-$ or $f-$metal orbitals here is two-fold. Their population with unpaired electrons participating in intramolecular spin-spin interactions ensures the validity of the expression (1). Besides, it is just unpaired electron on these orbitals, being free relative to its magnetic properties, is transferred for a while to other state needed for modeling the entanglement of quantum particle. By changing the structure and composition of a paramagnetic compound as well as the external conditions one can control the entanglement degree of ferron state and state of a free electron, thus controlling also the calculation procedure.

4. CONCLUSIONS

In conclusion, one should make the following remarks. The experimental investigations carried out by the present time are still far from practical realization of the quantum calculations idea. Therefore, while the suitable objects for realization of quantum computers idea will be searched, certain intermediate variants could appear. In such a situation, an approach based on preliminary modeling the operations which should be realized in a real quantum computer with their subsequent application in specific electronic schemes, seems to be attractive. For this purpose the compounds containing the atoms with vacant $3d-$, $4f-$ and $5f-$shells could be suitable. We mean here the compounds (for example, heterospin complexes), which unique properties are caused by strong interactions of electronic and magnetic degrees of freedom, *i.e.* strongly correlated systems. Among these compounds could be, in particular, heterospin systems, *i.e.* the complexes of paramagnetic ions of transition metals with organic radicals, since spin-spin coupling between unpaired electron spin of different paramagnetic centers of the molecule is typical for such objects. The coupling mentioned can result in phase immiscibility to afford heterogeneous spin states. In its turn, such states can be used for modeling the processes characteristic of quantum computer.

REFERENCES

[1] Voronov, V.K. (2005) Possible approach to the solution of quantum computers problem. *Quantum Computers & Computing*, **5(1)**, 3-6.

[2] Voronov, V.K. (2006) NMR and the problem of quantum computer creation: New outlook. In: Susan Shannon, Ed., Trends in Quantum Computing Research, NOVA Publisher, New York, 73-90.

[3] Shor, P.W. (1994) Algorithms for computation: Discreta logarithms and factoring. *Proceeding of the 35th Annual Symposium on the Foundation of Computer Science*, Los Alamitos, CA, USA, 1994, 124-134.

[4] Jones, J.A. and Mosca, M.J. (1998) Implementation of a quantum algorithm on a nuclear magnetic resonance quantum computer. *Journal of Chemical Physics*, **109(5)**, 1648-1653.

[5] Chuang, I.L., Gershenfeld, N. and Kubinec, M. (1998) Experimental implementation of fast quantum searching. *Physical Review Letters*, **80(15)**, 3408-3411.

[6] Vandersypen, L.M.K., Steffen, M., Breyta, G., Yannoni, C.S., Sherwood, M.H. and Chuang, I.L. (2002) Experimental realization of Shor's quantum factoring algorithm using nuclear magnetic resonance. *Nature*, **414**, 883-887.

[7] Shklyaev, A.A. and Ichikawa, M. (2006) Germanium and

silicon nanostructure fabrication using a scanning tunneling microscope tip. *Uspekhi Physics Nauk*, **176(9)**, 913-930.

[8] Kilin, S.Ya. (1999) Quantum information. *Uspekhi Physics Nauk*, **169(5)**, 507-526.

[9] Valiev, K.A. (2005) Quantum computers and quantum computing. *Uspekhi Physics Nauk*, **175(1)**, 3-39.

[10] Izyumov, Yu.A. and Kurmaev, È.Z. (2008) Strongly electron-correlated materials. *Uspehi Physics Nauk*, **178(1)**, 25-60.

[11] Ovcharenko, V., Fursova, E., Romanenko, G., Eremenko, I., Tretyakov, E. and Ikorski, V. (2006) Synthesis, structure and magnetic properties of (6-9)-Nuclear Ni(II) trimethylacetates and their heterospin complexes with nitroxides. *Inorganic Chemistry*, **45(14)**, 5338-5350.

[12] Kagan, M.Yu., Klaptsov, A.V., Brodskii, I.V., Kugel, K.I., Sboichakov, A.O. and Rakhmanov, A.L. (2003) Small scale phase separation and electron transport in manganites. *Uspekhi Physics Nauk*, **173(8)**, 877-883.

Call for Papers

Natural Science

A Journal Published by Scientific Research Publishing, USA
www.scirp.org/journal/ns

Natural Science is an international journal dedicated to the latest advancement of natural sciences. The goal of this journal is to provide a platform for scientists and academicians all over the world to promote, share, and discuss various new issues and developments in different areas of natural sciences. All manuscripts must be prepared in English, and are subject to a rigorous and fair peer-review process. Accepted papers will immediately appear online followed by printed hard copy. The journal publishes original papers including but not limited to the following fields:

- **Astronomy & Space Sciences**
  - Astronomy
  - Astrophysics
  - Atmospheric Science
  - Space Physics

- **Earth Science**
  - Geography
  - Geology
  - Geophysics/Geochemistry
  - Oceanography

- **Chemistry**
  - Analytical Chemistry
  - Biochemistry
  - Computational Chemistry
  - Inorganic Chemistry
  - Organic Chemistry
  - Physical Chemistry

- **Life Science**
  - Cell Biology
  - Computational Biology

- Genetics
- Immunology
- Medicine/Diseases
- Microbiology
- Molecular Biology
- Neuroscience
- Pharmacology/Toxicology
- Physiology
- Psychology
- Virology

- **Physics**
  - Applied Physics
  - Atomic, Molecular, and Optical Physics
  - Biophysics
  - High Energy/Particle Physics
  - Material Science
  - Plasma Physics

- **Others**
  - Education
  - History of Science
  - Science and Innovations

We are also interested in: 1) Short Reports—2-5 page papers where an author can either present an idea with theoretical background but has not yet completed the research needed for a complete paper or preliminary data; 2) Book Reviews—Comments and critiques.

➷ Notes for Intending Authors

Submitted papers should not be previously published nor be currently under consideration for publication elsewhere. Paper submission will be handled electronically through the website. For more details, please access the website.

➷ Website and E-Mail

http://www.scirp.org/journal/ns   ns@scirp.org

TABLE OF CONTENTS

Volume 2   Number 8   August 2010